



Measurement of the neutron electric dipole moment at the Paul Scherrer Institute: production of magnetic fields

Pierrick Flaux

► To cite this version:

Pierrick Flaux. Measurement of the neutron electric dipole moment at the Paul Scherrer Institute: production of magnetic fields. Physics [physics]. Normandie Université, 2019. English. NNT: 2019NORMC222 . tel-02409339

HAL Id: tel-02409339

<https://theses.hal.science/tel-02409339>

Submitted on 13 Dec 2019

HAL is a multi-disciplinary open access archive for the deposit and dissemination of scientific research documents, whether they are published or not. The documents may come from teaching and research institutions in France or abroad, or from public or private research centers.

L'archive ouverte pluridisciplinaire **HAL**, est destinée au dépôt et à la diffusion de documents scientifiques de niveau recherche, publiés ou non, émanant des établissements d'enseignement et de recherche français ou étrangers, des laboratoires publics ou privés.



Normandie Université

THÈSE

Pour obtenir le diplôme de doctorat

Spécialité PHYSIQUE

Préparée au sein de l'Université de Caen Normandie

Measurement of the neutron electric dipole moment at the Paul Scherrer Institute : Production of magnetic fields

**Présentée et soutenue par
Pierrick FLAUX**

**Thèse soutenue publiquement le 21/10/2019
devant le jury composé de**

M. NOËL BURAIS	Professeur des universités, Université Lyon 1 Claude Bernard	Rapporteur du jury
M. MAURITS VAN DER GRINTEN	Directeur de recherche, Science and Technology Facilities Council	Rapporteur du jury
Mme FABIENNE LEDROIT-GUILLOU	Directeur de recherche, Université Grenoble Alpes	Président du jury
M. THOMAS LEFORT	Maître de conférences, Université Caen Normandie	Membre du jury
M. GUILLAUME PIGNOL	Maître de conférences HDR, Université Grenoble Alpes	Membre du jury
M. GILLES BAN	Professeur des universités, ENSICAEN	Directeur de thèse

Thèse dirigée par GILLES BAN, Laboratoire de physique corpusculaire (Caen)



UNIVERSITÉ
CAEN
NORMANDIE



Remerciements

Mes premiers remerciements sont adressés au LPC Caen, à l'ensemble de son personnel, et à Gilles Ban, qui a beaucoup fait pour la cohésion du laboratoire, y compris pour les doctorants. Je veux ensuite remercier le jury de thèse de prendre le temps pour évaluer le travail que j'ai effectué. Je souhaite remercier particulièrement Thomas Lefort, qui a été un professeur, puis un encadrant formidable. Il a su dès la licence m'intéresser à nEDM, et son accompagnement durant toute la thèse a été d'un grand secours. Je tiens également à remercier Damien Goupillère, qui arrive à accomplir l'impossible, tout en sachant que ça l'était, et toujours dans la bonne humeur. Je remercie également Xavier qui m'a laissé partager son bureau, et qui a rendu ces trois ans très agréables. Je laisse également un merci à Benjamin Dechenaux qui m'a appris les bases de COMSOL et m'a beaucoup guidé au début de ma thèse, avec beaucoup de patience. Un grand merci aussi à Guillaume qui a su débloquer plus d'une situation dans lesquelles je ne trouvais pas d'issue.

Je remercie également tout les membres de la collaboration nEDM, Philipp, Bernard, Georg, Vira et j'en passe, et plus particulièrement les doctorants avec qui on a passé des soirées formidables dans un pays ou dans un autre. Merci donc Laura, Estelle, Nick, Jacob, Pin-Jung, Duarte, Romain, Arnaud et tant d'autres.

Bien sûr, je ne peux pas ne pas citer dans cette liste de remerciement mes collègues doctorants, avec qui j'ai partagé tant de repas, de soirées et surtout de café ! Merci énormément à vous, Joël, Belen, Edgar, Thomas, Cyril, Yoann (bon, pas vraiment un doctorant, mais on fait une exception !) Raphaël, Alexandre et William (bonne chance à vous deux !), Jienqi, Valentin, Gabriel, Yiyan, Daniel, Debi, Guilherme, Bira, Kendi et Matt. Merci infiniment.

Je termine presque cette liste en remerciant ma famille, qui m'a soutenu tout le long de ces trois ans, et bien avant cela, qui ont fait ce que je suis. Je vous aime.

Enfin, je veux remercier Ai, dont la rencontre à été un nouveau souffle, beau et calme dans la nuit d'Oulan-Bator, qui me soutient dans tous les moments, et qui illumine ma vie de sa joie et de son amour.

谢谢你, 我的土豆, 我的狐狸, 我爱你!

List of figures

1.1	Estimation of the baryon asymmetry η	18
1.2	Electroweak Baryogenesis Principle	20
1.3	The Electroweak Baryogenesis mechanism.	21
1.4	One and two loops EDM diagram from Standard model	23
1.5	Three loops EDM diagram from Standard model	24
1.6	The penguin diagram, leading contribution to the nEDM in the SM	24
1.7	One loop diagram in SUSY violating CP.	24
1.8	Simulation of UCN storage	28
1.9	Neutron lifetime state of art	29
1.10	nEDM state of art	30
1.11	UCN polarization	31
1.12	Spin evolution under a RF field	36
2.1	Principle of the nEDM experiment	40
2.2	Ramsey separated oscillating fields method	41
2.3	The Ramsey pattern	42
2.4	Scheme of the n2EDM apparatus	52
2.5	Schematic view of the PSI UCN source.	53
2.6	Double precession chamber design	55
2.7	Devices monitoring the magnetic field online or offline	56
2.8	The n2EDM detection system	57
3.1	A single circular coil simulated in the COMSOL software	60
3.2	Several COMSOL meshes	61
3.3	Symmetries in COMSOL	63
3.4	Scheme of the single loop	64
3.5	Scheme of an infinite solenoid	65
3.6	Square coil model	67
3.7	Magnetic images of current loops and solenoid.	68
3.8	B_0 coil design	70
3.9	B_0 field variation.	71
3.10	Geometry of the MSR innermost mu-metal layer simulated in COMSOL	73
3.11	Example of oscillating wires simulated in COMSOL	76
3.12	B_0 coil foreseen technical solution	77
3.13	B ₀ door connectors	78

3.14 B_0 coil mounting	78
4.1 TRIM Coil array design	83
4.2 Design of the $G_{1,0}$ and $G_{3,0}$ coils	85
4.3 Design of the $G_{2,0}$ coil	86
4.4 Design of the $G_{1,1}$ and $G_{1,-1}$ coil	88
4.5 Scheme of one $G_{1,1}$ loop	89
4.6 $G_{0,1}$ and $G_{0,-1}$ Harmonic coil design	90
4.7 Correcting coil technical design	90
5.1 EDM from a magnetic dipole aligned along the z axis in nEDM	93
5.2 EDM from a magnetic dipole aligned along the x axis in nEDM	94
5.3 EDM from a magnetic dipole aligned along the z axis in n2EDM	96
5.4 EDM from a magnetic dipole aligned along the x axis in n2EDM	97
1.1 UCN polarisation	108
1.2 Evolution du spin sous un champ uniforme $B_c(t)$ et un champ uniforme B_0	110
2.1 Principe de la mesure de l'EDM du neutron	112
2.2 Méthode des champs oscillants séparés de Ramsey	112
2.3 Figure de Ramsey	113
2.4 Schéma du dispositif expérimental de n2EDM	118
3.1 Image magnétique de boucle de courant et de solénoïdes.	124
3.2 Design de la bobine B_0	125
3.3 Design technique de la bobine B_0	128
3.4 Connecteurs de la porte de B_0	128
4.1 Design du TRIM Coil array	130
4.2 Design des bobines $G_{1,0}$ et $G_{3,0}$	132
4.3 Design de la bobine $G_{2,0}$	132
4.4 Design des bobines $G_{1,1}$ et $G_{1,-1}$	133
4.5 Design des bobines $G_{0,1}$ et $G_{0,-1}$	134
5.1 Faux EDM du à un dipôle et EDM résiduel pour l'expérience nEDM	136
5.2 Faux EDM et EDM résiduel dûs à un dipôle magnétique aligné selon l'axe z dans n2EDM	137
B.1 The COMSOL interface	146
B.2 Finite Element Method meshing in a 1D case	147
B.3 FEM in 1D case with 3 nodes	148
B.4 FEM in 1D case with 5 nodes	150
B.5 FEM results for the 1D exemple	151
B.6 FEM system for the 2D exemple	152
B.7 FEM meshes for the 2D exemple	152
B.8 FEM local functions for the 2D exemple	153
E.1 $G_{1,1}$ Crawford Coil design	161
E.2 First $G_{1,1}$ loop design	161
E.3 Second $G_{1,1}$ loop design	162

List of tables

1.1	Main observables transformations under C,P and T violation	21
1.2	Summary of Electric Dipole Moment limits	25
1.3	Neutron energy classification	26
1.4	Fermi potential V_F and absorption potential W of some materials	26
1.5	Worldwide nEDM experiments	30
2.1	Comparison of the main parameters for the nEDM experiment and the n2EDM experiment	44
2.2	Mercury motional EDM up to the fifth order	50
3.1	B_0 field requirements	60
3.2	Comparison of meshes results from COMSOL simulation	61
3.3	Comparison between several COMSOL simulations using different symmetries .	62
3.4	Main characteristics of the B_0 coil.	69
3.5	Main characteristics of the lamé loops.	69
3.6	Amplitude of the field gradients produced by a perfect B_0 coil.	72
3.7	Influence of MSR on the produced B_0 field	73
3.8	Field requirements for a global misalignment of B_0 in the x or y directions . .	74
3.9	Field gradients and uniformity as a function of a varying vertical misalignment of B_0	74
3.10	Variations of the $G_{2,0}$ and $G_{4,0}$ gradients and of $\sigma(B_z)$ obtained for several shield homotethies.	75
4.1	Trim coils array correction	83
4.2	Misreading of the CsM position depending of their height	87
5.1	Maximum false EDM d_{dip} and residual EDM d_{res} from a dipole in n2EDM and limit on the dipole strength	98
3.1	Contraintes sur le champ B_0	121
3.2	Comparaison des maillages et fonctions d'interpolation dans COMSOL	122
3.3	Comparaison entre plusieurs simulations COMSOL utilisant différentes symétries	122
3.4	Caractéristiques principales de la bobine B_0	124
3.5	Caractéristiques principales des boucles aux extrémités	124
3.6	Amplitude des gradients du champ produit par la bobine parfaite B_0	126
3.7	Evolution des caractéristiques du champ créé par un déplacement vertical de B_0	127

B.1	Quantities introduced for the FEM	151
B.2	Comparision of linear and quadratic functions.	153
C.1	Harmonic Polynomial basis	156
D.1	Formidden and allowed gradient depending of the broken symmetries	158
E.1	Characteristics of $G_{1,0}$ coil	159
E.2	Characteristics of $G_{2,0}$ coil	159
E.3	Characteristics of $G_{3,0}$ coil	160
E.4	Numerical values of the quantities defining the $G_{1,1}$ loops	162

List of abbreviations

EDM	E lectric D ipole M oment
nEDM	n eutron E lectric D ipole M oment
n2EDM	n ew n eutron E lectric D ipole M oment
LPC Caen	L aboratoire de P hysique C orpusculaire de C aen
PSI	P aul S cherrer I nstitute
ILL	I nstitut L aue L angevin
SNS	S pallation N eutron S ource
PNPI	P etersburg Nuclear Physics Institute
UCN	U ltra C old N
MSR	M agnetic S hielding R oom
HgM	M ercury co M agnetometer
CsM	C esium M agnetometer
SM	S tandard M odel
BSM	B eyond S tandard M odel
SUSY	S Uper S Ymmetry
FEM	F inite E lement M ethod

Contents

I The English part	13
Introduction	15
1 Motivations	17
1.1 Physical motivations	17
1.1.1 Matter-antimatter asymmetry	18
1.1.2 Sakharov conditions	19
1.1.3 Electroweak Baryogenesis	19
1.2 C, P and T symmetries	20
1.3 The Electric Dipole Moment and CP violation	21
1.3.1 Definition and CP violation	21
1.3.2 Searches of symmetry violation	22
1.3.3 Status of CP violation in the strong sector	22
1.3.4 Status of CP violation in the weak sector	23
1.3.5 EDM measurements in the world	25
1.4 The neutron Electric Dipole Moment	25
1.4.1 Ultra-Cold Neutrons (UCN)	25
1.4.2 Neutron Electric Dipole Moment experiments	29
1.5 Ultracold neutrons and magnetic field	30
1.5.1 Neutron polarization	30
1.5.2 Neutron spin evolution in a uniform magnetic field	31
1.5.3 Neutron spin evolution with an additional rotating field	33
2 The n2EDM experiment @ PSI	39
2.1 The measurement principle	40
2.1.1 Principle	40
2.1.2 The Ramsey separated oscillating fields method	41
2.1.3 Expected n2EDM statistical sensitivity	44
2.2 Magnetic field requirements	44
2.2.1 Field uniformity: top-bottom matching condition	44
2.2.2 Field uniformity: the neutron depolarization	45
2.2.3 Main systematic effect : the false motional EDM	47
2.2.4 Local Magnetic dipole	51
2.2.5 Gravitational shift and uncompensated field drift	52
2.3 The n2EDM experiment	52

2.3.1	The PSI UCN source	53
2.3.2	UCN transport: guides, switch and holding coils	53
2.3.3	The Precession chambers	54
2.3.4	Magnetic field production	54
2.3.5	Control of the magnetic field	54
2.3.6	The detection system: USSA and detectors	57
3	The B_0 coil	59
3.1	COMSOL simulations	60
3.1.1	Influence of the meshing	60
3.1.2	Simplifying the simulation by the use of symmetries	61
3.2	B_0 coil design	62
3.2.1	Circular single loop and infinite solenoid	62
3.2.2	Squared single loop and infinite solenoid	65
3.2.3	Finite solenoid in a magnetic shield	68
3.2.4	B_0 coil design	69
3.3	Characteristics of the simulated B_0 field	69
3.3.1	B_0 field uniformity	71
3.3.2	Gradient decomposition	71
3.3.3	Influence of the MSR	72
3.4	Study of some mechanical imperfections	73
3.4.1	Global misalignment of the B_0 coil with respect to the shield	73
3.4.2	Influence of the shield innermost dimensions	75
3.4.3	Other imperfections	75
3.4.4	Conclusion about the mechanical imperfections	76
3.5	B_0 technical design	76
4	The correcting coils	81
4.1	TRIM coils array	81
4.1.1	Purpose and working principle	81
4.1.2	Design	82
4.1.3	Performances	82
4.2	Harmonic Coils	83
4.2.1	Purposes	83
4.2.2	Design of $G_{1,0}$, $G_{2,0}$ and $G_{3,0}$ coils	84
4.2.3	Design of $G_{1,-1}$ and $G_{1,1}$ coil	86
4.2.4	Design of $G_{0,-1}$ and $G_{0,1}$ coils	88
4.3	Technical design	89
5	Influence and constraints on magnetic dipoles	91
5.1	Motional EDM produced by a single magnetic dipole	91
5.2	The nEDM experiment case	93
5.2.1	Residual EDM produced by the dipole in the nEDM case	93
5.3	The n2EDM experiment case	95
5.3.1	Residual EDM produced by the dipole in the n2EDM case	95
5.3.2	Constraints on the magnetic moment	95
Conclusion		99

II La partie Française	101
Introduction	103
1 Motivations	105
2 L'expérience nEDM @ PSI	111
3 La bobine B_0	121
4 Les bobines correctrices	129
5 Influence d'un dipôle magnétique et ses contraintes	135
Conclusion	139
 Appendices	 143
A The Wigner-Eckart theorem	143
B General description of COMSOL	145
C The Harmonic polynomal Basis	155
D Allowed Gradients due to broken symmetries	157
E Description of the others Harmonic Coils	159
 Bibliography	 163

Part I

The English part

Introduction

Since more than 60 years, the search for the neutron electric dipole moment (nEDM) is a warm and fundamental topic [1]. Such a permanent EDM, which may also exist for several systems like the electrons, some atoms or molecules, is a signature of a new source of violation of the charge conjugation and parity symmetries (CP). This is one of the Sakharov's conditions required to explain the predominance of matter over antimatter in the universe [2]. Furthermore, if this EDM is predicted to be about $10^{-31}\text{--}10^{-32}$ e cm by the electroweak standard model (SM), the SM extensions foresee a higher value, reaching the 10^{-28} e cm range. The current upper limit on the nEDM measurement is $< 3 \times 10^{-26}$ e cm (90% C.L.) [3]. In the next few years, several experiments are about to probe the 10^{-28} e cm range, starting to test the SM extensions predictions [4].

This thesis takes place between the nEDM experiment at the Paul Scherrer Institute, which will publish a new upper limit in 2019, and the n2EDM experiment, the future project of the nEDM collaboration, which aims at exploring the $10^{-27}\text{--}10^{-28}$ e cm range. Both projects use polarized ultra-cold neutron which are stored in a precession chamber submitted to an electric and a magnetic field. Using the Ramsey oscillating separated field method and counting the number of polarized neutron of each spin state, one can measure the neutron EDM. However, n2EDM benefits of upgraded equipment, and use two precession chambers instead of one.

The work presented here explains in detail the investigations performed for the design of the n2EDM coils system. Indeed, the production and the control of the magnetic field constitute the core of the experiment. The constraints on the field uniformity and stability are extremely severe. They are directly linked to the statistical sensitivity of the measurement and also to several systematic effects. The relation with the neutron polarisation and the motional EDM will be presented in this document.

In the first chapter, the motivations for the nEDM searches are exposed. It also presents the ultra-cold neutrons and their properties, as well as their interaction with a magnetic field.

The second chapter presents the measurement principle, as well as the magnetic field requirements. It ends by a presentation of the n2EDM experiment.

The third chapter is dedicated to the B_0 coil, which produces the main field of the experiment. The COMSOL software, used to perform the simulations, is described, then the B_0 coil design and its performances are shown. Finally, it describes the influence of several mechanical imperfections, and ends by presenting the technical design of the coil.

The fourth chapter presents the correcting coils. It corresponds to the TRIM coil array, a set of 56 coils which have to correct for the B_0 field non-uniformities, and the Harmonic coils (seven coils) dedicated to the production of single specific gradients. The technical designs of the correcting coils are shown.

Finally, the last chapter presents a study of the motional false EDM produced by magnetic dipoles in the nEDM and n2EDM experiments. Constraints on their strength are given in the n2EDM case.

Motivations

Contents

1.1 Physical motivations	17
1.1.1 Matter-antimatter asymmetry	18
1.1.2 Sakharov conditions	19
1.1.3 Electroweak Baryogenesis	19
1.2 C, P and T symmetries	20
1.3 The Electric Dipole Moment and CP violation	21
1.3.1 Definition and CP violation	21
1.3.2 Searches of symmetry violation	22
1.3.3 Status of CP violation in the strong sector	22
1.3.4 Status of CP violation in the weak sector	23
1.3.5 EDM measurements in the world	25
1.4 The neutron Electric Dipole Moment	25
1.4.1 Ultra-Cold Neutrons (UCN)	25
1.4.2 Neutron Electric Dipole Moment experiments	29
1.5 Ultracold neutrons and magnetic field	30
1.5.1 Neutron polarization	30
1.5.2 Neutron spin evolution in a uniform magnetic field	31
1.5.3 Neutron spin evolution with an additional rotating field	33

Introduction

This first chapter presents the physical motivations for the search of permanent electric dipole moment. The influence of the C, P and T symmetries on this property is described. The EDM will be deeply defined by answering at the following questions: what it is? Where it can be found? What is the current status of the EDM searches? A focus on the neutron electric dipole moment will be performed as well as on the ultra cold neutrons used for most of the current nEDM experiments. Finally, this chapter will describe the interaction of a neutron with several types of magnetic fields.

1.1 Physical motivations

The standard model of particle physics (SM) is one of the most accurate model nowadays. Its predictive power has been verified many times, the Higgs boson discovery being one of the

most recent confirmation of the SM predictions [5, 6]. However, this model have also some weaknesses and can't explain several phenomena. It includes:

- **The existence of the dark matter and the dark energy**, introduced to explain for instance the speed of galaxies rotations [7], the strength of gravitional lens and the acceleration of the universe expansion [8];
- **The existence of a neutrino mass**, which should be null in the SM, otherwise a coupling with the Higgs boson would imply a right chirality to the neutrino, contradicted by the observation of neutrino's oscillation [9];
- **The lack of CP violation sources in the SM**, one of the condition to explain the matter-antimatter asymmetry.

Because the electric dipole moment searches is about increasing this quantity of CP violation sources, let us dwell on the subject of matter-antimatter asymmetry.

1.1.1 Matter-antimatter asymmetry

A symmetric production of matter and antimatter in the early universe should have led to a universe of light, due to the annihilation reactions between particles and antiparticles. This is not the case, since we live in a world made of matter, where the antimatter is almost inexistant. The matter-antimatter asymmetry is estimated by

$$\eta = \frac{n_B - n_{\bar{B}}}{n_B + n_{\bar{B}}} = \frac{n_B - n_{\bar{B}}}{n_\gamma}, \quad (1.1)$$

where n_B , $n_{\bar{B}}$ and n_γ represents respectively the amount of matter, antimatter and gamma in the universe.

This ratio has been experimentally measured by two different ways. The observation of the light elements abundance like deuterium [10] gives an estimation of the asymmetry parameter of:

$$5.8 \times 10^{-10} \leq \eta \leq 6.6 \times 10^{-10} \text{ (95 \% CL).} \quad (1.2)$$

Other measurements have been performed by looking at the cosmic microwave background, the latest coming from the Planck satellite observations [11]. They estimated a baryon density $\Omega_b h^2 = 0.022 \pm 0.002$ (1σ), corresponding to a baryon asymmetry of :

$$\eta = 6.09(6) \times 10^{-10}. \quad (1.3)$$

The Fig. 1.1 shows the asymmetry parameter exclusion plot using those two measurements. It doesn't seems much, because of its normalisation to the amount of photons produced by eliminations, but it means that it is less than 1 antimatter particle for 10 000 000 000 matter particles.

However, the prediction from the Standard Model reaches only an asymmetry of $\eta \simeq 10^{-19}$ [12]. We therefore need to find new sources of this asymmetry to explain the remaining 10^9

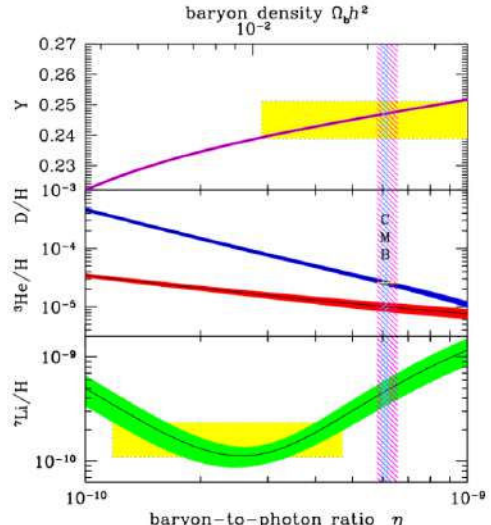


Figure 1.1 – Asymmetry parameter η from Cosmic microwave background results (the vertical hatched region) and light element abundance from standard model predictions (Y in purple, D in blue, ${}^3\text{He}/\text{H}$ in red and ${}^7\text{Li}/\text{H}$ in green). The yellow rectangles are experimental observed abundances (PDG 2018).

factor.

1.1.2 Sakharov conditions

In 1967, Andreï Sakharov enunciated three conditions necessary to explain this matter-antimatter asymmetry [2] :

1. **The violation of the baryonic number B** which allows the evolution of the universe from an initial state with $B = 0$ to a final state with $B \neq 0$;
2. **A non-equilibrium thermal phase.** Indeed, in an equilibrated state, the reactions which favors the production of matter would be counter balanced by the reactions which favors the production of antimatter;
3. **The violation of C and CP symmetry** which promotes the production of matter over the production of antimatter.

The third Sakharov condition is fulfilled for a few systems (see 1.3.4), but the strength of the found CP violating processes is not sufficient to explain the observed asymmetry. New CP violation sources are required. It is the main motivation for the EDM quest.

1.1.3 Electroweak Baryogenesis

Among the possible scenarii, the Electroweak Baryogenesis [13] (EWBG) satisfies the Sakharov conditions and, with the current experimental sensitivity, is testable by the EDM experiments. This scenario starts in the Early universe, around $t < 1 \text{ ps}$, where the temperature T is very high compare to the electroweak scale $T_c \simeq 100 \text{ GeV}$. At this point, the universe is dominated by a hot plasma which contains W,Z and t quarks. The Higgs field is homogeneous $\Phi_m = 0$ and its potential is defined by $V(\phi, T) = V(\phi) + V_{\text{plasma}}(T)$. The particles interact with sphalerons, which are able to converts baryons to antileptons and antibaryons to leptons (violating $B+L$, although the quantity $B-L$ is conserved) [14] at a rate Γ_s much higher than the expansion rate of the universe H . Thus, the B violating reactions are balanced by the B violating back reaction (thermal equilibrium), which implies a null baryon asymmetry.

Then the universe cools down, whereas its expansion rate H becomes larger, and starts to match Γ_s . When the temperature of the universe is close to T_c , the Higgs potential reaches a minimum for a non-zero Φ_i , as shown with the red line in Fig. 1.2. This leads to local nucleations of "bubbles" with a Higgs field Φ_i , inside which the weak and the electromagnetic forces are distinct, meaning that the bosons W and Z are massive. Outside of the bubbles however, those two forces are still unified. The bubbles extend and merge, as shown in the left panel of Fig. 1.3. This is the Electroweak Phase Transition. Particles interact on the bubbles walls where CP violation occurs, like in the right panel of Fig. 1.3. It results in an asymmetry converted by the Sphaleron mechanism into a Baryonic asymmetry. Then, this asymmetry is transferred inside the bubbles because the universe expansion rate H is larger than Γ_s . Finally, all the bubbles merged together, becoming the known universe where the electroweak and electromagnetism forces are separated, and where the W and Z bosons have a mass.

The Discovery of the Higgs mass $m_H \simeq 125 \text{ GeV}$ [5, 6] makes this scenario impossible in the Standard Model. Indeed, the nucleation of the bubbles requires that the Higgs potential doesn't allow a continuous evolution for the initial Higgs field to Φ_i . It means that the electroweak phase transition must be first-order, which is not possible with such a mass according to the Standard Model theory [15].

On the other hand, in some models beyond Standard Model, like the Two Higgs doublet model (2HDM), a first-order transition is compatible with the Higgs mass of $m=125 \text{ GeV}$ [16].

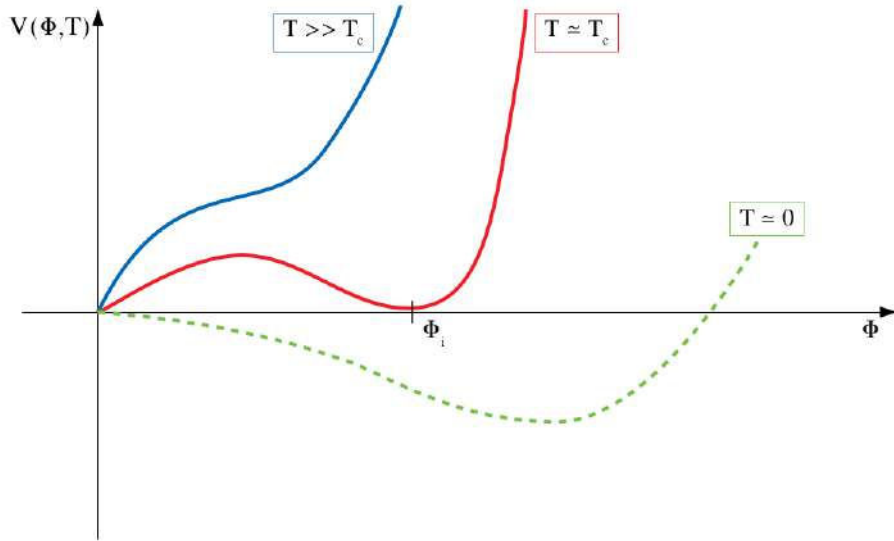


Figure 1.2 – This figure illustrates the evolution of the Higgs potential and the Higgs field for different temperatures of the universe. The red line shows the moment where the universe temperature reaches the electroweak scale, leading to a minimum of the Higgs potential with a non-null Higgs field, starting the nucleation of bubbles.

1.2 C, P and T symmetries

Let first introduce the notions of symmetries and symmetry violations.

The Charge reversal symmetry (C) consists in changing a particle into its antiparticle. It implies the transformation of its charge, its Lepton or Baryon number (and also some more specific quantic numbers as the Charm, the Strangeness etc.) in their opposite. Thus a state ϕ is transformed through this symmetry as :

$$\phi(q, B, L, \dots) \xrightarrow{C} \phi(-q, -B, -L, \dots) \quad (1.4)$$

The Parity symmetry (P) corresponds to an inversion of the coordinates system :

$$\phi(x, y, z) \xrightarrow{P} \phi(-x, -y, -z) \quad (1.5)$$

Finally, the time reversal parity (T) reverse the time :

$$\phi(t) \xrightarrow{T} \phi(-t) \quad (1.6)$$

The transformations of the main observables under those symmetries are summarized in the Table 1.1.

A symmetry violation occurs when the Hamiltonian of the system is not conserved under that symmetry. T.D.Lee demonstrates that the CPT symmetry is invariant [17].

To date, no observation contradicts this CPT invariance [18]. Consequently, a violation of the time-reversal symmetry T implies a violation of CP. Knowing so, the third Sakharov condition can be found in systems violating the T symmetry, such as systems with a non-null Electric Dipole Moment.

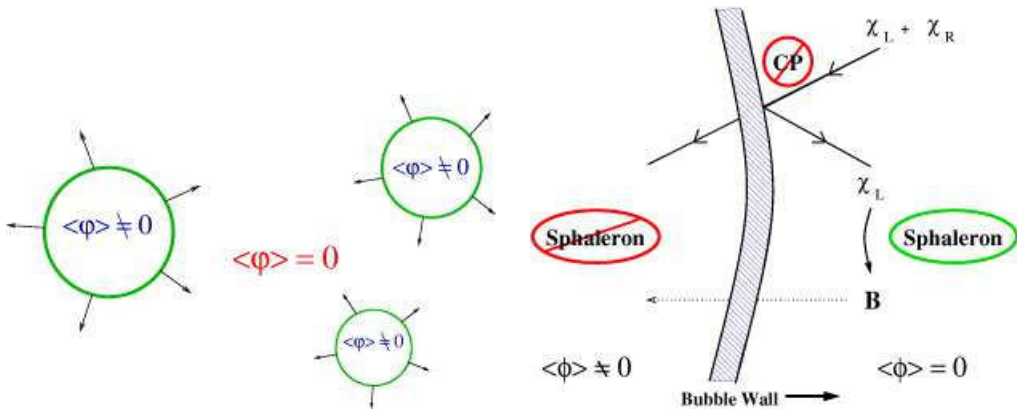


Figure 1.3 – The Electroweak Baryogenesis mechanism. Left panel : The bubble nucleation in which the Higgs field is non-null. Right panel : Particles interact on the Bubble walls in CP violating reaction. The resulting asymmetry is converted to a baryonic asymmetry through the sphaleron mechanism. Because the rate of baryon conversion is lower than the bubble expansion rate, the baryon is absorbed in the bubble, transferring the baryonic asymmetry [13].

Observable	C	P	T
Charge q	$-q$	q	q
Position \vec{r}	\vec{r}	$-\vec{r}$	\vec{r}
Time t	t	t	$-t$
Momentum \vec{p}	\vec{p}	$-\vec{p}$	$-\vec{p}$
Spin \vec{S}	\vec{S}	\vec{S}	$-\vec{S}$
Electric Field \vec{E}	$-\vec{E}$	$-\vec{E}$	\vec{E}
Magnetic Field \vec{B}	$-\vec{B}$	\vec{B}	$-\vec{B}$

Table 1.1 – Main observables transformations under C,P and T violation.

1.3 The Electric Dipole Moment and CP violation

1.3.1 Definition and CP violation

In classical physics, a permanent electric dipole moment corresponds to a positive (+q) and negative (-q) identical charge separated by a distance \vec{r} . It is defined by:

$$\vec{d} = q \cdot \vec{r}, \quad (1.7)$$

Such a permanent dipole doesn't violate CP. However, for a spin 1/2 particle in a non degenerated state, the intrinsic properties such as its EDM \vec{d} or its magnetic moment μ are aligned on the spin \vec{s} , as a result the Wigner-Eckart theorem (see Appendix A). The EDM is then defined by $\vec{d} = d \cdot \frac{\vec{s}}{s}$ (one may notice that the sign of d is currently unknown). The Hamiltonian of such a particle subjected to an electric field is:

$$H = -\vec{d} \cdot \vec{E}. \quad (1.8)$$

Under the P symmetry, this Hamiltonian becomes :

$$H = -\vec{d} \cdot \vec{E} \xrightarrow{P} H = -\vec{d} \cdot (-\vec{E}) = +\vec{d} \cdot \vec{E}, \quad (1.9)$$

and under T symmetry :

$$H = -\vec{d} \cdot \vec{E} \xrightarrow{T} H = -(-\vec{d}) \cdot \vec{E} = +\vec{d} \cdot \vec{E}. \quad (1.10)$$

In both cases, the Hamiltonian changes if the electric dipole moment is non-null. This means that the existence of such an EDM is a source of P and T violation, which corresponds to a CP violation (assuming CPT invariance).

1.3.2 Searches of symmetry violation

In 1950, Purcell and Ramsey suggest to test experimentally the CP symmetry violation by measuring the electric dipole moment of the neutron [1]. This leads to the first limit on the nEDM in 1957 [19] :

$$|d_n| < 5 \times 10^{-20} e \text{ cm}. \quad (1.11)$$

In 1956, Lee and Yang suggest the idea of parity violation to explain the $\theta - \tau$ puzzle [20]. Indeed, those mesons decays through two channels :

$$\theta^+ \rightarrow \pi^+ + \pi^0 \quad (1.12)$$

$$\tau^+ \rightarrow \pi^+ + \pi^+ + \pi^- \quad (1.13)$$

Despite a difference in the parity of the final state, the θ and the τ lifetimes and masses were precisely measured and turned out to be equal. Lee and Yang suggested that the parity is violated and that those two particles are indeed the same particle, known nowadays as the kaon K^+). One year after, in 1957, the parity violation was discovered by Wu et al.[21] in ^{60}Co disintegration experiment, confirming the Lee and Yang hypothesis.

1.3.3 Status of CP violation in the strong sector

Up to now, no experiment had shown a CP violation in the strong sector. The QCD Lagrangian can be written as :

$$\begin{aligned} \mathcal{L}_{QCD} &= \mathcal{L}_0 + \mathcal{L}_\theta \\ &= \bar{\psi}(i\gamma^\mu D_\mu - me^{i\theta' \gamma_5})\psi - \frac{1}{4}trF_{\mu\nu}F^{\mu\nu} - \frac{n_f g^2 \theta}{32\pi^2}trF_{\mu\nu}\tilde{F}^{\mu\nu}, \end{aligned} \quad (1.14)$$

where \mathcal{L}_0 contains the quark and gluon interactions, and \mathcal{L}_θ is related to the interactions with the quantum vacuum. This last term is parametrized by the QCD vacuum angle parameter θ which violates CP. Thus a non-zero θ lead to CP violating effects, easily detectable by the experiment. Moreover, the θ' term in \mathcal{L}_0 is expected to be large and to have CP violations effects too. In order to agree with the experimental results, the θ and θ' angles should balanced. A θ -like term, $\bar{\theta}$, have been introduced and corresponds to the difference of θ and a θ -equivalent of θ' . This new term is related to the neutron EDM by :

$$|d_n| \simeq \bar{\theta} \times 10^{-16} e \text{ cm}. \quad (1.15)$$

The last limit on the nEDM by Baker et al. $|d_n| < 2.9 \times 10^{-26} e \text{ cm}$ (90% C.L.) [22], revisited to $|d_n| < 3.0 \times 10^{-26} e \text{ cm}$ (90% C.L.) by Pendlebury et al. in 2015 [3] results in a limit on $\bar{\theta}$:

$$\bar{\theta} < 3 \cdot 10^{-10}. \quad (1.16)$$

Such a low value of $\bar{\theta}$ corresponds to a very fine-tuning between θ and θ' . The reason for such a very fine tuning is not understood and is called the strong CP problem.

The introduction of a new particle, the axion, can solve the strong CP problem [23]. Indeed, it forces the angle $\bar{\theta}$ to be 0. However, the axion mass is strongly constrained and its existence is still hypothetical. The latest exclusion limit on the axion was given in 2017 by the nEDM

collaboration [24]. An other solution has been proposed to solve the strong CP problem by removing the chiral phase on the mass term in the QDC Lagrangian, in which case the term θ' does not produce CP violation, and therefore we don't need to tune the θ angle to cancel that contribution. The strong CP problem has then no reason to exist, and the CP violation can be naturally canceled by having $\theta = 0$, without introducing any new particles [25].

1.3.4 Status of CP violation in the weak sector

In the weak sector, CP violation has been observed many times. In 1964, Christenson and al. provided evidences of an indirect CP violation looking at the decay of neutral kaons K^0 into two pions [26] (1980 Nobel Prize). In 1999, the KTeV [27] and the NA48 [28] collaborations corroborated this discovery through direct observation of CP violation. In 2001, the BABAR [29] and Belle [30] experiment showed a CP violation in a new system : the meson B. In 2013, the LHCb collaboration found that the CP violation also occurs in the strange B_s meson [31]. Finally in 2019, the LHCb collaboration found a CP violation in a charmed system, the meson D^0 [32].

The CP violation parameter is in the Cabibbo-Kobayashi-Maskawa matrix (CKM matrix) :

$$V_{CKM} = \begin{pmatrix} V_{ud} & V_{us} & V_{ub} \\ V_{cd} & V_{cs} & V_{cb} \\ V_{td} & V_{ts} & V_{tb} \end{pmatrix} \quad (1.17)$$

This matrix is a unitary matrix, and can be written as :

$$V_{CKM} = \begin{pmatrix} c_{12}c_{13} & s_{12}c_{13} & s_{13}e^{i\delta} \\ -s_{12}c_{23} - c_{12}s_{23}s_{13}e^{i\delta} & c_{12}c_{23} - s_{12}s_{23}s_{13}e^{i\delta} & s_{23}c_{13} \\ s_{12}s_{23} - c_{12}c_{23}s_{13}e^{i\delta} & -c_{12}s_{23} - s_{12}c_{23}s_{13}e^{i\delta} & c_{23}c_{13} \end{pmatrix} \quad (1.18)$$

where θ_{12} , θ_{13} , θ_{23} are three Euler's angles, δ a complex phase, and where $c_{ij} = \cos \theta_{ij}$ and $s_{ij} = \sin \theta_{ij}$.

The δ phase is the CP violating parameter. In the Standard model, the one loop contributions are proportional to $V_{qq'}V_{qq'}^*$, which is real. Thus it can't lead to CP violation. The two loops diagrams can individually involve a complex phase, but their sum leads to a null complex contribution [33]. Examples of one or two loops diagrams are shown in Fig. 1.4.

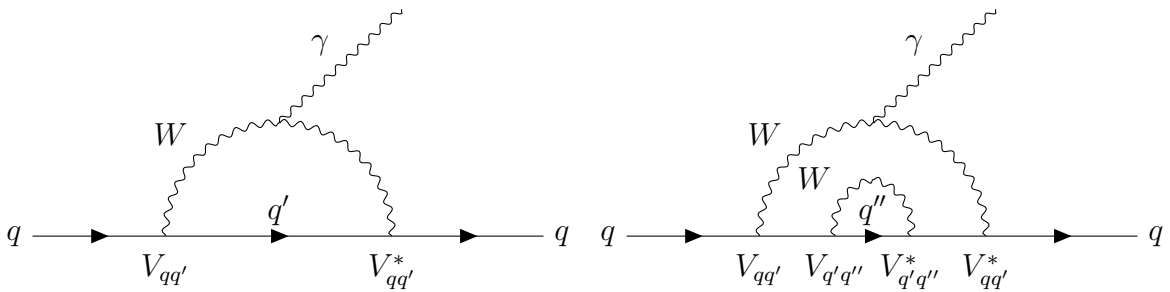


Figure 1.4 – One loop diagram on the left, and two loops diagram on the right.

Thus, the first contribution to the quark CP violation in the SM comes from three loops diagrams, like the one presented in Fig. 1.5.

This contribution can be computed from the quarks EDMs. The estimation of the up and down quark EDM is $d_d = -0.7 \times 10^{-34} e \text{ cm}$, and $d_u = -0.15 \times 10^{-34} e \text{ cm}$ [34]. From them it is possible to compute the neutron false EDM from the up and down quark EDM [35] :

$$|d_n| = \left| \frac{4d_d}{3} - \frac{d_u}{3} \right| < 1 \times 10^{-34} e \text{ cm.} \quad (1.19)$$

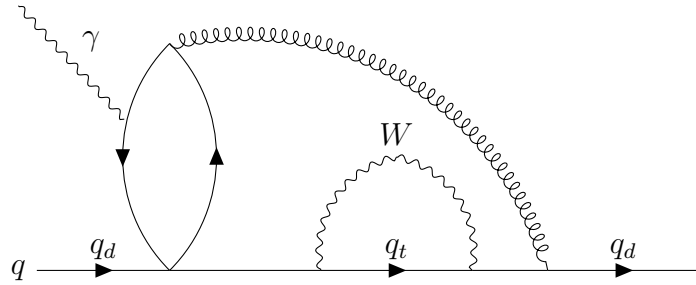


Figure 1.5 – Three loop diagram involving quarks, contributing to the neutron EDM.

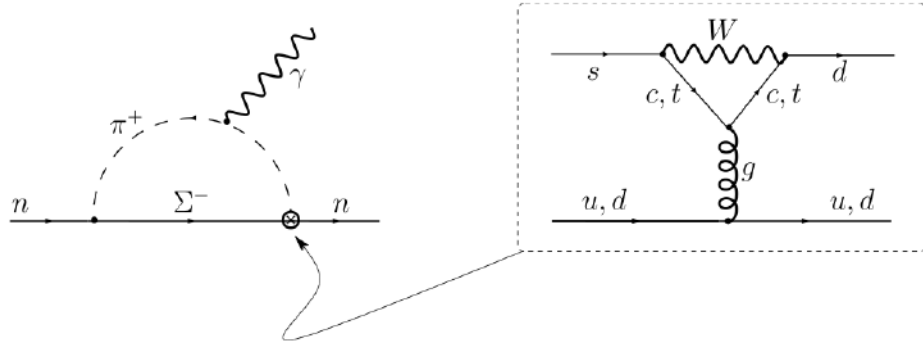


Figure 1.6 – The penguin diagram, leading contribution to the nEDM in the SM.

An another contribution in the weak sector comes from the two loops hadronic interactions, such as the famous penguin diagram shown in Fig. 1.6, estimated by Khriplovich and Zhitnitsky at the value of $d_n \simeq 2 \times 10^{-32} e \text{ cm}$ [36]. It brings the SM prediction of the nEDM at:

$$d_n^{SM} \simeq 10^{-32} e \text{ cm}, \quad (1.20)$$

which is very low.

In the physics beyond the standard model, other loops diagrams involving new particles are allowed. For instance the supersymmetry model (SUSY) allows one loop CP-violating diagrams using gluinos and squarks, as the one shown in Fig. 1.7, and bring the SUSY predicted nEDM at:

$$d_n^{SUSY} \simeq 10^{-30} - 10^{-25} e \text{ cm}, \quad (1.21)$$

whose top estimations can already be probed by the current nEDM experiments.

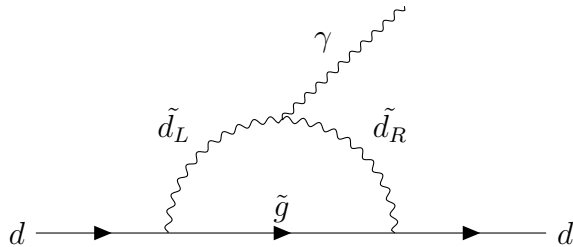


Figure 1.7 – One loop diagram in SUSY violating CP.

1.3.5 EDM measurements in the world

The first suggestion for a electric dipole moment experiment was made by Purcell and Ramsey in 1950 [1]. The first experiment was performed in 1957, by Smith, Purcell and Ramsey [19] on the nEDM. Then Salpeter gives a limit to the electron EDM $|d_e| < 1.6 \times 10^{-13} e\text{ cm}$ [37]. Since, the number of experiment has grown, expanding to other systems, not necessarily sensitive to the same physics. For instance, atomic EDM have to consider the nuclear interaction and the screening by the electron, the neutron is made of three quarks, so is sensitive to the QDC interaction. Each of those system brings a complementary understanding of the EDM and of the underlying mechanisms.

Table 1.2 summarizes the current electric dipole moments upper limits for several systems (composite or elementary). A more complete list of EDM searches in the world is available at the PSI website

Category	EDM	Limit value :	Year	Ref.	SM prediction
Quarks	down d	$< 1.27 \times 10^{-24} e\text{ cm}$	2018	[38]	
	up u	$< 1.17 \times 10^{-24} e\text{ cm}$	2018	[38]	
Leptons	electron e	$< 1.1 \times 10^{-29} e\text{ cm}$ (90% C.L.)	2018	[39]	10^{-40}
	muon μ	$< 1.8 \times 10^{-19} e\text{ cm}$ (95% C.L.)	2009	[40]	10^{-27}
	tau τ	$-2.2 < \text{Re}(d_\tau) < 4.5 (\times 10^{-17} e\text{ cm})$ (95% C.L.) $-2.5 < \text{Im}(d_\tau) < 0.8 (\times 10^{-17} e\text{ cm})$ (95% C.L.)	2002	[41]	10^{-24}
Nuclei	neutron n	$< 3.0 \times 10^{-26} e\text{ cm}$ (90% C.L.)	2015	[3]	10^{-32}
	proton p	$< 2.0 \times 10^{-25} e\text{ cm}$	2016 (erratum 2017)	[42]	10^{-31}
	deuteron d	$< 5.1 \times 10^{-31} e\text{ cm}$	2017	[43]	10^{-31}
Diamagnetic atoms	^{199}Hg	$< 7.4 \times 10^{-30} e\text{ cm}$ (95% C.L.)	2016 (erratum 2017)	[42]	$< 10^{-34}$
	^{129}Xe	$< 4.0 \times 10^{-27} e\text{ cm}$	2001	[44]	10^{-35}
	^{225}Ra	$< 1.4 \times 10^{-23} e\text{ cm}$ (95% C.L.)	2016	[45]	10^{-33}
Paramagnetic atoms	^{205}Tl	$< 9 \times 10^{-25} e\text{ cm}$	2002	[46]	10^{-34}
	^{133}Cs	$< 10.3 \times 10^{-24} e\text{ cm}$	1989	[47]	
	^{85}Rb	$< 1 \times 10^{-18} e\text{ cm}$	1966	[48]	

Table 1.2 – Summary of Electric Dipole Moment upper limits, years of publication, reference and SM prediction.

1.4 The neutron Electric Dipole Moment

The neutron is a good candidate for the Electric Dipole Moment searches. Firstly, it is sensitive to the weak and strong sectors, in which a CP violation term can arise. Then, because of its neutrality, the interaction of the electric dipole moment and the electric field is not affected by an electric charge. Moreover, because the neutron is a 1/2 spin particle, the orientation of the spin (and so of the electric and magnetic dipole moment) can be controlled using magnetic fields. The method used to measure the EDM takes advantage of it. Finally we can use Ultra-Cold Neutrons, which allows a long precession time.

1.4.1 Ultra-Cold Neutrons (UCN)

Definition

The neutron had been discovered by Chadwick in 1932 by looking at the properties of the penetrating radiation emitted from beryllium when bombarded by the α -particles of polonium [49]. The properties of the neutron depends on its energy. This is why they are often classified

Category	Energy	Wavelength (nm)	Temperature (K)	Speed (m/s)
Relativist	$> 57 \text{ MeV}$	$< 4.04 \times 10^{-6}$	$> 5.80 \times 10^{11}$	$> 0.33c$
Fast	$> 500 \text{ keV}$	$< 4.04 \times 10^{-6}$	$> 5.80 \times 10^9$	$> 9.78 \times 10^7$
Intermediate	$> 1 \text{ keV}$	$< 4.04 \times 10^{-5}$	$> 1.16 \times 10^7$	$> 4.37 \times 10^6$
Epithermal	$> 0.5 \text{ eV}$	$< 9.04 \times 10^{-4}$	> 5802	> 9780
Thermal	25 meV	0.18	290	2187
Cold	$> 50 \mu\text{eV}$	< 0.18	> 0.58	> 97.8
Very-cold	$> 300 \text{ neV}$	< 52.2	> 0.035	> 7.57
Ultra-cold	$< 300 \text{ neV}$	> 52.2	< 0.0035	< 7.57

Table 1.3 – Neutron energy classification.

in several energy categories. At those energies corresponds a wavelength, defined as:

$$\lambda_n = \frac{h}{\sqrt{2m_n E}} \quad (1.22)$$

and a temperature, computed as $T = k/E$. They are shown in Table 1.3.

For instance, a neutron with an energy of 300 neV have a wavelength of 52.2 nm. This is larger than the distance between atoms in a solid. Thus it will interact with several nuclei (not only one). This can be seen as a potential step of energy V_F , which is called the Fermi potential or optical potential. This potential is different from one material to an other, and is defined as:

$$V_F = \frac{2\pi\hbar^2}{m_n} \sum_i N_i b_i, \quad (1.23)$$

where N_i is atoms density, and b_i the coherent scattering length of the nuclei composing the material. The Table 1.4 gives some optical potential for typical materials [50].

Material	V_F [neV]	W [10^{-2} neV]
DLC	260	52.0
DPS	162	40.5
Ni	252	15.7
Fe	210	8.92
Al	54	0.62
NiMo	220	11.0
Diamond	300	60.0

Table 1.4 – Fermi potential of some materials V_F and absorption potential W of some materials.

A neutron of kinetic energy E can be reflected by a wall with a Fermi potential V_F if the incidence angle θ of a neutron on the wall fulfils [51]:

$$\sin(\theta) \leq \sqrt{\frac{V_F}{E}}. \quad (1.24)$$

If the neutron energy E is low enough, the equation Eq. 1.24 is fulfilled for every incident angle θ . This is the total reflection phenomena. The neutrons with such a property are called Ultra-Cold neutrons. This allows to store the UCN in a material vessel to study their properties, such as the nEDM or their lifetime τ .

Quantic calculation of the UCN reflection

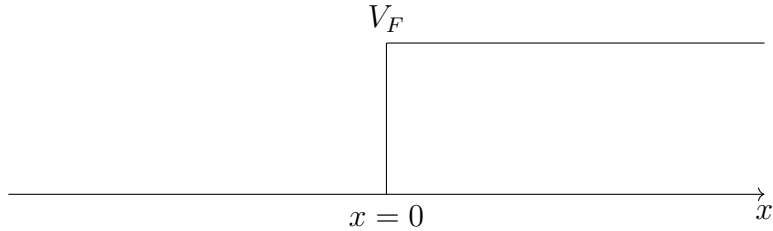
The UCN reflection probability can be computed by solving the Schrödinger equation :

$$\frac{-\hbar^2}{2m_n} \Delta \psi + V\psi = E\psi, \quad (1.25)$$

with a "step" potential starting at $x=0$

$$\begin{cases} V = 0 & x < 0 \\ V = V_F - iW & x > 0 \end{cases} \quad (1.26)$$

where the imaginary part W is the absorption potential of the material [52], which consider the probability of the UCN to be absorbed by the material when its energy is lower than V_F .



A solution to the Schrödinger equation from the boundary conditions is:

$$\begin{cases} \psi = e^{ikx} + Re^{ikx} & z < 0 \\ \psi = Te^{ik'x} & z > 0 \end{cases} \quad (1.27)$$

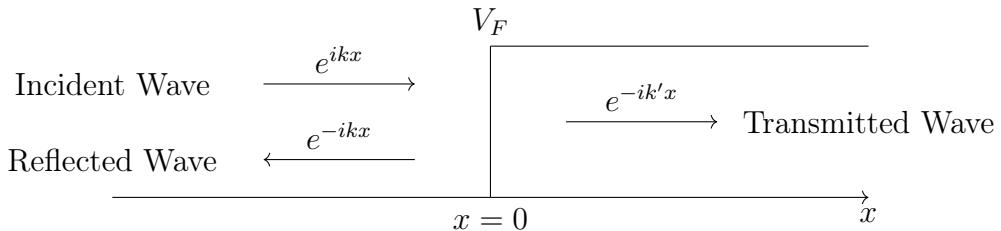
with $k = \frac{1}{\hbar} \sqrt{2m_n E_\perp}$ and $k' = \frac{1}{\hbar} \sqrt{2m_n (E_\perp - V)}$, R is the amplitude of the reflected wave and T the amplitude of the transmitted waves. They can be estimated form the boundaries conditions where $1 = R + T$, which leads us to :

$$R = \frac{\sqrt{E_\perp} - \sqrt{E_\perp - V}}{\sqrt{E_\perp} + \sqrt{E_\perp - V}} \quad \text{and} \quad T = \frac{2\sqrt{E_\perp}}{\sqrt{E_\perp} + \sqrt{E_\perp - V}} \quad (1.28)$$

Using the fact that, as shown in Table 1.4, $W \ll V_F$, one can compute the reflection probability :

$$\begin{cases} R^2 = \left(\frac{\sqrt{E_\perp} - \sqrt{E_\perp - V}}{\sqrt{E_\perp} + \sqrt{E_\perp - V}} \right)^2 & E_\perp > V_F \\ |R|^2 = 1 - \frac{2W}{V_F} \sqrt{\frac{E_\perp}{V_F - E_\perp}} & E_\perp < V_F \end{cases} \quad (1.29)$$

The previous equation shows that it is possible to have a transmitted (although evanescent) wave even for a neutron energy below the Fermi potential V_F .



Gravity interaction

The gravity has an impact on the ultra cold neutron physics. For a neutron, the potential energy from gravitation is :

$$m_n \cdot g \cdot z = 102.6 \cdot z \text{ neV} \quad (1.30)$$

This means that a UCN with an energy of 300 neV can reach a maximum height of 3 meters. This may be useful to control the neutron energy by making it go up and down. An other consequence (more related to our nEDM experiment) is that the UCN center of mass in a chamber is different than the center of the chamber, as shown in Fig. 1.8. For instance, in the precession chamber of the nEDM experiment, the difference is about a few millimeters.



Figure 1.8 – Influence of the gravity on UCN trajectories simulated using GEANT4-UCN, giving a parabolic trajectories to the neutrons [53].

Weak interaction : neutron decay

The neutron mostly decays into a proton following :

$$n \rightarrow p + e^- + \bar{\nu}_e \ (+0.782 \ MeV) \quad (1.31)$$

The neutron lifetime τ_n is a fundamental parameter in the weak interaction. It appears as an input parameter to Big Bang Nucleosynthesis (BBN) theory, which predicts light element synthesis in the early universe, and also in the determination of the V_{ud} element in CKM matrix. It can be measured by two different ways :

- **With beam experiments**, where some neutrons from a beam will decay into protons, electrons and antineutrinos (β decay). Detecting the protons and electrons, i.e. the "dead" neutrons which have decayed allows us to get the neutron lifetime. This technique measured an average neutron lifetime of 888.0 ± 2.1 seconds.
- **With bottle experiments**, where we fill a bottle of neutrons, and store them a certain amount of time, after what we count the neutrons which haven't decayed, i.e. the "living" neutrons. Reproducing this experiment with different storage times will allow, once again to get the neutron lifetime. This technique measured an average neutron lifetime of 879.3 ± 0.75 seconds. The $UCN\tau$ experiment at Los Alamos and Gravitrap at ILL intends to improve the precision on this measurement.

One can see that the two methods lead to two incompatible lifetimes, with a difference of about 3σ between them. This is known as the neutron lifetime discrepancy. The neutron lifetime discrepancy is shown in Fig. 1.9.

Production of ultra-cold neutrons

The ultracold neutrons are produced from fast or thermal neutrons, which are supplied either by a spallation target (PSI [54]) or by a nuclear reactor (ILL [55]). The neutrons are cooled with a bunch of techniques : the gravity can be used as a natural decelerator, moderators such as Solid Deuterium D₂ or superfluid Helium can be used to slow them down through elastic collision , or by using a turbine as it is done at ILL.

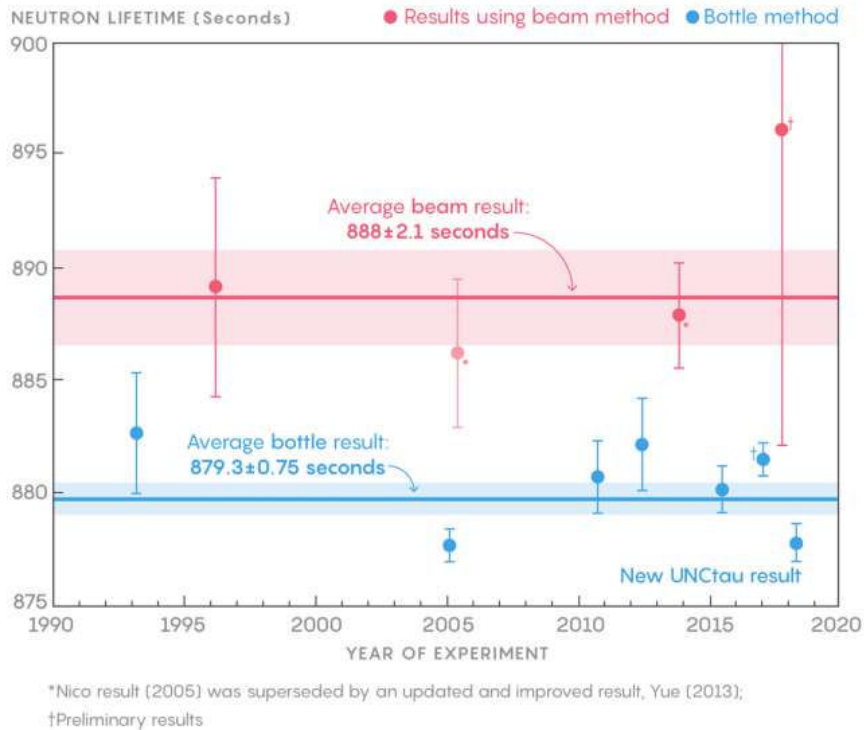


Figure 1.9 – Neutron lifetime estimated by the bottle experiments (in blue) and the beam experiments (in red). The difference between the two average results is bigger than 3σ . *Lucy Reading-Ikkanda/Quanta Magazine; Source: pre-2017, Particle Data Group; Serebrov 2017, arxiv:1712.05663; Pattie, 2018, arxiv:1707.01817 ; published in Quanta magazine on 13/10/2018.*

1.4.2 Neutron Electric Dipole Moment experiments

State of art of nEDM measurements

The first nEDM measurement was performed by Purcell and Ramsey in 1957 [19] and the measured upper limit was $|d_n| < 5 \times 10^{-20} e \text{ cm}$. UCN were first used in the 1980s by the LNPI collaboration [56]. This lead to a large improvement of the sensitivity. Indeed, the low average speed of the neutrons inside the precession chambers (around 4 m/s) allows to suppress the main systematic effect, called the motional false EDM of the neutron [57]. They can also be stored which allows to increase the precession time, leading to larger statistical sensitivity. Since, the nEDM experimental limit decreases with the improvement of the technology, especially of the neutron sources intensity. The current (revisited) upper limit is $|d_n| < 3.0 \times 10^{-26} e \text{ cm}$. (90% C.L.)[22, 3] This limit has been set with the apparatus that we were operating for the nEDM experiment. The Fig. 1.10 shows the evolution of the nEDM experimental limit through the years, with the addition of provisional sensitivity from nEDM @ PSI of $1.1 \times 10^{-26} e \text{ cm}$ and n2EDM @ PSI in the baseline scenario, and an upgraded version of this experiment, respectively $1 \times 10^{-27} e \text{ cm}$. and about $10^{-28} e \text{ cm}$. They are compared to some theoretical expectations of the nEDM (including the SM prediction in blue), on the right of the figure.

The future nEDM measurements

The measurement of the nEDM is more exciting than ever. The next years might be able to push the nEDM limit down to the $10^{-28} e \text{ cm}$ scale, deeply probing and constraining theoretical model predictions as supersymmetry ones. The use of double cells and superfluid Helium, as well as performing magnetometers and very uniform magnetic field are some of the improvements

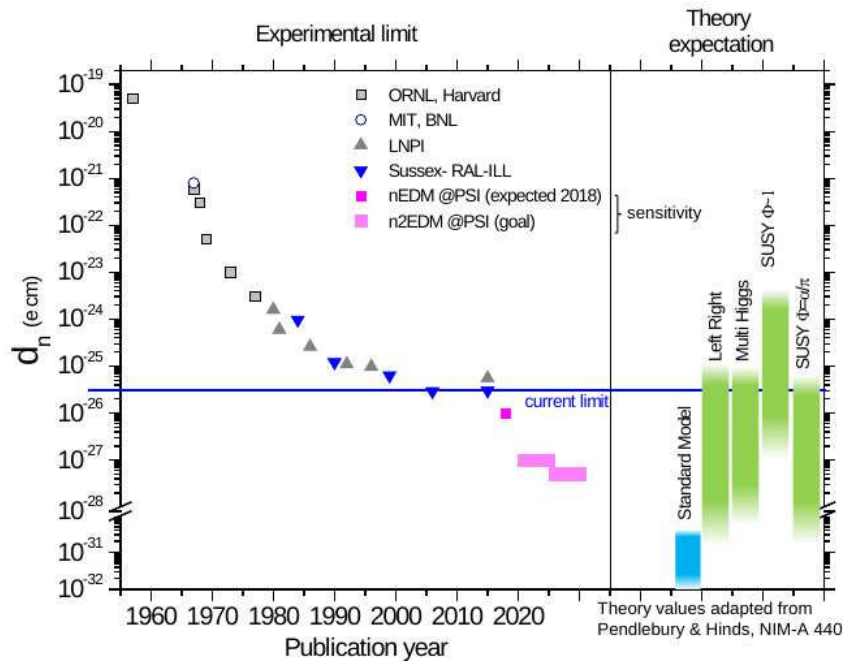


Figure 1.10 – nEDM upper limit over time. The blue line corresponds to the current limit $|d_n| < 3.0 \text{ e cm}$ established in 2006 by the RAL-Sussex-ILL collaboration. The pink areas corresponds to the expected limits settled by the nEDM and n2EDM experiments(baseline and upgraded version of the experiment). On the right, the range of the predicted limit from the Standard Model (in blue) and the extensions of the standard model (in green) are shown.

that will allow to reach the new range of sensitivities. The Table 1.5 presents a brief overview of the nEDM projects in the world.

Experiment	Source	Magnetometry	limit 90 % C.L. goal	planned start
n2EDM @ PSI	Solid D ₂	Hg, Cs	$2 \times 10^{-27} \text{ e cm}$	2021
TUCAN @ TRIUMF	Superfluid ⁴ He	Xe/Hg	$2 \times 10^{-27} \text{ e cm}$	2021
SNS @ Oak Ridge	Superfluid ⁴ He	³ He	$3 \times 10^{-28} \text{ e cm}$	2023
LANL @ Los Alamos	Solid D ₂	Hg, Cs/ ³ He	$3.4 \times 10^{-27} \text{ e cm}$	2021
PanEDM @ ILL	Superfluid ⁴ He	Hg, Cs	$7 \times 10^{-28} \text{ e cm}$	–
Beam nEDM @ ESS	Beam	–	$5 \times 10^{-28} \text{ e cm}$	–
ILL-PNPI	Solid D ₂ (PNPI)	–	ongoing at ILL	

Table 1.5 – Worldwide nEDM experiments.

Most of the new projects aims to built a more performing UCN source to improve the statistical sensitivity in order to continue the hunt of the nEDM.

1.5 Ultracold neutrons and magnetic field

1.5.1 Neutron polarization

The neutron interacts with the magnetic field through its magnetic moment $\mu_n = -9.6623650(23) \times 10^{-27} \text{ J/T}$ [58], often expressed when working with UCN's as $\mu_n \simeq 60.3 \text{ neV/T}$. Moreover, its magnetic moment is aligned along its spin, which gives the following Hamiltonian:

$$\hat{H} = -\vec{\mu}_n \cdot \vec{B} = -\gamma_n \hat{\vec{S}} \cdot \vec{B} \quad (1.32)$$

This interaction can be used to manipulate the UCN polarization. As shown in 1.11, if the neutron spin is anti-parallel to the magnetic field, it has to cross a region with a potential of -300 neV, i.e. UCN are accelerated. On the other hand, if the neutron spin is parallel to the magnetic field, UCNs find themselves in front of a potential barrier of +300 neV, higher than most of UCN energies. They aren't able to cross that region. As a result, only the neutron with the spin anti-parallel to the magnetic field can cross the large field region. This corresponds to a polarization by transmission.

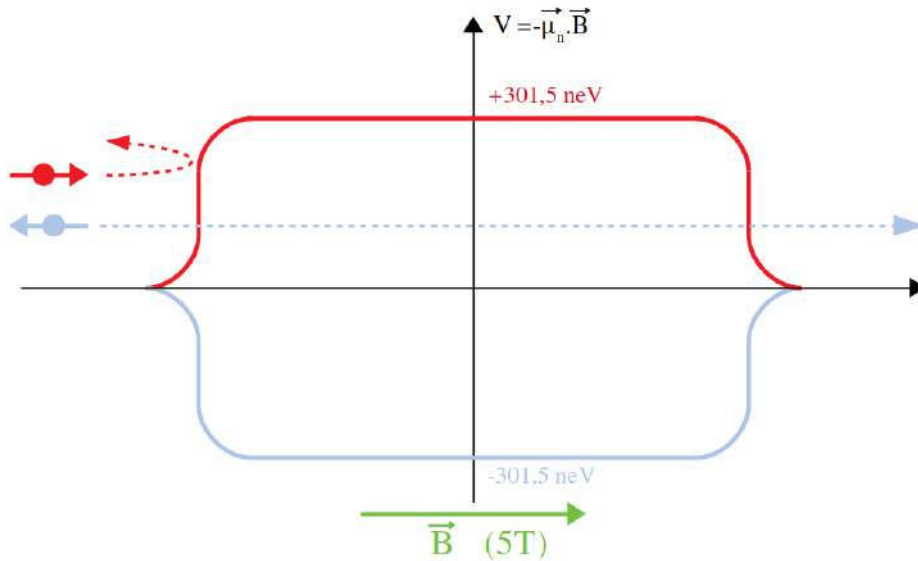


Figure 1.11 – UCN polarization with the use of a strong magnetic field.

This technique is used twice in the n2EDM apparatus, the first time with the superpolarising magnet to produce polarized neutron beam, and the second time in the USSA device, in order to analyze the UCN polarization.

1.5.2 Neutron spin evolution in a uniform magnetic field

Lets consider the wavefunction of the neutron spin state:

$$|\Psi(t)\rangle = \begin{pmatrix} a(t) \\ b(t) \end{pmatrix} = \begin{pmatrix} A(t)e^{i\Phi(t)} \\ B(t)e^{i\theta(t)} \end{pmatrix} \quad (1.33)$$

with $\langle\Psi(t)|\Psi(t)\rangle = A(t)^2 + B(t)^2 = 1$.

With a uniform magnetic field along the z axis $\vec{B} = B_0 \vec{u}_z$, the Hamiltonian can be express as :

$$\hat{H} = -\gamma_n \hat{\vec{S}} \cdot \vec{B} = -\gamma_n \hat{S}_z B_0 = -\gamma_n B_0 \frac{\hbar}{2} \hat{\sigma}_z, \text{ where } \hat{\sigma}_z = \begin{pmatrix} 1 & 0 \\ 0 & -1 \end{pmatrix} \text{ is the Pauli matrix.} \quad (1.34)$$

We can now look at the neutron spin evolution under this uniform field using the Schrödinger equation :

$$i\hbar \frac{\partial |\Psi(t)\rangle}{\partial t} = \hat{H} |\Psi(t)\rangle, \quad (1.35)$$

which gives :

$$\begin{pmatrix} \dot{a}(t) \\ \dot{b}(t) \end{pmatrix} = \frac{i\gamma_n B_0}{2} \begin{pmatrix} 1 & 0 \\ 0 & -1 \end{pmatrix} \begin{pmatrix} a(t) \\ b(t) \end{pmatrix}. \quad (1.36)$$

We then define $\omega_0 = -\gamma_n B_0$. We get the equations :

$$\begin{cases} \dot{a}(t) &= -\frac{i\omega_0}{2}a(t) \\ \dot{b}(t) &= \frac{i\omega_0}{2}b(t) \end{cases} \quad (1.37)$$

With the initial conditions $a(0) = a_0$ and $b(0) = b_0$, the solutions are :

$$\begin{cases} a(t) &= a_0 e^{-\frac{i\omega_0}{2}t}; \\ b(t) &= b_0 e^{\frac{i\omega_0}{2}t}. \end{cases} \quad (1.38)$$

which allows to write the wavefunctions of the spin as:

$$|\Psi(t)\rangle = \begin{pmatrix} a_0 e^{-\frac{i\omega_0}{2}t} \\ b_0 e^{\frac{i\omega_0}{2}t} \end{pmatrix}. \quad (1.39)$$

The probability of finding a spin up neutron (i.e along the z axis) at a given time t is then :

$$|\langle z|\Psi(t)\rangle|^2 = \left| \begin{pmatrix} 1 & 0 \end{pmatrix} \begin{pmatrix} a_0 e^{-\frac{i\omega_0}{2}t} \\ b_0 e^{\frac{i\omega_0}{2}t} \end{pmatrix} \right|^2 = |a_0^2| = A_0^2. \quad (1.40)$$

The probability of finding the neutron with a spin up along the x axis at a given time t is:

$$\begin{aligned} |\langle x|\Psi(t)\rangle|^2 &= \left| \begin{pmatrix} 1/\sqrt{2} & 1/\sqrt{2} \end{pmatrix} \begin{pmatrix} a_0 e^{-\frac{i\omega_0}{2}t} \\ b_0 e^{\frac{i\omega_0}{2}t} \end{pmatrix} \right|^2 = \frac{1}{2}(a_0^2 + b_0^2) + \frac{1}{2} \frac{a_0 b_0^*}{2} (2e^{-i\omega_0 t}) + \frac{1}{2} \frac{a_0^* b_0}{2} (2e^{i\omega_0 t}) \\ &= \frac{1}{2} + \frac{1}{2} \left(a_0 b_0^* \frac{e^{i\omega_0 t} + e^{-i\omega_0 t}}{2} - a_0 b_0^* \frac{e^{i\omega_0 t} - e^{-i\omega_0 t}}{2} + a_0^* b_0 \frac{e^{i\omega_0 t} + e^{-i\omega_0 t}}{2} + a_0^* b_0 \frac{e^{i\omega_0 t} - e^{-i\omega_0 t}}{2} \right) \\ &= \frac{1}{2} + \frac{1}{2} (a_0 b_0^* + a_0^* b_0) \cos(\omega_0 t) - \frac{i}{2} (a_0 b_0^* - a_0^* b_0) \sin(\omega_0 t) \\ &= \frac{1}{2} + \frac{1}{2} A_0 B_0 [e^{i(\theta-\Phi)} + e^{-i(\theta-\Phi)}] \cos(\omega_0 t) - \frac{1}{2} A_0 B_0 \left[\frac{e^{i(\theta-\Phi)} - e^{-i(\theta-\Phi)}}{i} \right] \sin(\omega_0 t) \\ &= \frac{1}{2} + A_0 B_0 [\cos(\theta - \Phi) \cos(\omega_0 t) - \sin(\theta - \Phi) \sin(\omega_0 t)] \\ |\langle x|\Psi(t)\rangle|^2 &= \frac{1}{2} + A_0 B_0 \cos(\omega_0 t + \theta - \Phi). \end{aligned} \quad (1.41)$$

Similarly, we can compute the probability of finding the neutron with a spin up along the y axis at a given time t:

$$|\langle y|\Psi(t)\rangle|^2 = \left| \begin{pmatrix} 1/\sqrt{2} & i/\sqrt{2} \end{pmatrix} \begin{pmatrix} a_0 e^{-\frac{i\omega_0}{2}t} \\ b_0 e^{\frac{i\omega_0}{2}t} \end{pmatrix} \right|^2 = \frac{1}{2} - A_0 B_0 \sin(\omega_0 t + \theta - \Phi). \quad (1.42)$$

As we can see, with a uniform magnetic field along the z axis, the probability of finding the neutron's spin z component up is constant, i.e. that spin state stays the same along time. However, along the x and y axis, the spin evolve in sine and cosine of $\omega_0 t$, describing a rotating trajectory : this is called the Larmor precession of the neutron. This is used by the guiding coils around the tubes to keep the neutron polarized during their transport.

1.5.3 Neutron spin evolution with an additional rotating field

Now we add to our uniform field a rotating $\vec{B}_c(t)$ field in the XY plane with an angular frequency ω and a phase ϕ . The field is then described as:

$$\vec{B} = \vec{B}_0(t) + \vec{B}_c(t) = B_c \cos(\omega t + \phi) \vec{u}_x + B_c \sin(\omega t + \phi) \vec{u}_y + B_0 \vec{u}_z, \quad (1.43)$$

and the neutron Hamiltonian becomes :

$$\hat{H} = -\gamma_n B_c \frac{\hbar}{2} \cos(\omega t + \phi) \hat{\sigma}_x - \gamma_n B_c \frac{\hbar}{2} \sin(\omega t + \phi) \hat{\sigma}_y - \gamma_n B_0 \frac{\hbar}{2} \hat{\sigma}_z, \quad (1.44)$$

where $\hat{\sigma}_x = \begin{pmatrix} 0 & 1 \\ 1 & 0 \end{pmatrix}$ and $\hat{\sigma}_y = \begin{pmatrix} 0 & -i \\ i & 0 \end{pmatrix}$ complete the set of Pauli Matrices.

Again, the evolution of the spin can be computed using the Schrödinger equation:

$$\begin{aligned} i\hbar \begin{pmatrix} \dot{a}(t) \\ \dot{b}(t) \end{pmatrix} &= -\gamma_n \frac{\hbar}{2} \left[B_c \cos(\omega t + \phi) \begin{pmatrix} 0 & 1 \\ 1 & 0 \end{pmatrix} \begin{pmatrix} a \\ b \end{pmatrix} + B_c \sin(\omega t + \phi) \begin{pmatrix} 0 & -i \\ i & 0 \end{pmatrix} \begin{pmatrix} a \\ b \end{pmatrix} + B_0 \begin{pmatrix} 1 & 0 \\ 0 & -1 \end{pmatrix} \begin{pmatrix} a \\ b \end{pmatrix} \right] \\ \Leftrightarrow \begin{pmatrix} \dot{a}(t) \\ \dot{b}(t) \end{pmatrix} &= \frac{i\gamma_n}{2} \left(B_c \cos(\omega t + \phi) \cdot b - i B_c \sin(\omega t + \phi) \cdot b + B_0 \cdot a \right). \end{aligned} \quad (1.45)$$

Noting $\omega_0 = -\gamma_n B_0$, and $\omega_c = -\gamma_n B_c$, we can rewrite the previous equation to get the system:

$$\begin{cases} \dot{a}(t) = -\frac{i}{2}(a\omega_0 + b\omega_c e^{-i(\omega t + \phi)}) \\ \dot{b}(t) = \frac{i}{2}(b\omega_0 - a\omega_c e^{i(\omega t + \phi)}) \end{cases} \quad (1.46)$$

In order to suppress the exponential, we introduce $c = ae^{i(\omega t + \phi)/2}$ and $d = be^{-i(\omega t + \phi)/2}$. in that way, we have :

$$a = ce^{-i(\omega t + \phi)/2}, \quad (1.47)$$

$$b = de^{i(\omega t + \phi)/2} \quad (1.48)$$

and their derivatives

$$\dot{a} = \dot{c}e^{-i(\omega t + \phi)/2} - \frac{i\omega}{2}ce^{-i(\omega t + \phi)/2}, \quad (1.49)$$

$$\dot{b} = \dot{d}e^{i(\omega t + \phi)/2} + \frac{i\omega}{2}de^{i(\omega t + \phi)/2}. \quad (1.50)$$

We can then rewrite the first equation of Eq. 1.46:

$$\begin{aligned} \dot{c}e^{-i(\omega t + \phi)/2} - \frac{i\omega}{2}ce^{-i(\omega t + \phi)/2} &= -\frac{i}{2}(c\omega_0 e^{-i(\omega t + \phi)/2} - d\omega_c e^{i(\omega t + \phi)/2})e^{-i(\omega t + \phi)} \\ \Leftrightarrow \dot{c}e^{-i(\omega t + \phi)/2} &= \frac{-i}{2}e^{-i(\omega t + \phi)/2}[-\omega c + \omega_0 c + \omega_c d] \\ \Leftrightarrow \dot{c} &= \frac{i}{2}[c(\omega - \omega_0) - d\omega_c]. \end{aligned} \quad (1.51)$$

In the same way, we can rewrite the second equation of Eq. 1.46, giving us:

$$\dot{d} = -\frac{i}{2}[c\omega_c + d(\omega - \omega_0)]. \quad (1.52)$$

To get the solution, we derive \dot{d} :

$$\begin{aligned}\ddot{d} &= -\frac{i}{2}[\dot{c}\omega_c + \dot{d}(\omega - \omega_0)] \\ &= -\frac{i}{2}\left[\frac{i}{2}[c(\omega - \omega_0) - d\omega_c]\omega_c - \frac{i}{2}[c\omega_c + d(\omega - \omega_0)(\omega - \omega_0)]\right] \\ \ddot{d} &= -\left(\frac{\omega_c^2 + (\omega - \omega_0)^2}{4}\right)d,\end{aligned}\quad (1.53)$$

which is a second order differential equation. Its solution is :

$$d = \alpha \cos(\Omega t) + \beta \sin(\Omega t), \quad (1.54)$$

with $\Omega = \frac{\sqrt{\omega_c^2 + (\omega - \omega_0)^2}}{2}$, and α and β are two constants deduced from the initial conditions and boundary conditions.

We can solve the other equation the same way, which gives us :

$$c = \gamma \cos(\Omega t) + \delta \sin(\Omega t), \quad (1.55)$$

where γ and δ are again two constants deduced from the initial conditions and boundary conditions.

Implementing Eq. 1.55 and Eq. 1.54 in Eq. 1.52, we can deduce a relation between the constants α , β , γ and δ :

$$\gamma = \frac{2i\beta\Omega - \alpha(\omega - \omega_0)}{\omega_c}, \quad (1.56)$$

$$\delta = -\frac{2i\alpha\Omega + \beta(\omega - \omega_0)}{\omega_c}. \quad (1.57)$$

$$(1.58)$$

We can now returns to our initial variables a and b :

$$a(t) = c(t)e^{-i(\omega t+\phi)/2} = e^{-i(\omega t+\phi)/2}(\gamma \cos(\Omega t) + \delta \sin(\Omega t)) \quad (1.59)$$

$$b(t) = d(t)e^{i(\omega t+\phi)/2} = e^{-i(\omega t+\phi)/2}(\alpha \cos(\Omega t) + \beta \sin(\Omega t)) \quad (1.60)$$

Using the initial conditions $a(0) = a_0$ and $b(0) = b_0$, we get:

$$a(0) = \gamma e^{-i\phi/2} = a_0 \Rightarrow \gamma = a_0 e^{i\phi/2}, \quad (1.61)$$

$$b(0) = \alpha e^{i\phi/2} = b_0 \Rightarrow \alpha = b_0 e^{-i\phi/2}. \quad (1.62)$$

Using the relations in Eq. 1.56, the two last constant can be derived as:

$$\beta = -\frac{i}{2\Omega} [a_0 \omega_c e^{i\phi/2} + b_0 (\omega - \omega_0) e^{-i\phi/2}] \quad (1.63)$$

$$\delta = \frac{i}{2\Omega} [a_0 (\omega - \omega_0) e^{i\phi/2} - b_0 \omega_c e^{-i\phi/2}] \quad (1.64)$$

$$(1.65)$$

Finally, we can write the evolution of the spin wavefunction:

$$|\Psi(t)\rangle = \begin{pmatrix} a(t) \\ b(t) \end{pmatrix} = \begin{pmatrix} e^{-i(\omega t+\phi)/2} \left[a_0 e^{i\phi/2} \cos(\Omega t) + \frac{i}{2\Omega} [a_0 (\omega - \omega_0) e^{i\phi/2} - b_0 \omega_c e^{-i\phi/2}] \sin(\Omega t) \right] \\ e^{-i(\omega t+\phi)/2} \left[b_0 e^{-i\phi/2} \cos(\Omega t) - \frac{i}{2\Omega} [a_0 \omega_c e^{i\phi/2} + b_0 (\omega - \omega_0) e^{-i\phi/2}] \sin(\Omega t) \right] \end{pmatrix}. \quad (1.66)$$

As we did for the uniform field, the probability of finding the z component of a neutron's spin in a spin up state at a time t can be extracted from:

$$\begin{aligned} |\langle z|\Psi(t)\rangle|^2 &= \left| \begin{pmatrix} 1 & 0 \end{pmatrix} \begin{pmatrix} a(t) \\ b(t) \end{pmatrix} \right|^2 = |a(t)|^2 \\ &= a_0^2 \cos^2(\Omega t) + \delta^2 \sin^2(\Omega t) + (a_0 \delta^* e^{i\phi/2} + a_0^* \delta e^{-i\phi/2}) \cos(\Omega t) \sin(\Omega t). \end{aligned} \quad (1.67)$$

The delta notation is kept for readability.

We can also look at the same probability for the x and y spin components at a time t:

$$\begin{aligned} |\langle x|\Psi(t)\rangle|^2 &= \frac{1}{2} (a^2(t) + b^2(t) + a(t)b^*(t) + a^*(t)b(t)) \\ &= \frac{1}{2} \\ &+ \frac{1}{2} (a_0 b_0^* e^{-i\omega t} + a_0^* b_0 e^{i\omega t}) \cos^2(\Omega t) \\ &+ \frac{1}{2} (\delta \beta^* e^{-i(\omega t+\phi)} + \delta^* \beta e^{i(\omega t+\phi)}) \sin^2(\Omega t) \end{aligned} \quad (1.68)$$

$$\begin{aligned} |\langle y|\Psi(t)\rangle|^2 &= \frac{1}{2} (a^2(t) + b^2(t) + i a^*(t)b(t) - i a(t)b^*(t)) \\ &= \frac{1}{2} \\ &+ \frac{i}{2} (a_0^* b_0 e^{i\omega t} - a_0 b_0^* e^{-i\omega t}) \cos^2(\Omega t) \\ &+ \frac{i}{2} (\delta^* \beta e^{i(\omega t+\phi)} - \delta \beta^* e^{-i(\omega t+\phi)}) \sin^2(\Omega t) \\ &+ \frac{i}{2} ((\beta a_0^* + \delta^* b_0) e^{i(\omega t+\phi/2)} - (\beta^* a_0 + \delta b_0^*) e^{-i(\omega t+\phi/2)}) \cos(\Omega t) \sin(\Omega t) \end{aligned} \quad (1.69)$$

This time, one can see that the probability of finding a spin up along the z axis is not constant, and is dependent of the frequency ω .

We can take a particular case where the spin is prepared in the state $|\Psi(0)\rangle = \begin{pmatrix} a_0 = e^{i\phi} \\ b_0 = 0 \end{pmatrix}$.

In that case, the previous probabilities can be reduced to :

$$|\langle z|\Psi(t)\rangle|^2 = \cos^2(\Omega t) + \frac{(\omega - \omega_0)^2}{4\Omega^2} \sin^2(\Omega t), \quad (1.70)$$

$$|\langle x|\Psi(t)\rangle|^2 = \frac{1}{2} - \frac{(\omega - \omega_0)\omega_c}{4\Omega^2} \cos(\omega t + \phi) \sin^2(\omega t) + \frac{\omega_c}{2\Omega} \sin(\omega t + \phi) \cos(\Omega t) \sin(\Omega t), \quad (1.71)$$

$$|\langle y|\Psi(t)\rangle|^2 = \frac{1}{2} + \frac{(\omega - \omega_0)\omega_c}{4\Omega^2} \sin(\omega t + \phi) \sin^2(\omega t) + \frac{\omega_c}{2\Omega} \cos(\omega t + \phi) \cos(\Omega t) \sin(\Omega t), \quad (1.72)$$

At the resonance, with a radiofrequency field with an angular frequency $\omega = \omega_0$, the equation becomes:

$$|\langle z|\Psi(t)\rangle|^2 = \cos^2\left(\frac{\omega_c}{2}t\right) \quad (1.73)$$

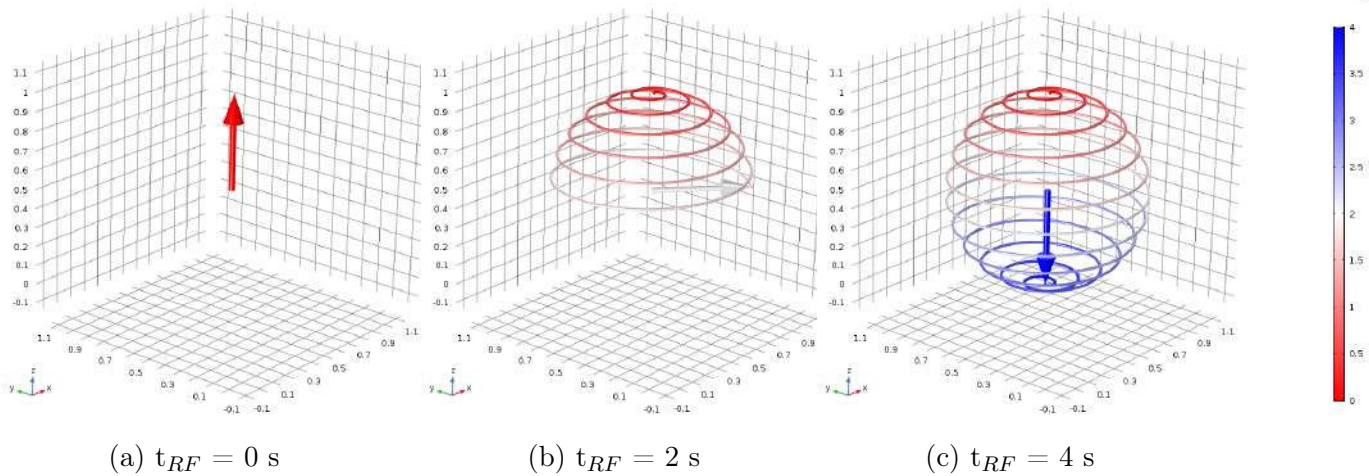


Figure 1.12 – Spin evolution under a radiofrequency $B_c = 8.5 \text{ nT}$ and a uniform field $B_0 = 1 \mu\text{T}$ at the resonance condition $\omega = \omega_0$. The neutron polarization is longitudinal (spin up state) at $t=0 \text{ s}$ (left figure). After 2 s, it becomes transverse as shown on the middle figure. There the neutron spin can freely precess if the RF field is no longer applied. Otherwise, after 4 s of RF field, the spin is fully reversed, and the neutron polarization is again longitudinal (but in the spin down state).

$$|\langle x | \Psi(t) \rangle|^2 = \frac{1}{2} + \sin(\omega t + \phi) \cos\left(\frac{\omega_c}{2}t\right) \sin\left(\frac{\omega_c}{2}t\right), \quad (1.74)$$

$$|\langle y | \Psi(t) \rangle|^2 = \frac{1}{2} + \cos(\omega t + \phi) \cos\left(\frac{\omega_c}{2}t\right) \sin\left(\frac{\omega_c}{2}t\right), \quad (1.75)$$

In that case the spin can do an entire transition from spin up to spin down along the z axis.

Considering a radiofrequency field of $B_c = 8.57 \text{ nT}$, which corresponds to a frequency $\omega_c = 1.57 \text{ rad/s}$, the time needed to bring the spin in the orthogonal plan corresponds to :

$$\begin{aligned} \cos\left(\frac{\omega_c}{2}t\right)^2 &= 0 \\ \Leftrightarrow \frac{\omega_c}{2}t &= \frac{\pi}{2} \\ \Leftrightarrow t &= \frac{\pi}{\omega_c} = 2.00 \text{ s}. \end{aligned} \quad (1.76)$$

To achieve a full spin-flip, we need to apply the radio frequency field during 4s.

This capacity to manipulate the spin with a radiofrequency magnetic field is very useful: it is the base of the spin-flippers which inverts the spin of the neutrons. This feature is used in the simultaneous spin analyzer [59, 53] to inverse the spin of the neutrons. It is also on the nEDM precession chamber to flip the neutron spin orthogonally to the main B_0 field : then it precesses, and if the nEDM is non-null, accumulate a phase, which is the variable we measure to sign the existence of an EDM.

Conclusion

The electric dipole moment research allows to probe the extensions of the standard model as well as to partially explain the matter-antimatter asymmetry, being a source of CP violation. The EDM is searched in several system, one of them being the neutron, which possess several advantages (neutrality, 1/2 spin, sensitive to weak and strong forces). Because the neutron have a 1/2 spin, its magnetic moment and electric dipole moment are aligned on its spin. Since

the years 1980, specific neutrons is used for the nEDM experiment : the ultra-cold neutrons. Because of their low energy (below 300 neV), they can be stored in material vessels and thus studied for a long time. They can interact through their magnetic moment with magnetic field. We can therefore manipulate them with magnetic fields. For instance, a neutron beam can be polarised by crossing a magnetized foil. Using uniform magnetic field, we can hold the spin polarisation. Finally, using rotating field allows to flip the spin from the spin up to the spin down state. Those manipulations are used in several part of the experiment, and constitute the core of the EDM measurement principle, explained in the next chapter.

The n2EDM experiment @ PSI

Contents

2.1	The measurement principle	40
2.1.1	Principle	40
2.1.2	The Ramsey separated oscillating fields method	41
2.1.3	Expected n2EDM statistical sensitivity	44
2.2	Magnetic field requirements	44
2.2.1	Field uniformity: top-bottom matching condition	44
2.2.2	Field uniformity: the neutron depolarization	45
2.2.3	Main systematic effect : the false motional EDM	47
2.2.4	Local Magnetic dipole	51
2.2.5	Gravitational shift and uncompensated field drift	52
2.3	The n2EDM experiment	52
2.3.1	The PSI UCN source	53
2.3.2	UCN transport: guides, switch and holding coils	53
2.3.3	The Precession chambers	54
2.3.4	Magnetic field production	54
2.3.5	Control of the magnetic field	54
2.3.6	The detection system: USSA and detectors	57

Introduction

The n2EDM experiment is the second step of the nEDM experiment, which started in 2005 at ILL and was pursued at PSI in 2009 with the move of the OILL spectrometer. The UCN source commissioning and the upgrades of the OILL spectrometer lasted a few years. Then the data taking took place in 2015 and 2016. A new best limit is expected to be published in 2019, with a statistical sensitivity of the order of $1 \times 10^{-26} e\text{ cm}$. The n2EDM experiment aims at improving the experimental statistical sensitivity by a factor 10 by the end of 2025. Then a second phase of the n2EDM experiment is planned in order to explore the $10^{-28} e\text{ cm}$ range. In this chapter, the measurement principle is presented, followed by the magnetic field requirements for the n2EDM experiment. Finally an overview of the n2EDM apparatus is presented.

2.1 The measurement principle

2.1.1 Principle

The nEDM measurement takes advantage of the neutron interaction with the magnetic and the electric fields through its magnetic moment μ_n and its potential electric dipole moment d_n . In the presence of both fields, the Hamiltonian reads:

$$H = -\vec{\mu}_n \cdot \vec{B} - \vec{d}_n \cdot \vec{E}, \quad (2.1)$$

where $\vec{\mu}_n$ and \vec{d}_n are aligned with the spin direction (see section 1.3.1). The neutron energy splits in several level depending on the spin orientation with respect to the directions of the magnetic and electric fields, as shown in Fig. 2.1. Both fields can be either in a parallel or in an anti-parallel configuration.

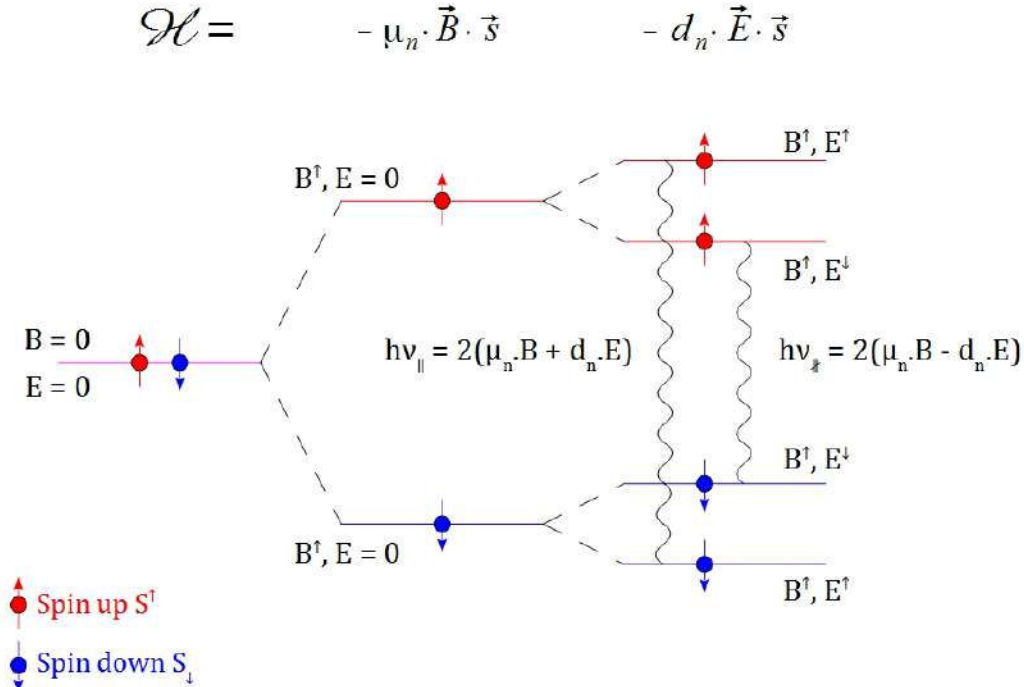


Figure 2.1 – The splitting of the neutron energy levels depends on the neutron spin orientation, as well as on the relative directions of the electric and magnetic fields. Both fields can be either parallel (\parallel) or anti-parallel (\nparallel). One must reminds that μ_n is negative since the neutron gyromagnetic ratio factor γ_n is negative. It is assumed here that the neutron EDM d_n behaves in the same way.

For each fields configuration, the neutron Larmor frequency can be extracted: ν_{\parallel} for the parallel configuration and ν_{\nparallel} for the anti-parallel configuration. The measurement of the frequency difference ($\nu_{\parallel} - \nu_{\nparallel}$) leads to the estimation of the neutron EDM d_n :

$$|d_n| = \left| \frac{h(\nu_{\parallel} - \nu_{\nparallel}) + 2\mu_n(B_{\parallel} - B_{\nparallel})}{2(E_{\parallel} - E_{\nparallel})} \right|. \quad (2.2)$$

With a same magnetic field in both configurations ($B_{\parallel} = B_{\nparallel}$), and an electric field which only changes its sign ($E_{\parallel} = -E_{\nparallel} = E$), Eq. 2.2 becomes:

$$|d_n| = \left| \frac{h(\nu_{\parallel} - \nu_{\nparallel})}{4E} \right|. \quad (2.3)$$

While the electric field can be operated with a rather well defined stability, the magnetic field production requires a complex procedure which constitutes the heart of the experiment (see section 2.3.4 and 2.3.5). The requirements on its stability and its uniformity are extremely severe (see section 2.2).

2.1.2 The Ramsey separated oscillating fields method

In order to compute d_n , the neutron Larmor frequencies must be measured in parallel and anti-parallel fields configurations. The Ramsey separated oscillating fields method [60], shown in Fig. 2.2, is used for this purpose. It works as follow: first polarised UCNs are stored in the precession chamber in which parallel or anti-parallel \vec{E} and \vec{B} fields are applied. The neutron spin is aligned along the magnetic field direction. Then a radiofrequency (RF) pulse is applied during 2s ($\tau_{RF} = 2s$). If the RF frequency corresponds to the neutron Larmor frequency ($f_n = \frac{\gamma_n}{2\pi} B_0$), the neutron spin flips in the plane orthogonal to the magnetic field B_0 . Then it precesses during a period T ($\simeq 180s$) called the precession time. The existence of an EDM leads to a frequency shift during this precession time, which depends of the configuration between the electric and magnetic field. The shift is positive if the electric and the magnetic field are parallel, negative if they are anti-parallel (see Fig. 2.2). At the end of the precession time, a second RF pulse is performed. Then, the precession chamber is emptied and the neutron polarisation is analysed (see section 2.3.6). This operation is repeated every cycle. A cycle lasts about 5 minutes and corresponds to the filling of the precession chamber, the free neutron precession, the emptying of the chamber and the measurement of the neutron polarisation. The goal is to record as many cycles as possible in order to improve the statistical sensitivity. At the end, the nEDM is measured (at first approximation) through the Eq. 2.3.

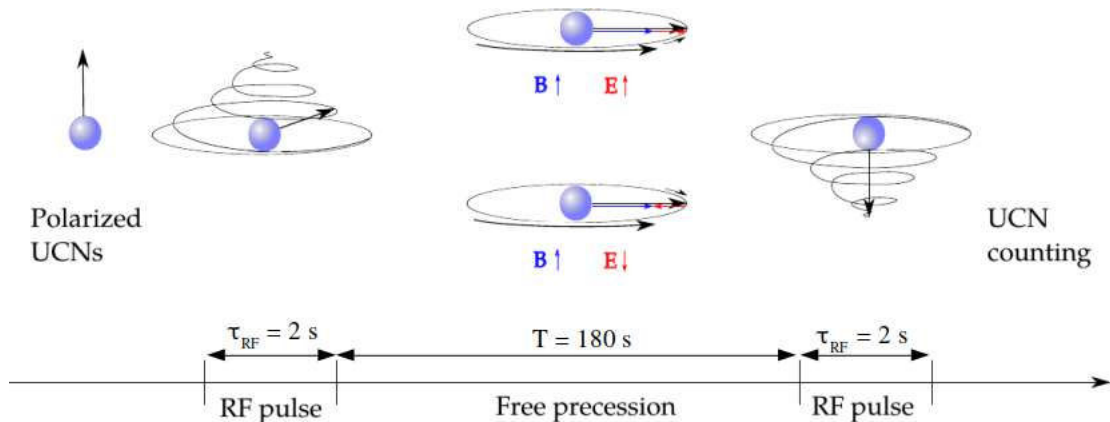


Figure 2.2 – Ramsey separated oscillating fields method.

Varying the frequency of the RF pulse leads to the so-called Ramsey pattern, shown in Fig. 2.3. The Larmor frequency is derived from this figure by fitting the central fringe of the Ramsey pattern.

Formerly, the number of spin up neutron (N^\uparrow) and spin down neutron (N^\downarrow) were counted as a function of the RF frequency [61]. Since, the nEDM collaboration made the choice to use the asymmetry [53], this variable being by definition normalized to the total number of events (and therefore naturally compensate for the fluctuation of the UCN source output). It is defined as:

$$A = \frac{N^\uparrow - N^\downarrow}{N^\uparrow + N^\downarrow}; \quad \sigma_A = \frac{2\sqrt{N^\uparrow N^\downarrow}}{(N^\uparrow + N^\downarrow)^{3/2}} \quad (2.4)$$

where $N^{\uparrow/\downarrow}$ corresponds to the number of detected spin up\down UCN and σ_A is the statistical uncertainty of the asymmetry.

The asymmetry can be expressed as a function of the RF frequency [62]:

$$A(f_{RF}) = A_0 - \alpha \cos\left(\pi \frac{f_{RF} - f_n}{\Delta\nu}\right) \quad (2.5)$$

where A_0 corresponds to the mean asymmetry, $\Delta\nu = [2(T + 4\tau_{RF}/\pi)]^{-1}$ is the width at half-height of the central fringe and α corresponds to the visibility of the central fringe, computed as :

$$\alpha = \frac{N_{max} - N_{min}}{N_{max} + N_{min}} = \frac{A_{max} - A_{min}}{A_{max} + A_{min}}. \quad (2.6)$$

During the data taking, only four working points (WP) are used. They are located close to the half height of the central fringe since the sensitivity of the frequency measurement is the largest where the slope is the steepest. Their frequencies is given by $f_{RF} = f_n \pm \frac{\Delta\nu}{2}(1 \pm 0.1)$.

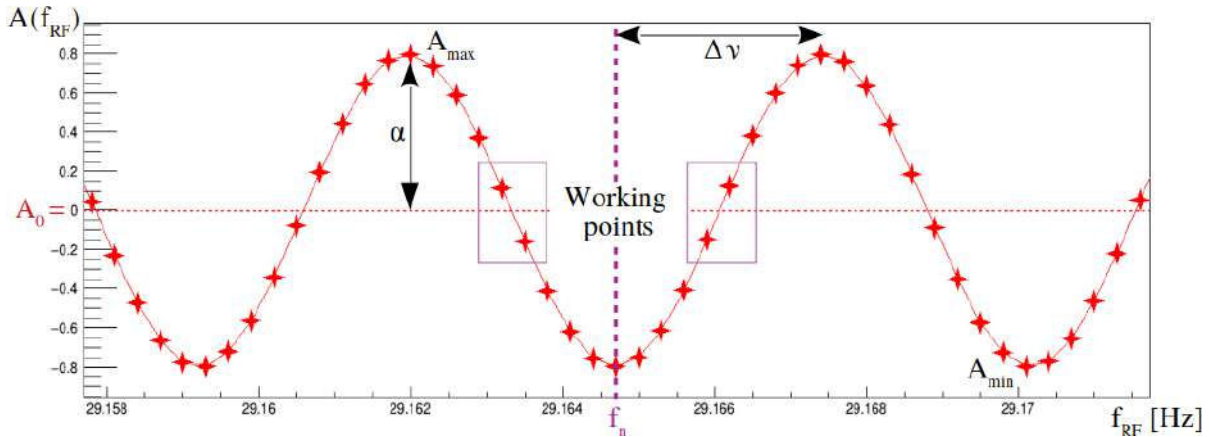


Figure 2.3 – The Ramsey pattern is obtained by plotting the asymmetry as a function of the RF frequency. The amplitude of the pattern is characterized by the visibility α . The 4 working points used to extract the neutron frequency f_n are inside the rectangular purple boxes.

The fit of the central fringe by 2.5 allows to extract the neutron frequency f_n .

The EDM statistical sensitivity is derived from the statistical error of the neutron frequency. By inverting the Eq. 2.5, the neutron frequency can be estimated by:

$$f_n = f_{RF} - \frac{\Delta\nu}{\pi} \arccos\left(-\frac{A_0 - A}{\alpha}\right) \quad (2.7)$$

Assuming that the precession time T , the RF pulse duration τ_{RF} and the RF frequency f_{RF} are perfectly known, one can derive the statistical sensitivity of the neutron frequency from Eq. 2.7 :

$$\sigma_{f_n} = \frac{\Delta\nu}{\pi\alpha} \sqrt{1 - \left(\frac{A_0 - A}{\alpha}\right)^2}^{-1} \sqrt{\sigma_{A_0}^2 + \sigma_A^2 + \sigma_\alpha^2 \left(\frac{(A_0 - A)^2}{\alpha^2}\right)} \quad (2.8)$$

The factor $1 - \left(\frac{A_0 - A}{\alpha}\right)^2$ in Eq. 2.8 corresponds to the loss of sensitivity in the frequency measurement due to the use of the working points. Two extreme cases can be explored for this parameter:

- If the RF frequency of the working points are $f_{RF} = f_n + \Delta\nu/2$ (at the half height of the central fringe of the Ramsey pattern), the asymmetry $A(\Delta\nu/2) = A_0$ and the sensitivity on the neutron frequency measurement is null $\sigma_{f_n} = 0$. This is the best case.

- If the RF frequency of the working points are $f_{RF} = f_n \pm \Delta\nu$ (at the top of the central fringe), then the asymmetry is $A(\Delta\nu) = A_0 - \alpha$, and the sensitivity on the neutron frequency measurement is infinite $\sigma_{f_n} = \infty$. This is the worst case.

However, since it is necessary to use four working points to fit the central fringe, their RF frequency are slightly detuned with respect to the best case. They are $f_{RF} = f_n + \frac{\Delta\nu}{2}(1 \pm 0.1)$. This corresponds to an asymmetry of $A(f_n + \frac{\Delta\nu}{2}(1 \pm 0.1)) = A_0 - \alpha\cos(1.1\pi/2) \simeq A_0 - 0.16\alpha$, and therefore give a sensitivity loss of $\sigma(f_n + \frac{\Delta\nu}{2}(1 \pm 0.1)) = \sqrt{1 - 0.16^2}^{-1} = 1.013$, so about 1.3 %. This is the cost of the fitting procedure.

The EDM statistical sensitivity can be found using Eq. 2.3 and Eq. 2.8 :

$$\begin{aligned}\sigma_{d_n} &= \sqrt{\left(\frac{\partial d_n}{\partial \nu_{||}}\right)^2 \sigma_{\nu_{||}}^2 + \left(\frac{\partial d_n}{\partial \nu_{\#}}\right)^2 \sigma_{\nu_{\#}}^2} \\ &= \frac{h}{4E} \sqrt{\sigma_{\nu_{||}}^2 + \sigma_{\nu_{\#}}^2} \simeq \frac{h}{4E} \sqrt{2\sigma_{f_n}^2} \\ &\simeq \frac{h}{4E} \frac{\Delta\nu}{\pi\alpha} \sqrt{\frac{2}{1 - \left(\frac{A_0 - A}{\alpha}\right)^2}} \sqrt{\sigma_{A_0}^2 + \sigma_A^2 + \sigma_\alpha^2 \left(\frac{(A_0 - A)^2}{\alpha^2}\right)}\end{aligned}\quad (2.9)$$

At the four working points, the number of neutrons $N_0^{\uparrow/\downarrow}$ is close to the half of the resonance $N_0^{\uparrow/\downarrow}$, i.e $A \simeq A_0$ and $\sigma_A \simeq \sigma_{A_0}$. Thus Eq. 2.10 becomes:

$$\begin{aligned}\sigma_{d_n} &\simeq \frac{\hbar}{2\alpha(2T)E} \sqrt{4\sigma_{A_0}^2} \\ &\simeq \frac{\hbar}{2\alpha TE} \frac{2\sqrt{N_0^{\uparrow} N_0^{\downarrow}}}{(N_0^{\uparrow} + N_0^{\downarrow})^{3/2}}\end{aligned}\quad (2.10)$$

Finally, since $N_0^{\uparrow} \simeq N_0^{\downarrow} \simeq N_{tot}/2$, we have:

$$\sigma_{d_n} \simeq \frac{\hbar}{2\alpha TE \sqrt{N_{tot}}}.\quad (2.11)$$

This formula shows the critical parameters that need to be improved in order to get lower the EDM statistical sensitivity. They are four: the visibility α , the precession time T, the electric field E and the number of detected neutrons in the two chambers N_{tot} . The visibility is mainly limited by the UCN depolarisation. It requires a magnetic field as uniform as possible (see section 2.2.2). The precession time T is limited by the neutron losses mainly due to wall collisions and in a less extent by the neutron decay. The electric field is constrained by the electric discharges, and finally, the number of neutron N_{tot} is mainly governed by the UCN source production.

In order to be able to combine all the neutron frequency measurements, one has to take into account the drift of the magnetic field. This is the role of the Hg comagnetometer which measure the field in the precession chamber during every cycle (see section 2.3.5). The drift of the magnetic field is then taken into account by using the ratio $\mathcal{R} = \frac{f_n}{f_{Hg}}$ instead of f_n (f_{Hg} corresponds to the Larmor frequency of the Mercury atoms). Eq. 2.3 can be then rewrite using the ratio \mathcal{R} :

$$d_n = \frac{\pi\hbar f_{Hg}}{4|E|} (\mathcal{R}_{\uparrow\downarrow}^T - \mathcal{R}_{\uparrow\uparrow}^T + \mathcal{R}_{\uparrow\downarrow}^B - \mathcal{R}_{\uparrow\uparrow}^B),\quad (2.12)$$

where the label "T" is used for the quantities related to the top chamber, and "B" for the bottom one.

2.1.3 Expected n2EDM statistical sensitivity

The most important upgrades of the n2EDM experiment with respect to nEDM are:

- The use of two precession chambers with a larger diameter;
- A higher electric field intensity;
- A new magnetic shield;
- A coil system allowing a better magnetic field uniformity;
- A better monitoring of the magnetic field (laser driven the Hg comagnetometers and large number of Cs magnetometers)

The Table 2.1 shows the main parameters of the nEDM and n2EDM experiments. The main improvement comes from the number of detected neutrons, provided by the size and the use of two chambers, and also because of a better adaptation between the height of the UCN source exit and the precession chamber entrance. The expected statistical of n2EDM is $1.1 \times 10^{-27} e\text{ cm}$ after four years of data taking (i.e. 500 days).

	nEDM	n2EDM
Chamber coating	DLC & dPS	DLC & dPS
Number of chambers	1	2
Chamber's diameter	47 cm	80 cm
Number of neutrons N	15000	121000
Precession time T	180 s	180 s
Electric field E	11 kV/cm	15 kV/cm
Visibility α	0.75	0.8
$\sigma(d_n)$ (per day)	$11 \times 10^{-26} e\text{ cm}$	$2.6 \times 10^{-26} e\text{ cm}$
$\sigma(d_n)$ (final)	$9.5 \times 10^{-27} e\text{ cm}$ (253 days)	$1.1 \times 10^{-27} e\text{ cm}$ (500 days)

Table 2.1 – Comparison of the main parameters for the nEDM experiment and the n2EDM experiment.

2.2 Magnetic field requirements

The control of the magnetic field is a critical issue for the n2EDM experiment. This section presents the requirements on the B_0 field. It is based on the 2018 Technical Design Report [63].

2.2.1 Field uniformity: top-bottom matching condition

The procedure used to measure the neutron frequency, the Ramsey's oscillating fields method, requires to apply a RF pulse at the beginning and the end of the precession time. Any bad tuning of the RF frequency induces a loss of sensitivity in the neutron frequency measurement. The top-bottom matching condition comes from the fact that the same RF frequency pulse will be used for both chambers.

The Larmor frequency of the neutron f_n is linked to the magnetic field by:

$$f_n = \frac{\gamma_n B}{2\pi}. \quad (2.13)$$

This implies that in a presence of a vertical gradient of the magnetic field, the Larmor frequency differs for the top and the bottom chamber. The difference is:

$$\Delta f_n = f_n^T - f_n^B = \frac{\gamma_n \Delta B}{2\pi} \quad (2.14)$$

Therefore, any vertical gradient induces a RF frequency detuning and a loss of sensitivity in the neutron frequency measurement.

In order to keep a loss of sensitivity below 2%, the difference between the top and bottom frequencies must be lower than $\Delta f_n < \frac{0.2\Delta\nu}{2}$, which can be translated to the vertical gradient :

$$\frac{\gamma_n \Delta B}{2\pi} < \frac{0.2\Delta\nu}{2} \Leftrightarrow \Delta B < \frac{0.2\pi}{2\gamma_n(T + \tau_{RF}/4\pi)} \Leftrightarrow \Delta B < 9.52 \text{ pT}. \quad (2.15)$$

The two chamber centers being separated by a height $H' = 17 \text{ cm}$, the requirement on the vertical linear gradient is:

$$\frac{\partial B_z}{\partial z} = G_{1,0} < 0.6 \text{ pT/cm}. \quad (2.16)$$

This is known as the "top-bottom matching condition".

2.2.2 Field uniformity: the neutron depolarization

As presented in 2.7, the statistical sensitivity of the nEDM measurement is:

$$\sigma_{d_n} = \frac{\hbar}{2\alpha TE\sqrt{N_{tot}}}, \quad (2.17)$$

where T is the precession time, E the electric field strength, N_{tot} the total number of detected neutrons and α the visibility of the Ramsey resonance. Assuming a fully polarized neutron beam, the visibility accounts for our ability to hold the polarization during the neutron transport, the precession time and also reflects the analysing power of the spin analyser.

Several type of depolarizations can be distinguished. The first type is called the *transverse* depolarization and occurs when the neutrons spins are transverse to the magnetic field B_0 (i.e. during the precession time). The second depolarisation is called *longitudinal* depolarisation and occurs when the spins are along the B_0 field.

The variation of the visibility α due to the transverse depolarisation is given by:

$$\frac{d\alpha}{dT} = -\frac{\alpha}{T_{2,wall}} - \frac{\alpha}{T_{2,mag}} + \dot{\alpha}_{grav}, \quad (2.18)$$

and the one due to the longitudinal depolarisation is:

$$\frac{d\alpha}{dT} = -\frac{\alpha}{T_{1,wall}} - \frac{\alpha}{T_{1,mag}}, \quad (2.19)$$

where $T_{1,wall}$ and $T_{2,wall}$ corresponds to wall depolarisation, $T_{1,mag}$ and $T_{2,mag}$ are due to the non-uniformities of the magnetic field and $\dot{\alpha}_{grav}$ is due to a phenomenon called *Gravitationally enhanced depolarisation* [64]. Because we are only interested by the depolarisation occurring during the precession time, the equation Eq. 2.19 is not considered.

The following paragraphs describe all of these depolarisation process.

Wall depolarization

The wall depolarization is induced by the presence of magnetic impurities in the wall or on its surface. It is modelised by a depolarization probability per wall collision β . This probability has been measured between $10^{-6} \lesssim \beta \lesssim 10^{-5}$ for most of the common material used for wall coating, such as Nickel-Molybdenum (NiMo), copper and deuterated polystyrene (dPS) [50]. Knowing that the average frequency of wall collisions ν is about 50 Hz for the nEDM experiment

at PSI, and that the depolarization process doesn't depend of the initial spin's orientation, we have for both longitudinal and transverse polarization:

$$T_{1,wall} = T_{2,wall} = (\beta\nu)^{-1} \gtrsim 2000 \text{ s.} \quad (2.20)$$

Those quantities have been measured $\simeq 4000$ s in the nEDM experiment [63]. The corresponding loss of visibility due to wall collisions during the precession time ($T=180\text{s}$) can be estimated by :

$$\Delta\alpha_{wall} = \alpha(0) - \alpha(T) = 1 - e^{-\frac{T}{T_{wall}}} \lesssim 0.04. \quad (2.21)$$

Thus, the impact of the wall depolarization is weak, and doesn't constitute a major factor.

Intrinsic depolarization

The intrinsic depolarization happens when neutrons are travelling in a non-uniform field (here, the neutrons are supposed to have the same energy). A dephasing occurs because they don't have all the same trajectories and therefore don't feel exactly the same magnetic field along their moving.

The intrinsic transverse depolarization rate is mainly induced by the linear gradient of the vertical components of the field $\frac{\partial B_z}{\partial z}$, $\frac{\partial B_z}{\partial x}$ and $\frac{\partial B_z}{\partial y}$. In [65] Afach and al. expressed the transverse depolarization rate as :

$$\frac{1}{T_{2,mag}} = \frac{\mathcal{H}^3\gamma_n^2}{16v} \left(\frac{\partial B_z}{\partial z} \right)^2 + \frac{8R^3\gamma_n^2}{9\pi v} \left[\left(\frac{\partial B_z}{\partial x} \right)^2 + \left(\frac{\partial B_z}{\partial y} \right)^2 \right], \quad (2.22)$$

where v is the UCN speed, γ_n is the gyromagnetic ratio of the neutron, R is the chamber radius, and \mathcal{H} corresponds to the maximum height that can be reached by a neutron in the precession chamber, so the lesser between the height of the chamber H and the height-equivalent energy $\epsilon = E/(m_n g)$, where E is the neutron kinetic energy. It can be rewritten in terms of gradients:

$$\frac{1}{T_{2,mag}} = \frac{\mathcal{H}^3\gamma_n^2}{16v} G_{1,0}^2 + \frac{8R^3\gamma_n^2}{9\pi v} (G_{1,-1}^2 + G_{1,1}^2). \quad (2.23)$$

Considering large field gradients $G_{1,0} = G_{1,-1} = G_{1,1} = 50 \text{ pT/cm}$, and typical values : $v = 3 \text{ m/s}$, $H = 12 \text{ cm}$, $R = 23.5 \text{ cm}$, one gets a transverse depolarization time of $T_{2,mag} \sim 121 \text{ s}$. This corresponds to a huge visibility loss of 77%. The intrinsic depolarization is indeed the main process for neutron depolarization.

Using the spin relaxation theory introduced by Redfield [66] and applied to spin 1/2 particles in a bottle, one can compute the relaxation rate involved in transverse depolarization [67] :

$$\frac{1}{T_{2,mag}} = \frac{\gamma_n^2}{2} \int_0^\infty \langle B_x^c(0)B_x^c(t) + B_y^c(0)B_y^c(t) \rangle \cos(\omega t) dt + \gamma_n^2 \int_0^\infty \langle B_z^c(0)B_z^c(t) \rangle dt, \quad (2.24)$$

where $B_i^c = B_i - \langle B_i \rangle$ is the deviation from the mean value of the field component i .

A requirement on the field non uniformity has been defined : the goal is to have a visibility loss lower than 2%. This corresponds to a transverse depolarization time of $T_{2,mag} > 8900\text{s}$, and translates in a field uniformity requirement defined thereafter :

$$\begin{aligned} \sigma(B_z) &< \sqrt{\langle (B_z^c)^2 \rangle} = \sqrt{\frac{1}{T_{2,mag} \cdot \gamma_n^2 \cdot \tau_c(n2EDM)}} \\ \sigma(B_z) &< 170 \text{ pT}. \end{aligned} \quad (2.25)$$

where the quantity $\tau_c(n2EDM) \simeq 119 \text{ ms}$ is called the correlation time and is extrapolated from the correlation time of the nEDM experiment $\tau_c(nEDM) \simeq 70\text{s}$ (see [63] for more details).

Gravitationally enhanced depolarization

The last phenomenon inducing depolarization is called the *gravitationally enhanced depolarization* [64]. Since UCN are impacted by gravity, the maximum height that they can reach in the precession chambers depends on their energy. As a result, in presence of a vertical field gradient $\frac{\partial B_z}{\partial z}$, UCN with different energies don't feel the same magnetic field. This induces, in average, different precession rates. The depolarization rate $\dot{\alpha}_{grav}$ can be written as:

$$\dot{\alpha}_{grav} = -\gamma_n^2 \left(\frac{\partial B_z}{\partial z} \right)^2 Var[\bar{z}] T, \quad (2.26)$$

where γ_n is the gyromagnetic ratio of the neutron, and $Var[\bar{z}]$ is the variance of the neutrons height distribution :

$$Var[\bar{z}] = \int (\bar{z}(\epsilon) - \langle z \rangle)^2 n(\epsilon) d\epsilon, \quad (2.27)$$

where, $n(\epsilon)d\epsilon$ corresponds to the probability of a neutron to be in the group of energy ϵ , $\bar{z}(\epsilon)$ corresponds the mean height of that group, and $\langle z \rangle$ stands for the mean height of all neutrons.

In the nEDM experiment, $Var[\bar{z}]$ was estimated to be about 0.2 cm^2 , and the modulus of the vertical gradient was at most $|\frac{\partial B_z}{\partial z}| \simeq 30 \text{ pT/cm}$. The loss of visibility was then estimated to be:

$$\Delta\alpha_{grav} = -\frac{1}{2}\gamma_n^2 \left(\frac{\partial B_z}{\partial z} \right)^2 Var[\bar{z}] T^2 \lesssim 0.10. \quad (2.28)$$

In the n2EDM experiment, the variance $Var[\bar{z}]$ is attended to be about the same. However, the vertical gradient will be $|\frac{\partial B_z}{\partial z}| \leq 0.6 \text{ pT/cm}$, due to the top-bottom matching requirement (see subsection 2.2.1). This strongly limits the loss of visibility due to the gravitationally enhanced depolarization: it is less than 4×10^{-5} .

2.2.3 Main systematic effect : the false motional EDM

A particle with a speed \vec{v} moving in an electric field \vec{E} feels a motional magnetic field defined as:

$$\vec{B} = \frac{\vec{E} \times \vec{v}}{c^2}, \quad (2.29)$$

where c is the speed of light. In the presence of a non-uniform magnetic field, the motional field induces a frequency-shift which is linearly dependent on the electric field $|\vec{E}|$. This mimics the signal from a true EDM and is called the false motionalEDM [68]. The effect of the motional EDM has been experimentally observed in [69] by adding deliberately a vertical linear gradient.

The motional EDM can be computed from the spin relaxation theory. It depends of the speed of the particle. If the particle is slow, such as the ultracold neutrons, the Larmor frequency is higher than the rate of the wall collisions, determined by $1\tau_c = v_{RMS}/2R$, where $v_{RMS} = \sqrt{\langle v^2 \rangle}$ is the mean square velocity of the neutron. This corresponds to the adiabatic regime. Considering a uniform vertical gradient of the B_z component, the false EDM can be written as [67]:

$$d^{false} = -\frac{\hbar v_{RMS}^2}{2c^2 B_0^2} \langle \frac{\partial B_z}{\partial z} \rangle. \quad (2.30)$$

The false EDM can be rewritten as:

$$\begin{aligned} d_n^{false} &= -\frac{\hbar v_{RMS}^2}{2c^2 B_0^2} G_{1,0} \\ &\simeq -\frac{1.465 \times 10^{-28} G_{1,0}}{pT/cm} e \text{ cm}, \end{aligned} \quad (2.31)$$

considering a mean square speed of $v_{RMS} = 2 \text{ m/s}$ and a main field of $B_0 = 1 \mu\text{T}$. The $G_{1,0}$ gradient is constrained by the Top-Bottom matching condition to a maximum value of 0.6 pT/cm . This induces a motional EDM of $d_n^{false} = 9.9 \times 10^{-29} e \text{ cm}$. Thus, the geometrical phase effect coming from the motion of the neutron is negligible.

However, the mercury atoms have a much higher speed. In that case, the adiabatic condition is not satisfied : we are in a non-adiabatic regime and the false EDM is approximated by [67]:

$$d_{Hg}^{false} = -\frac{\hbar\gamma_{Hg}^2}{2c^2} \langle xB_x + yB_y \rangle. \quad (2.32)$$

Because the mercury atoms are used to correct the neutron frequency from the magnetic field drifts, the motional mercury EDM is transferred to the neutron through the relation:

$$d_{n \rightarrow Hg}^{false} = \left| \frac{\gamma_n}{\gamma_{Hg}} \right| d_{Hg}^{false}. \quad (2.33)$$

Considering again only a linear gradient $G_{1,0}$, one gets:

$$d_{n \rightarrow Hg}^{false} = \frac{\hbar\gamma_{Hg}\gamma_n}{8c^2} R^2 G_{1,0} \quad (2.34)$$

$$\simeq \frac{1.280 \times 10^{-26} G_{1,0}}{pT/cm} e \text{ cm} \quad (2.35)$$

with the n2EDM chamber radius of $R = 40 \text{ cm}$ and height of $H = 12 \text{ cm}$. With the top-bottom matching condition $G_{1,0} = 0.6 \text{ pT/cm}$, this leads to a false EDM of $d_{n \rightarrow Hg}^{false} = 7.683 \times 10^{-27} e \text{ cm}$, which is a huge systematic effect. This is for this reason that the crossing point technique has been set up [22].

The motional EDM is not only due to the gradient $G_{1,0}$, and can be induced by higher order field gradients. Let's establish the formula for several of them.

The first one is the motional EDM due to an l-odd gradient: let's start with the $G_{1,0}$ gradient. It produces the following transverse field components $B_x = -x/2 \cdot G_{1,0}$ and $B_y = -y/2 \cdot G_{1,0}$. Therefore, we get:

$$\begin{aligned} \langle x.B_x + y.B_y \rangle &= -\frac{G_{1,0}}{2V} \int \int_0^R \int_0^{2\pi} (x^2 + y^2) r dr d\phi dz = -\frac{G_{1,0}}{2V} \int \int_0^R \int_0^{2\pi} r^3 (\cos^2 \phi + \sin^2 \phi) dr d\phi dz \\ \langle x.B_x + y.B_y \rangle &= -\frac{G_{1,0}}{2V} \frac{2\pi R^4}{4} \int dz \end{aligned}$$

Because the vertical position of the two chambers are different, we have to compute this expression for both cases. This gives for the top chamber :

$$\begin{aligned} \langle x.B_x + y.B_y \rangle^T &= -\frac{G_{1,0}}{2V} \frac{2\pi R^4}{4} \int_{H'/2-H/2}^{H'/2+H/2} dz \\ \langle x.B_x + y.B_y \rangle^T &= -\frac{G_{1,0}}{2H\pi R^2} \frac{2\pi R^4}{4} H = -\frac{R^2}{4} G_{1,0} \end{aligned} \quad (2.36)$$

and for the bottom chamber :

$$\begin{aligned} \langle x.B_x + y.B_y \rangle^B &= -\frac{G_{1,0}}{2V} \frac{2\pi R^4}{4} \int_{-H'/2-H/2}^{-H'/2+H/2} dz \\ \langle x.B_x + y.B_y \rangle^B &= -\frac{G_{1,0}}{2H\pi R^2} \frac{2\pi R^4}{4} H = -\frac{R^2}{4} G_{1,0} \end{aligned} \quad (2.37)$$

which led finally to:

$$d_{n \leftarrow Hg}^{false,T}(1, 0) = d_{n \leftarrow Hg}^{false,B}(1, 0) = \frac{\hbar \gamma_n \gamma_{Hg}}{4c^2} \frac{R^2}{4} G_{1,0} = \frac{\hbar \gamma_n \gamma_{Hg}}{32c^2} D^2 G_{1,0}. \quad (2.38)$$

As we can see, for the $G_{1,0}$ gradient (and it is true for all l-odd gradient), the motional EDMs of the top and the bottom chambers are identical. The total motional EDM is then doubled.

Let's now do the calculation with a l-even gradient : the $G_{2,0}$ gradient. Its corresponding transverse field components are $B_x = -xz \cdot G_{2,0}$ and $B_y = -yz \cdot G_{2,0}$. Thus :

$$\begin{aligned} \langle x.B_x + y.B_y \rangle &= -\frac{G_{2,0}}{V} \int \int_0^R \int_0^{2\pi} (x^2 + y^2) r z dr d\phi dz = -\frac{G_{2,0}}{V} \int \int_0^R \int_0^{2\pi} r^3 (\cos^2 \phi + \sin^2 \phi) z dr d\phi dz \\ \langle x.B_x + y.B_y \rangle &= -\frac{G_{2,0}}{V} \frac{2\pi R^4}{4} \int z dz \end{aligned}$$

Considering the top chamber, we have:

$$\begin{aligned} \langle x.B_x + y.B_y \rangle^T &= -\frac{G_{2,0}}{V} \frac{2\pi R^4}{4} \int_{H'/2-H/2}^{H'/2+H/2} z dz \\ &= -\frac{G_{2,0}}{H\pi R^2} \frac{2\pi R^4}{4} \frac{(H'/2+H/2)^2 - (H'/2-H/2)^2}{2} \end{aligned} \quad (2.39)$$

$$\langle x.B_x + y.B_y \rangle^T = -\frac{R^2}{4} H' G_{2,0} \quad (2.40)$$

Now for the bottom chamber, we have :

$$\begin{aligned} \langle x.B_x + y.B_y \rangle^T &= -\frac{G_{2,0}}{V} \frac{2\pi R^4}{4} \int_{-H'/2-H/2}^{-H'/2+H/2} z dz \\ &= -\frac{G_{2,0}}{H\pi R^2} \frac{2\pi R^4}{4} \frac{(-H'/2+H/2)^2 - (-H'/2-H/2)^2}{2} \end{aligned} \quad (2.41)$$

$$\langle x.B_x + y.B_y \rangle^T = +\frac{R^2}{4} H' G_{2,0} \quad (2.42)$$

Finally, we get the motional EDM:

$$d_{n \leftarrow Hg}^{false,T}(2, 0) = -d_{n \leftarrow Hg}^{false,B}(2, 0) = \frac{\hbar \gamma_n \gamma_{Hg}}{4c^2} \frac{R^2}{4} H' G_{2,0} = \frac{\hbar \gamma_n \gamma_{Hg}}{32c^2} D^2 \frac{H'}{2} G_{2,0}. \quad (2.43)$$

This time, the false EDM created by the top chamber is the opposite of the one created by the bottom chamber. Considering both chambers allows to cancel the motional EDM produced by l-even gradients (this is true for the $G_{2,0}$ gradient ans also all l-even gradients).

Finally, we can compute the motional EDM created by a $m \neq 0$ gradients, such as the $G_{1,1}$ gradient. The transverse field components created by this gradient are $B_x = zG_{1,1}$ and $B_y = 0$. Thus we have:

$$\begin{aligned} \langle x.B_x + y.B_y \rangle &= \frac{G_{1,1}}{V} \int \int_0^R \int_0^{2\pi} (xz) r dr d\phi dz = \frac{G_{1,1}}{V} \int \int_0^R \int_0^{2\pi} r^2 (\cos \phi) z dr d\phi dz \\ \langle x.B_x + y.B_y \rangle &= 0 \end{aligned} \quad (2.44)$$

Because of the cylindrical symmetry of the precession chambers, all $m \neq 0$ led to a null contribution to the motional EDM. Therefore, only the gradient with $m = 0$ contributes to this systematic effect. Their expression has been computed up to the 7th order in Table 2.2. The chamber center is at a distance $H'/2$ from the origin of the coordinate system (i.e. the center of the n2EDM experiment).

$Falsed_{n \leftarrow Hg}$	Expression	Numerical values
$d_{n \leftarrow Hg}^{false}(G_{1,0})$	$\frac{\hbar\gamma_n\gamma_{Hg}}{32c^2} \cdot D^2 \cdot G_{1,0}$	$2.00 \times 10^{-30} \cdot 6.4 \times 10^3 \cdot G_{1,0} \text{ e cm}$
$d_{n \leftarrow Hg}^{false}(G_{2,0})$	$\frac{\hbar\gamma_n\gamma_{Hg}}{32c^2} \cdot D^2 \frac{H'}{2} \cdot G_{2,0}$	$2.00 \times 10^{-30} \cdot 5.44 \times 10^4 \cdot G_{2,0} \text{ e cm}$
$d_{n \leftarrow Hg}^{false}(G_{3,0})$	$\frac{\hbar\gamma_n\gamma_{Hg}}{32c^2} \cdot D^2 \left[-\frac{D^2}{8} + \frac{3H'^2 + H^2}{4} \right] \cdot G_{3,0}$	$-2.00 \times 10^{-30} \cdot 3.5 \times 10^6 \cdot G_{3,0} \text{ e cm}$
$d_{n \leftarrow Hg}^{false}(G_{4,0})$	$\frac{\hbar\gamma_n\gamma_{Hg}}{32c^2} \cdot D^2 \frac{H'}{2} \left[-\frac{D^2}{4} + \frac{H'^2 + H^2}{2} \right] \cdot G_{4,0}$	$-2.00 \times 10^{-30} \cdot 7.526 \times 10^7 \cdot G_{4,0} \text{ e cm}$
$d_{n \leftarrow Hg}^{false}(G_{5,0})$	$\frac{\hbar\gamma_n\gamma_{Hg}}{32c^2} \cdot D^2 \frac{5}{8} \left[\frac{D^4}{32} - \frac{D^2}{2} \left(\frac{3H'^2 + H^2}{3} \right) + H'^2 H^2 + \frac{1}{2} \left(\frac{5H'^4 + H^4}{5} \right) \right] \cdot G_{5,0}$	$2.00 \times 10^{-30} \cdot 1.148 \times 10^9 \cdot G_{5,0} \text{ e cm}$
$d_{n \leftarrow Hg}^{false}(G_{6,0})$	$\frac{\hbar\gamma_n\gamma_{Hg}}{32c^2} \cdot D^2 \frac{H'}{2} \left[\frac{15D^4}{256} - \frac{5D^2}{16} (H'^2 + H^2) + \frac{1}{16} (3H'^2 + H^2)(H'^2 + 3H^2) \right] \cdot G_{6,0}$	$-2.00 \times 10^{-30} \cdot 8.593 \times 10^{10} \cdot G_{6,0} \text{ e cm}$
$d_{n \leftarrow Hg}^{false}(G_{7,0})$	$\begin{aligned} & \frac{\hbar\gamma_n\gamma_{Hg}}{32c^2} \cdot D^2 \frac{7}{64} \left[\frac{D^6}{32} - \frac{5D^4}{16} (3H'^2 + H^2) \right. \\ & \left. + \frac{D^2}{2} (5H'^4 + 10H'^2 H^2 + H^4) - (7H'^6 + 35H'^4 H^2 + 21H'^2 H^4 + H^6) \right] \cdot G_{7,0} \end{aligned}$	$2.00 \times 10^{-30} \cdot 1.913 \times 10^{12} \cdot G_{7,0} \text{ e cm}$

Table 2.2 – Mercury motional EDM transferred to the neutron calculated for single gradients up to the seventh order. The last column gives a numerical value in e.cm with $D = 80$ cm, $H = 12$ cm and $H' = 17$ cm and with a gradient expressed in pT/cm^l . The expressions given for $G_{2,0}$, $G_{4,0}$ and $G_{6,0}$ gradients are computed by taking into account only one chamber (since it cancels in two chambers). Two chambers are considered in the calculations for the other gradients.

In the n2EDM experiment, the two precession chambers are symmetric with respect to the horizontal plan at $z=0$. It implies that the motional EDM created by l-even gradients cancels $d_n(\text{top}) + d_n(\text{bottom}) = 0$, whereas the motional EDM created by the l-odd gradients is doubled $d_n(\text{top}) + d_n(\text{bottom}) = 2d_n(\text{top})$.

The motional EDM is then (up to the 5th order):

$$d_{n \leftarrow Hg}^{\text{false}} = \frac{\hbar \gamma_n \gamma_{Hg}}{32c^2} D^2 \left(G_{1,0} - \left[\frac{D^2}{8} - \frac{3H'^2 + H^2}{4} \right] G_{3,0} + \frac{5}{8} \left[\frac{D^4}{32} - \frac{D^2}{2} \left(\frac{3H'^2 + H^2}{3} \right) + H'^2 H^2 + \frac{5H'^4 + H^4}{10} \right] G_{5,0} \right) \quad (2.45)$$

The procedure used to suppress this effect is to extrapolate the gradients to zero. It was indeed applied in the nEDM experiment through the crossing-point technique analysis [61]. In n2EDM, the Hg magnetometers present in the two chambers will allow to measure the Top/Bottom gradient:

$$G_{TB} = \frac{\langle B_z \rangle^T - \langle B_z \rangle^B}{H'} \quad (2.46)$$

Then it will be possible to extrapolate G_{TB} to $G_{TB} = 0$. G_{TB} can be computed as a function of the gradients of the harmonic basis. We then have up to the 5th order :

$$\begin{aligned} G_{TB} &= G_{1,0} \\ &+ \frac{1}{16} (4H'^2 + 4H^2 - 3D^2) G_{3,0} \\ &+ \frac{5}{8} \left(\frac{D^4}{16} - \frac{D^2}{4} (H'^2 + H^2) + \frac{H'^2 H^2}{3} + \frac{H'^4 + H^4}{10} \right) G_{5,0}. \end{aligned} \quad (2.47)$$

Introducing G_{TB} in Eq. 2.45, one gets:

$$\begin{aligned} d_{n \leftarrow Hg}^{\text{false}} &= \frac{\hbar \gamma_n \gamma_{Hg}}{32c^2} D^2 \left(G_{TB} \right. \\ &\quad \left. + \left[\frac{D^2}{16} - \frac{H'^2}{2} \right] G_{3,0} \right. \\ &\quad \left. + \frac{5}{8} \left[-\frac{D^4}{32} - \frac{D^2}{12} (3H'^2 - H^2) + \frac{2H'^2 H^2}{3} + \frac{2}{5} H'^4 \right] G_{5,0} \right) \end{aligned} \quad (2.48)$$

Measuring and extrapolating G_{TB} to zero suppress then the contribution arising from the linear gradient $G_{1,0}$. However, the presence of higher order gradient such as $G_{3,0}$ or $G_{5,0}$ still induces a false EDM, which cannot be fully corrected by G_{TB} . Therefore it is plan to measure those gradients either online using the Cesium magnetometers array, or offline with a dedicated mapping campaign.

2.2.4 Local Magnetic dipole

An other source of false EDM can arises from the presence of local magnetic dipoles close to the precession chambers. They corresponds to small magnetised pieces, characterized by a magnetic moment \vec{m} . The dipole creates a local magnetic field which induced a motional EDM. The EDM strength depends on the intensity and the orientation of the dipole's magnetic moment, as well as the position of the dipole itself.

The issues related to the presence of magnetic dipoles are developed in detail in the chapter 5.

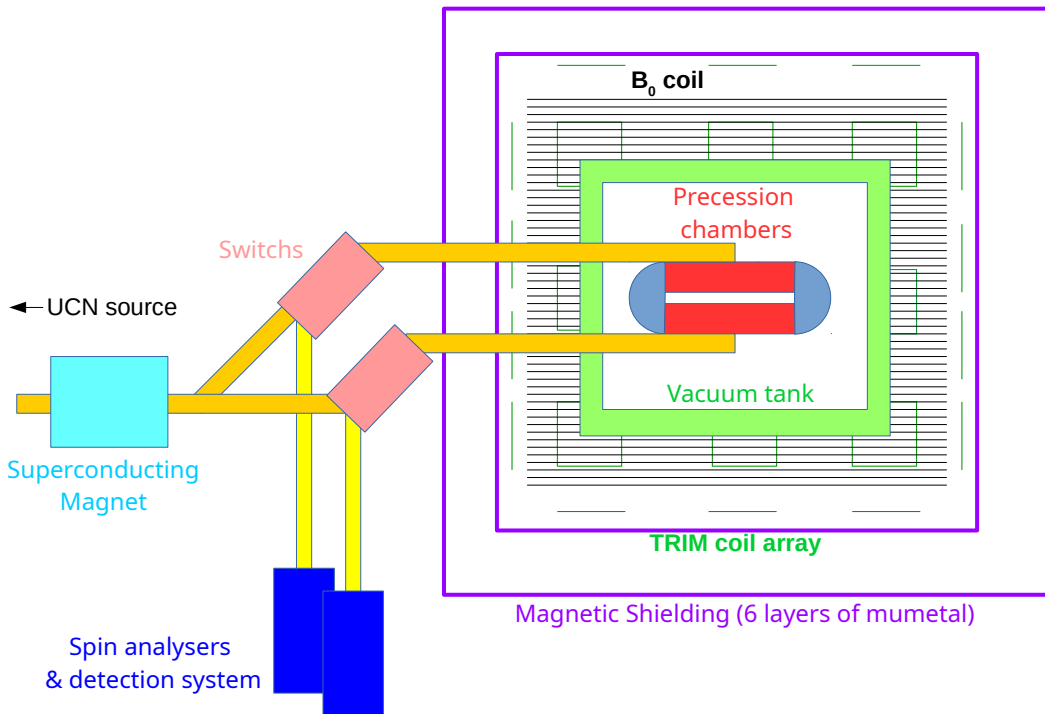


Figure 2.4 – A scheme of the n2EDM apparatus. The magnetometers, the high voltage as well as the SFC correcting coils are not shown here.

2.2.5 Gravitational shift and uncompensated field drift

Due to the gravity, the center of mass of the UCN gas does not coincide with the center of the precession chamber. It is actually a few mm lower. On the contrary, the mercury atoms, which are at the room temperature, fill uniformly the precession chamber. In the presence of a vertical magnetic gradient, both species won't see in average the same magnetic field. The difference is given by $h \times \frac{\partial B_z}{\partial z}$ where h is the difference between both center of mass. This is the gravitational shift. This effect cannot be compensated by the mercury atoms : it is called the uncompensated field drift.

2.3 The n2EDM experiment

In this section, the n2EDM experiment is described [70]. Fig. 2.4 shows the basic scheme of the n2EDM apparatus. It will be operating as follow:

1. The UCNs come from the PSI UCN source (from the left part of the scheme).
2. They are polarized by a Superconducting magnet producing a strong magnetic field of 5T, and then guided to the precession chambers crossing the switch boxes. Their polarisation will be held thanks to guiding coils wounded around the UCN guides.
3. There they are stored during a time T. The Ramsey oscillation field method is applied.
4. Finally, the precession chambers are emptied and the number of spin up\down neutron are counted in the detection system.

Let's now have a closer look to the main components of the experiment.

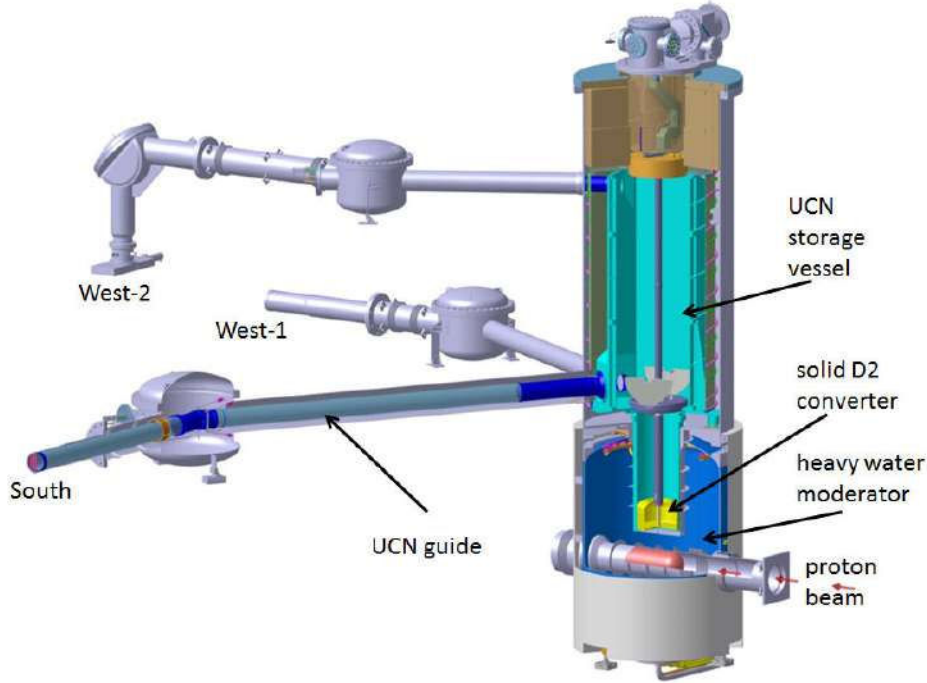


Figure 2.5 – Schematic view of the PSI UCN source.

2.3.1 The PSI UCN source

The PSI UCN source is described in Fig. 2.5. Fast neutrons are produced by the spallation process : a 590 MeV pulsed proton beam with an intensity of 2.2 mA hits a lead target [54]. About 7-8 neutrons are produced per proton, which leads to a rate of 10^{17} neutrons/s. The neutrons are then thermalized in an heavy water D₂O tank, and then cooled in a 5K solid deuterium crystal D₂ (30 dm³). There they become cold and ultra-cold. A large vessel is used to store the UCN. Then they are delivered to three possible beamports (West 1, West 2 and South). The measured UCN density of the PSI source is 22.31(71) UCN/cm³ after 2 s of storage [71] and 9.27(5) UCN/cm³ after a storage time of 50 s [72].

2.3.2 UCN transport: guides, switch and holding coils

The Ultra Cold Neutrons coming from the source are first polarized by a 5T superconducting magnet, with a polarization probability of $P > 99\%$. They are guided by glass tubes with an inner diameter of 130 mm, coated with NiMo ($V_F = 220$ neV). The height between the UCN source exit and the precession chambers has been optimised in order to efficiently fill the precession chambers. The optimisation is based on UCN transports calculations performed with the MCUCN simulation code [73] benchmarked by experimental tests [71]. A height difference of 80 cm has been found to be the optimal value.

Then the neutrons cross the switch boxes. These pieces are used to guide the neutrons to the precession chamber or to the neutron detectors. The latter one is performed during the precession time for the beam monitoring or at the end of the precession time.

The spin transport is performed with holding coils surrounding the guides. They ensure an adiabatic transport characterized by the adiabaticity parameter k:

$$k = \frac{\omega_L}{\Omega} = \frac{\gamma_n B^2}{|dB/dt|} > 10 \quad (2.49)$$

This parameter compares the spin precession frequency (ω_L) to the temporal variation of the magnetic field (Ω). If the magnetic field changes are slow compare to the spin precession, then the spin is able to follow the field variations and the spin polarization is held. An adiabaticity parameter larger than 10 is sufficient.

2.3.3 The Precession chambers

One of the major improvements is the use of two large precession chambers instead of a small one. They both have a diameter of $D = 80\text{ cm}$ and a height of $H = 12\text{ cm}$. Their centers are separated by a distance $H' = 17\text{ cm}$. The electrodes constitute the bottom and roof of the chambers. They are made of aluminum and coated with DLC (with a Fermi potential of $V_F = 230\text{ neV}$). The central electrode will be operated at High Voltage while the two external ones are at ground. The electric field is expected to reach 15 kV/cm. The insulator rings constitute the vertical walls. They are made of polystyrene (PS) and coated with a deuterated polystyrene (dPS), providing a Fermi potential of $V_F = 160\text{ neV}$.

2.3.4 Magnetic field production

The nEDM measurement technique requires two type of magnetic field in the precession chambers : a static vertical magnetic field B_0 and an horizontal RF field. They are mainly produced by two coils :

- **The B_0 coil** produces the static vertical magnetic field of $1\text{ }\mu\text{T}$. The B_0 field must be highly uniform. More details about field requirements are given in section 2.2. The B_0 coil design is described in the chapter 3.
- **The RF coils** produces a radiofrequency field. They are used to produce the RF pulses required by the Ramsey separated oscillating fields method (see 1.5.3).

An additional set of coils are also used to improve the field uniformity (the TRIM coils array) and to produce some specific gradients required for the experiment (the Harmonic coils). They are fully described in chapter 4.

2.3.5 Control of the magnetic field

The control and the monitoring of the magnetic field are the key parts of the experiment. For this purpose, the apparatus includes two type of magnetometers (a Mercury comagnetometer and a Cesium magnetometers array), a large magnetically shield room (MSR) and a set of active field compensating coils.

The monitoring of the field is performed with two magnetometers:

- **The Mercury comagnetometers (HgM)** allows to correct for the temporal variations of the magnetic field. A polarised Hg gas is injected in the precession chambers at the beginning of the measurement cycle. Then a RF magnetic field perpendicular to the main field is applied in order to flip the spin of the Hg atoms in the plan transverse to the B_0 field. There they start to precess at their Larmor frequency. The Larmor frequency measurement is performed with a laser crossing the precession chamber. If the photon spin is anti-parallel to the Hg atoms spin, then it is absorbed. The laser's light which is not absorbed by the Hg is detected by a pin diode placed outside the vacuum tank. Then the Larmor frequency of the Hg atoms is derived. Knowing the gyromagnetic ratio of the Hg atoms, the magnetic field can be determined. This measurement is performed every cycle: it gives the mean magnetic field seen by the neutron during the precession time.

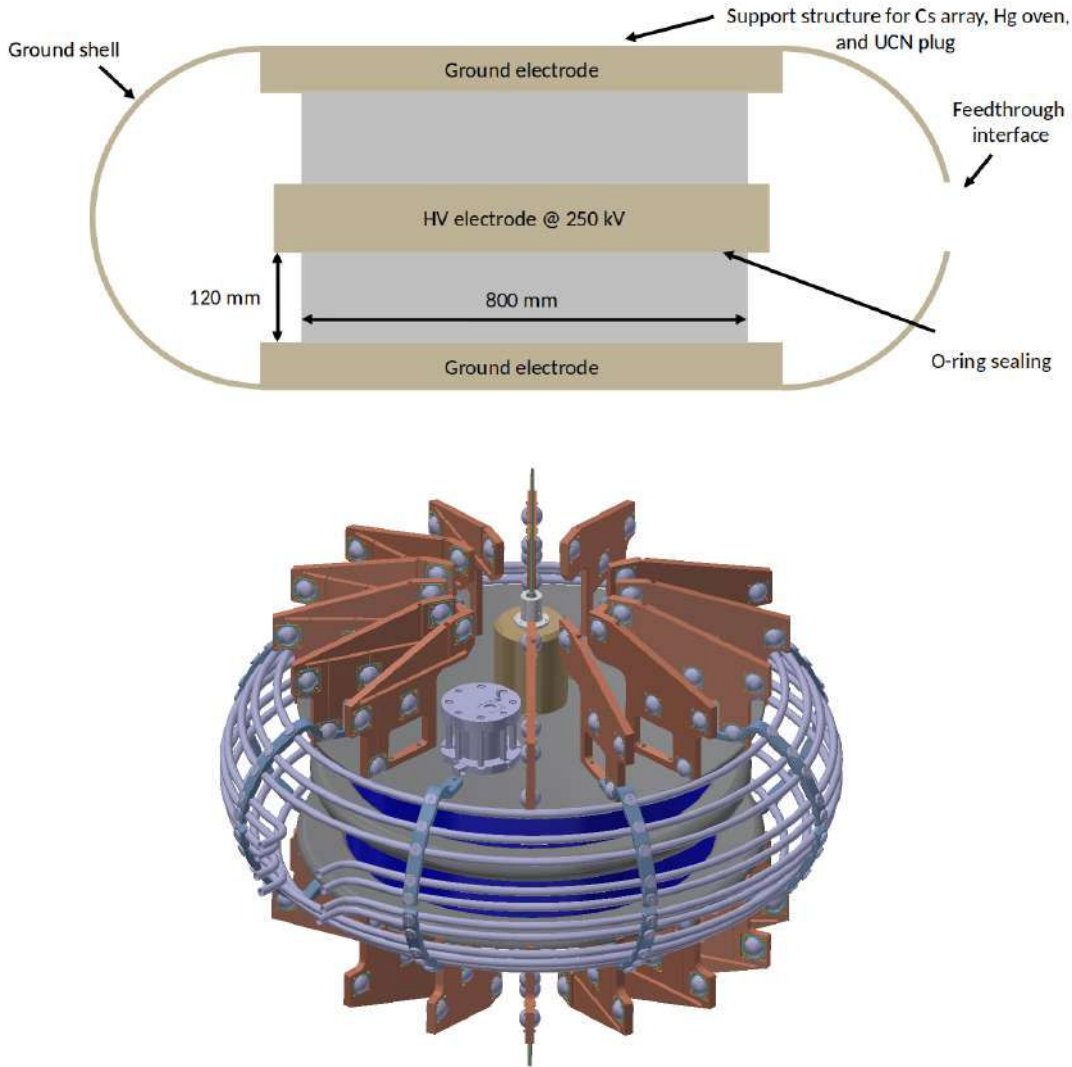


Figure 2.6 – The first figure shows a scheme of the double precession chamber. It consists of a central HV electrode, surrounded by two ground electrodes. A ground shell is added to re-enforce the uniformity and the confinement of the electric field. The second figure display a design of the precession chambers. Are also shown the UCN plug at the center of the ground cell, the Hg oven, as well as the Cs Magnetometer array.

The correction of the field drift is therefore performed on the cycle basis. This is showed in 2.7a : the blue squares shows the neutron frequency before the correction, subject to the magnetic drift, which is corrected on the neutron frequency corrected by the HgM represented by the red dots. The requirements on the Hg comagnetometer precision is 30 fT per cycle per chamber. Its accuracy requirement is 100 fT per chamber. A more complete description of the HgM operation is presented in [74].

- **The Cesium magnetometers array** measures the spatial distribution of the field modulus. It will be composed of a hundred magnetometers dispatched above and below the precession chambers as shown in Fig. 2.7b. Each of them is filled with a ^{133}Cs vapor polarised by a laser light. The magnetic field is measured with the precession of the Cs atoms through the recording of their Larmor frequency. It is thus possible to know the magnetic field modulus for each of the CsM composing the array. This array will allow

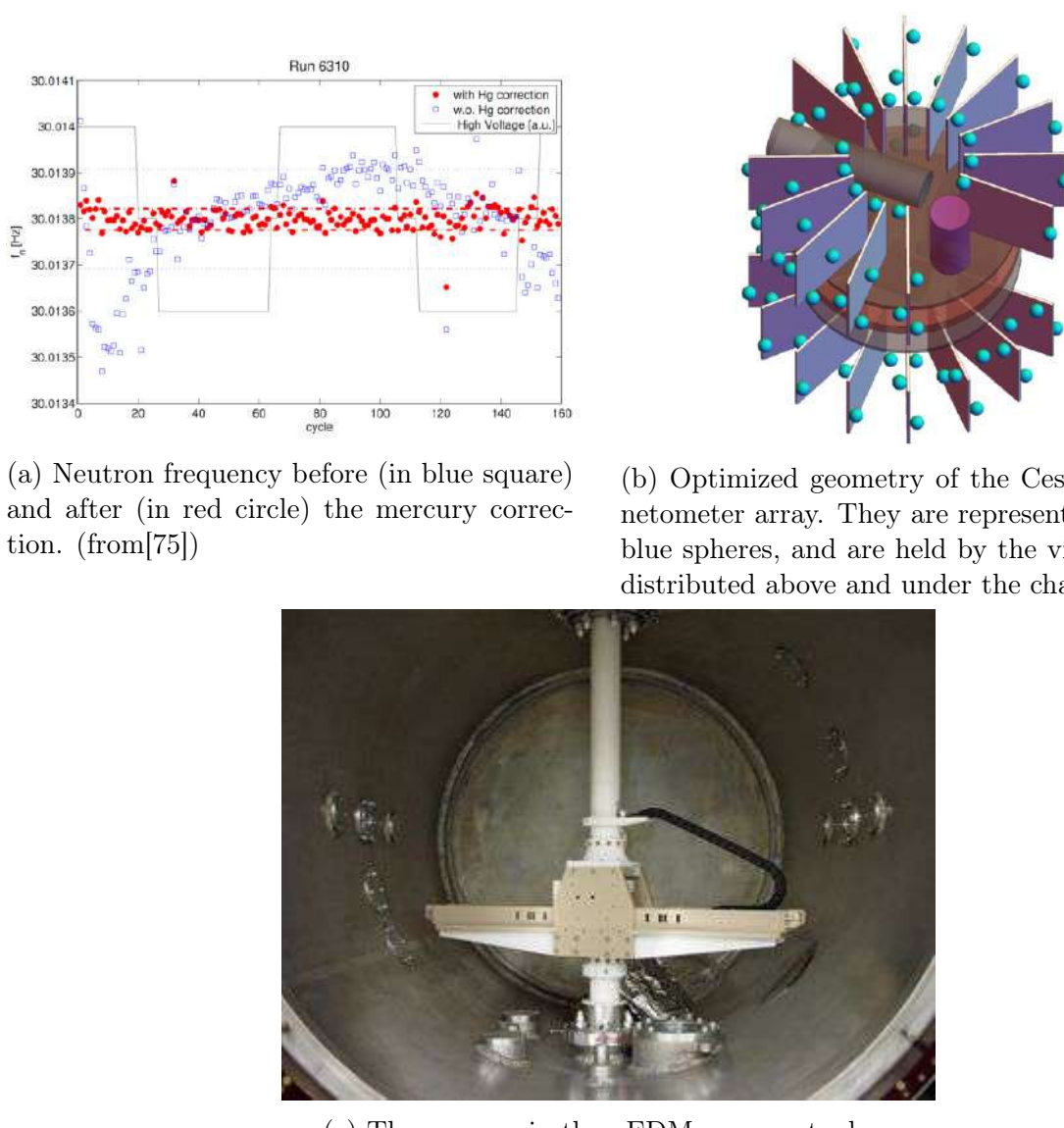


Figure 2.7 – Devices monitoring the magnetic field online ((a) and (b)) or offline (c).

to measure the most important gradient of the magnetic field (see section 2.2.3). The Cs magnetometers array must have an accuracy on the G_{3,0} gradient measurement of 4×10^{-5} pT/cm³ [63].

The nEDM experiment has also a mapper. It is a device made of a three-axis fluxgate mounted on a mobile and non-magnetic support which allows to map the magnetic field offline. It is used for the coils commissioning, the measurement of field non-uniformities, and the cartography of the TRIM coil array. The nEDM mapper is shown on 2.7c.

In addition to the field monitoring, several devices are used to correct for static or varying external fields. They are:

- **The magnetically shielded room (MSR)**, which is a large cube. It is made of two "rooms", inner and outer. the inner room is composed of four layers of mu-metal, and the outer room is made of two layers of mu-metal and two layers of aluminum (in order to shield high frequency field). The outermost layer dimensions are 5.2 m × 5.2 m × 4.8 m while the innermost layer dimensions are 2.93 m × 2.93 m × 2.93 m. The overall shielding

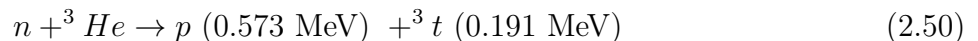
factor is expected to be 70000 at 0.01 Hz and 1000000 at 70 Hz in the three direction of space (to compare, the nEDM shielding factor was at most 10000 in the transverse direction).

- **The Surrounding Field Compensation (SFC)** are a set of large coils installed around the MSR. Their role is to dynamically suppress the external magnetic field, such as the field variations produced by the ramp up/down of the superconducting magnet SULTAN (located at about 20m from the experiment). They are coupled to an array of fluxgates which measure the field variation that they have to correct.

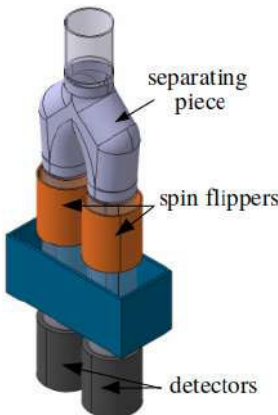
2.3.6 The detection system: USSA and detectors

Once UCN leave the precession chamber, they are guided through the switch box towards the detection system. They first enter in the U-shape Simultaneous Spin Analyser (USSA) where the separating piece guide them in one of its two arms. Each arm is able to analyse one spin component. They are made of an adiabatic spin-flipper, an analysing foil and a neutron detector. The adiabatic spin-flipper is able to flip the neutron spin component. The analysing foil are only crossed by the spin down component. The arm with a spin-flipper OFF is able to count the spin down neutrons while the arm with the spin-flipper ON is able to count the spin up neutrons. The USSA geometry is optimised so that a neutron which enter an arm with the wrong state bounces on the analysing foil and is redirected to the other arm, where its spin component can be analysed.

The n2EDM detectors are gaseous. The gas is a mixture of ${}^3\text{He}$ and CF_4 . Typical pressures are 15 mbar for the ${}^3\text{He}$ and 1000 mbar for the CF_4 . The detection is based on the capture of the neutron by the Helium:



The capture cross-section is $\sigma_{abs} \simeq 2.3 \times 10^7$ barns in the UCN velocity range. The CF_4 gas converts this energy into photons in the UV range (scintillation process). The light is then detected by three Photomultiplier Tubes (PMT). The output signals are sent to the FASTER acquisition system.



(a) Preliminary design of the n2EDM Simultaneous Spin Analyser. Each arm have a spin flipper (orange cylinder) and a analysing foil magnetized by a magnet, represented by the blue box.



(b) Gaseous Detector for the n2EDM experiment. The entrance is at the top, leading to the gaseous chamber filled with CF_4 and ${}^3\text{He}$. The three black tubes contains the PMTs.

Figure 2.8 – The n2EDM detection system.

Conclusion

Using the magnetic interaction, one can manipulate the neutron spin in order to make it freely precess. During this precession, the presence of a nEDM shifts the Larmor frequency, depending of the relative direction of the magnetic and electric fields. Measuring the frequency in both configurations, one allows to measure the electric dipole moment. It requires a high control of the magnetic field and a complex apparatus. The measurement is mostly affected by the neutron depolarisation and a systematic effect called the motional EDM. In order to limit these two effects, the magnetic field production have to fulfill some requirements: the field produced by the B_0 coil must be very uniform ($\sigma(B_z) < 170$ pT). Moreover its linear vertical gradient must stays below $G_{1,0} < 0.6$ pT/cm. The following chapter presents the design and the performances of the B_0 coil.

The B_0 coil

Contents

3.1 COMSOL simulations	60
3.1.1 Influence of the meshing	60
3.1.2 Simplifying the simulation by the use of symmetries	61
3.2 B_0 coil design	62
3.2.1 Circular single loop and infinite solenoid	62
3.2.2 Squared single loop and infinite solenoid	65
3.2.3 Finite solenoid in a magnetic shield	68
3.2.4 B_0 coil design	69
3.3 Characteristics of the simulated B_0 field	69
3.3.1 B_0 field uniformity	71
3.3.2 Gradient decomposition	71
3.3.3 Influence of the MSR	72
3.4 Study of some mechanical imperfections	73
3.4.1 Global misalignment of the B_0 coil with respect to the shield	73
3.4.2 Influence of the shield innermost dimensions	75
3.4.3 Other imperfections	75
3.4.4 Conclusion about the mechanical imperfections	76
3.5 B_0 technical design	76

Introduction

The B_0 coil has to produce a magnetic field of $1 \mu\text{T}$ with a high uniformity in the precession chambers volume. Because of its proximity to the MSR innermost layer, the field is indeed produced by the coupling between the coil and this layer. The B_0 field uniformity requirements, are presented in Section 2.2 and summarized in the Table 3.1. This chapter will start with a short presentation of the COMSOL software used for the simulations. Then, the design of the B_0 coil is discussed as well as its performances. The study of mechanical imperfections and their influence on the field performances are then shown. Finally, the technical design of the coil is presented.

The stability requirements of the B_0 field and its gradients rely on the current source stability. They do not depend on the coil design. This is why they are not considered in this thesis.

Origin of the requirement	Field requirement
Mean field in the precession chamber	$\langle B_0 \rangle = 1 \mu\text{T}$
Top-Bottom resonance matching condition	$G_{1,0} < 0.6 \text{ pT/cm}$
Field uniformity	$\sigma(B_z) < 170 \text{ pT}$

Table 3.1 – B_0 field requirements.

3.1 COMSOL simulations

Before looking at the design of the B_0 coil, we introduce the COMSOL software used to perform the simulations. It is based on the Finite Element Method (FEM). This method decomposes the geometry of the system in many small elements. Each element is a mesh and the overall constitutes the meshing. The mesh shape can be for instance a tetrahedron, a parallelepiped, a triangle, a quadrangle, etc. The mesh summit are called nodes. The magnetic field calculation is performed at every nodes. Then its value is interpolated between them. Different interpolation functions can be used (linear, quadratic, etc.). A further description of the COMSOL software and the FEM method is given in Appendix B. In this section, we will focus on the influence of the meshing. For this purpose, a single loop of current is simulated and its field is compared to the analytical solution. The computation loads will be also investigated.

3.1.1 Influence of the meshing

A single coil of radius $R = 0.25 \text{ m}$ with a current $I = 0.25/(2\pi) \text{ A}$ is simulated. It creates a field $B(\vec{0}) = 1 \times 10^{-7} \text{ T}$ at its center. It is surrounded by a first cylinder of radius $R = 1 \text{ m}$ and height $H = 2 \text{ m}$ where the meshing will be showed. A larger cylinder with a radius $R = 2 \text{ m}$ and a height of $H = 4 \text{ m}$ is used to defined the boundary conditions. Those are $\vec{n} \times \vec{A} = \vec{0}$ on the cylinder surface (n being the normal vector, orthogonal to the cylinder surface, and A being the magnetic vector potential), which corresponds to a field $B = 0$, i.e. far away from the coil the field is null. The whole volume is made of air. The geometry is represented in Fig. 3.1.

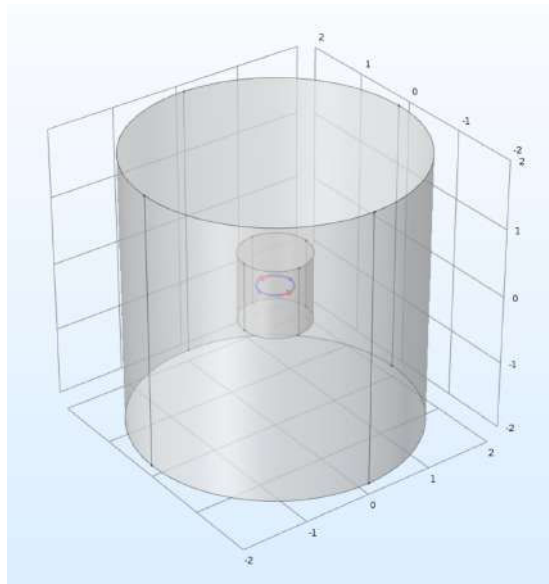


Figure 3.1 – A single circular coil simulated in the COMSOL software

The goal is to compare the field created by COMSOL using several meshing shown and the analytically calculated field. The meshing used to perform these simulations are shown in Fig. 3.2. The influence of the linear or quadratic functions for the interpolation between the

Mesh size	Coarse		Finer		Extremely Fine	
Functions	Linear	Quadratic	Linear	Quadratic	Linear	Quadratic
Nb of elements	3038		81179		1710809	
Elmts min size (m)	0.26		0.16		0.05	
Elmts max size (m)	0.47		0.22		0.10	
Computation time (s)	2	3	5	18	70	381
Field $B_{sim}(\vec{0})$ (nT)	113.57	105.54	97.55	116.9	100.82	99.87
Error (%)	13.6	5.54	2.45	1.69	0.82	0.43

Table 3.2 – Comparison of the results obtained with linear or quadratic functions and several meshing to the analytical solution ($B_{th}(\vec{0}) = 100 \text{ nT}$).

nodes is also investigated. The results are summarize in the Table 3.2. The error in this table is given by $\frac{B_{sim}-B_{th}}{B_{th}}$, with B_{sim} being the field at the center of the coil given by the simulation, and B_{th} the theoretical value of the field at the center of the coil.

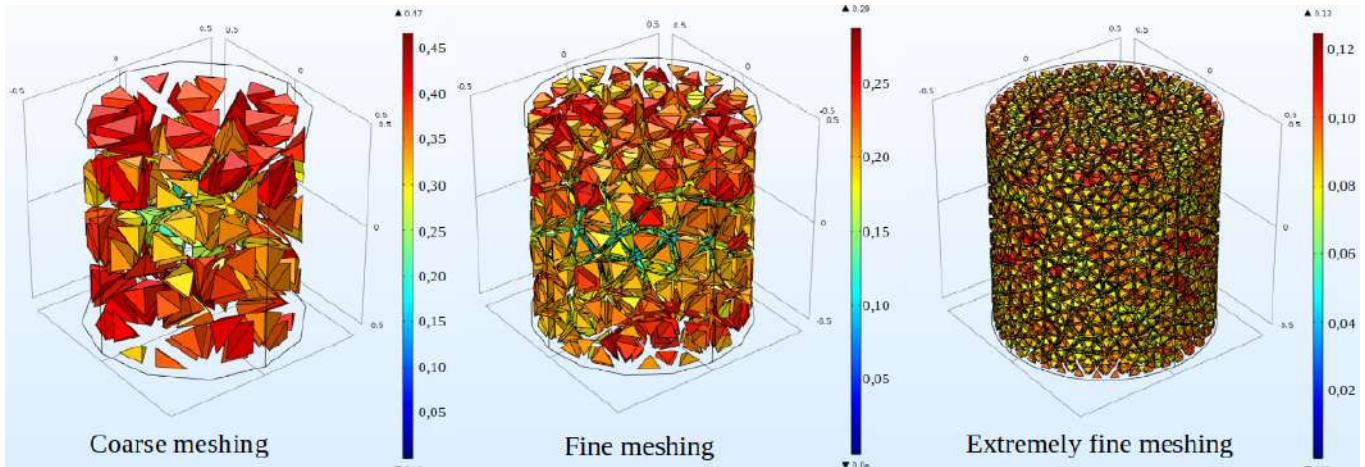


Figure 3.2 – View of the three meshing used in the COMSOL simulations. The first one is a coarse mesh, the second a fine mesh and the last one an extremely fine mesh. This can be seen by comparing the mesh size shown in their respective legend scale at the right of each figure.

As expected, the better results are obtained with the finest meshing, and the quadratic functions. The only drawback is a larger load for the computation time.

3.1.2 Simplifying the simulation by the use of symmetries

The computation loads increases considerably with the refinement of the meshing. In this section, we show how to use the system symmetries in order to simplify the simulation and therefore reduce the computation loads.

As stated by Pierre Curie [76]:

*"Lorsque certaines causes produisent certains effets, les éléments de symétrie des causes doivent se retrouver dans les effets produits"*¹

For the electromagnetism, this indicates that the current symmetries implies symmetries for the produced magnetic fields. We can distinguish two cases :

- In the first case, there is a plane of symmetry for the currents. This plane is a plane of antisymmetry for the magnetic field (because it is a pseudo-vector). The vector \vec{H} must

1. "the symmetries of the causes have to be found in the effects"

be orthogonal to it. This property can be used as a boundary condition on this plan where $\vec{n} \times \vec{H} = 0$ with \vec{n} the normal vector to the plan. In COMSOL, this is defined as a "Perfect Magnetic Conductor Boundary Condition". It is important to notice that if a current wire is included in the plane, its intensity must be halved due to the boundary condition (i.e. the symmetric current will be added during the solving).

- In the second case, the plan is a plan of antisymmetry for the currents. This corresponds to a plan of symmetry for the magnetic field. This time, \vec{B} belongs to the plan (the boundary condition is defined as $\vec{n} \times \vec{A} = 0$. Since $\vec{B} = \vec{\nabla} \times \vec{A}$, it corresponds well to a case where \vec{B} is parallel to \vec{n}). In COMSOL, this corresponds to the "Magnetic Insulation Boundary Condition".

For the single coil example, each vertical plan dividing the cylinders in two halves is an antisymmetric plan for the currents, and the horizontal plan is a symmetric plan (in some way, the plan divides the coil in two halves).

It is therefore possible to simulate a slice of our geometry by imposing Magnetic Insulation Boundary Conditions to vertical plans, and a Perfect Magnetic Conductor Boundary Conditions to the horizontal plan. Several geometries using the symmetries are compared to the whole geometry. Their meshing are shown in Fig. 3.3, and their performances are shown in Table 3.3. The symmetries helps to reduce the number of mesh, while at the same time improving the precision of the final result.

Geometry fraction	1	1/2	1/4	1/8	1/16	1/144
Corresponds to	Fig. 3.3a	Fig. 3.3b	Fig. 3.3c	Fig. 3.3d	Fig. 3.3e	Fig. 3.3f
Number of elements	1710809	849274	420690	206754	103297	28734
Elements min size (m)	0.05	0.03	0.04	0.05	0.05	0.002
Elements max size (m)	0.10	0.11	0.12	0.11	0.11	0.09
Computation time (s)	381	201	103	68	26	18
$B(0)$ (nT)	99.57	99.85	100.42	100.18	99.75	99.84
Error (%)	0.43	0.15	0.42	0.18	0.25	0.16
Magnetic Insulator boundaries		✓	✓	✓	✓	✓
Perfect Magnetic Conductor boundaries					✓	✓

Table 3.3 – Comparison between several COMSOL simulations using different symmetries.

As a conclusion, the Finite Element Method requires to make a compromise between the refinement of the solution, brought by a finer meshing, and the computation loads. These constrains can be relaxed by using the system symmetries, and by adapting the meshing, which can be smaller in the most sensitive regions (i.e. close to complex geometries where the solution is expected to have a bigger variation).

3.2 B_0 coil design

The main goal of the B_0 coil design is to have the best uniformity that we can achieve. This is why in this section, we will show with simple model how to produce a coil with a perfect uniformity, which is the starting point of the B_0 design.

3.2.1 Circular single loop and infinite solenoid

The easiest way to produce an homogeneous magnetic field is to use an infinite solenoid. Let's first consider one circular loop \mathcal{C} around the axis $(0z)$, of radius R and traversed by a current I . P is a point of this loop and O its center. Be M a point on the axis $(0z)$. The angle

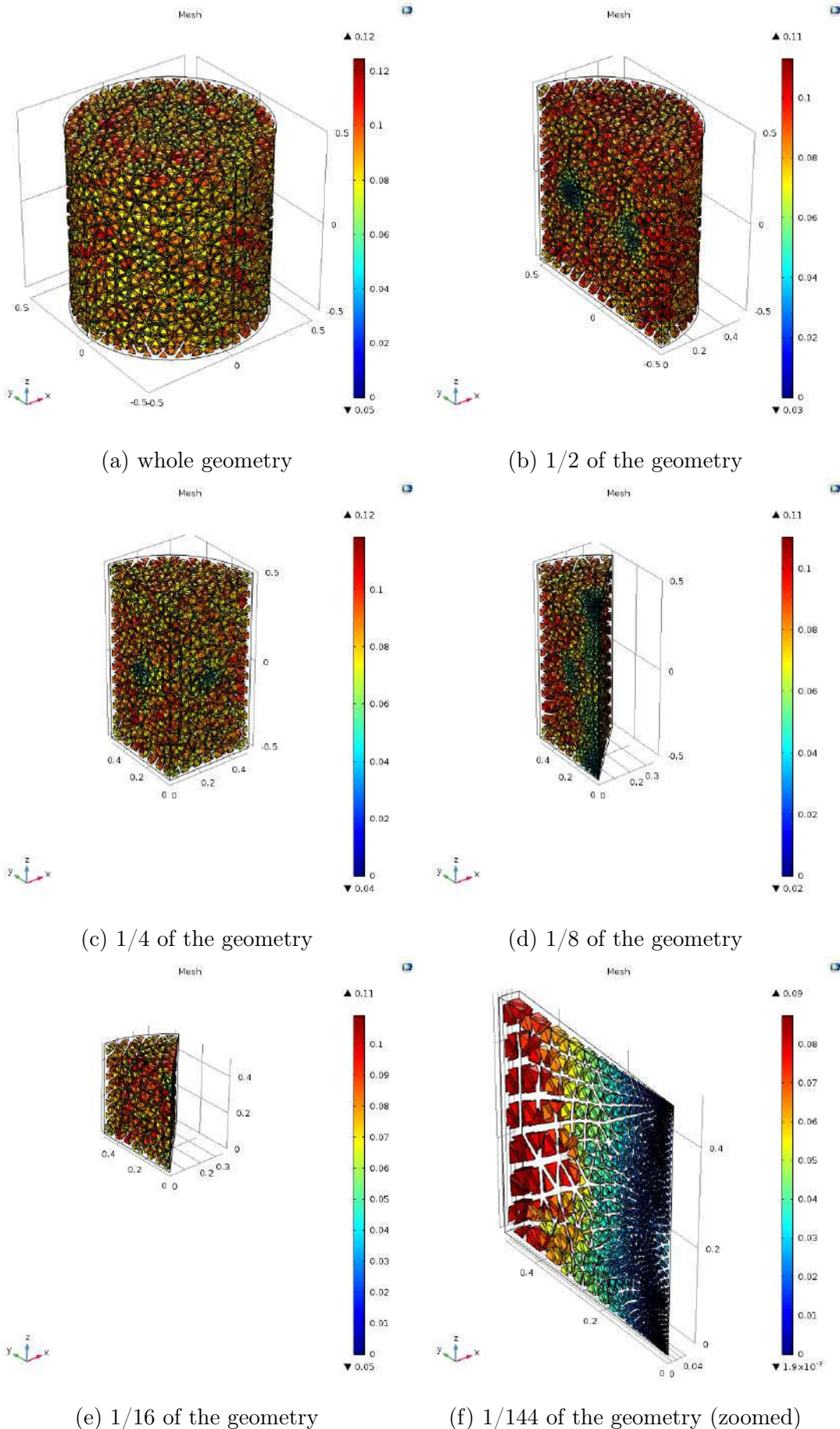


Figure 3.3 – The meshing of several geometries are shown. In (a) the full geometry is simulated. Using the system symmetries, (b),(c),(d),(e) and (f) represents the meshing of respectively 1/2, 1/4; 1/8, 1/16 and 1/144 of the full geometry.

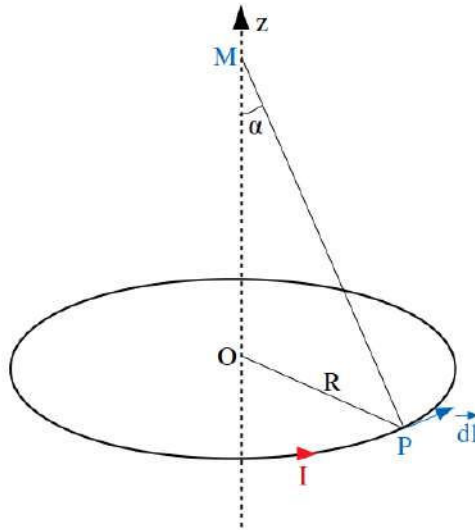


Figure 3.4 – Scheme of the single loop.

between the segment $[PM]$ and the axis is called α . The scheme Fig. 3.4 shows the geometry of this example.

The field at M created by a loop element dl is given by the Biot and Savart law :

$$\vec{B}(M) = \oint_C \frac{\mu_0}{4\pi} \frac{I d\vec{l} \times \vec{PM}}{\|PM\|^3}. \quad (3.1)$$

Every plan passing by the $(0z)$ axis is an antisymmetric plan for the current I . Therefore the vector \vec{B} belongs to all those plan, meaning that it is along the $(0z)$ axis. Then one can write :

$$\begin{aligned} \vec{B}(M) &= \oint_C \frac{\mu_0}{4\pi} \frac{(Idl \times \vec{PM}) \cdot \vec{u}_z}{\|PM\|^3} \vec{u}_z = \oint_C \frac{\mu_0 I}{4\pi} \frac{R dl}{(R/\sin \alpha)^3} \vec{u}_z \\ &= \oint_0^{2\pi} \frac{\mu_0 I}{4\pi} \frac{R^2}{(R/\sin \alpha)^3} d\theta \vec{u}_z = \frac{\mu_0 I}{2R} \sin^3 \alpha \vec{u}_z. \end{aligned} \quad (3.2)$$

Let us now consider that along the vertical segment dz are $N \cdot dz$ loops where N is the linear loop density along $(0z)$, as shown in Fig. 3.5.

They create a field $d\vec{B}(M)$ at the point M . It reads:

$$d\vec{B}(M) = \frac{\mu_0 N I dz}{2R} \sin^3 \alpha \vec{u}_z. \quad (3.3)$$

The height z is linked to the angle α by $z = -R/\tan \alpha$, meaning that :

$$dz = \frac{R}{\sin^2 \alpha} d\alpha. \quad (3.4)$$

We then compute the field created by the entire solenoid at the point M :

$$\vec{B}(M) = \int_{\alpha=0}^{\alpha=\pi} \frac{\mu_0 N I}{2} \sin \alpha d\alpha \vec{u}_z = \mu_0 N I \vec{u}_z. \quad (3.5)$$

Then we can use the Ampere's law to show that the field is uniform inside this solenoid. It says that:

$$\oint_C \vec{B} \cdot d\vec{l} = \mu_0 \sum I_{\text{enclosed}} \quad (3.6)$$

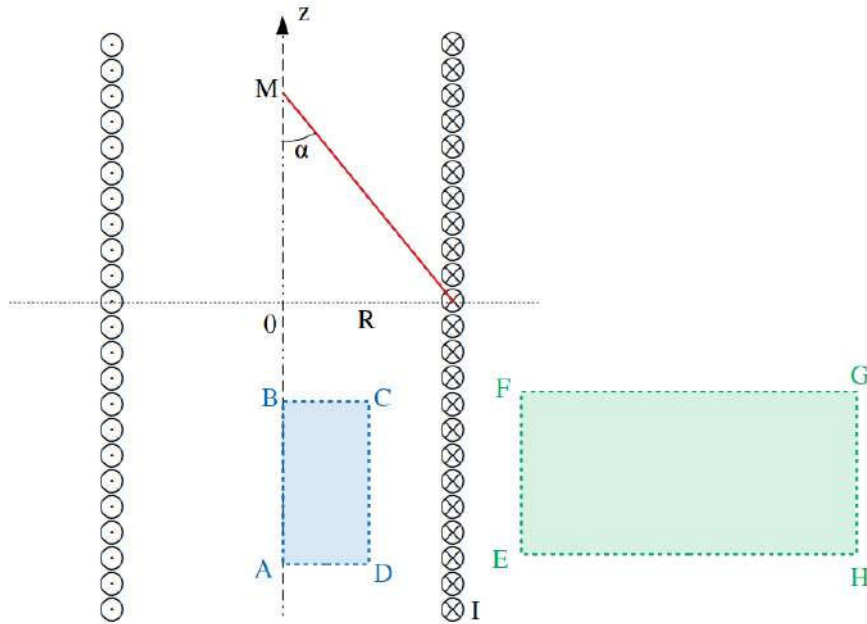


Figure 3.5 – Scheme of an infinite solenoid. The contours ABCD and EFGH, used to show the uniformity of the field are also shown.

If that contour is completely outside the solenoid, i.e. the contour $EFGH$, it encloses no current. Therefore $\oint_C \vec{B} \cdot d\vec{l} = 0$, so the field is uniform outside the solenoid. Intended that infinity far from it, the field is 0, we can conclude that the field outside the infinite solenoid is $B_{\text{outside}} = 0$. Choosing a contour completely inside the solenoid, like $ABCD$, leads to the same conclusion concerning the uniformity. However, we already showed that the field on the axis is $B = \mu_0 NI$. Thus, the field inside the infinite solenoid is also $B = \mu_0 NI$.

3.2.2 Squared single loop and infinite solenoid

Let's consider a square loop $ABCD$ of side a , in which flows a current I (see Fig. 3.6a). The center of the loop O corresponds to the frame origin with the coordinate system $(\vec{u}_x, \vec{u}_y, \vec{u}_z)$. H is the center of the $[AB]$ segment, and P a point on this segment. Let's choose a point M at the height z on the $(0z)$ axis.

In order to compute the magnetic field created by the square loop at the point M , we first consider the segment $[AB]$ and compute the magnetic field created by this segment. For this, we introduce a new plan defined by the points A , B and M , as well as a new coordinate system linked to that plane. $\vec{u}_{x'}$ is equal to \vec{u}_x , $\vec{u}_{y'}$ is defined by the direction of \vec{HM} , and $\vec{u}_{z'}$ is orthogonal to the (AMB) plan. This plan is shown in green in Fig. 3.6a and in Fig. 3.6b. The field created by the segment $[AB]$ is derived from the Biot and Savard law:

$$\begin{aligned} \vec{B}_{AB}(M) &= \int_{AB} \frac{\mu_0 I}{4\pi} \frac{d\vec{l} \times \vec{PM}}{\|\vec{PM}\|^3} \\ &= \frac{\mu_0 I}{4\pi} \int_{AB} \frac{\vec{HM} \cdot d\vec{l} \vec{u}_{z'}}{\|\vec{PM}\|^3} \end{aligned} \quad (3.7)$$

We have :

$$dl = dx' = d(rt \tan \theta) = \frac{r}{\cos^2 \theta} d\theta, \quad (3.8)$$

$$HM = r, \quad (3.9)$$

$$\|PM\| = \frac{r}{\cos\theta}, \quad (3.10)$$

leading to :

$$\begin{aligned} \vec{B}_{AB}(M) &= \frac{\mu_0 I}{4\pi} \int_{\theta_A}^{\theta_B} \frac{r}{\cos^2\theta} \frac{\cos^3\theta}{r^3} d\theta \vec{u}_{z'} \\ &= \frac{\mu_0 I}{4\pi r} \int_{\theta_A}^{\theta_B} \cos\theta d\theta \vec{u}_{z'} \\ &= \frac{\mu_0 I}{4\pi r} (\sin\theta_B - \sin\theta_A) \vec{u}_{z'} \end{aligned} \quad (3.11)$$

Due to the system geometry, $\sin\theta_B = -\sin\theta_A = \frac{a/2}{\sqrt{r^2 + (a/2)^2}}$, so the magnetic field created by the segment $[AB]$ is :

$$\vec{B}_{AB}(M) = \frac{\mu_0 I}{4\pi r} \frac{a}{\sqrt{r^2 + (a/2)^2}} \vec{u}_{z'}. \quad (3.12)$$

The field produced by the loop is the sum of the field created by each of its segments. The $(x0z)$ and $(y0z)$ plans are antisymmetric planes with respect to the current I . Therefore the field belongs to both planes, meaning that it must be along the $(0z)$ axis. As a result, the magnetic field of the square loop is indeed the sum of the magnetic field z component produced by the four segments. Introducing the angle β between the two unitary vectors \vec{u}_z and $\vec{u}_{z'}$, as shown in Fig. 3.6c, we write:

$$\begin{aligned} \vec{B}(M) &= 4B_{AB} \cos(\beta) \vec{u}_z = 4B_{AB} \cos(\pi/2 - \alpha) \vec{u}_z = 4B_{AB} \sin(\alpha) \vec{u}_z \\ &= 4 \cdot \frac{\mu_0 I}{4\pi r} \frac{a}{\sqrt{r^2 + (a/2)^2}} \cdot \frac{a}{2r} \vec{u}_z \\ \vec{B}(M) &= 4 \cdot \frac{\mu_0 I}{4\pi r} \frac{a}{\sqrt{r^2 + (a/2)^2}} \cdot \frac{a}{2r} \vec{u}_z \end{aligned} \quad (3.13)$$

Finally, we can substitute r by $\sqrt{(a/2)^2 + z^2}$, which gives :

$$\begin{aligned} \vec{B}(M) &= 4 \cdot \frac{\mu_0 I}{4\pi \sqrt{(a/2)^2 + z^2}} \frac{a}{\sqrt{(a/2)^2 + z^2 + (a/2)^2}} \cdot \frac{a}{2\sqrt{(a/2)^2 + z^2}} \vec{u}_z \\ \vec{B}(M) &= \frac{\mu_0 I}{2\pi} \frac{a^2}{(a^2/4 + z^2)\sqrt{a^2/2 + z^2}} \vec{u}_z. \end{aligned} \quad (3.14)$$

Again, if we consider an infinite squared solenoid, the magnetic field created at the point (M) by Ndz loops around the position z is given by:

$$\vec{B}(M) = \frac{\mu_0 NI}{2\pi} \frac{a^2}{(a^2/4 + z^2)\sqrt{a^2/2 + z^2}} dz \vec{u}_z. \quad (3.15)$$

Then, the field created by an infinite solenoid at the point (M) is obtained by integrating the previous equation :

$$\begin{aligned} \vec{B}(M) &= \frac{\mu_0 NI}{2\pi} \int_{z=-\infty}^{z=+\infty} \frac{a^2}{(a^2/4 + z^2)\sqrt{a^2/2 + z^2}} dz \vec{u}_z \\ &= \frac{\mu_0 NI}{2\pi} \cdot 2\pi \\ \vec{B}(M) &= \mu_0 NI, \end{aligned} \quad (3.16)$$

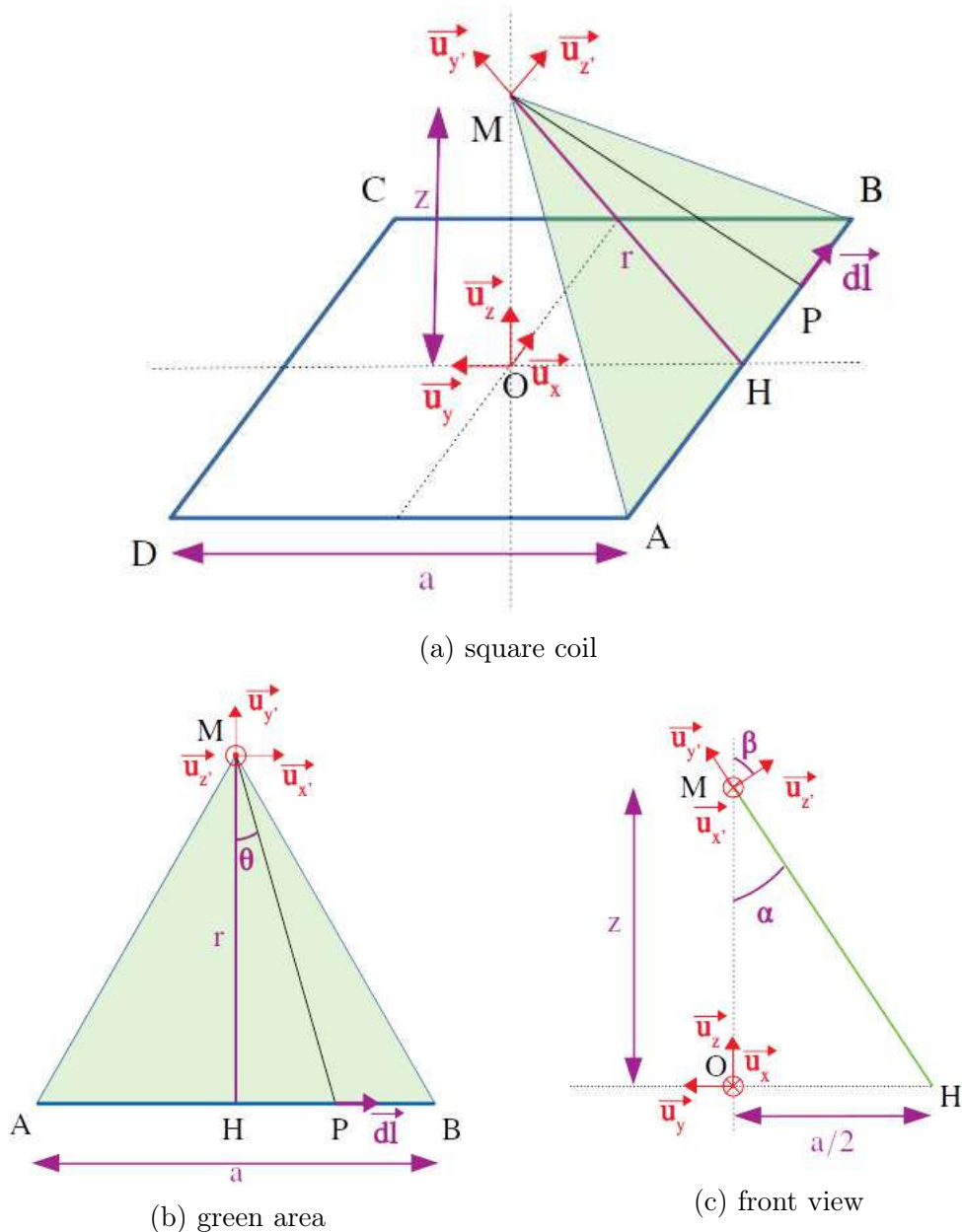


Figure 3.6 – Square coil model

which is the same expression as an infinite solenoid made of circular loops. Using the same argument as previously, one can use the Ampere's law to show that the field in the solenoid is uniform (so $B_{inside} = \mu_0 NI$) and null outside the solenoid.

Obviously, it is not feasible to build an infinite solenoid, neither a sufficiently long solenoid to produce a homogeneous field in the region of interest (volume including the precession chambers and the Cesium magnetometers array). The trick is to use the coupling between a finite solenoid and the magnetic shielding.

3.2.3 Finite solenoid in a magnetic shield

The coupling of a finite solenoid with a magnetic shield allows to mimic an infinite solenoid. In the paper of P. Hammond about Electric and Magnetic images [77] the concept of magnetic images is described. The reaction of a magnetic material to a current flowing nearby can be described by a current I_{image} flowing in the same direction and symmetrically with respect to the magnetic material. Several examples are shown in Fig. 3.7 to illustrate this point.

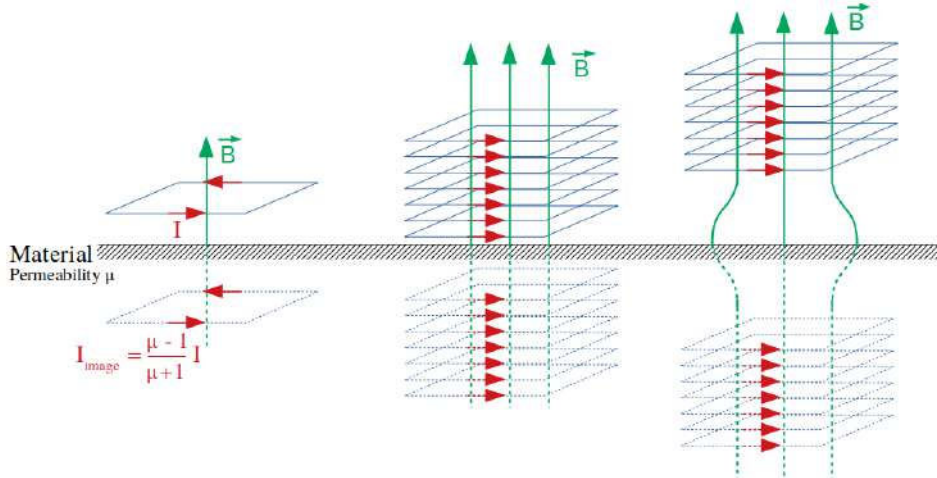


Figure 3.7 – On the left the image of a squared coil parallel to the shield is shown. In the middle, a solenoid close enough to the shield give uniform field. On the right is shown a solenoid which is further away from the shield. In that case, the field becomes less homogeneous at the solenoid extremities.

Considering the case of a single loop parallel to the shield surface, its image is a single loop parallel and symmetric with respect to the shield with a current $I_{image} = \frac{\mu-1}{\mu+1} I$ flowing in the same direction (see the left panel of Fig. 3.7). If the material permeability μ is large enough (around 35000 for the mu-metal used in the MSR), then $I_{image} = I$. Applying the same principle to a finite solenoid in front of a shield surface, one may conceive the design of an infinite solenoid (see the middle panel of Fig. 3.7).

The n2EDM B_0 coil is based on this idea. However, due to the coil support, it is not possible to build a coil close enough to the shield. The gap between the B_0 coil extremities and the shield is of the order of 10 cm. This partially breaks the advantage of their coupling. The real solenoid and its images act like two solenoids separated by a gap of 20 cm. This reduces the field uniformity (see the right panel of Fig. 3.7). This is why the B_0 coil is provided with additional current loops at the top and the bottom of the solenoid. These coils are called Lamé curves. They help to uniformize the field at the two solenoid exit.

3.2.4 B_0 coil design

The B_0 coil design is a vertical cubic solenoid with 181 loop and 14 endcaps loops at the top and at the bottom (see Fig. 3.8). The cube side is 2.73 m so that the central part of the experiment (vacuum tank, precession chambers, etc.) can be installed in the coil. It is located at around 10 cm from the MSR innermost layer. The surrounding shielding layer contributes to the field at the level of 30% (see section 3.3.3 for more details). The coil has to bypass the openings which targets the precession chambers, such as the UCN guides or the lasers openings. In those areas, the gap between the loops is reduced so that the overall current surface density is weakly changed (see Fig. 3.8). The main characteristics of the coil are shown in table 3.4.

The endcaps loops are designed as Lamé loops. They are defined by :

$$\begin{cases} x_i = a_i \cdot \cos^{n_i}(\theta) \\ y_i = a_i \cdot \sin^{n_i}(\theta) \end{cases}$$

with $\theta \in [0, \pi/2]$. The whole loop is then built by symmetry. The table 3.5 summarizes the parameters a_i and n_i of the endcaps loops.

The optimisation of the B_0 design has been performed with the "optimisation" module of the COMSOL software. The goal is to minimize the transverse field :

$$B_T = \sqrt{B_x^2 + B_y^2} \quad (3.17)$$

in a volume of 1 m³ around the precession chamber by modifying several parameters such as the parameters a_i and n_i of the Lamé loops or their height, taking into account the mechanical constraints. This optimisation leads to the B_0 parameters presented in Table 3.4, and to the optimized Lamé loops parameters a_i and n_i given in Table 3.5. The vertical gap between two side loop was set to 15 mm. It is not possible to further reduce this distance due to mechanical constraints : first some room is needed between two side loops in order to link the B_0 coil support to the MSR. Second, the opening bypasses would have been not feasible since they require a minimum gap between the wires. This is due to the necessary decrease of this gap at the bypass location (see Fig. 3.8). However, as soon as the vertical wires density is large enough, this parameter doesn't play an important role for the field uniformity.

Number of side loops	181
Number of endcap loops	2×7
Vertical wire gap	15 mm
Coil length	2121.6 m
Coil current	11.94 mA
Coil resistance	11.34 Ω

$a_0 = 1360$ mm	$n_0 = 0.25$
$a_1 = 1350$ mm	$n_1 = 0.30$
$a_2 = 1340$ mm	$n_2 = 0.30$
$a_3 = 1330$ mm	$n_3 = 0.30$
$a_4 = 1320$ mm	$n_4 = 0.30$
$a_5 = 1310$ mm	$n_5 = 0.30$
$a_6 = 1300$ mm	$n_6 = 0.30$

Table 3.4 – Main characteristics of the B_0 coil.

Table 3.5 – Main characteristics of the lamé loops.

One may notice that as for the shield, the coil is fully symmetric with respect to x,y,z, in order to forbid several gradients and then reduce the field non-uniformities (see Appendix D). The only unavoidable non-symmetric part is the entrance door.

3.3 Characteristics of the simulated B_0 field

The field produced by the B_0 coil at the center is $B(\vec{0}) = 1.000275$ μT with a current of 11.94 mA. In order to quantify the goodness of that field, we have introduced several estimators.

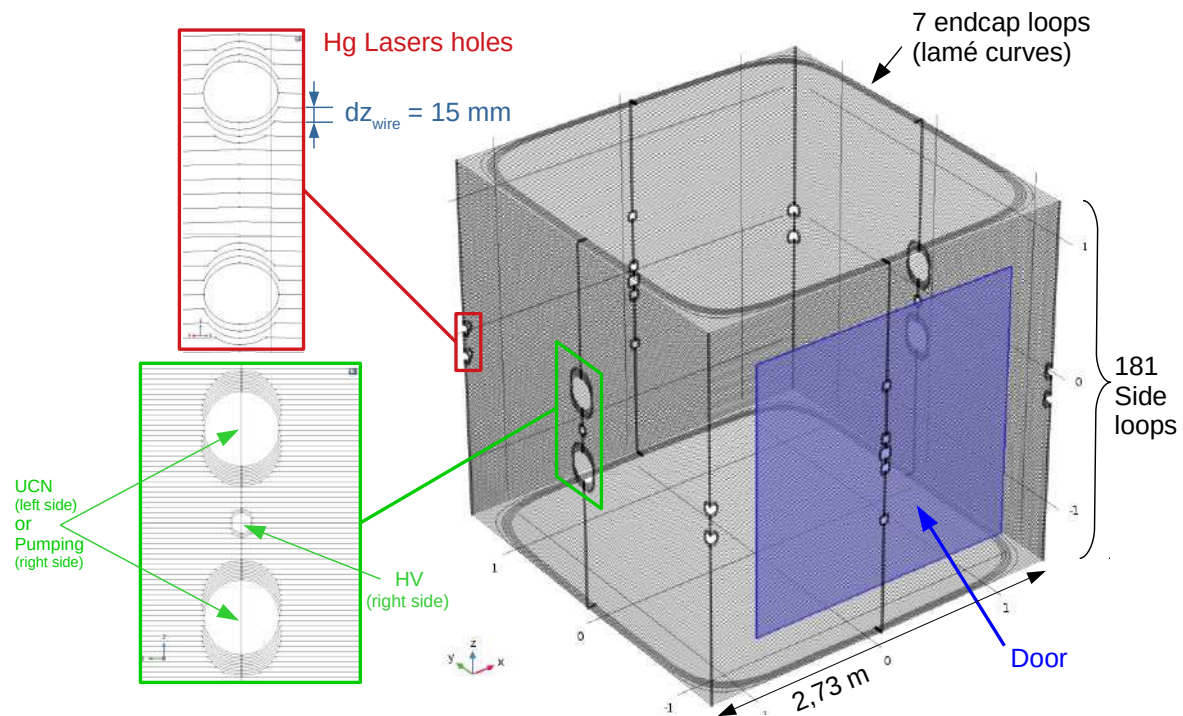


Figure 3.8 – B_0 coil design. In the zoomed frames, the bypass around the UCN guides and lasers openings are shown. The blue area corresponds to the entrance door ($2\text{m} \times 2\text{m}$).

3.3.1 B_0 field uniformity

Two estimators are used to characterize the field uniformity. A first estimation is performed by looking at its variations with respect to the field at the center of the system $B(\vec{0})$. This estimator is defined as:

$$\Delta B(\vec{r}) = \left\| \vec{B}(\vec{r}) - \vec{B}(0) \right\|. \quad (3.18)$$

The field variations of the B_0 field $\Delta B(\vec{r})$ are shown in Fig. 3.9. Due to the coil symmetries, only $1/8^{th}$ of the field map needs to be shown. The field variations don't exceed 100 pT in

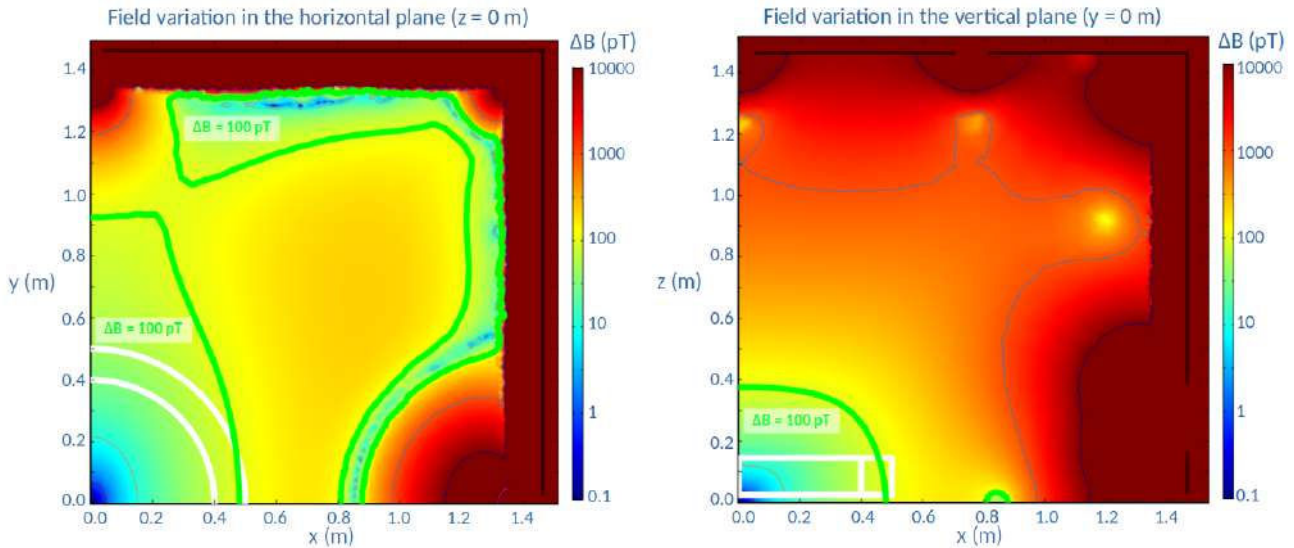


Figure 3.9 – Field variation produced by the B_0 coil in the horizontal plane at $z = 0$ m (left panel), and in the vertical plane at $y = 0$ m (right panel). The bold green line highlights $\Delta B = 100$ pT. The contours of the precession chambers with a diameter of 80 cm and 100 cm are shown in white. Finally, the MSR innermost layer is visible in black. The discontinuities on this layer corresponds to the openings.

a large volume including the precession chambers. This corresponds to a relative uniformity lower than 10^{-4} .

The second estimator is defined as :

$$\sigma(B_z) = \sqrt{\langle (B_z - \langle B_z \rangle)^2 \rangle}; \quad (3.19)$$

where the symbols " $\langle \rangle$ " refers to the average computed over the precession chamber volume. This is indeed the standard deviation of the main B_0 field component, i.e. the B_z component. The field uniformity produced by the B_0 coil can then be computed. It is equal to:

$$\sigma(B_z) = 17.3 \text{ pT}, \quad (3.20)$$

which is under the requirement of 170 pT (see section 2.2.2).

The field uniformity is only a rough estimator of the field quality. A deeper analysis of the field goodness is obtained by its decomposition into gradients [78, 79].

3.3.2 Gradient decomposition

Since 2010, a basis of harmonic polynomial is used in the collaboration to parametrize the magnetic field [78]. It has been re-evaluated in 2016 in order to separates the purely transverse modes (which lead to a null B_z component) and the longitudinal modes [79].

The basis is built so that the magnetic field respects the Maxwell equations. In a region free of currents and magnetizing material, both equations $\text{div}(\vec{B}) = 0$ and $\text{rot}(\vec{B}) = 0$ must be satisfied. This implies that the magnetic field can be expressed as a function of a scalar potential $\Sigma(\vec{r})$ which obeys the Laplace equation $\Delta\Sigma = 0$. The solution chosen by the collaboration is [80] :

$$\begin{aligned}\Sigma_{l,m} &= \frac{(l-1)!(-2)^{|m|}}{(l+|m|)!}r^l P_l^m(\cos\theta)\cos(m\phi) \quad \text{for } m \geq 0 \\ \Sigma_{l,m} &= \frac{(l-1)!(-2)^{|m|}}{(l+|m|)!}r^l P_l^m(\cos\theta)\sin(m\phi) \quad \text{for } m < 0\end{aligned}\quad (3.21)$$

where $P_l^m(\cos\theta)$ corresponds to the Legendre polynomials, l is the degree of the polynomial and m is an integer belonging to $[-l, l]$. To get the harmonic polynomials $\Pi_{l,m}$ in Cartesian $\{x, y, z\}$ coordinates, one only need to derive this potential :

$$\Pi_{x,l,m} = \partial_x \Sigma_{l+1,m} \quad (3.22)$$

$$\Pi_{y,l,m} = \partial_y \Sigma_{l+1,m} \quad (3.23)$$

$$\Pi_{z,l,m} = \partial_z \Sigma_{l+1,m} \quad (3.24)$$

The harmonic polynomial basis is presented in the Appendix C up to the degree $l=4$. Finally, the magnetic field can be expressed in this basis using the gradient amplitudes $G_{l,m}$:

$$\vec{B}(\vec{r}) = \sum_{l,m} G_{l,m} \begin{pmatrix} \Pi_{x,l,m}(\vec{r}) \\ \Pi_{y,l,m}(\vec{r}) \\ \Pi_{z,l,m}(\vec{r}) \end{pmatrix}. \quad (3.25)$$

By definition, an harmonic of degree 1 corresponds to a dependency on position at the order 1. In other words, the harmonics with a degree $l=0$ corresponds to uniform gradients (ex : $G_{0,-1} = B_x$, $G_{0,0} = B_z$, $G_{0,1} = B_y$) $l=1$ corresponds to linear gradients (ex : $G_{1,-1} = \frac{\partial B_z}{\partial y}$, $G_{1,0} = \frac{\partial B_z}{\partial z}$, $G_{1,1} = \frac{\partial B_z}{\partial x}$), $l=2$ to quadratic gradients and so on.

Using this field decomposition, we can compare the field gradients produced by the B_0 coil to the gradients requirements (Table 3.1). Due to the symmetries of the B_0 coil and the shield, only a few gradients can be produced : $G_{0,0}$, $G_{2,0}$, $G_{2,2}$, $G_{4,0}$, $G_{4,2}$, $G_{4,4}$, ... (see Appendix D). This holds only if the system is perfectly symmetric (i.e. in absence of mechanical imperfections).

The amplitude of the field gradients are given in the table 3.6. The $G_{0,0}$, which corresponds to the pure vertical field component and is very close to $1 \mu\text{T}$.

Gradient	Amplitude
$G_{0,0}$	1000275 pT
$G_{2,0}$	$6.71 \times 10^{-2} \text{ pT/cm}^2$
$G_{2,2}$	$1.10 \times 10^{-2} \text{ pT/cm}^2$
$G_{4,0}$	$2.55 \times 10^{-6} \text{ pT/cm}^4$
$G_{4,2}$	$1.04 \times 10^{-6} \text{ pT/cm}^4$
$G_{4,4}$	$1.10 \times 10^{-7} \text{ pT/cm}^4$

Table 3.6 – Amplitude of the field gradients produced by a perfect B_0 coil.

As we can see, a perfect B_0 coil fulfills all requirements.

3.3.3 Influence of the MSR

The magnetic shield participates to the field production, and contributes to the field uniformity. The Fig. 3.10 shows the innermost layer of the MSR which has been simulated in the

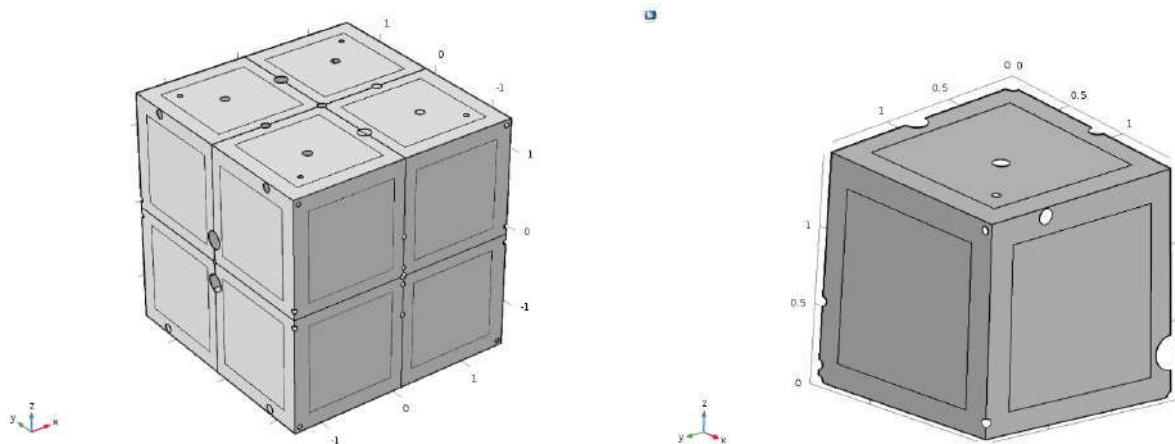


Figure 3.10 – Geometry of the MSR innermost mu-metal layer simulated in COMSOL. The full geometry is shown in the left panel. Because of the shield and coil symmetries, only 1/8th of the system can be simulated. This is shown in the right panel. The layer thickness is 6 mm except on the side where reinforcement is used to hold the plates together: this leads to a larger thickness of 7.5 mm.

COMSOL software. The other layers don't contribute to the B_0 field production (this has been checked in a previous simulation).

The Table 3.7 shows the comparison between two simulations: one with the MSR and one without. The shield contributes to about 30% of the field produced and lower significantly the field non uniformities.

Estimators	Without MSR	With MSR
$G_{0,0}$ (pT)	683353	1000275
$G_{2,0}$ (pT/cm ²)	11.8	6.71×10^{-2}
$G_{4,0}$ (pT/cm ⁴)	5.25×10^{-5}	2.55×10^{-6}
$G_{6,0}$ (pT/cm ⁶)	2.72×10^{-9}	7.99×10^{-11}
$\sigma(B_z)$ (pT)	2816	17.3

Table 3.7 – Influence of MSR on the produced B_0 field.

3.4 Study of some mechanical imperfections

The previous section has presented the performances of a perfect B_0 coil, without any mechanical imperfections. These latter can't be totally avoided when building and installing the coil in the shield. The influence of the most probable imperfections have been simulated with COMSOL. Two types are shown in this section.

3.4.1 Global misalignment of the B_0 coil with respect to the shield

At the time of the coil installation, it may be difficult to precisely match the magnetic centers of the coil and the MSR: a global misalignment of the B_0 coil with respect to the shield may appear. It is important to know what is the sensitivity of the produced field with respect to these misalignments. Such a misalignment breaks the field symmetries and produces some formerly forbidden gradients. The sensitivity of the gradients subject to a requirements need to be investigated. The misalignment can be horizontal (x,y) and/or vertical (z). We will therefore study those two cases.

Horizontal misalignment

Let's first study the case of an horizontal misalignment of the B_0 coil with respect to the shield. If it is a misalignment along the x axis, the current (and thus field) symmetry along the YZ plan is broken. As indicated in Appendix D, this produces gradients such as $G_{1,1}$ or $G_{3,1}$. It also induces for our simulation that we have to build $1/4^{th}$ of the geometry instead of $1/8^{th}$ given that the symmetry condition can't be applied anymore on the YZ plane. In a case of the misalignment along the y axis, it is the XZ symmetry plan which is broken, and the gradient produced are $G_{1,-1}$, $G_{3,-1}$ etc. Again it mean for our simulation that $1/4^{th}$ of the geometry has to be build since XZ is no longer a symmetry plan. The influence of the misalignment on $G_{1,-1}$ and $G_{1,1}$ is closely watched because they are required to be less than 8 pT/cm. The influence of the other gradients are studied across the field uniformity $\sigma(B_z)$.

We simulated misalignments in both x and y directions with a displacement of $\Delta x = 5$ mm and $\Delta y = 5$ mm. The results are shown in Table 3.8.

Δx (mm)	Δy (mm)	$B(\vec{0})$ (μT)	$\sigma(B_z)$ (pT)	$G_{1,-1}$ (pT/cm)	$G_{1,1}$ (pT/cm)
Requirements		1	< 170	-	-
0	0	0.999998	17.3	-	-
5	0	1.000002	17.7	-	0.180
0	5	0.999998	17.6	0.168	-
5	5	1.000002	18.1	0.168	0.180

Table 3.8 – Field requirements for a global misalignment of B_0 in the x or y directions.

The results shows that for a horizontal misalignment of 5 mm, the gradient and the field uniformity stay under their requirements. Since the mechanical alignment can be performed at the level of about 1 mm, they are not considered as a threat.

Vertical misalignment

A vertical misalignment of the coil with respect to the shield breaks the z-symmetry. Therefore it will produces the following gradients : $G_{1,0}$, $G_{3,0}$, $G_{5,0}$, ... which may overcome their requirements or decrease the field uniformity. We simulate several vertical misalignment with the COMSOL software by vertically moving the entire coil . Because of the vertical misalignment, $1/4^{th}$ of the full geometry needs to be simulated (instead of $1/8^{th}$). The Table 3.9 shows the evolution of the field estimators as a function of the misalignment. The cell "Requirements" for the gradients of higher order than $G_{1,0}$ is an indication of the gradient amplitude which produces a false motional EDM of $5 \times 10^{-28} \text{ e cm}$.

Δz (mm)	$B(\vec{0})$ (μT)	σB_z (pT)	$G_{1,0}$ (pT/cm)	$G_{3,0}$ (pT/cm^3)	$G_{5,0}$ (pT/cm^5)	$G_{7,0}$ (pT/cm^7)
Requirements	1	< 170	< 0.6	< 7.17×10^{-5}	< 6.54×10^{-8}	< 7.30×10^{-11}
0	1.000275	17.3	-	-	-	-
0.05	1.000000	17.6	0.33	3.60×10^{-6}	-3.08×10^{-10}	3.28×10^{-15}
0.25	1.000001	19.4	1.62	1.68×10^{-5}	1.50×10^{-9}	7.43×10^{-15}
1.00	1.000001	31.0	6.45	6.72×10^{-5}	5.98×10^{-9}	4.88×10^{-14}
3.00	1.000000	72.2	19.4	2.02×10^{-4}	-1.80×10^{-8}	1.56×10^{-13}
5.00	1.000001	115.8	32.3	3.37×10^{-4}	2.99×10^{-8}	2.63×10^{-13}

Table 3.9 – Field gradients and uniformity as a function of a varying vertical misalignment of B_0 . The dashed lines indicate from where the requirements are no longer fulfilled.

The vertical alignment of the coil with respect to the shield is a critical issue: the requirement on the $G_{1,0}$ gradient due to the top-bottom matching condition is already exceeded with a

displacement $\Delta z = 0.25$ mm. Moreover, a displacement higher than 1 mm might create a motional false EDM larger than 5×10^{-28} e cm via the $G_{3,0}$ gradient contribution. However, the ones created by the $G_{5,0}$ or the $G_{7,0}$ are still under their requirements with a displacement of 5 mm, as well as the field uniformity.

This implies that the vertical installation of the B_0 coil requires a specific procedure. A field mapping campaign is planned: during the B_0 coil installation, the B_0 field will be mapped as a function of its height z . A 1 mm range is mechanically foreseen. The goal will be to find the optimal vertical position. Moreover, an other coil is dedicated to suppress too large $G_{1,0}$ gradient contribution arising from the B_0 field (see section 4.2.2).

3.4.2 Influence of the shield innermost dimensions

Any change of the distance between the B_0 coil and the shield will deteriorate the field uniformity. Since the exact shield internal size cannot be known before its installation, it is important to study this imperfection.

The imperfection can be mimic by a homothety of the shield size: the magnetic centers of the shield and the B_0 coil are identical, but the dimensions of the shield change (either extending or shrinking). This modify the amplitude of the authorized gradients (mostly $G_{2,0}$ and $G_{4,0}$). In order to have a conservative but also a realistic idea of the influence of the shield dimensions, we simulate both extending and shrinking with two size variations: 5 mm (conservative) and 1 mm(realistic). The results are summarized in Table 3.10.

Shield position	$B(\vec{0})$ (μT)	σB_z (pT)	$G_{2,0}$ (pT/cm^2)	$G_{4,0}$ (pT/cm^4)
Requirements	1	< 170	-	-
Perfect shield	1.000275	17.3	0.07	2.55×10^{-6}
closer to B_0 by 5 mm	1.002455	62.7	0.26	4.70×10^{-7}
closer to B_0 by 1 mm	1.000490	26.0	0.11	1.96×10^{-6}
away from B_0 by 1 mm	0.999509	9.97	0.03	3.14×10^{-6}
away from B_0 by 5 mm	0.997563	31.3	0.12	5.43×10^{-6}

Table 3.10 – Variations of the $G_{2,0}$ and $G_{4,0}$ gradients and of $\sigma(B_z)$ obtained for several shield homotethies.

The result indicates that even by being conservative, the field uniformity $\sigma(B_z)$ stays under 170 pT. The uncertainty on the shield innermost dimensions is therefore not a big threat.

Still, when the shield will be installed, its size will be carefully measured. Then the design of the B_0 coil will be optimized. The shape and the number of the Lamé loops will be adjusted so that the B_0 field uniformity can be set to an optimum.

3.4.3 Other imperfections

In addition to the two imperfections studied above, a few more cases have been studied. The shield permeability of the different plates which composed the layers may vary by at most $\pm 20\%$ (Vacuumschmelze private communication). One of the worst case might be if that variation occurs between the roof plates and the bottom plates, in which case the z-symmetry is broken. Therefore we simulated this issue in COMSOL, with the roof plate permeability increased by 10% and the bottom one decreased by 10%. The result of the simulation showed that it don't constitute an issue for the field uniformity. On other case concerns the fact that the B_0 wires will be inserted in a groove made in polycarbonate supports (see section 3.5 for more details). The wire diameter (1.8 mm) is slightly smaller than the groove width (2.00 mm). This means that the wire may deviate from the optimal path. This has been simulated by considering that the

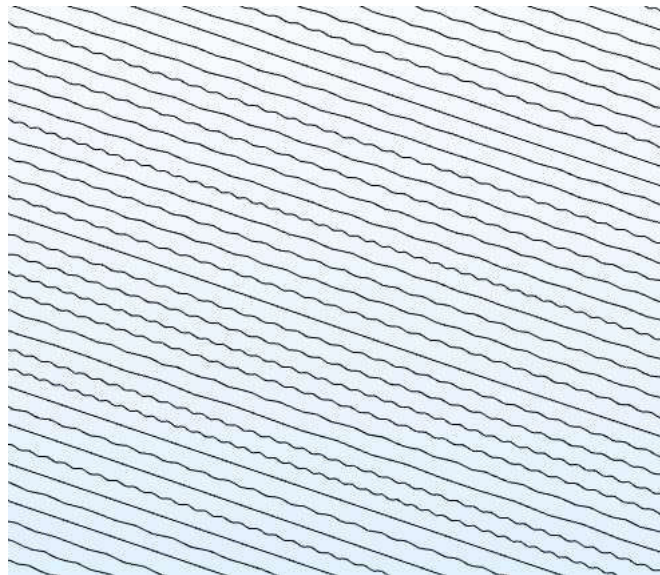


Figure 3.11 – Example of oscillating wires simulated in COMSOL.

wire oscillate on the groove. Each wire has therefore been considered as being a sinusoid with its own frequency randomly chosen in $f_{\text{wire}} \in [0, 350] \text{ m}^{-1}$ and phase chosen in $\phi_{\text{wire}} \in [-\pi; \pi]$. All of the wires however share an oscillation amplitude $A = 0.25 \text{ mm}$. The fig Fig. 3.11 shows a small part of the simulated oscillating wires in which we can see different wires frequencies.

Once again the result shows that the field uniformity is poorly affected by those oscillations. The disorganized movement result in an averaged null movement.

3.4.4 Conclusion about the mechanical imperfections

The major part of the simulated imperfections, like the horizontal displacement of the coil, the shield innermost layer dimensions, the shield permeability variation or the oscillations of the wires inside the grooves showed that they have a low influence on the field uniformity and that they are not considered as a threat. This illustrates the robustness of the coil design and the produced field.

However, a global misalignment of the B_0 coil with respect to the MSR is a critical issue and compromises the field quality. To palliate this misalignment, a mapping campaign is planned: during the installation of the coil, it will be possible to adjust its height (in a 1 cm range) and measure for every selected position the produced magnetic field. The optimal height will be hence determined. Moreover, an additional coil able to produce the $G_{1,0}$ gradient is planned to suppress the remaining $G_{1,0}$ gradient.

Even if that imperfection is compensated, it is not possible to foresee all possible mechanical imperfections. This is why a correction system will be installed to correct the residuals non-uniformities of the B_0 field. This is the goal of the TRIM coil array and the harmonic coils presented in the next chapter.

3.5 B_0 technical design

The B_0 coil will be made of polycarbonate plates in which grooves will be machined. The groove width is 2.0 mm, and its depth is 3.0 mm. A copper wire with a diameter of $\varnothing_{\text{wire}} = 1.8 \text{ mm}$ will be glued inside the grooves. The groove path corresponds to the shape of the simulated coil. The technical feasibility was tested at LPC with some typical parts of the coil

with a focus on the opening bypass : for a UCN guide opening (the large one), and the Hg lasers openings (the small ones). The support made of Polycarbonate plates screwed on aluminium profiles were also tested (see right panel of Fig. 3.12).

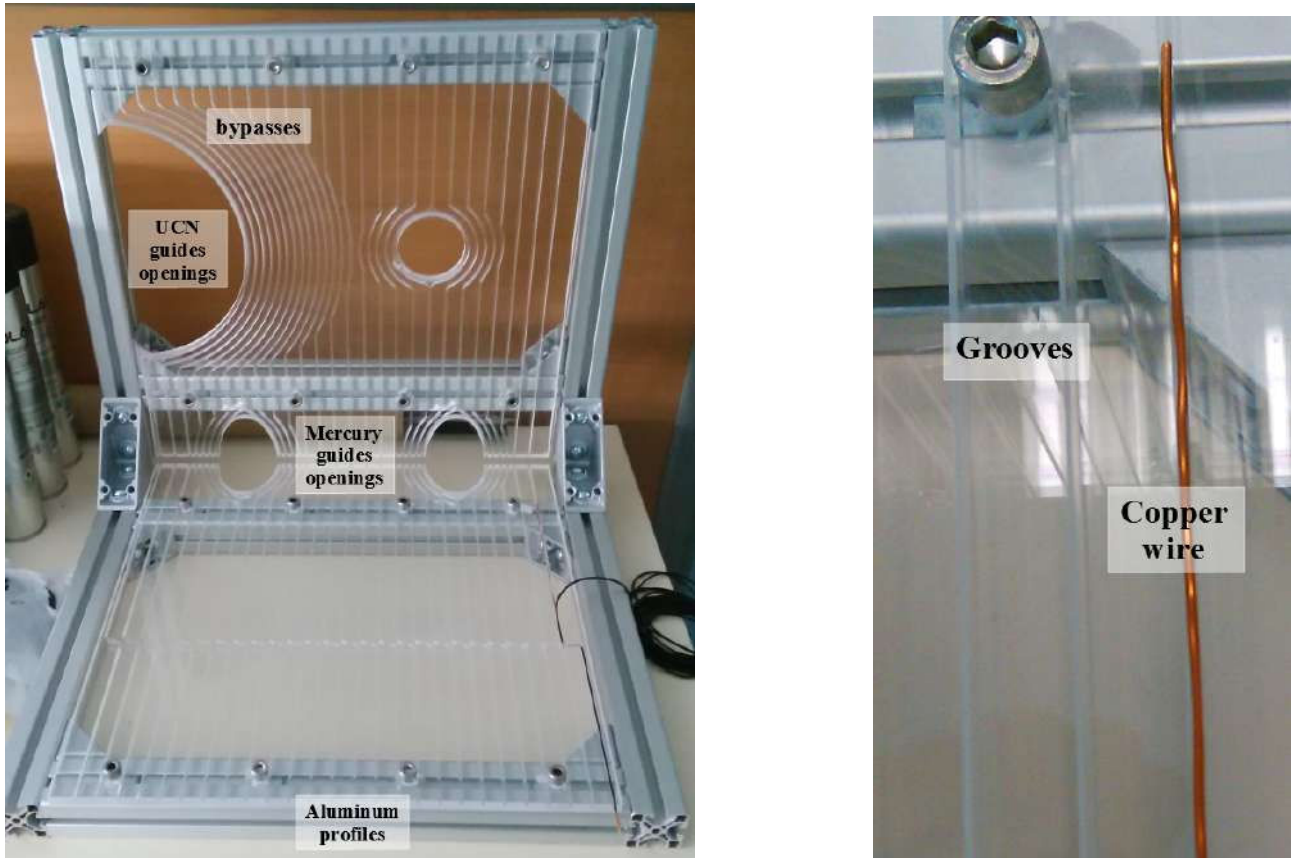


Figure 3.12 – The left panel shows the foreseen technical solution with a focus on the opening bypass : for a UCN guide opening (the large one), and the Hg lasers openings (the small ones). Polycarbonate plates are screwed on aluminium profiles. The right panel shows a copper wire inside a groove.

The entrance door is a very sensitive part of the system : it has to be robust and easy to operate. In addition, the closed position must be reproducible (or measured) in order to ensure the reproducibility of the produced field. This is why one of the main issue of the technical design relies on the door connectors. They have to be non magnetic, to fit the coil design but to stay flexible and accept small misalignment, they must have a good and reproducible contact, they must be robust, but also removable, they must be compact and last but not least, they must be easy and quick to connect because of the high number of door connectors (274 for the moment). Several connectors design are studied. One of them is showed in Fig. 3.13. This solution involves a split cylinder which can slide to make the connection between the two sides. Several tests will be performed at LPC to check the reproducibility of the wire resistance after several hundred connections.

The overall mechanical design is shown in Fig. 3.14. A mechanical structure (Al profile) will be first installed and fixed to the MSR fixation points. Then the B_0 coil will be fixed to this structure. The total weight of the coil is estimated at around 600 kg. The B_0 coil installation is planned for 2020.

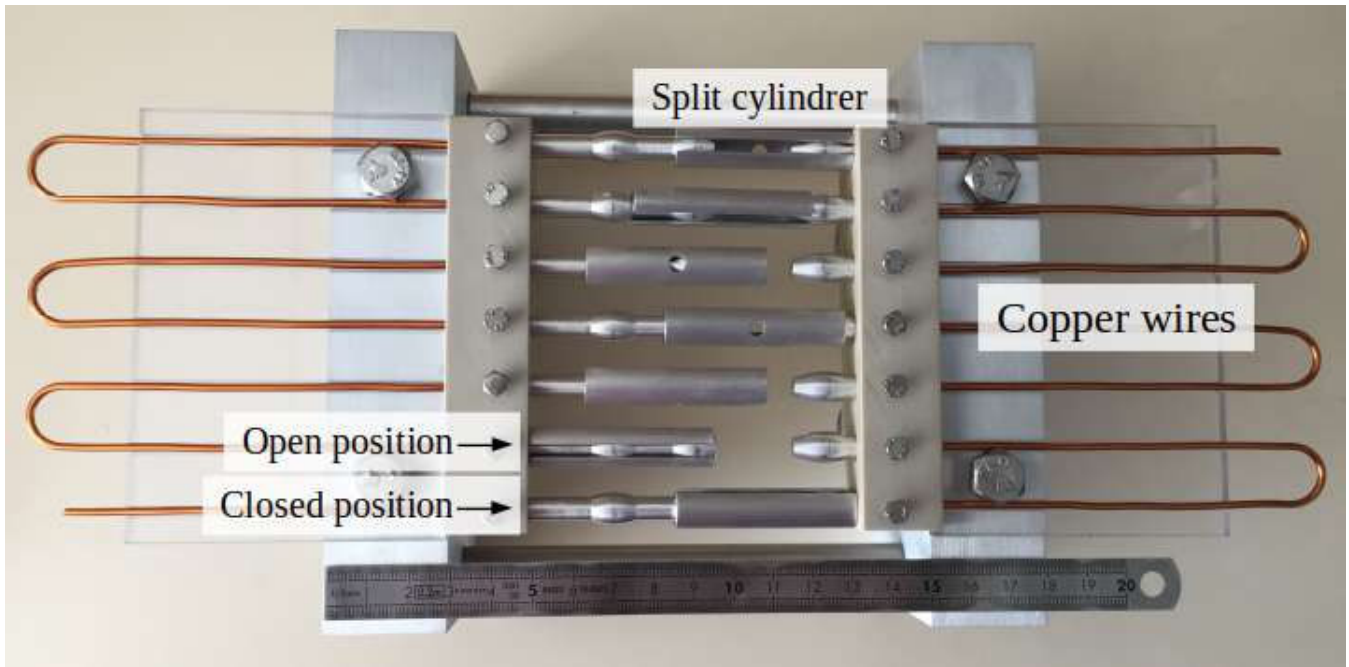


Figure 3.13 – One of the possible solution for the door connectors is shown: it consists of split cylinders that can slide in order to connect or disconnect the copper wires representing the coil.

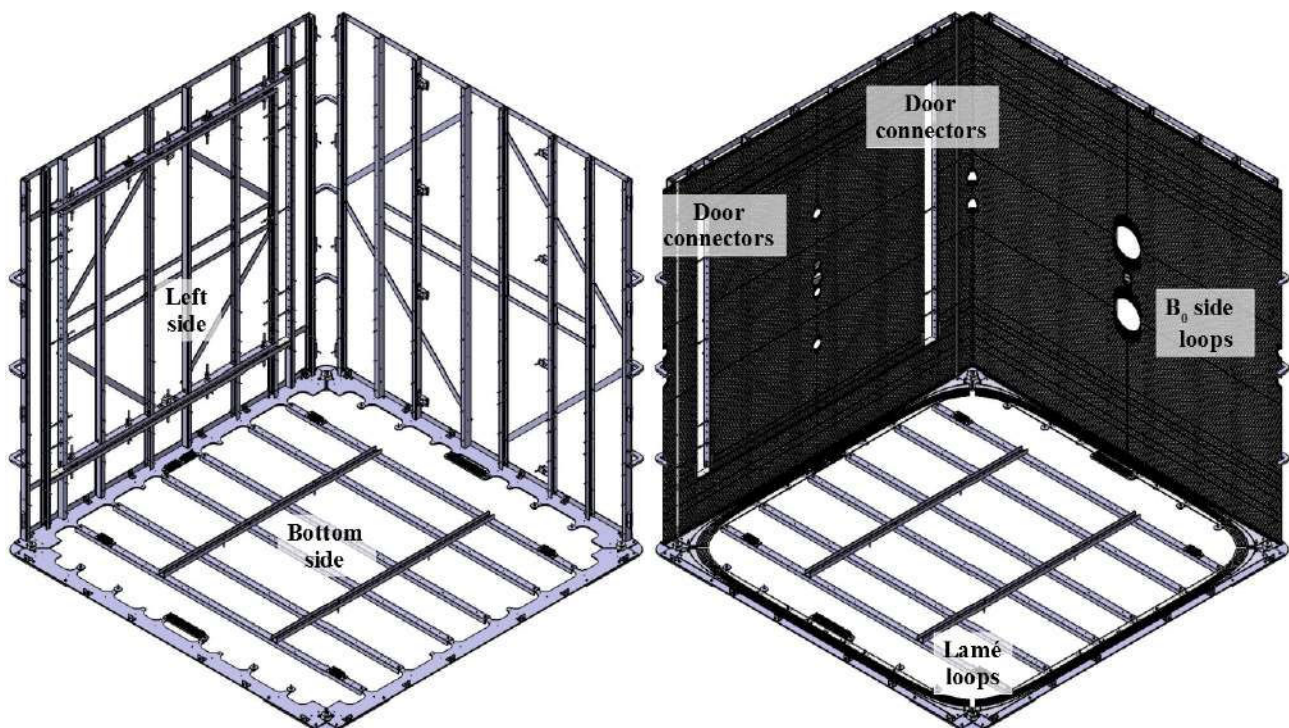


Figure 3.14 – The aluminum structure is shown in the top figure. The B_0 coil will be fixed on this structure, as shown on the bottom figure.

Conclusion

Based on the idea of an infinite coil, the B_0 coil design has been shown : a vertical solenoid surrounded by a magnetic shield, with 14 additional Lamé curves at the top and the bottom. The simulations made with the COMSOL software, using the symmetries of the coil, has shown

that the perfect coil fulfills the requirements. Several mechanical imperfections has been simulated. A vertical misalignment of the coil with respect to the shield is considered to be an important issue, since a 0.25 mm displacement already exceeds the $G_{1,0}$ requirement. The n2EDM experiment will then requires a set of correcting coils, which is the topic of the next chapter. Finally, the present chapter ended by the presentation of the technical design of the B_0 coil.

4

The correcting coils

Contents

4.1 TRIM coils array	81
4.1.1 Purpose and working principle	81
4.1.2 Design	82
4.1.3 Performances	82
4.2 Harmonic Coils	83
4.2.1 Purposes	83
4.2.2 Design of $G_{1,0}$, $G_{2,0}$ and $G_{3,0}$ coils	84
4.2.3 Design of $G_{1,-1}$ and $G_{1,1}$ coil	86
4.2.4 Design of $G_{0,-1}$ and $G_{0,1}$ coils	88
4.3 Technical design	89

Introduction

It is not possible to anticipate all the mechanical imperfections which will arise when the B_0 coil will be installed in the MSR. Therefore it is necessary to build an additional coils system to correct for the possible remaining field non-uniformities. This is the purpose of the TRIM coils array, presented in the first section of this chapter. In addition, a few field gradients play a crucial role in the experiment: $G_{1,0}$, $G_{2,0}$, $G_{3,0}$, $G_{1,-1}$ and $G_{1,1}$. For the same reason, static transverse component $G_{0,-1}$ and $G_{0,1}$ need to be produced. It is important to be able to produce them with a high degree of reliability. This is the purpose of the harmonic coils. The role of these coils is fully detailed in the section 4.2.

4.1 TRIM coils array

4.1.1 Purpose and working principle

The purpose of the TRIM coils array is to suppress the residual field non-uniformities. The array is made of 56 square coils (see the section 4.1.2). Each coil is powered by a dedicated power supply. The range of the supplied current is from -200 mA to 200 mA with a resolution of 1 μA ¹. Using different combinations of currents, it is possible to produce field gradients up to the order 6 (higher orders cannot be produced due to the limited number of coils). During the

1. specifications from the Confluence specification sheet

experiment, the unwanted gradients will be first measured by the Cs array and then suppress with the TRIM coils array. The working procedure is as follow :

- First the field produced by each TRIM coil will be measured during a dedicated mapping campaign. The supplied current will be $I = \text{mA}$ for instance.
- Then each field map will be decomposed into gradients. These gradient are used to fill the matrix G_{TC} . Thus, the element on the i^{th} row and j^{th} column corresponds to the i^{th} gradient created by the j^{th} TRIM coil.
- In order to suppress the undesirable gradients, we solve the Eq. 4.1: $\mathbf{G} = \mathbf{G}_{TC} \cdot \mathbf{I}_{TC}$.
 1. The matrix \mathbf{G} , of size $(1 \times n)$ is filled with the gradient that we want to correct for.
 2. The matrix \mathbf{G}_{TC} , as we said earlier, is filled with the gradients produced by each TRIM coil. Its element (i,j) corresponds to the i^{th} gradient created by the j^{th} TRIM coil with a current of 1 mA.
 3. The matrix \mathbf{I}_{TC} of size (1×56) contains the currents of each TRIM coil. This matrix is the solution, obtained by a matrix inversion: it gives the combination of currents required to produce the gradients of interest.

$$\underbrace{\begin{pmatrix} G \\ G_{1,-1} \\ G_{1,0} \\ G_{1,-1} \\ \vdots \\ G_{7,8} \end{pmatrix}}_G = \underbrace{\begin{pmatrix} G_{1,-1}^{TC1} & G_{1,-1}^{TC2} & \cdots & G_{1,-1}^{TC56} \\ G_{1,0}^{TC1} & G_{1,0}^{TC2} & \cdots & G_{1,0}^{TC56} \\ G_{1,1}^{TC1} & G_{1,1}^{TC2} & \cdots & G_{1,1}^{TC56} \\ \vdots & \vdots & \ddots & \vdots \\ G_{7,8}^{TC1} & G_{7,8}^{TC2} & \cdots & G_{7,8}^{TC56} \end{pmatrix}}_{G_{TC}} \cdot \underbrace{\begin{pmatrix} I_{TC1} \\ I_{TC2} \\ \vdots \\ I_{TC56} \end{pmatrix}}_{I_{TC}} \quad (4.1)$$

4.1.2 Design

The TRIM coils array design is shown in Fig. 4.1. It is composed of 56 one-turn coils. They are distributed on a cube of side 2.706 m. This corresponds to the 3rd layer of the coil system, described in section 4.3. The top/bottom and rear/front faces are made of 3×3 coils of the same dimensions: $0.3 \text{ m} \times 0.3 \text{ m}$. On the left and right sides, an adjustment has to be made in order to take into account the UCN guides and the pumping pipes. The central coil is replaced by two $0.4 \text{ m} \times 0.4 \text{ m}$ coils, placed around the openings.

4.1.3 Performances

In order to test the performances of the TRIM coils array, we start from a field map with large field non-uniformities. This map has been produced by vertically shifting the B_0 coil with respect to the MSR by 5 mm. This is the worst imperfection that has been generated (see section 3.4.1). We then apply the procedure in order to suppress the field non-uniformities. The Table 4.1 shows a comparison of the field characteristics before and after the correction. The range of currents used for this correction, [1.4 ; 22.9] mA, belongs to the available current range delivered by the power supplies.

As observed, the TRIM coil array is able to suppress large field non-uniformities. It includes non-uniformities coming from the mechanical imperfections (in the example, $G_{1,0}$, $G_{3,0}$ and $G_{5,0}$) but also non-uniformities already present without any mechanical imperfections (as the $G_{2,0}$ gradient).

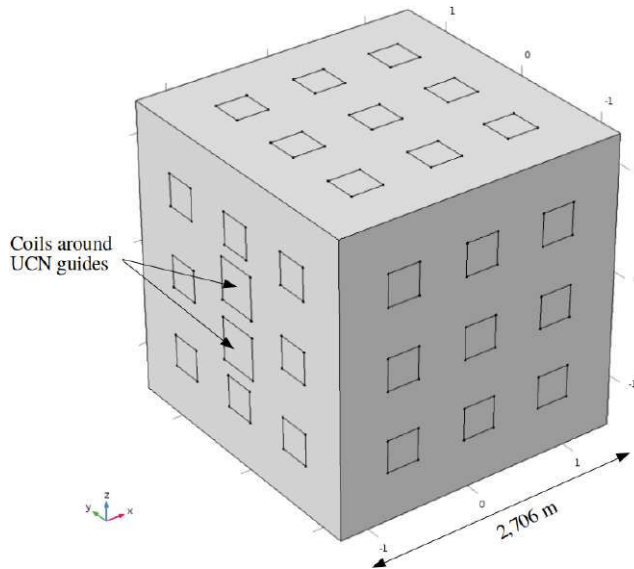


Figure 4.1 – The TRIM coil array design.

Field characteristics	Before correction	After correction
$B(\vec{0})$ (pT)	1.000001	1.000000
$\sigma(B_z)$ (pT)	115.8	0.009
$G_{1,0}$ (pT/cm)	32.3	1.00×10^{-6}
$G_{2,0}$ (pT/cm ²)	6.72×10^{-2}	5.17×10^{-9}
$G_{3,0}$ (pT/cm ³)	3.37×10^{-4}	5.18×10^{-10}
$G_{5,0}$ (pT/cm ⁵)	2.99×10^{-8}	1.26×10^{-12}

Table 4.1 – Evolution of the field characteristics before and after the application of the TRIM coil array correction. The farmer field is produced by a B_0 coil misaligned by 5 mm with respect to the MSR.

4.2 Harmonic Coils

4.2.1 Purposes

A set of seven harmonic coils is foreseen for the n2EDM experiment. Each coil aims at producing a single gradient among the following ones : $G_{1,0}$, $G_{2,0}$, $G_{3,0}$, $G_{1,1}$, and $G_{1,-1}$ and static components $G_{0,1}$, $G_{0,-1}$. There must be no admixture from other gradients in the produced field (i.e. no pollution from other gradients). The reproducibility must be as high as possible.

The coils purposes are the following :

- **Satisfy the Top-bottom matching condition** using the $G_{1,0}$ coil. It requires a $G_{1,0}$ gradient under 0.6 pT/cm (see section 2.2.1), also meaning that the coil has to produce a $G_{1,0}$ gradient with a resolution below 0.1 pT/cm.
- **Control the $G_{1,0}$, $G_{2,0}$ and $G_{3,0}$ gradients:** the motional false EDM is the limiting systematic effect in the experiment. It is important to control (and be able to produce) the gradients which generate this effect. This is why three dedicated coils, corresponding to the $G_{1,0}$, $G_{2,0}$ and $G_{3,0}$ gradients have been studied.
- **Probe the position of the Cs magnetometers:** in situ, the magnetic field will be measured by the Cs array. This measurement requires to know at the mm level the

position of the Cs magnetometers [81]. For this purpose, three coils producing the linear gradient of the B_z component i.e. $\frac{\partial B_z}{\partial x}$ ($G_{1,1}$), $\frac{\partial B_z}{\partial y}$ ($G_{1,-1}$) and $\frac{\partial B_z}{\partial z}$ ($G_{1,0}$) have been investigated. The field measured by the Cesium Magnetometers will be linearly proportional to the position and will therefore allow to easily probe their position. Three harmonic coils are needed in order to probe the three space directions.

- **Produce a static transverse field** which can be used to characterize the Mercury light shift effect [82]. The corresponding "gradients" are $G_{0,1}$, equivalent to a uniform B_x field, and $G_{0,-1}$, equivalent to a uniform B_y field.

4.2.2 Design of $G_{1,0}$, $G_{2,0}$ and $G_{3,0}$ coils

Coil purpose and criteria

The goal of $G_{1,0}$, $G_{2,0}$ and $G_{3,0}$ coils is to better control the Mercury motional EDM. Since the polynomials functions associated to the $G_{1,0}$, $G_{3,0}$, $G_{5,0}$ and $G_{7,0}$ gradients share the same symmetries (with respect to the XZ, YZ and XY plans), natural admixture may arise. The same problem is encountered with the $G_{2,0}$, $G_{4,0}$ and $G_{6,0}$ gradients. A criteria which characterizes this possible pollution needs to be defined. It is not easy to use a criteria directly based on the gradients since they don't have the same units. Instead, we defined a criteria which is related to the produced false EDM. It reads as follow:

$$\text{For } G_{1,0} \text{ coil : } d_{ratio}(G_{1,0}) = \frac{|d_{n \leftarrow Hg}^{false}(G_{1,0})|}{|d_{n \leftarrow Hg}^{false}(G_{3,0})| + |d_{n \leftarrow Hg}^{false}(G_{5,0})| + |d_{n \leftarrow Hg}^{false}(G_{7,0})|} \quad (4.2)$$

$$\text{For } G_{2,0} \text{ coil : } d_{ratio}(G_{2,0}) = \frac{|d_{n \leftarrow Hg}^{false}(G_{2,0})|}{|d_{n \leftarrow Hg}^{false}(G_{4,0})| + |d_{n \leftarrow Hg}^{false}(G_{6,0})|} \quad (4.3)$$

$$\text{For } G_{3,0} \text{ coil : } d_{ratio}(G_{3,0}) = \frac{|d_{n \leftarrow Hg}^{false}(G_{3,0})|}{|d_{n \leftarrow Hg}^{false}(G_{1,0})| + |d_{n \leftarrow Hg}^{false}(G_{5,0})| + |d_{n \leftarrow Hg}^{false}(G_{7,0})|} \quad (4.4)$$

where the quantities $|d_{n \leftarrow Hg}^{false}(G_{1,0})|$, $|d_{n \leftarrow Hg}^{false}(G_{3,0})|$, $|d_{n \leftarrow Hg}^{false}(G_{5,0})|$ and $|d_{n \leftarrow Hg}^{false}(G_{7,0})|$ correspond to the absolute value of the mercury false motional EDM produced by the respective gradient $G_{1,0}$, $G_{3,0}$, $G_{5,0}$ and $G_{7,0}$ in the two precession chambers. On the other hand, the $|d_{n \leftarrow Hg}^{false}(G_{2,0})|$, $|d_{n \leftarrow Hg}^{false}(G_{4,0})|$ and $|d_{n \leftarrow Hg}^{false}(G_{6,0})|$ correspond to the absolute value of the mercury false motional EDM produced respectively by the gradient $G_{2,0}$, $G_{4,0}$ and $G_{6,0}$ in only one precession chamber (because they cancel if we consider both chambers). Their expression is given in the Table 2.2.

Design Procedure

These coils and the B_0 coil share the same symmetries with respect to the XZ and YZ plan. For this reason, it was decided to use the same support frame to install all of them ($G_{1,0}$, $G_{2,0}$, $G_{3,0}$ and B_0 coils). Since the wires cannot be at the same location, the $G_{1,0}$, $G_{2,0}$ and $G_{3,0}$ wires will be inserted between adjacent B_0 wires. According to the B_0 coil geometry, this offers 180 possible locations. Then, for each position, the field produced by the corresponding single loop was simulated and decomposed into gradients. The goal was to search for the most appropriate combination of loops which produces the gradient of interest. For each loop two current direction are possible.

This task is simplified by the symmetries of the expected field which are also present in the current. The field can be symmetric or antisymmetric with respect to the $z=0$ plan. Thus

we can define "symmetric pairs", made of two loops symmetric one to the other with respect to the $z=0$ plan, with the same current direction. In the same way we define "antisymmetric pairs" if the currents direction in the wires are opposed. Because of their field symmetries, we deduced that the $G_{2,0}$ has to be composed of symmetric pairs, and the $G_{1,0}$ and $G_{3,0}$ coils have to be composed of antisymmetric pairs. As a result, only pairs of loops were simulated. Since the magnetic field produced by the pairs of loops add linearly, it is possible to write :

$$\vec{B}_{tot} = \sum_n \vec{B}_n(I_n), \quad (4.5)$$

where $\vec{B}_n(I_n)$ is the field created by the n^{th} pair of loop with a current I_n . The total field is then decomposed into gradients and the criteria defined in Eq. 4.2 is computed. This calculation is performed for all combinations of n pairs with $n \leq 4$ due to computation load. Solutions for which no wire crosses the entrance door are privileged when it is possible. This limits the number of door connectors (mechanical constraint) and ensure a better field reproducibility. The design of the $G_{1,0}$, $G_{2,0}$ and $G_{3,0}$ coil are presented below. A more complete description of their design (loops position, current direction, produced gradients) is given in Appendix E.

$G_{1,0}$ coil design

The $G_{1,0}$ coil is made of two pairs of antisymmetric wires. The $d_{ratio}(G_{1,0})$ obtained from the COMSOL simulation is larger than $d_{ratio}(G_{1,0}) > 5000$. The requirement is fulfilled. The Fig 4.2 shows in the left panel the $G_{1,0}$ coil design.

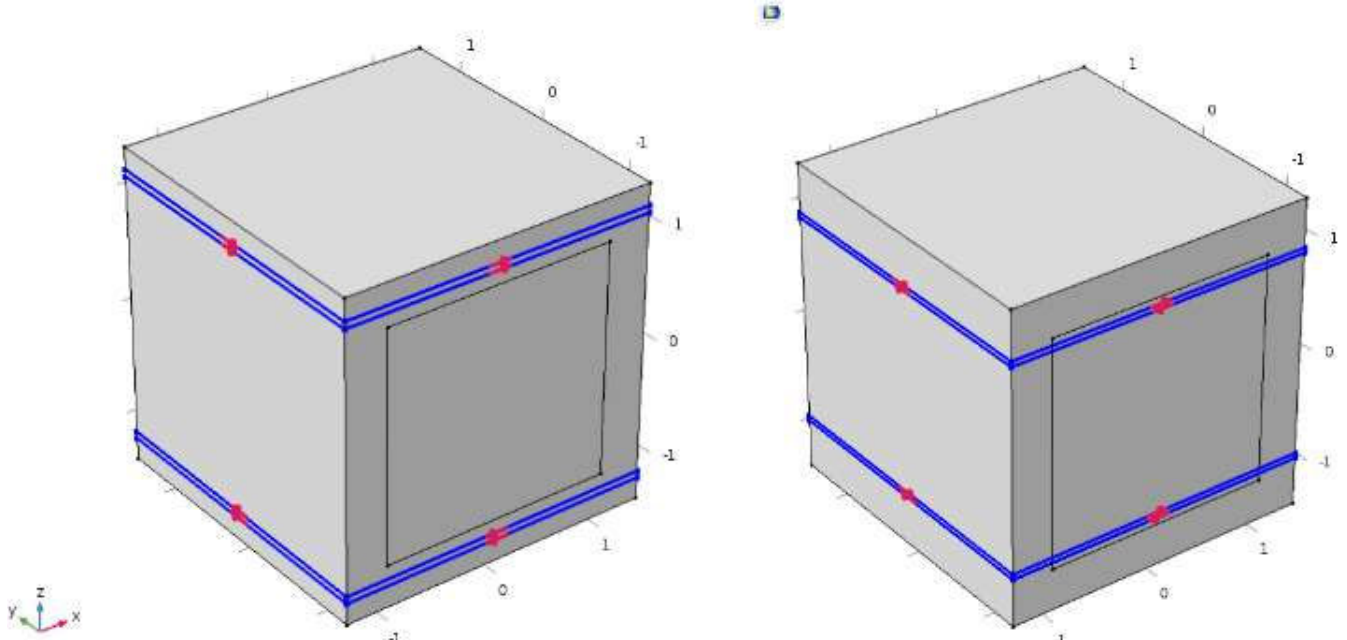


Figure 4.2 – Design of the $G_{1,0}$ coil in the left panel and $G_{3,0}$ coil in the right panel. The central square on the front face represents the entrance door.

The resolution of the power supply should be less than 500 nA^2 . It corresponds to a $G_{1,0}$ resolution of $G_{1,0} = 0.012 \text{ pT/cm}$, which is under the required resolution of 0.1 pT/cm asked for the top-bottom matching condition.

2. specifications from the Confluence specification sheet

G_{2,0} coil design

The G_{2,0} coil is made of 3 pairs of symmetric wires. The d_{ratio} computed from the COMSOL simulation is higher than $d_{ratio}(G_{2,0}) > 200$. The Fig 4.3 shows the G_{2,0} coil design.

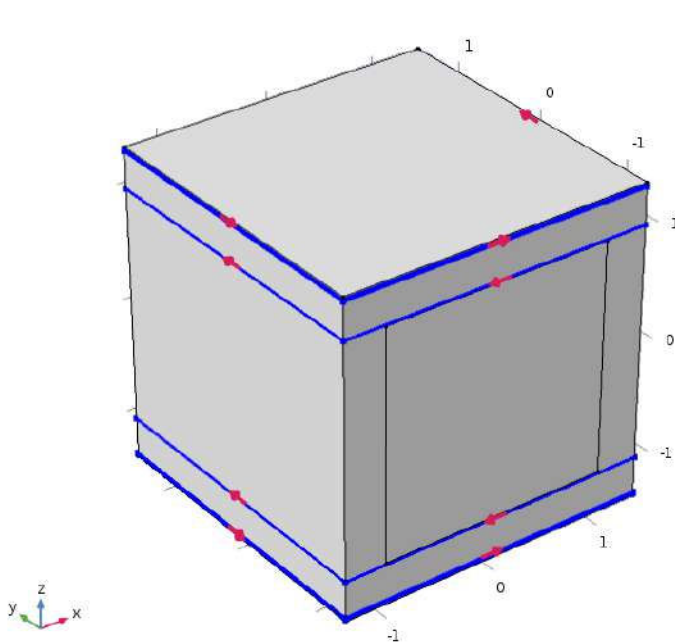


Figure 4.3 – Design of the G_{2,0} coil.

G_{3,0} coil design

The G_{3,0} coil is made of 2 pairs of antisymmetric wires. The d_{ratio} obtained for the COMSOL simulation is higher than $d_{ratio}(G_{3,0}) > 60$. Unfortunately, no solution with wires not crossing the entrance door has been found. The Fig 4.2 shows the G_{3,0} coil design in the right panel.

4.2.3 Design of G_{1,-1} and G_{1,1} coil

The Cesium magnetometers array is composed of about a 100 Cs magnetometers, dispatched above and below the precession chamber (see section 2.3.5). It has to measure the spatial distribution of the field modulus. Therefore it is very important to precisely know the position of the Cs magnetometers. This can be done mechanically. Moreover, to ensure the knowledge of their position directly for the outside, the collaboration chose to use G_{1,1} and G_{1,-1} coils to probe the position with respect to the precession chambers of the Cesium Magnetometers. The relation between the field components and the gradients G_{1,1} and G_{1,-1} are given by :

$$\begin{aligned} B_x(G_{1,-1}) &= 0 & B_x(G_{1,1}) &= z \cdot G_{1,1} \\ B_y(G_{1,-1}) &= z \cdot G_{1,-1} & \text{and} & \\ B_z(G_{1,-1}) &= y \cdot G_{1,-1} & B_y(G_{1,1}) &= 0 \\ & & B_z(G_{1,1}) &= x \cdot G_{1,1} \end{aligned} \quad (4.6)$$

In a horizontal plan defined by z, it is therefore possible by measuring the B_z component to scan the x and y coordinates. The G_{1,1} and G_{1,-1} coils produce their corresponding field,

every single magnetometers measures it and their position is derived from this measurement. The linearity of the relation between B_z and the gradients presents the advantage to be easy to interpret. Since the $G_{1,1}$ and $G_{1,-1}$ coils presents the same symmetries once they are rotated by $\pi/2$, only the $G_{1,1}$ coil case will be presented in the rest of this section.

Two issues need to be considered. The first issue comes from the Cs magnetometers performances : they are only able to measure the magnetic field modulus. This issue can be solved for the $G_{1,1}$ ($G_{1,-1}$) coil. The measured field is:

$$B = \sqrt{B_x^2(G_{1,1}) + B_z^2(G_{1,1})} = G_{1,1} \sqrt{x^2 + z^2}. \quad (4.7)$$

Thus for each support plan of the Cs magnetometers (defined by a constant height z), one can extract w with the relation:

$$x = \sqrt{\left(\frac{B}{G_{1,1}}\right)^2 - z^2}. \quad (4.8)$$

The height z of the plate is then treated as a constant offset. For the higher order gradients, the B_x and B_y components also depends of x and y . Which leads us to the second issue: it is not possible to avoid the presence of other gradients which share the same symmetries as $G_{1,1}$ (the gradient $G_{3,1}$ for instance). The strategy is to consider the unwanted fields due to the additional gradients as a misreading on the position of the Cs magnetometers. Considering only the B_z component, one writes:

$$B_z(x) = B_z^{G_{1,1}}(x) + B_z^{G_{other}}(x) = G_{1,1} \cdot (x + dx), \quad (4.9)$$

where dx represents the position misreading. dx is then measured for each Cs magnetometers. Their position can vary at most between -40 cm and 40 cm on the x direction. The standard deviation $\sigma(dx)$ of the misreading position dx is then used to define a criteria. The upper limit for $\sigma(dx)$ is given by:

$$\sigma(dx) < 1 \text{ mm} \quad (4.10)$$

The goal is then to find the most appropriate design which minimize $\sigma(dx)$. The study has been performed for several height z . The minimal height of the Cs magnetometers is $z=17$ cm (in this case, the Cs magnetometer is laying on the electrode) and the maximal height at $z=45$ cm [81].

The table 4.2 shows the spread $\sigma(dx)$ of the misreading position dx computed for several height z and for the optimal design.

CsM height [cm]	17	21	25	29	33	37	41	45
$\sigma(dx)$ [mm]	0.23	0.31	0.48	0.20	0.72	1.04	1.51	2.19

Table 4.2 – $\sigma(dx)$ calculated for several CsM height z .

The optimal coil design fulfills the requirement up to $z=37$ cm : for $z < 37$ cm the linearity between the measured field and the x coordinate is achieved. For $z > 37$ cm, this is not anymore the case. This only means that the relation between the measured field and the position is anymore linear. It will be however possible from the map of the coil to get back to the magnetometers position, which requires a high level of reproducibility between both measurement.

The Fig. 4.4 shows the $G_{1,1}$ coil optimal design. It is composed of three quatuor of wires. The two largest coils have been adapted to bypass the entrance door. The detailed design is given in Appendix E.

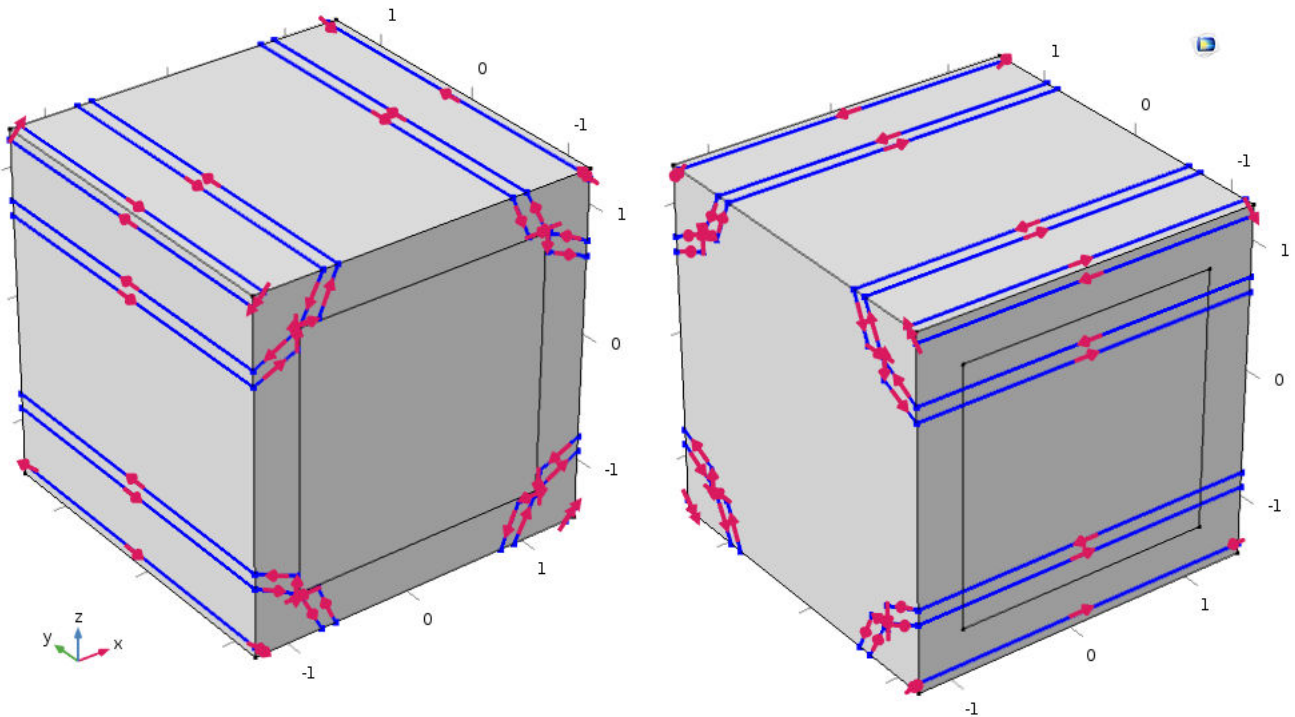


Figure 4.4 – Design of the $G_{1,1}$ coil (on the left) and $G_{1,-1}$ coil (on the right). The central square in the front face represents the entrance door.

The main parameter of the $G_{1,1}$ coil loops is the parameter a , which corresponds to the distance between the loop and axis x (or y for $G_{1,-1}$), shown in Fig. 4.5. Similarly to $G_{1,0}$, $G_{2,0}$ and $G_{3,0}$ coils, the optimisation was done by simulating the field created by a coil composed of $n < 4$ quatuors, varying the parameters a and the current direction. We computed then $\sigma(dx)$ for each simulation and for different height z . The optimal coil design minimizes $\sigma(dx)$. It is made of three quatuors of wires.

The $G_{1,-1}$ coil will be the same as the $G_{1,1}$, rotated by 90 degrees. It means that this coil has no choices but to cross the door, and will require 2 connectors. The $G_{1,0}$ coil will be used to measure the z component of the Cs magnetometers. Using the same procedure as for the $G_{1,1}$ coil, it has been shown that it is able to measure this position with a standard deviation $\sigma(dz) < 1$ mm.

4.2.4 Design of $G_{0,-1}$ and $G_{0,1}$ coils

The $G_{0,1}$ and $G_{0,-1}$ coils have to produce a static transverse field respectively B_x and B_y up to 300 pT with a uniformity below 1% in order to create a transverse field strong enough to probe the light shift effect [82]. Their design is based on the Helmholtz coils concept. Several pairs of coils were simulated with COMSOL. The number of pairs and their position were varied to achieve the best uniformity in a central volume of 1 m³ using the "optimisation" module on COMSOL. For the $G_{0,1}$ coil the minimization of $\sqrt{B_y^2 + B_z^2}$ is performed to find the optimal position of the loops. For the $G_{0,-1}$ coil, this optimal position is found by minimizing $\sqrt{B_x^2 + B_z^2}$.

The optimized design for the $G_{0,1}$ coil consists of two pairs of coils, located at $x = \pm 1121$ mm and $x = \pm 359.1$ mm. It creates a field $B_x = 1.7$ nT/mA with a uniformity $\sigma(B_x) = 0.09$ pT. The $G_{0,-1}$ coil is exactly the same as the $G_{0,1}$ one but rotated by 90 degrees.

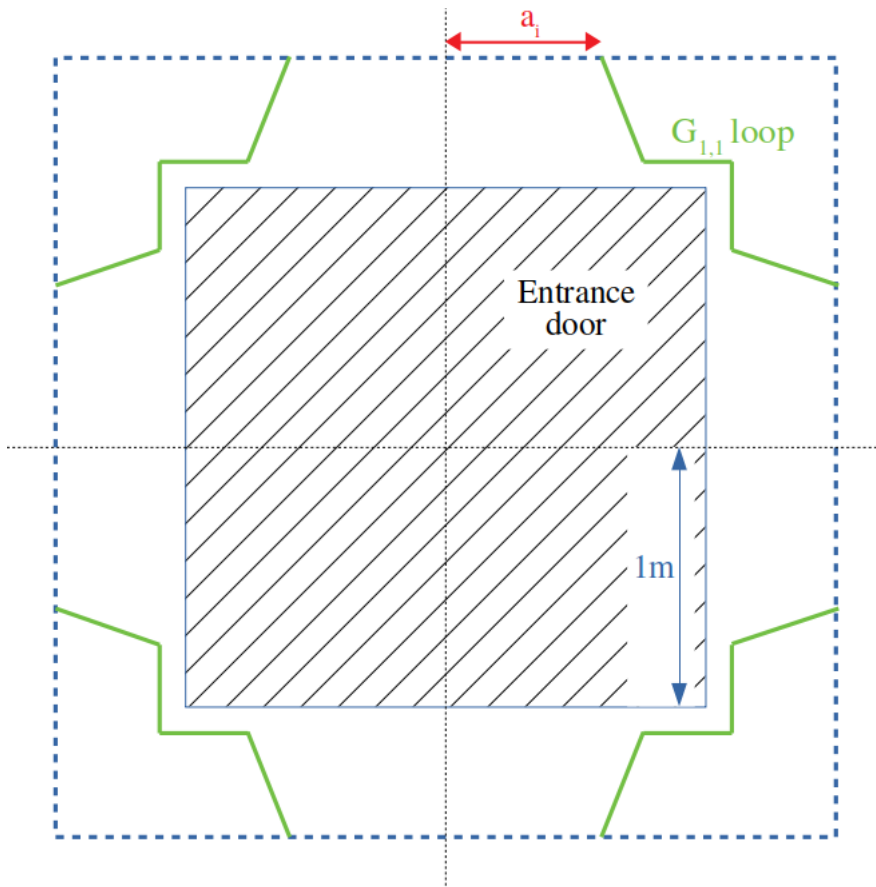


Figure 4.5 – Scheme of one $G_{1,1}$ loop, which bypasses the door.

The design of the two coils are shown in Fig. 4.6.

4.3 Technical design

As for B_0 , the correcting coils will be made of a 1.8 mm diameter copper wire glued in a 2 mm groove made in polycarbonate plates. Because the $G_{1,0}$, $G_{2,0}$ and $G_{3,0}$ Harmonic coils share the same symmetry as the B_0 coil, they will be installed on the same frame.

Then, closer to the vacuum chamber, a second layer will be mounted. It is made of the harmonic coils $G_{1,1}$, $G_{1,-1}$, $G_{0,1}$ and $G_{0,-1}$. This second layer is shown in yellow in the top figure of Fig. 4.7 . It comports many holes in order to reduce its weight. Finally, a third layer, the innermost one, will be installed to support the TRIM Coil array, shown in the bottom figure of Fig. 4.7.

Conclusion

This chapter started by the presentation of the design and the performance of the TRIM coil array. It consists of 56 squared coils which are able to correct for large B_0 field non-uniformities. Then the chapter presents the Harmonic coils, a set of seven coils dedicated to the production of specific gradients with several purposes. All of them fulfils their own purpose. Their design are also shown. Finally, this chapter ended by looking at the technical design of the correcting coils.

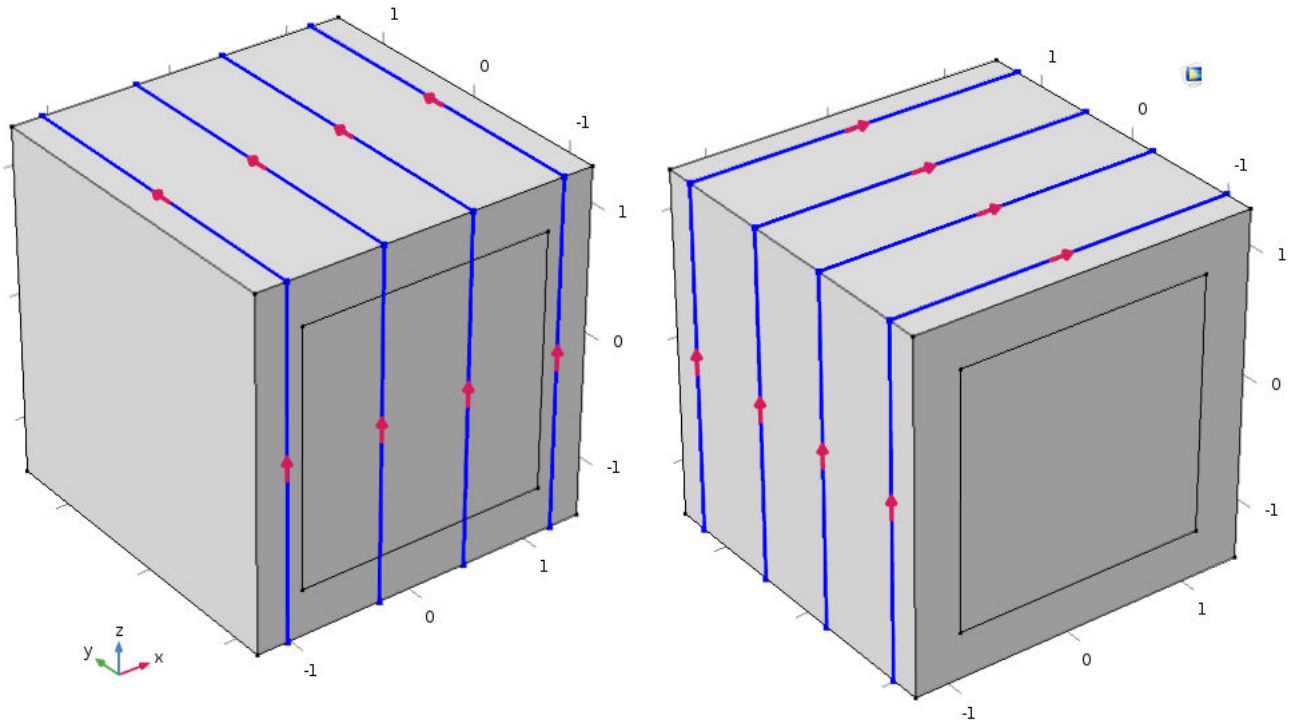


Figure 4.6 – $G_{0,1}$ coil design (on the left) and $G_{0,-1}$ coil design (on the right). The central square on the front face represents the door entrance.

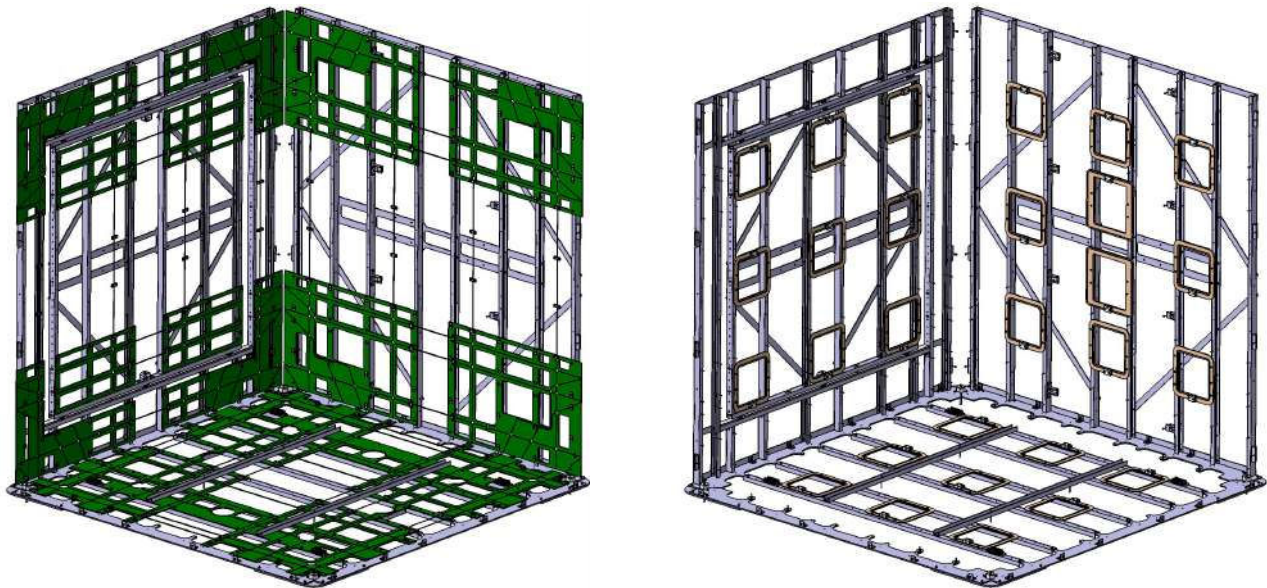


Figure 4.7 – Correcting coil technical design. The green layer in the top figure corresponds to the polycarbonate plates supporting the Harmonic coils $G_{1,1}$, $G_{1,-1}$, $G_{0,1}$ and $G_{0,-1}$. The squares in the bottom figures shows the plates holding the TRIM coil array.

Influence and constraints on magnetic dipoles

Contents

5.1	Motional EDM produced by a single magnetic dipole	91
5.2	The nEDM experiment case	93
5.2.1	Residual EDM produced by the dipole in the nEDM case	93
5.3	The n2EDM experiment case	95
5.3.1	Residual EDM produced by the dipole in the n2EDM case	95
5.3.2	Constraints on the magnetic moment	95

Introduction

As presented in section 2.2.4, a systematic motional EDM arises from the presence of magnetic dipoles. This motional EDM is of the order of magnitude of the measurement goal. This is why it must be kept under control. This chapter focus on this subject, describing first the EDM produced by a single dipole for the nEDM and n2EDM experiments. Then will be defined some constraints on the dipole moments for the n2EDM case.

5.1 Motional EDM produced by a single magnetic dipole

A dipole with a magnetic moment \vec{m} creates a field $\vec{B}(\vec{r})$ at a distance \vec{r} :

$$\vec{B}(\vec{r}) = \frac{\mu_0}{4\pi} \left[\frac{3\vec{r}(\vec{m} \cdot \vec{r})}{r^5} - \frac{\vec{m}}{r^3} \right] \quad (5.1)$$

To have an idea of the order of magnitude of the produced field , let's study a dipole located at the origin of the coordinate system (x,y,z) with a magnetic moment \vec{m} aligned along the z axis $m_z = 1 \text{ nA.m}^2$. This dipole creates the field components ($B_x = 0.1 \text{ pT}$, $B_y = 0.1 \text{ pT}$, $B_z = 0.2 \text{ pT}$) at the point M(x=0 cm, y=0 cm, z=10 cm).

The horizontal components B_x and B_y produce a false motional EDM which can be computed with (see section 2.2.4 and [83]):

$$d_{dip} = -\frac{\hbar|\gamma_n\gamma_{Hg}|}{2c^2} \langle xB_x^{dip} + yB_y^{dip} \rangle, \quad (5.2)$$

where the quantity $\langle xB_x^{dip} + yB_y^{dip} \rangle$ is averaged on the precession volume chamber. This false EDM is partly corrected by the crossing point analysis procedure (see section 2.2.3). This procedure allows to perform the EDM measurement at zero vertical gradient $\partial_z B_z = 0$. Therefore,

the false EDM contribution coming from the vertical gradient is suppressed. At first order, the false motional EDM is corrected by:

$$d_{\text{correction}} = \frac{\hbar |\gamma_n \gamma_{Hg}|}{2c^2} \frac{R^2}{4} \left\langle \frac{\partial B_z^{\text{dip}}}{\partial z} \right\rangle. \quad (5.3)$$

The constraint on the presence of magnetic dipole is then derived from the calculation of the residual false EDM, defined as:

$$\begin{aligned} d_{\text{res}} &= d_{\text{dip}} - d_{\text{correction}} \\ d_{\text{res}} &= -\frac{\hbar |\gamma_n \gamma_{Hg}|}{2c^2} \left(\langle xB_x^{\text{dip}} + yB_y^{\text{dip}} \rangle + \frac{R^2}{4} \left\langle \frac{\partial B_z^{\text{dip}}}{\partial z} \right\rangle \right). \end{aligned} \quad (5.4)$$

One may notice that the linear dependency of the field \vec{B} with respect to the magnetic moment strength m is transferred to the false motional EDM.

Indeed, we can write the quantities $\langle xB_x^{\text{dip}} + yB_y^{\text{dip}} \rangle$ and $\langle \partial B_z^{\text{dip}} / \partial z \rangle$ for a dipole located at (x_d, y_d, z_d) using Eq. 5.1. We get:

$$\begin{aligned} \langle xB_x^{\text{dip}} + yB_y^{\text{dip}} \rangle &= \frac{\mu_0}{4\pi} \iiint dx dy dz \left[\left(\frac{3x(x-x_d)[(x-x_d)m_x + (y-y_d)m_y + (z-z_d)m_z]}{r^5} - \frac{m_x}{r^3} \right) \right. \\ &\quad \left. + \left(\frac{3y(y-y_d)[(x-x_d)m_x + (y-y_d)m_y + (z-z_d)m_z]}{r^5} - \frac{m_y}{r^3} \right) \right] \\ \langle \partial B_z^{\text{dip}} / \partial z \rangle &= \frac{-3\mu_0}{4\pi} \iiint dx dy dz \left[\left(\frac{2m_z(z-z_d)^3 + 4[m_x(x-x_d) + m_y(y-y_d)](z-z_d)^2}{r^7} \right) \right. \\ &\quad \left. - \left(\frac{3m_z[(x-x_d)^2 + (y-y_d)^2](z-z_d)}{r^7} \right. \right. \\ &\quad \left. \left. + \frac{[(x-x_d)^2 + (y-y_d)^2][m_x(x-x_d) + m_y(y-y_d)]}{r^7} \right) \right] \end{aligned}$$

Assuming a magnetic moment aligned along x, y or z axis simplifies those equations. In these cases the corresponding magnetic moment m_x , m_y and m_z can be factorised. As an example, with a magnetic moment aligned along the z axis, we have:

$$\langle xB_x^{\text{dip}} + yB_y^{\text{dip}} \rangle = \frac{\mu_0}{4\pi} m_z \iiint dx dy dz \left[\left(\frac{3x(x-x_d)(z-z_d)}{r^5} \right) + \left(\frac{3y(y-y_d)(z-z_d)}{r^5} \right) \right] \quad (5.5)$$

$$\langle \partial B_z^{\text{dip}} / \partial z \rangle = \frac{-3\mu_0}{4\pi} m_z \iiint dx dy dz \left[\left(\frac{2(z-z_d)^3}{r^7} \right) - \left(\frac{3[(x-x_d)^2 + (y-y_d)^2](z-z_d)}{r^7} \right) \right] \quad (5.6)$$

Thus, the residual EDM is linearly dependent of m_z :

$$\begin{aligned} d_{\text{res}} &= -\frac{\hbar |\gamma_n \gamma_{Hg}|}{2c^2} \frac{\mu_0}{4\pi} m_z \left(\iiint dx dy dz \left[\left(\frac{3x(x-x_d)(z-z_d)}{r^5} \right) + \left(\frac{3y(y-y_d)(z-z_d)}{r^5} \right) \right] \right. \\ &\quad \left. - \frac{3R^2}{4} \iiint dx dy dz \left[\left(\frac{2(z-z_d)^3}{r^7} \right) - \left(\frac{3[(x-x_d)^2 + (y-y_d)^2](z-z_d)}{r^7} \right) \right] \right). \end{aligned}$$

As a result, the false EDM produced by a dipole of 100 nA.m² is half of the one produced by a dipole of 200 nA.m² (assuming the same position and orientation).

5.2 The nEDM experiment case

5.2.1 Residual EDM produced by the dipole in the nEDM case

For sake of simplicity, let's first study the nEDM experiment case. It was also studied in [80]. The Fig. 5.1 and Fig. 5.2 show the false motional EDM d_{dip} and d_{res} computed for the nEDM experiment. They are plotted as a function of the dipole position in two different planes. The precession chamber has a diameter of 47 cm and a height of 12 cm. It is centered on the origin of the coordinate system (shown in white in the figure). The magnetic moment is aligned along the z axis $m_z = 10 \text{ nA.m}^2$ in Fig. 5.1 and along the x axis $m_x = 10 \text{ nA.m}^2$ in Fig. 5.2. For each figure, four panels are shown:

- The top-left panel shows the false EDM d_{dip} created by the dipole in the XZ plane ($y=0 \text{ m}$).
- The top-right panel shows the residual false EDM d_{res} in the XZ plane ($y=0 \text{ m}$).
- The bottom-left panel shows the false EDM d_{dip} created by the dipole in the XY plane at ($z=0 \text{ m}$).
- The bottom-right panel shows the residual false EDM d_{res} in the XY plane at ($z=0 \text{ m}$).

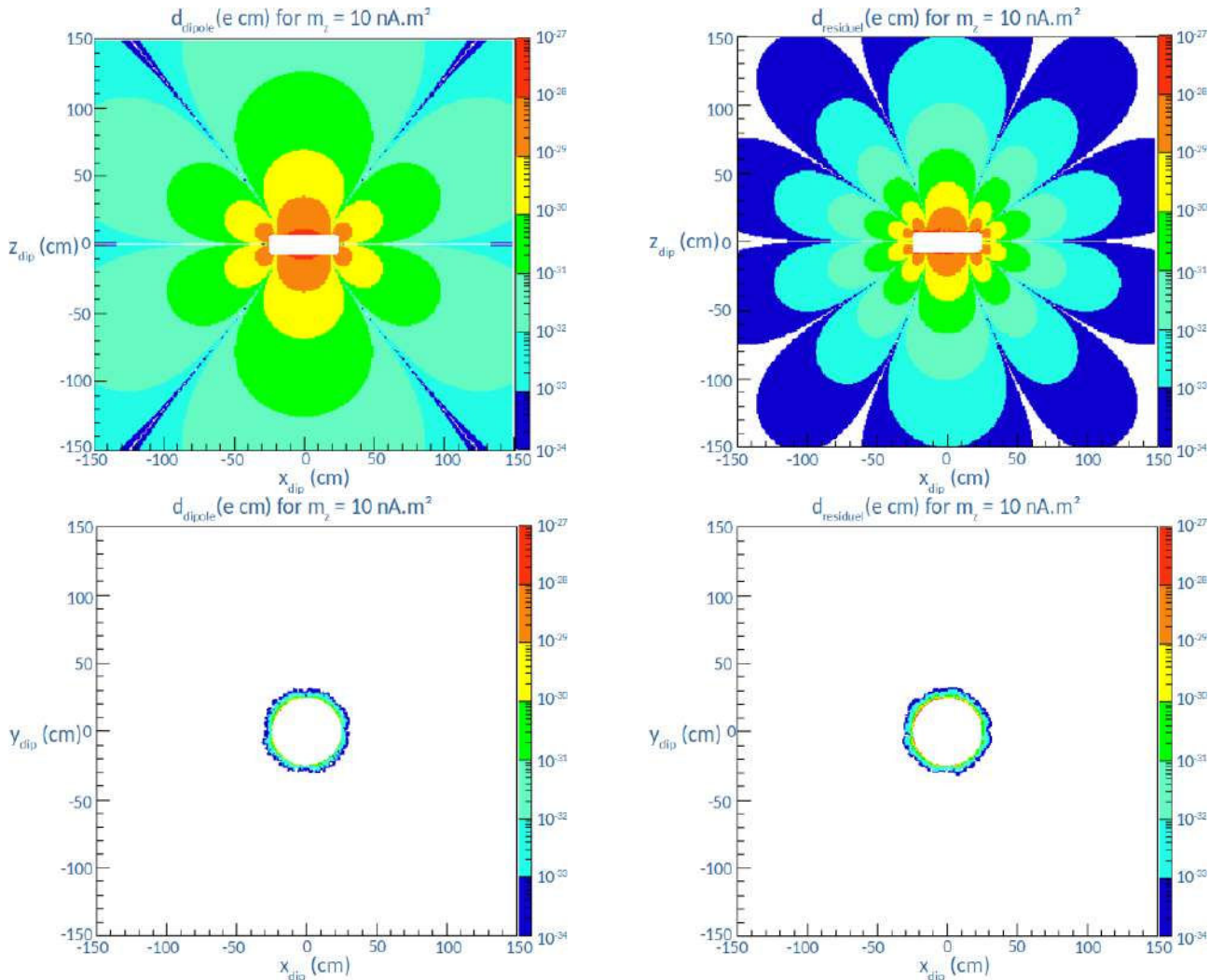


Figure 5.1 – The false EDM d_{false}^{dip} (left panels) and the residual EDM d_{res} induced by a dipole of a strength of $m = m_z = 10 \text{ nA.m}^2$ in the XZ plane (top panels) and the XY plane (bottom panels). The white rectangles (or circle) corresponds to the precession chamber.

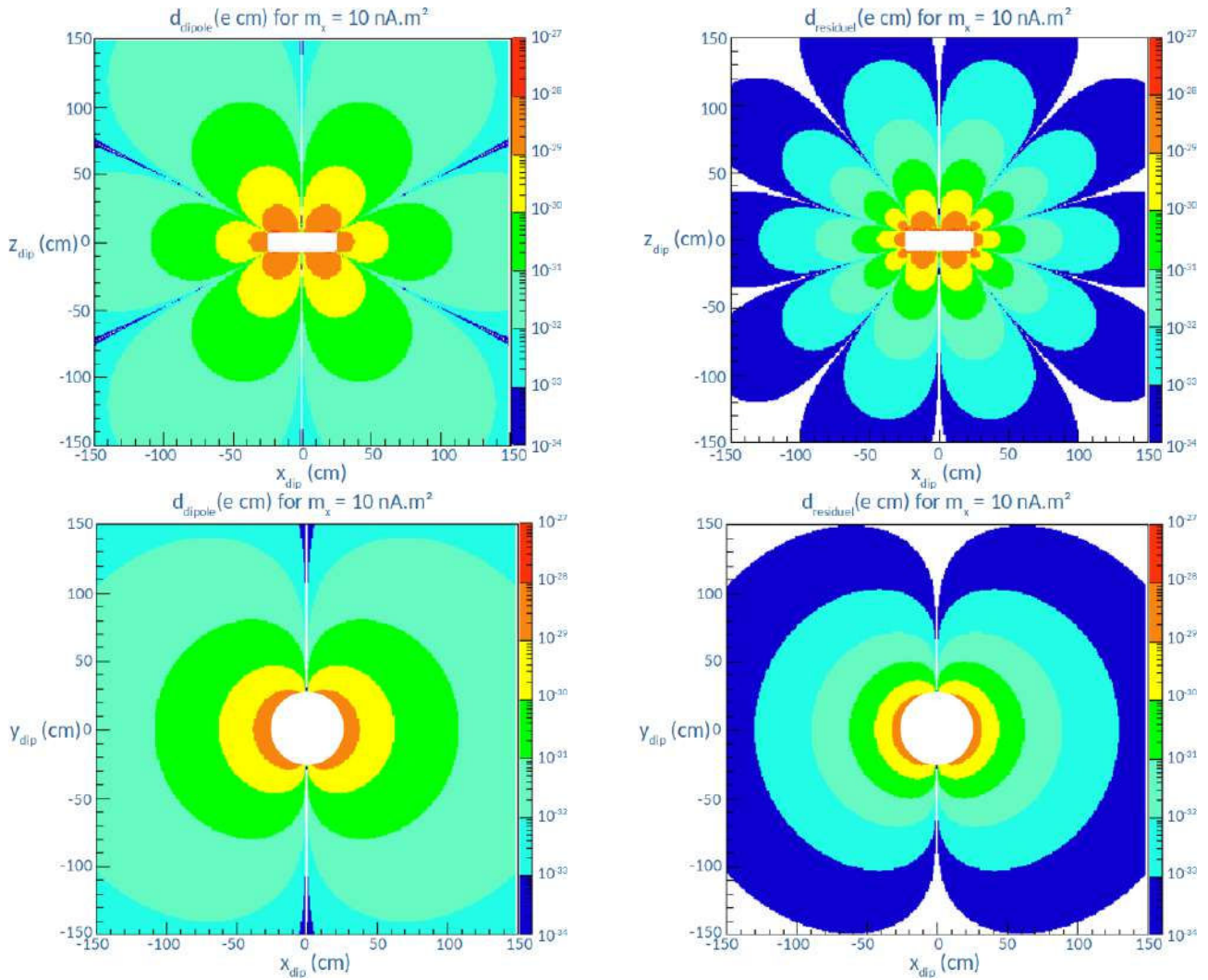


Figure 5.2 – The false EDM d_{false}^{dip} (left panels) and the residual EDM d_{res} (right panels) induced by a dipole of a strength of $m = m_x = 10 \text{ nA.m}^2$ in the XZ plane (top panels) and the XY plane (bottom panels). The small white rectangle (or circle) corresponds to the precession chamber.

As we can see, the residual EDM d_{res} is lower by about a factor 10 compared to the false EDM d_{dip} created by a dipole. The residual EDM created by a dipole located further than 50 cm from the center of the chamber is below 10^{-30} e cm . However, around the electrode this residual EDM is about 10^{-28} e cm , which is not that far from the range of the EDM measurement. The bottom panels of 5.1 shows an interesting result: the false EDM is below 10^{-34} e cm almost everywhere (it corresponds to the white area). It can be understood by looking at the Eq. 5.5 and Eq. 5.6 with $z_d = 0$. In such a case, the quantity $\langle xB_x^{dip} + yB_y^{dip} \rangle$ is proportional to:

$$\langle xB_x^{dip} + yB_y^{dip} \rangle \propto \int_{-H/2}^{H/2} zdz = \frac{(H/2)^2 - (-H/2)^2}{2} = 0 \quad (5.7)$$

and the quantity $\langle \partial B_z^{dip} / \partial z \rangle$ is proportional to:

$$\langle xB_x^{dip} + yB_y^{dip} \rangle \propto \int_{-H/2}^{H/2} (z^3 - z) dz = \frac{(H/2)^4 - (-H/2)^4}{4} - \frac{(H/2)^2 - (-H/2)^2}{2} = 0. \quad (5.8)$$

Both of those quantities equal zero, leading to a null EDM.

5.3 The n2EDM experiment case

5.3.1 Residual EDM produced by the dipole in the n2EDM case

In n2EDM, the EDM can be estimated from the average of the top and bottom chambers EDM as shown in Eq. 2.8. The false EDM due to a local dipole becomes :

$$\begin{aligned} d_{dip} &= \frac{d_{dip}^T + d_{dip}^B}{2} \\ &= -\frac{\hbar|\gamma_n\gamma_{Hg}|}{2c^2} \frac{\langle xB_x^{dip} + yB_y^{dip} \rangle^T + \langle xB_x^{dip} + yB_y^{dip} \rangle^B}{2}. \end{aligned} \quad (5.9)$$

The estimation of the EDM correction $d_{correctioon}$ takes advantage of the use of the two chambers. The vertical gradient will be estimated with the two Hg comagnetometer i.e. by measuring the difference of the volumic average of the B_z component in each chamber (see section 2.2.3). As a result, Eq. 5.4 becomes:

$$d_{res} = -\frac{\hbar|\gamma_n\gamma_{Hg}|}{2c^2} \left[\frac{\langle xB_x^{dip} + yB_y^{dip} \rangle^T + \langle xB_x^{dip} + yB_y^{dip} \rangle^B}{2} + \frac{R^2}{4} \frac{\langle B_z \rangle^T - \langle B_z \rangle^B}{H'} \right] \quad (5.10)$$

The left panels of Fig. 5.3 show the false EDM d_{dip} created by a dipole with a magnetic moment aligned along the z axis with a strength $m = m_z = 10 \text{ nA.m}^2$. The residual EDM d_{res} is shown on the right panels. Again, the correction leads to a residual EDM d_{res} about 10 times lower than the EDM d_{dip} created by the dipole. The top panels show the computed EDM when the dipole is located in XZ plan ($y=0 \text{ cm}$), and the bottom panels show the same calculation but in the XY plan ($z = 8.5 \text{ cm}$). The same calculation with a dipole characterized by a magnetic moment $m_x = 10 \text{ nA.m}^2$ aligned along the x axis are shown in Fig. 5.4.

5.3.2 Constraints on the magnetic moment

From this study it is possible to define the constraint on the maximum allowed dipole strength. to quantify the systematic effect produced by a single dipole.

First a maximum false EDM has to be defined. It is called d_{target} . Thus the strength \vec{m} of the dipole producing such a false EDM, d_{target} , can be studied.

The procedure to extract the strength of the magnetic moment \vec{m} is:

- $\langle xB_x^{dip} + yB_y^{dip} \rangle$ and $\frac{\partial B_z^{dip}}{\partial z}$ are calculated for a given dipole strength (10 nA.m^2 for instance).
- The corresponding d_{res} is computed.
- The calculation is repeated as a function of the dipole locations.
- The location where the false EDM is the largest is identified.
- The dipole strength producing a false EDM d_{target} at this location is linearly computed.

The Table 5.1 gives the positions of a dipole either located on the B_0 coil or the vacuum tank with a strength of 10 nA.m^2 which produces the largest false EDM d_{dip} as well as the largest residual EDM d_{res} . The constraint on the magnetic moment strength of the dipole is set with a false EDM $d_{target} = 1 \times 10^{-28} \text{ e cm}$. It is reported in the last column of Table 5.1.

As we can see, the minimum value allowed for a dipole located on the vacuum tank is about 1431 nA.m^2 , and about 56306 nA.m^2 if it is located on the B_0 coil. Assuming N dipoles with a random orientation, a random location either on the vacuum tank or on the B_0 coil, and producing individually the same false EDM d_{dip} , the total produced false EDM can be estimated to be $\sqrt{N} \cdot d_{max}$. If their orientations are the same, which can occurs if they are magnetised for example, the total produced false EDM is $N \cdot d_{max}$. Therefore the magnetic

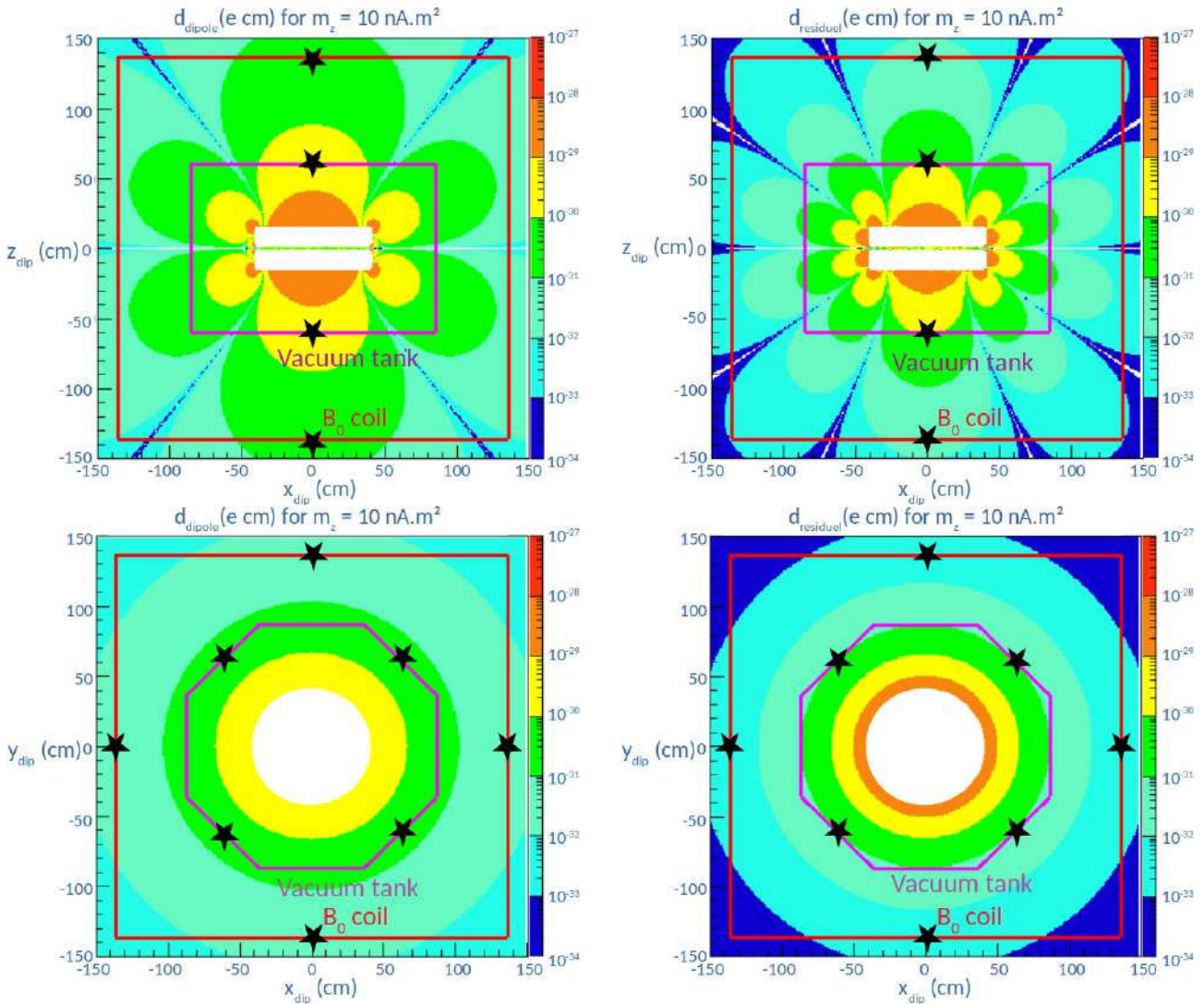


Figure 5.3 – The false EDM d_{dip} produced by a magnetic dipole of strength $m = m_z = 10 \text{ nA.m}^2$ is drawn in the top left panel as a function of the dipole position in the XZ plane ($y=0$ m). In the top right panel, the residual EDM d_{res} is shown in the same plane. In the bottom panels are shown the same quantities in the XY plane, at $z=8.5$ cm (corresponding to the center of the precession chamber). The large red rectangle corresponds to the B_0 coil while the large violet rectangle (or octagon) shows the vacuum tank. The white rectangles (or circles) corresponds to the precession chambers. The stars corresponds to the location of the dipole which produces the largest false EDM with such a strength.

constraint on 100 dipoles localised on the vacuum tank corresponding to a residual false EDM between $1431/\sqrt{100} = 143.1 \text{ nA.m}^2$ and $1431/100 = 14.31 \text{ nA.m}^2$. In order to avoid such dipole moments, the collaboration is controlling each piece of the n2EDM apparatus. At PTB for instance, the pieces are magnetized with a magnet, then probed using SQUIDS inside a magnetic shielded room, demagnetized, and probed again. The field before and after the demagnetisation is then compared to the magnetic constraints established here.

Conclusion

A magnetic dipole with a magnetic moment \vec{m} creates a local magnetic field which echoes in a false EDM. That EDM is partially corrected by the crossing point technique in

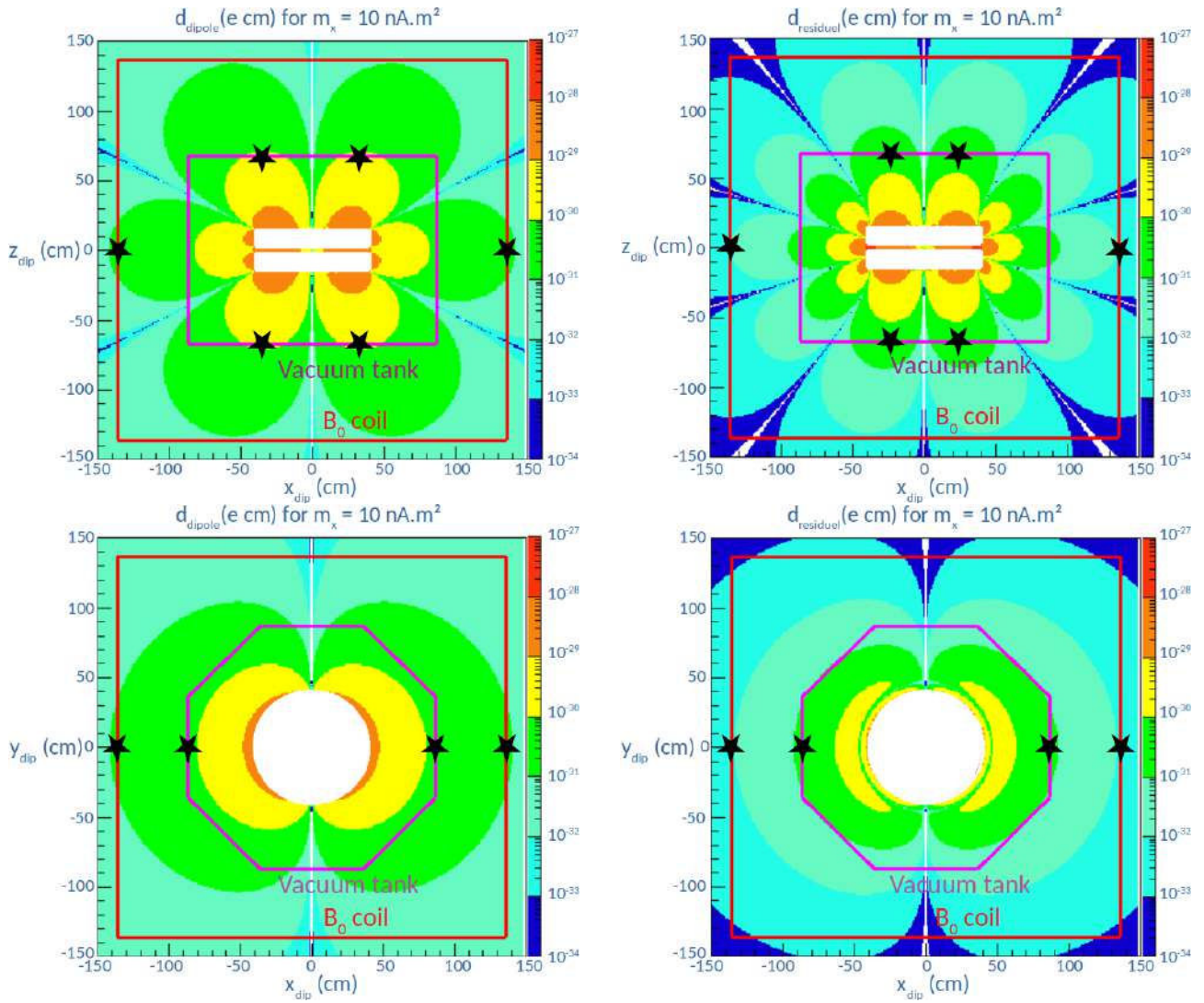


Figure 5.4 – The false EDM d_{dip} produced by a magnetic dipole of strength $m = m_x = 10 \text{ nA} \cdot \text{m}^2$ is drawn in the top left panel as a function of the dipole position in the XZ plane ($y = 0 \text{ m}$). In the top right panel the residual EDM d_{res} is shown in the same plane. In the bottom panels are shown the same quantities on the XY plane, at $z = 8.5 \text{ cm}$ (corresponding to the center of the precession chamber). The large red rectangle corresponds to the B_0 coil while the large violet rectangle (or octagon) shows the vacuum tank. The white rectangles (or circles) corresponds to the precession chambers. The stars corresponds to the location of the dipole which produces the largest false EDM with such a strength.

nEDM and by the G_{TB} gradient in n2EDM. The resulting residual EDM can be computed depending on the location of the dipole and it strength. This has been done for the nEDM and n2EDM cases. Because of the linearity between the residual EDM and the magnetic moment, one can set a limit on the dipole magnetic moment strength. For the n2EDM experiment in the worst case, a residual EDM is obtained with a magnetic moment about $1500 \text{ nA} \cdot \text{m}^2$ if the dipole is localised on the vacuum chamber and about $55000 \text{ nA} \cdot \text{m}^2$ if localised on the B_0 coil. This is a constraint on a single magnetic dipole.

$\mathbf{m}_x = 10 \text{ nA.m}^2$		x (cm)	y (cm)	z (cm)	max EDM (e cm)	m_{limit} (nA.m ²)
Vacuum tank	d_{dip}	33	0	67	1.21×10^{-30}	828
	d_{res}	-24	0	-67	3.59×10^{-31}	2788
B_0 coil	d_{dip}	136	0	0	1.19×10^{-31}	8375
	d_{res}	-136	0	0	9.76×10^{-33}	102406
$\mathbf{m}_z = 10 \text{ nA.m}^2$		x (cm)	y (cm)	z (cm)	max EDM (e cm)	m_{limit} (nA.m ²)
Vacuum tank	d_{dip}	0	0	67	2.51×10^{-30}	398
	d_{res}	0	0	-67	6.99×10^{-31}	1431
B_0 coil	d_{dip}	0	0	136	2.01×10^{-31}	5000
	d_{res}	0	0	-136	1.78×10^{-32}	56306

Table 5.1 – Maximum false EDM d_{dip} and residual EDM d_{res} from a dipole located either on vacuum chamber or on the B_0 coil for two orientation: the upper table corresponds to a magnetic moment aligned along the x axis, and the bottom table to a magnetic moment aligned along the z axis. The strength of the magnetic dipole moment which produces a false EDM of $1 \times 10^{-28} \text{ e cm}$ is given in the last column.

Conclusion

The purpose of this thesis is to work on the design of the coil system for the n2EDM experiment. This experiment intends to lower the upper limit of the nEDM to the $10^{-27} - 10^{-28}$ $e\text{cm}$ range. It requires to improve the magnetic field uniformity and to reduce the systematic errors.

The design of the B_0 coil which must produce the main vertical magnetic field of the experiment has been presented. The B_0 coil produces a field of $1 \mu\text{T}$ with a field uniformity $\sigma(B_z) < 170 \text{ pT}$ using a current of 11.94 mA . However, mechanical imperfections creates field non-uniformities that might be dangerous. Among the studied imperfections, the most critical is a vertical misalignment of the B_0 coil with respect to the shield, which must be under 0.25 mm . A map campaign during the coil installation is planned to avoid such misalignment.

In order to correct the non-uniformities of the B_0 field, a set of 56 coils, called TRIM coils array has been studied. It has been shown that they are able to correct for huge non-uniformities in the foreseen range of current. The experiment requires also several coils which must produce specific gradients. The $G_{1,0}$, $G_{2,0}$ and $G_{3,0}$ coils are mainly designed to correct the corresponding gradient, in order to fulfill the requirements such as the top-bottom matching condition or the mercury motional false EDM. The $G_{1,1}$ and $G_{1,-1}$ coils must be able to measure the Cesium magnetometers position with a standard deviation below 1 mm . Finally, the $G_{0,1}$ and $G_{0,-1}$ coils must be able to produce a static transverse field of 300 pT . The optimized design of each of those coils have been shown. They all fulfills their requirements.

Finally, a study on the influence of a magnetic dipole has been done in the nEDM and n2EDM cases. Indeed, the presence of a magnetic dipole creates a systematic error called motional EDM. This study allows us to give some constraints on the magnetic moment of the dipole depending of its position. For the n2EDM case, if it is located on the vacuum tank, the dipole magnetic moment must be lower than 1400 nA.m^2 in order to limit the associated effect to $1 \times 10^{-28} e\text{cm}$, and lower than 56300 nA.m^2 if it is located on the B_0 coil.

In addition of the coil system studied in this thesis, the n2EDM will benefit of several improvement. The most noticeable is the use of two large chambers (instead of one in n2EDM), in order considerably improve the number of neutrons and so the statistical sensitivity. The electric field is also improved, as well as the control of the magnetic field mainly due to a 6 layers magnetic shielded room, and its monitoring, performed by two types of magnetometers: the mercury magnetometers and the Cesium magnetometers. It should allow the experiment to probe the $10^{-27} e\text{cm}$, and open the perspective to an improved version of n2EDM, with two larger rooms with a diameter of 100 cm , and a "magic" magnetic field around $10 \mu\text{T}$ for which the main systematic effect, the motional EDM is highly suppressed. Such improvements might allow to reach the $10^{-28} e\text{cm}$ and therefore probe the physics beyond the standard model.

Deuxième partie

La partie Française

Introduction

Depuis plus de 60 ans, la recherche du moment dipolaire électrique du neutron (nEDM) est resté un sujet fondamental. Un tel EDM, qui peut également exister dans d'autres systèmes, tel que les électrons, les atomes et les molécules par exemple, est la signature d'une nouvelle source de violation des symétries de conjugaison de charge et de parité (CP), qui est une des conditions de Sakharov permettant d'expliquer la prédominance de la matière sur l'antimatière dans l'univers. De plus, si cette propriété est prédite avec une valeur de $10^{-31}\text{--}10^{-32}$ $e\text{ cm}$ par le modèle standard, les extensions de celui-ci lui prévoit une valeur plus grande, pouvant atteindre 10^{-28} $e\text{ cm}$. Bien que la limite actuelle sur la mesure du nEDM est de $d_n < 3 \times 10^{-26}$ $e\text{ cm}$ (90% C.L.), les expériences dans quelques années à venir seront capables de sonder la gamme du 10^{-28} $e\text{ cm}$, et ainsi commencer à contraindre les extensions du modèle standard.

Cette thèse prend place entre l'expérience nEDM à l'institut Paul Scherrer, qui va publier une nouvelle limite supérieure du nEDM en 2019, et l'expérience n2EDM, future projet de la collaboration nEDM, qui vise à explorer le nEDM autour de $10^{-27}\text{--}10^{-28}$ $e\text{ cm}$. Ces deux projets utilisent pour ce faire des neutrons ultra-froids polarisés qui sont stockés dans une chambre de précession soumise à un champ électrique et à un champ magnétique. En utilisant la méthode des champs oscillants séparés de Ramsey et en comptant le nombre de neutrons dans chaque état de spin, on peut mesurer l'EDM du neutron. Cependant, n2EDM bénéficie d'un équipement amélioré, et utilise deux chambre de précession au lieu d'une seule.

Le travail présenté ici explique en détail les investigations menées sur le design du système de bobines de l'expérience n2EDM. En effet, la production et le contrôle du champ magnétique constitue le cœur de l'expérience. Les contraintes sur l'uniformité et la stabilité du champ magnétique sont extrêmement sévère. Elles sont directement liées à la sensibilité statistique de la mesure et également à plusieurs effets systématiques. La relation entre la polarisation des neutrons et le faux EDM $v \times E$ sera présenté dans ce document.

Dans le premier chapitre, les motivations de la recherche du nEDM sont exposées. Il introduit aussi les neutrons ultra-froids et leurs propriétés, ainsi que leur interaction avec un champ magnétique.

Le second chapitre présente le principe de la mesure, ainsi que les exigences sur la production du champ magnétique. Il se conclut par une présentation de l'appareillage expérimental de l'expérience n2EDM.

Le troisième chapitre est dédié à la bobine B_0 qui doit produire le champ magnétique principal de l'expérience. Le logiciel COMSOL utilisé pour les simulations est décrit, puis le design et les performances de la bobine B_0 sont montrés. Enfin, ce chapitre décrit l'influence sur le champ de plusieurs imperfections mécaniques, et se termine en présentant le design technique de la bobine. Le quatrième chapitre présente les bobines de corrections. Elles correspondent au

TRIM coils array, un set de 56 bobines devant corriger les non-uniformités du champ magnétique B_0 , et aux bobines Harmoniques (sept bobines) dédiés à la production de gradients spécifiques purs. Le design technique des bobines de corrections est également montré.

Enfin, le dernier chapitre s'intéresse à l'étude du faux EDM $v \times E$ produit par des dipôles magnétiques pour les expériences nEDM et n2EDM. Des contraintes sur leurs moments sont données dans le cas de l'expérience n2EDM.

Motivations

Motivations Physiques

L'asymétrie matière-antimatière

Le modèle standard de la physique des particules (SM) est celui étant le plus complet et décrivant le mieux les interactions fondamentales à ce jour. Son pouvoir prédictif a été éprouvé de nombreuses fois, et a mené à d'importantes découvertes, comme celle du boson de Higgs en 2012 [5, 6]. Cependant ce modèle reste imparfait, et de nombreuses problématiques n'y trouvent pas de solutions.

La problématique nous concernant est celle de l'asymétrie matière-antimatière. Supposons qu'aux premiers instants de l'univers, la création de matière et d'antimatière est un processus symétrique. Or, lorsque matière et antimatière se rencontrent, ils s'annihilent pour créer des photons. Au bout d'un certain temps, les quantités égales de matière et d'antimatière auraient donc dûs entièrement s'annihiler, et faire de l'univers un océan de lumière. Ce qui n'est pas le cas : l'antimatière est absente de l'univers, mis à part celle créée au CERN, et la matière domine, composant tout le reste jusqu'aux mains qui écrivent ces lignes. Pour expliquer cela, il faut donc supposer une asymétrie matière-antimatière, dont l'excédant de matière initiale correspond aujourd'hui à l'ensemble de l'univers connu. Cette asymétrie est mesurable, et est définie comme :

$$\eta = \frac{n_B - n_{\bar{B}}}{n_\gamma}, \quad (1.1)$$

où n_B , $n_{\bar{B}}$ and n_γ représentent respectivement la quantité de matière, antimatière et gamma dans l'univers.

Cette asymétrie a été mesurée en regardant le fond diffus cosmologique du satellite Planck [11] et l'abondance des noyaux légers dans l'univers [10], s'accordant sur la valeur de

$$\eta = 6.09(6) \times 10^{-10}. \quad (1.2)$$

Cependant, les prédictions du Modèle Standard de la physique des particules ne prévoient qu'une asymétrie de $\eta \simeq 10^{-19}$, soit neuf ordres de grandeur en dessous de celle mesurée expérimentalement. Il nous faut donc trouver de nouvelles sources permettant de combler ce manque d'asymétrie.

Les conditions de Sakharov

En 1967, Andreï Sakharov énonça trois conditions nécessaires et suffisantes pour expliquer l'asymétrie matière-antimatière [2] :

1. **La violation du nombre baryonique B** qui permet des réactions avec un état initial $B = 0$ à un état final $B \neq 0$, rendant possible une surabondance de la matière sur l'antimatière ;
2. **Une phase de non-équilibre thermique**, sans laquelle les réactions favorisant la production de matière serait contrebalancée par celles favorisant la production d'antimatière ;
3. **La violation des symétries C et CP** qui favorise la production de matière sur l'antimatière.

Cette troisième condition est pour nous la plus importante, puisque le moment dipolaire électrique est un marqueur de violation CP dans de nombreux systèmes, y compris le neutron.

Moment dipolaire électrique et violation CP

Dans un cadre classique, le moment dipolaire électrique est le signe d'une séparation des charges positive et négative d'un système, et de sa capacité à se polariser sous l'influence d'un champ électrique. Il est défini comme :

$$\vec{d} = q \cdot \vec{r}, \quad (1.3)$$

où q est la valeur de la charge électrique ; et \vec{r} est la distance séparant les pôles négatif et positif.

Pour une particule, le moment dipolaire électrique est une propriété intrinsèque, interagissant avec le champ électrique, et (pour les particules de spin 1/2) est orienté selon le spin de la particule, comme le prévoit le théorème Wigner-Eckart, décrit dans l'annexe A.

L'hamiltonien d'une particule possédant un Moment Dipolaire électrique \vec{d} (EDM) non-nul soumis à un champ électrique \vec{E} est :

$$H = -\vec{d} \cdot \vec{E} \quad (1.4)$$

Or, sous des transformations de symétries de parité P ou de temps T, cet hamiltonien devient :

$$H_P = -\vec{d} \cdot (-\vec{E}) = -H \xleftarrow{P} H = -\vec{d} \cdot \vec{E} \xrightarrow{T} H_T = -(-\vec{d}) \cdot \vec{E} = -H \quad (1.5)$$

L'hamiltonien n'est pas conservé par ses transformations. L'existence d'un moment dipolaire électrique constitue dans ce cas une source de violation C et CP (qui correspond à une violation de T car l'invariance de CPT doit être respectée [17, 18]) et de ce fait contribue à l'asymétrie matière-antimatière.

En 1950 Purcell et Ramsey suggèrent une expérience pour mesurer le moment dipolaire électrique du neutron [1], qu'ils réalisent en compagnie de Smith en 1957, aboutissant à la première limite sur ce moment dipolaire électrique $|d_n| < 5 \times 10^{-20} e.cm$ [19].

Neutrons ultra-froids et moment dipolaire électrique du neutron.

Le neutron est un candidat intéressant pour chercher le moment dipolaire électrique. Tout d'abord il est sensible aux interactions faible et forte, et permet de sonder la violation CP dans ces deux secteurs. Ensuite parce qu'il est neutre, ce qui ne camoufle pas l'interaction de son EDM avec un champ électrique. De plus, étant de spin 1/2, l'orientation de son spin (sur lequel son moment électrique dipolaire et son moment magnétique sont alignés) peut être manipulé en utilisant des champs magnétiques, ce dont la méthode de mesure de l'EDM tire profit. Enfin il est possible d'utiliser des neutrons ultra-froids qui permettent un long temps de précession.

Depuis 1980, les expériences utilisent des neutrons ultra-froids (UCN). Ceux-ci sont caractérisé par leur énergie, inférieure à 300 neV, ce qui correspond à une température en dessous

de 3.5 mK, d'où leur appellation, et a une longueur d'onde au-delà de 52.2 nm. Cette large longueur d'onde, supérieure à la distance inter-atomique permet au neutron d'interagir non pas avec un, mais une multitude d'atome, ce qui peut être vu comme une barrière de potentiel. La valeur de ce potentiel dépend du matériau, de sa composition et densité, et est nommé potentiel de Fermi V_F .

La probabilité de réflexion et de transmission d'un UCN sur cette barrière est obtenue en résolvant l'équation de Schrödinger :

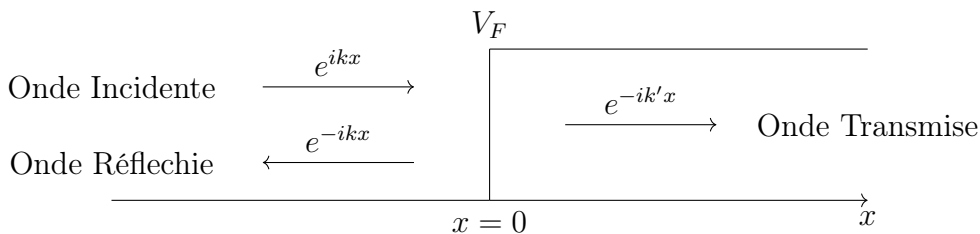
$$\frac{-\hbar^2}{2m_n} \Delta \psi + V\psi = E\psi, \quad (1.6)$$

avec une potentiel "marche" non-nul pour $x > 0$:

$$\begin{cases} V = 0 & x < 0 \\ V = V_F - iW & x > 0 \end{cases} \quad (1.7)$$

où la partie imaginaire W corresponds au potentiel d'absorption du matériau qui quantifie la probabilité de l'UCN d'être absorbé par ce matériau si son énergie est inférieure à V_F . On trouve alors les probabilités de réflexion dépendante de la composante transverse de l'énergie du neutron (par rapport à la paroi) E_\perp :

$$\begin{cases} R^2 = \left(\frac{\sqrt{E_\perp} - \sqrt{E_\perp - V}}{\sqrt{E_\perp} + \sqrt{E_\perp - V}} \right)^2 & E_\perp > V_F \\ |R|^2 = 1 - \frac{2W}{V_F} \sqrt{\frac{E_\perp}{V_F - E_\perp}} & E_\perp < V_F \end{cases} \quad (1.8)$$



Ainsi en utilisant des matériaux adaptés, il est possible de stocker des neutrons ultra-froids.

Due à la faible énergie des UCN, la gravité joue aussi un rôle important. En effet, un neutron prenant de l'altitude perd :

$$m_n \cdot g \cdot z = 102.6 \cdot z \text{ neV/m} \quad (1.9)$$

Cela signifie qu'un UCN avec une énergie de 300 neV peut atteindre une hauteur maximum de 3 m. C'est un processus utile pour contrôler l'énergie des neutrons en faisant varier leur altitude. Il permet également de ce fait un stockage vertical des UCN. Une autre conséquence qui aboutit à un effet systématique dans l'expérience nEDM, est que le centre de masse des neutrons est différent du centre de la chambre où ils sont stockés (de quelque millimètres pour nEDM).

Expériences sur le moment dipolaire électrique du neutron

L'usage des Neutrons ultra-froids dans les expériences EDM a permis deux changements importants : tout d'abord il permet de passer d'une expérience faisceau à une expérience où les neutrons sont stockés. Cela présente un avantage puisque la mesure de l'EDM est liée à l'accumulation d'une phase sur la fréquence de précession du neutron. Or, plus le temps de

précession est grand, plus grand cette phase est. Ensuite, l'usage d'UCN a permis de rendre négligeable l'effet systématique dominant : un faux EDM du au champ magnétique du neutron traversant à une vitesse \vec{v}_n un champ électrique \vec{E} , proportionnel à $\vec{v}_n \times \vec{E}$.

La limite la plus récente sur l'EDM du neutron est attribué à la collaboration RAL-Sussex-ILL obtenue en 2006 (revue en 2015) est et de $|d_n| < 3.0 \times 10^{-26} e\text{cm}$ (90% C.L.) [22, 3].

Neutron ultra-froid et champ magnétique

Le neutron interagit avec le champ magnétique grâce à son moment magnétique $\mu_n = -9.6623650(23) \times 10^{-27} J/T$ [58], souvent exprimé lorsqu'on travaille avec des UCN comme $\mu_n \simeq 60.3 \text{ neV}/T$. De plus, ce moment magnétique est aligné sur le spin du neutron, celui-ci étant de spin 1/2. L'interaction du neutron avec un champ magnétique \vec{B} peut donc se transcrire à travers son hamiltonien :

$$\hat{H} = -\vec{\mu}_n \cdot \vec{B} = -\gamma_n \hat{\vec{S}} \cdot \vec{B} \quad (1.10)$$

Polarisation des neutrons

Cela peut être mis à profit pour manipuler la polarisation des UCN. Comme le montre la Fig. 1.1, on peut appliquer dans une région donnée un champ magnétique. Le potentiel à franchir dépend alors de l'orientation relative du spin du neutron et du champ magnétique. Avec un champ de 5T, les neutrons avec un spin anti-parallèle au champ magnétique doivent traverser une région avec un potentiel de -300 neV, ce dont ils sont capables. En revanche, si leur spin est parallèle au champ magnétique, alors cette région a un potentiel de +300 neV, supérieur à l'énergie de la plupart des UCN, qui ne peuvent donc pas traverser. En définitive, seul les neutrons avec la composante de spin anti-parallèle au champ magnétique ont pu traverser, ce qui correspond à une polarisation par transmission.

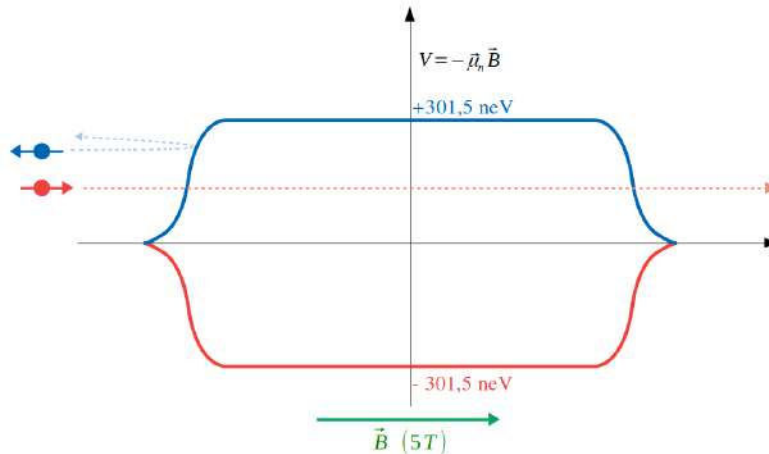


FIGURE 1.1 – Polarisation par transmission des UCN en utilisant un champ magnétique fort.

Evolution du spin du neutron dans un champ magnétique uniforme

Considérons tout d'abord la fonction d'onde du spin du neutron :

$$|\Psi(t)\rangle = \begin{pmatrix} a(t) \\ b(t) \end{pmatrix} = \begin{pmatrix} A(t)e^{i\Phi(t)} \\ B(t)e^{i\theta(t)} \end{pmatrix} \quad (1.11)$$

avec $\langle \Psi(t) | \Psi(t) \rangle = A(t)^2 + B(t)^2 = 1$.

Sous l'effet d'un champ magnétique vertical uniforme $\vec{B} = B_0 \vec{u}_z$, l'hamiltonien du neutron devient :

$$\hat{H} = -\gamma_n \hat{\vec{S}} \cdot \vec{B} = -\gamma_n \hat{S}_z B_0 = -\gamma_n B_0 \frac{\hbar}{2} \hat{\sigma}_z, \text{ où } \hat{\sigma}_z = \begin{pmatrix} 1 & 0 \\ 0 & -1 \end{pmatrix} \text{ est une matrice de Pauli. (1.12)}$$

L'évolution temporelle du spin du neutron s'étudie en utilisant l'équation de Schrödinger :

$$i\hbar \frac{\partial |\Psi(t)\rangle}{\partial t} = \hat{H} |\Psi(t)\rangle, \quad (1.13)$$

La résolution de cette équation en posant les conditions initiales $a(0) = a_0$ et $b(0) = b_0$ donne :

$$|\Psi(t)\rangle = \begin{pmatrix} a_0 e^{-\frac{i\omega_0}{2}t} \\ b_0 e^{\frac{i\omega_0}{2}t} \end{pmatrix}. \quad (1.14)$$

avec $\omega_0 = -\gamma_n B_0$.

On peut donc déduire la probabilité de trouver le spin du neutron selon la direction x,y et z au bout d'un temps t :

$$|\langle z | \Psi(t) \rangle|^2 = A_0^2. \quad (1.15)$$

$$|\langle x | \Psi(t) \rangle|^2 = \frac{1}{2} + A_0 B_0 \cos(\omega_0 t + \theta - \Phi) \quad (1.16)$$

$$|\langle y | \Psi(t) \rangle|^2 = \frac{1}{2} - A_0 B_0 \cos(\omega_0 t + \theta - \Phi) \quad (1.17)$$

Cela décrit un mouvement circulaire du spin dans le plan horizontal, appelé précession de Larmor, tandis que sa composante verticale reste constante au cours du temps. Ce procédé permet donc de conserver la polarisation du neutron selon une direction et est utilisé dans l'expérience nEDM par les bobines de guidage.

Evolution du spin du neutron avec un champ tournant supplémentaire

On ajoute au champ uniforme un champ $\vec{B}_c(t)$ tournant dans le plan XY avec une fréquence angulaire ω et une phase ϕ . Le champ total est ainsi décrit par :

$$\vec{B} = \vec{B}_0(t) + \vec{B}_c(t) = B_c \cos(\omega t + \phi) \vec{u}_x + B_c \sin(\omega t + \phi) \vec{u}_y + B_0 \vec{u}_z, \quad (1.18)$$

et le hamiltonien du neutron devient :

$$\hat{H} = -\gamma_n B_c \frac{\hbar}{2} \cos(\omega t + \phi) \hat{\sigma}_x - \gamma_n B_c \frac{\hbar}{2} \sin(\omega t + \phi) \hat{\sigma}_y - \gamma_n B_0 \frac{\hbar}{2} \hat{\sigma}_z, \quad (1.19)$$

où $\hat{\sigma}_x = \begin{pmatrix} 0 & 1 \\ 1 & 0 \end{pmatrix}$ et $\hat{\sigma}_y = \begin{pmatrix} 0 & -i \\ i & 0 \end{pmatrix}$ complètent le set des matrice de Pauli.

Encore une fois, résoudre l'équation de Schrödinger nous donne l'évolution temporelle du spin du neutron, et nous permet de trouver les probabilités de présence de ce spin selon les axes x,y et z en supposant un état initial $a_0 = e^{i\phi}$ et $b_0 = 0$:

$$|\langle z | \Psi(t) \rangle|^2 = \cos^2(\Omega t) + \frac{(\omega - \omega_0)^2}{4\Omega^2} \sin^2(\Omega t), \quad (1.20)$$

$$|\langle x | \Psi(t) \rangle|^2 = \frac{1}{2} - \frac{(\omega - \omega_0)\omega_c}{4\Omega^2} \cos(\omega t + \phi) \sin^2(\omega t) + \frac{\omega_c}{2\Omega} \sin(\omega t + \phi) \cos(\Omega t) \sin(\Omega t), \quad (1.21)$$

$$|\langle y | \Psi(t) \rangle|^2 = \frac{1}{2} + \frac{(\omega - \omega_0)\omega_c}{4\Omega^2} \sin(\omega t + \phi) \sin^2(\omega t) + \frac{\omega_c}{2\Omega} \cos(\omega t + \phi) \cos(\Omega t) \sin(\Omega t), \quad (1.22)$$

avec $\omega_0 = -\gamma_n B_0$, $\omega_c = -\gamma_n B_c$ et $\Omega = \frac{\sqrt{(\omega_c^2 + (\omega - \omega_0)^2)}}{2}$.

A la résonance $\omega = \omega_0$, ces équations deviennent :

$$|\langle z | \Psi(t) \rangle|^2 = \cos^2\left(\frac{\omega_c}{2}t\right) \quad (1.23)$$

$$|\langle x | \Psi(t) \rangle|^2 = \frac{1}{2} + \sin(\omega t + \phi) \cos\left(\frac{\omega_c}{2}t\right) \sin\left(\frac{\omega_c}{2}t\right), \quad (1.24)$$

$$|\langle y | \Psi(t) \rangle|^2 = \frac{1}{2} + \cos(\omega t + \phi) \cos\left(\frac{\omega_c}{2}t\right) \sin\left(\frac{\omega_c}{2}t\right), \quad (1.25)$$

Ces équations décrivent toujours un mouvement circulaire dans le plan XY, accompagné d'une transition entre spin up et spin down de la composante z du spin, comme le montre la Fig. 1.12 à différentes étapes de son évolution. En prenant comme champ uniforme $B_0 = 1 \mu\text{T}$ et comme champ tournant $B_c = 8.5 \text{ nT}$, cette transition s'effectue en 4 secondes. Cela signifie aussi qu'arrêter le champ tournant B_c au bout de 2 secondes amène le spin dans le plan orthogonal au champ B_0 , et permet au neutron de précesser librement.

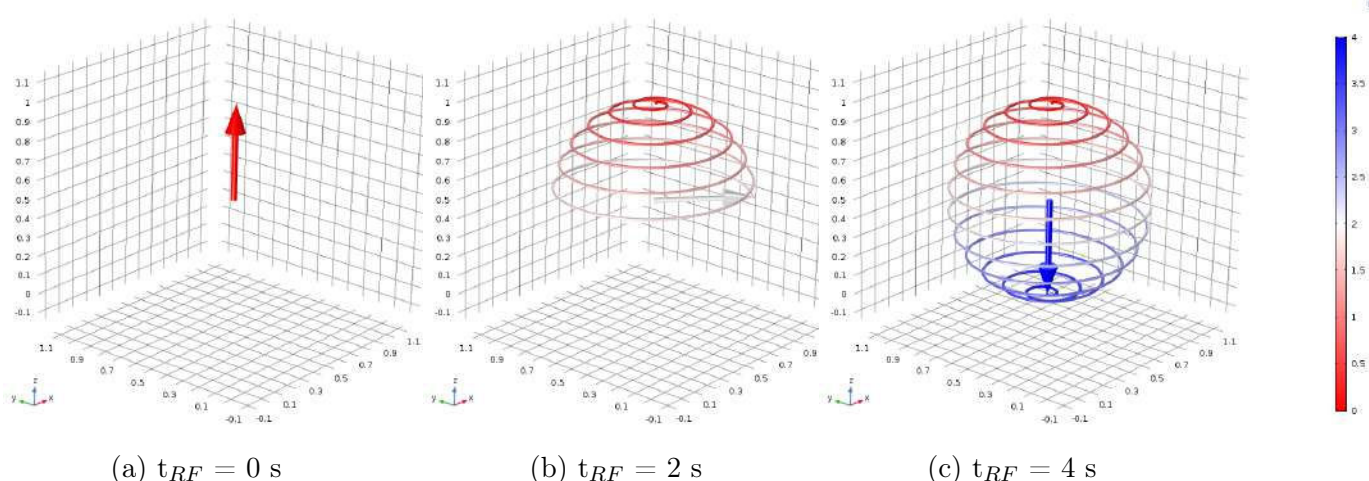


FIGURE 1.2 – Evolution du spin sous un champ tournant $B_c = 8.5 \text{ nT}$ et un champ uniforme $B_0 = 1 \mu\text{T}$ à la résonance $\omega = \omega_0$. La polarisation initiale à $t=0 \text{ s}$ du neutron est longitudinale (spin up) (à gauche). Après 2 s, il devient transverse (au centre). Le spin du neutron peut ainsi précesser librement si le champ tournant n'est plus appliqué. Sinon, après 4 s de champ tournant, le spin est totalement renversé et la polarisation du neutron est de nouveau longitudinale (mais dans l'état spin down).

L'expérience nEDM @ PSI

L'expérience n2EDM prend place suite à l'expérience nEDM. Cette dernière a débuté en 2005 à l'ILL et a été poursuivie en 2009 à PSI où le spectromètre OILL a été transféré. Après la phase de commissionnement et quelques améliorations du spectromètre, les données ont été récoltées entre 2015 et 2016. Cette expérience permettra l'établissement d'une nouvelle limite sur l'EDM du neutron qui devrait être publiée en 2019, avec une sensibilité statistique de l'ordre de $1 \times 10^{-26} e\text{ cm}$. L'expérience n2EDM vise à réduire cette sensibilité d'un facteur 10 d'ici à 2025. Ensuite une seconde phase de n2EDM est prévue pour sonder la gamme du $10^{-28} e\text{ cm}$.

Principe de la mesure

Le principe de la mesure de l'EDM du neutron prend avantage de l'interaction de celui-ci avec les champs magnétique et électrique au travers de son moment magnétique μ_n et de son potentiel moment dipolaire électrique d_n . En présence de ces deux champs, le hamiltonien du neutron est :

$$H = -\vec{\mu}_n \cdot \vec{B} - \vec{d}_n \cdot \vec{E}, \quad (2.1)$$

où, du fait du spin 1/2 du neutron, μ_n et d_n sont alignés sur celui-ci. Ainsi, le niveau d'énergie du neutron dépend de l'orientation de son spin vis-à-vis de l'orientation des champs électrique et magnétique, comme le montre la Fig. 2.1. Ces champs peuvent être entre eux parallèles ou anti-parallèles.

Pour chaque configuration, la fréquence de Larmor peut être extraite : ν_{\parallel} pour la configuration parallèle et ν_{\perp} pour la configuration anti-parallèle. La différence de ces deux fréquences nous donne accès à l'EDM du neutron :

$$|d_n| = \left| \frac{h(\nu_{\parallel} - \nu_{\perp}) + 2\mu_n(B_{\parallel} - B_{\perp})}{2(E_{\parallel} - E_{\perp})} \right|. \quad (2.2)$$

En utilisant le même champ magnétique dans les deux configurations, et un champ électrique dont seul le signe change, Eq. 2.2 devient :

$$|d_n| = \left| \frac{-h(\nu_{\parallel} - \nu_{\perp})}{4E} \right|. \quad (2.3)$$

Tandis que le champ électrique possède une stabilité bien définie, le champ magnétique quand à lui nécessite une procédure complexe qui constitue le cœur de l'expérience. Les exigences sur sa stabilité et son uniformité sont donc très sévères.

La méthode utilisée pour mesurer la fréquence de Larmor des neutrons dans les configurations parallèle et anti-parallèle est appelée méthode des champs oscillant séparés de Ramsey ;

$$\mathcal{H} = -\mu_n \cdot \vec{B} \cdot \vec{s} - d_n \cdot \vec{E} \cdot \vec{s}$$

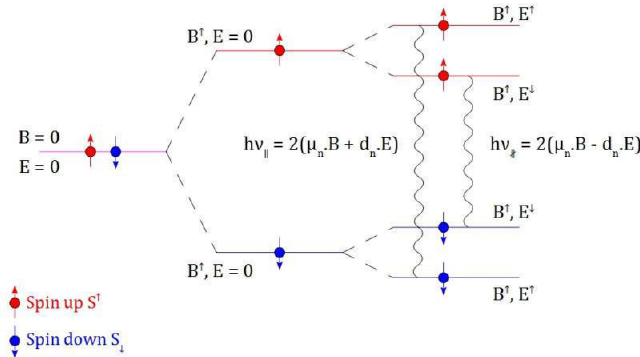


FIGURE 2.1 – La séparation des niveaux d'énergie du neutron dépend de l'orientation de son spin ainsi que de l'orientation relative des champs électrique ou magnétique, pouvant être soit parallèle (\parallel) soit anti-parallèle (\perp). Le signe moins en face de $\mu_n \vec{B} \cdot \vec{s}$ prend en compte le fait que $\gamma_n < 0$ et assure ainsi que d_n se comporte comme μ_n .

dont le principe est montré sur la Fig. 2.2. On stocke dans un premier temps des UCN polarisés dans une chambre de précession soumise aux champs parallèles ou anti-parallèles \vec{E} et \vec{B} . Ensuite, un pulse radiofréquence (RF) est appliqué pendant 2 s ($\tau_{RF} = 2$ s). Si la fréquence du pulse RF correspond à la fréquence de Larmor du neutron ($f_n = \frac{\gamma_n}{2\pi} B_0$), le spin de celui-ci se tourne dans le plan orthogonal au champ magnétique B_0 . Il va ainsi précesser librement pendant une période T ($\simeq 180$ s) appelé temps de précession. L'existence d'un EDM conduit à un décalage en fréquence qui s'accumule durant cette phase de précession, et qui dépend de l'orientation relative des champs électrique et magnétique. Le décalage est positif si les champs sont parallèle, négatif sinon. A la fin du temps de précession, un second pulse RF est appliqué. Enfin, la chambre de précession est vidée, et la polarisation du neutron est analysée. Cette procédure constitue un cycle de mesure.

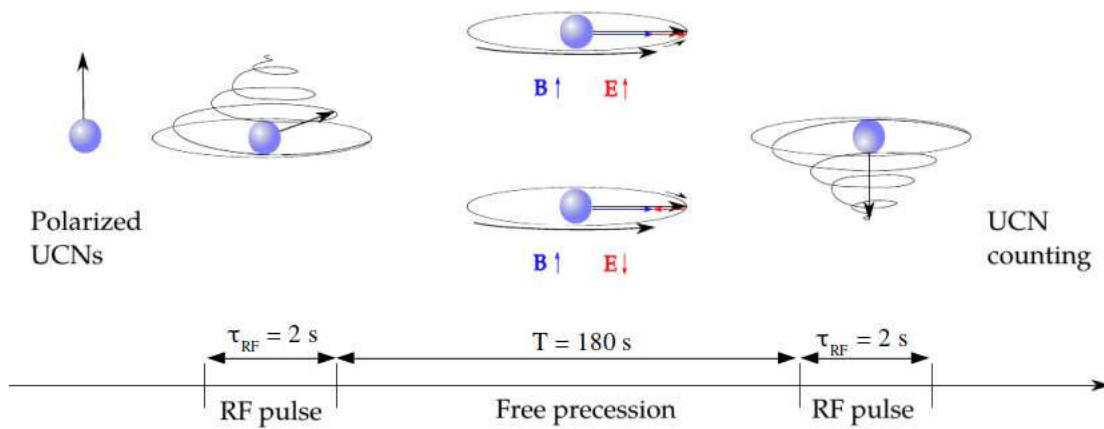


FIGURE 2.2 – Méthode des champs oscillants séparés de Ramsey

En faisant varier la fréquence RF, on aboutit à la figure de Ramsey, montrée sur la Fig. 2.3. Au lieu d'utiliser directement le nombre de neutrons détecté dans chaque état de spin $N^{\uparrow/\downarrow}$, la collaboration a fait le choix d'utiliser à la place une quantité appelée asymétrie, et définie comme :

$$A = \frac{N^\uparrow - N^\downarrow}{N^\uparrow + N^\downarrow}; \sigma_A = \frac{2\sqrt{N^\uparrow N^\downarrow}}{(N^\uparrow + N^\downarrow)^{3/2}} \quad (2.4)$$

L'asymétrie peut être exprimée en fonction de la fréquence RF :

$$A(f_{RF}) = A_0 - \alpha \cos \left(\pi \frac{f_{RF} - f_n}{\Delta\nu} \right) \quad (2.5)$$

où A_0 corresponds à l'asymétrie moyenne, $\Delta\nu = [2(T + 4\tau_{RF}/\pi)]^{-1}$ est la largeur à mi-hauteur de la frange principale et α correspond à la visibilité de la frange centrale, définie par :

$$\alpha = \frac{A_{max} - A_{min}}{A_{max} + A_{min}}. \quad (2.6)$$

Dans l'expérience n2EDM, seuls quatre points de fonctionnement (WP) sont utilisés autour de la fréquence $f_{RF} = f_n$ (voir 2.3). C'est en effet ici que la sensibilité de la mesure de la fréquence est la plus grande (i.e. là où la pente est la plus grande).

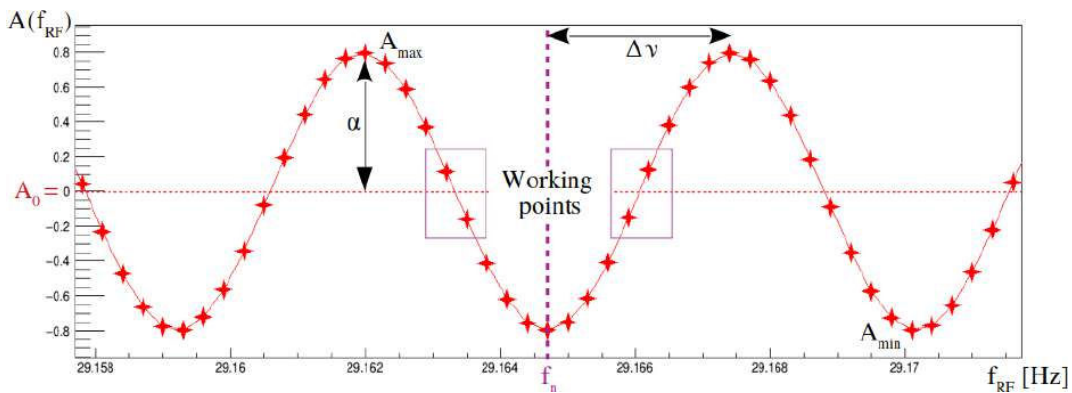


FIGURE 2.3 – La figure de Ramsey est obtenue en traçant l'asymétrie A en fonction de la fréquence RF. L'amplitude de cette figure est déterminée par la visibilité α . Les 4 points de fonctionnement utilisés pour extraire la fréquence neutron f_n sont à l'intérieur des boîtes rectangulaires violettes.

Le fit de la frange centrale par l'équation Eq. 2.5 permet d'extraire la fréquence neutron f_n . Cette opération est répétée chaque cycle. Le but est d'opérer le plus de cycles possible afin d'améliorer la sensibilité statistique sur la mesure de l'EDM. A la fin, l'EDM du neutron est mesuré par l'équation Eq. 2.3, avec une sensibilité statistique donné par :

$$\sigma_{d_n} \simeq \frac{\hbar}{2\alpha TE\sqrt{N_{tot}}}. \quad (2.7)$$

Cette formule résume les quatre paramètres à améliorer pour obtenir une faible sensibilité : la visibilité α , limitée par la dépolarisation des UCN, le temps de précession T , limité par dépolarisation des neutrons par les parois et par la décroissance du neutron dans une moindre mesure, le champ électrique E , contraint par les décharges électriques, et le nombre total de neutrons détectés N_{tot} restreint par la production de la source UCN. Afin de pouvoir combiner toutes les mesures de la fréquence neutron, il faut prendre en compte les dérives du champ magnétique. C'est le rôle des magnétomètres mercure qui mesure à chaque cycle le champ des chambres de précession. Ainsi, il est possible de prendre en compte cette dérive en utilisant

le ratio $\mathcal{R} = \frac{f_n}{f_{Hg}}$ au lieu de f_n (f_{Hg} correspond à la fréquence de Larmor des atomes de mercure). On peut donc réécrire Eq. 2.3 en fonction de ce ratio :

$$d_n = \frac{\pi \hbar f_{Hg}}{4|E|} (\mathcal{R}_{\uparrow\downarrow}^T - \mathcal{R}_{\uparrow\uparrow}^T + \mathcal{R}_{\uparrow\downarrow}^B - \mathcal{R}_{\uparrow\uparrow}^B), \quad (2.8)$$

où le label "T" est utilisé pour les quantités reliées à la chambre de précession du haut, et le label "B" est utilisé pour celles reliées à la chambre de précession du bas.

Les modifications les plus importantes apportées à l'expérience n2EDM comparé à nEDM sont l'utilisation de deux chambres de précession avec un plus grand diamètre, un champ électrique plus intense, un nouveau blindage magnétique, et un nouveau système de bobines permettant d'avoir un meilleur contrôle du champ magnétique et une meilleure uniformité. La sensibilité statistique finale attendue est donc de $1.1 \times 10^{-27} e\text{cm}$.

Exigences du champ magnétique

Le contrôle du champ magnétique est une problématique critique pour l'expérience n2EDM. Cette section a pour objectif de définir des exigences sur le champ magnétique produit par la bobine B_0 .

Uniformité du champ : contrainte du champ RF commun au deux chambres

Afin de mesurer la fréquence neutron, il faut appliquer une fréquence RF au début et à la fin du temps de précession. A un décalage de cette fréquence correspond une perte de sensibilité sur la mesure de la fréquence neutron. Dans n2EDM, le même pulse RF est utilisé pour les chambres de précession du haut et du bas. En présence d'un gradient vertical, le champ magnétique dans la chambre du haut est légèrement différent de celui de la chambre du bas. Cela entraîne un décalage de la fréquence RF et donc une perte de sensibilité statistique. Afin de limiter cette perte en dessous de 2%, le gradient vertical doit être inférieur à :

$$\frac{\partial B_z}{\partial z} = G_{1,0} < 0.6 \text{ pT/cm}. \quad (2.9)$$

Cette exigence est connue sous le nom de "contrainte du champ RF commun au deux chambres".

Uniformité du champ : la dépolarisation du neutron

Supposant un faisceau de neutron totalement polarisé, la visibilité α , présentée plus tôt, reflète la capacité à conserver cette polarisation pendant le transport des neutrons, le temps de précession et également le pouvoir d'analyse de l'analyseur de spin. On distingue plusieurs types de dépolarisation. Cependant une seule nous intéresse ici : la dépolarisation dite transverse, qui se produit lorsque le spin du neutron est transverse au champ magnétique B_0 , c'est-à-dire pendant le temps de précession.

La variation de la visibilité α due à la dépolarisation transverse est donnée par :

$$\frac{d\alpha}{dT} = -\frac{\alpha}{T_{2,wall}} - \frac{\alpha}{T_{2,mag}} + \dot{\alpha}_{grav}, \quad (2.10)$$

où $T_{2,wall}$ corresponds à la dépolarisation par collision sur les parois, $T_{2,mag}$ est due aux non-uniformité du champ magnétique et $\dot{\alpha}_{grav}$ est du à un phénomène appelé "dépolarisation gravitationnellement renforcée".

Dépolarisation par collision sur les parois

Cette dépolarisation est due aux impuretés magnétiques présentes dans les parois ou à leurs surfaces. Elle est représentée par la probabilité de dépolarisation par collision sur les parois β , dont la valeur est comprise entre $10^{-6} \lesssim \beta \lesssim 10^{-5}$ pour la plupart des matériaux utilisés pour le revêtement des parois. La fréquence moyenne des collisions étant de 50 Hz pour l'expérience nEDM, on obtient :

$$T_{2,wall} = (\beta\nu)^{-1} \gtrsim 2000 \text{ s.} \quad (2.11)$$

Lors de l'expérience nEDM, cette quantité a été mesuré $\simeq 4000$ s. La perte de visibilité associée pendant le temps de précession ($T = 180$ s) est donc de :

$$\Delta\alpha_{wall} = \alpha(0) - \alpha(T) = 1 - e^{-\frac{T}{T_{wall}}} \lesssim 0.04. \quad (2.12)$$

Ainsi, la contribution de cette forme de dépolarisation reste faible et ne représente pas une menace.

Dépolarisation intrinsèque

La dépolarisation intrinsèque se produit lorsque les neutrons traversent un champ non-uniforme. Du fait de leur trajectoires différentes, les neutrons ne voient pas le même champ. Afin de limiter la perte de visibilité à 2%, l'uniformité du champ est soumise à la contrainte suivante :

$$\sigma(B_z) = \sqrt{\langle (B_z^c)^2 \rangle} < 170 \text{ pT.} \quad (2.13)$$

Dépolarisation gravitationnellement renforcée

Parce que les UCN sont impactés par la gravité, la hauteur maximum qu'ils peuvent atteindre dans la chambre de précession dépend de leur énergie. En présence d'un gradient vertical $\frac{\partial B_z}{\partial z}$, les neutrons ne voient donc pas tous le même champ magnétique. Cela induit encore une fois une dépolarisation, dont le taux s'exprime comme étant :

$$\dot{\alpha}_{grav} = -\gamma_n^2 \left(\frac{\partial B_z}{\partial z} \right)^2 Var[\bar{z}] T, \quad (2.14)$$

ce qui induit une perte de sensibilité de :

$$\Delta\alpha_{grav} = -\frac{1}{2} \gamma_n^2 \left(\frac{\partial B_z}{\partial z} \right)^2 Var[\bar{z}] T^2. \quad (2.15)$$

$Var[\bar{z}]$ corresponds à la variance de la distribution en hauteur des neutrons, valant 0.2 cm^2 pour nEDM ; ce qui est également attendu pour n2EDM. En prenant pour limite supérieure un gradient linéaire vertical $|\frac{\partial B_z}{\partial z}| \leq 0.6 \text{ pT/cm}$, donné par la contrainte du champ RF commun au deux chambres, la perte de visibilité attendue est inférieure à 4×10^{-5} , ce qui est très faible.

Effet systématique principal : le faux EDM $v \times E$

Lorsqu'une particule avec une vitesse \vec{v} bouge dans un champ électrique \vec{E} , il ressent un champ magnétique lié à son mouvement :

$$\vec{B} = \frac{\vec{E} \times \vec{v}}{c^2}, \quad (2.16)$$

où c est la vitesse de la lumière. En présence de non-uniformité du champ magnétique, cet effet induit un décalage en fréquence proportionnel linéairement au champ électrique, et qui imite donc la signature d'un EDM. Cet effet est appelé "faux EDM $v \times E$ ". Pour un neutron, dont la fréquence de Larmor est supérieure au taux de collision contre les parois $\tau_c = 2R/v_{RMS}$ (où $v_{RMS} = \sqrt{\langle v^2 \rangle}$ est la vitesse carrée moyenne des neutrons dans la chambre de rayon R), nous sommes dans le cas dit adiabatique. En supposant un gradient vertical uniforme de B_z (i.e. le gradient $G_{1,0}$), le faux EDM associé au mouvement du neutron est donc :

$$d^{false} = -\frac{\hbar v_{RMS}^2}{2c^2 B_0^2} G_{1,0}. \quad (2.17)$$

En prenant une vitesse moyenne des neutrons $v_{RMS} = 2 \text{ m/s}$ et la limite imposée par la contrainte du champ RF commun aux deux chambres $G_{1,0} = 0.6 \text{ pT/cm}$, on obtient un faux EDM $d_n^{false} = 9.9 \times 10^{-29} e \text{ cm}$. Cette contribution est donc négligeable.

Cependant il faut aussi considérer le mouvement des atomes de mercure, beaucoup plus rapide que les neutrons. On est alors dans le régime adiabatique et le faux EDM se calcule grâce à la relation :

$$d_{Hg}^{false} = -\frac{\hbar \gamma_{Hg}^2}{2c^2} \langle xB_x + yB_y \rangle. \quad (2.18)$$

Le mercure étant utilisé pour corriger les variations du champ magnétique, son faux EDM se transfère en un faux EDM du neutron :

$$d_{n \rightarrow Hg}^{false} = \left| \frac{\gamma_n}{\gamma_{Hg}} \right| d_{Hg}^{false}. \quad (2.19)$$

En ne considérant que le gradient linéaire $G_{1,0}$, on obtient :

$$d_{n \rightarrow Hg}^{false} = \frac{\hbar \gamma_{Hg} \gamma_n}{8c^2} R^2 G_{1,0} \quad (2.20)$$

Ce qui donne en reprenant la valeur $G_{1,0} = 0.6 \text{ pT/cm}$ et une chambre de rayon $R=40 \text{ cm}$ un faux EDM de $d_{n \rightarrow Hg}^{false} = 7.683 \times 10^{-27} e \text{ cm}$, ce qui est un grand effet systématique.

Ce faux EDM n'est pas uniquement du au gradient $G_{1,0}$, mais également à des gradients d'ordre supérieur. Cependant, grâce à la symétrie cylindrique de la chambre, les gradients avec $m \neq 0$ donnent un EDM nul. De plus, les termes avec un l pair créent dans les deux chambres de précession un EDM opposé, de tel sorte que la contribution totale est également nulle. On se retrouve donc uniquement avec les termes ayant un l impair et un $m=0$. L'expression du faux EDM exprimé jusqu'à l'ordre $l=5$ est exprimé ci-dessous :

$$\begin{aligned} d_{n \leftarrow Hg}^{false} = & \frac{\hbar \gamma_n \gamma_{Hg}}{32c^2} D^2 \left(G_{1,0} \right. \\ & - \left[\frac{D^2}{8} - \frac{3H'^2 + H^2}{4} \right] G_{3,0} \\ & \left. + \frac{5}{8} \left[\frac{D^4}{32} - \frac{D^2}{2} \left(\frac{3H'^2 + H^2}{3} \right) + H'^2 H^2 + \frac{5H'^4 + H^4}{10} \right] G_{5,0} \right) \end{aligned} \quad (2.21)$$

La procédure employée pour supprimer cet effet est généralement de mesurer les gradients et les extrapolier à zéro. C'est ce qui est appelé la technique d'analyse du point de croisement dans nEDM. Pour n2EDM, on met à profit le fait d'avoir deux chambres en mesurant à l'aide des magnétomètres mercure le gradient Haut/Bas (Top/Bottom) :

$$G_{TB} = \frac{\langle B_z \rangle^T - \langle B_z \rangle^B}{H'}. \quad (2.22)$$

Celui-ci s'exprime sous la forme de gradient jusqu'à l'ordre 5 comme :

$$\begin{aligned} G_{TB} &= G_{1,0} \\ &+ \frac{1}{16}(4H'^2 + 4H^2 - 3D^2)G_{3,0} \\ &+ \frac{5}{8} \left(\frac{D^4}{16} - \frac{D^2}{4}(H'^2 + H^2) + \frac{H'^2 H^2}{3} + \frac{H'^4 + H^4}{10} \right) G_{5,0}. \end{aligned} \quad (2.23)$$

On insère ainsi l'expression de G_{TB} dans l'expression du faux EDM :

$$\begin{aligned} d_{n \leftarrow Hg}^{false} = & \frac{\hbar \gamma_n \gamma_{Hg}}{32c^2} D^2 \left(G_{TB} \right. \\ &+ \left[\frac{D^2}{16} - \frac{H'^2}{2} \right] G_{3,0} \\ &+ \left. \frac{5}{8} \left[-\frac{D^4}{32} - \frac{D^2}{12}(3H'^2 - H^2) + \frac{2H'^2 H^2}{3} + \frac{2}{5}H'^4 \right] G_{5,0} \right) \end{aligned} \quad (2.24)$$

Mesurer G_{TB} et l'extrapoler à zéro permet de supprimer toute la contribution provenant du gradient $G_{1,0}$. Cependant il n'est pas capable de supprimer l'effet des autres gradients comme $G_{3,0}$ ou $G_{5,0}$. Il est donc prévu de mesurer ses gradients à l'aide des magnétomètres Césium et du mapper.

Dipôle magnétique local

Une autre source de faux EDM peut émerger de la présence locale de dipôles magnétiques. Ils peuvent correspondre à de petites impuretés magnétisées, et sont caractérisés par leurs moments magnétiques \vec{m} . Un tel dipôle crée autour de lui un champ magnétique qui est une source de non-uniformité, et induit ainsi un faux EDM, dont l'intensité est directement lié à la force et à la position du dipôle. Le chapitre 5 développe avec plus de détail l'impact de tel dipôles.

L'expérience n2EDM

Dans cette section, le dispositif expérimental de n2EDM est brièvement décrit. La Fig. 2.4 montre un schéma basique de ce dispositif. Il opère de la façon suivante.

La source UCN de PSI (à gauche, non montrée sur le schéma) produit dans un premier temps des neutrons rapides via le processus de spallation, lors duquel un faisceau de proton de 590 meV heurte une cible de plomb. Environ 7-8 neutrons sont produits par proton, menant à un taux de production de 10^{17} neutrons/s. Ces neutrons sont ensuite thermalisés dans de l'eau lourde D_2O , puis refroidis par un cristal de deutérium solide D_2 (30 dm^3) à 5K. Les neutrons devenus UCN sont stockés, puis délivrés dans un des trois ports de faisceau. La densité de neutron mesurée à PSI est de $22.31(71) \text{ UCN/cm}^3$ après 2 s de stockage.

Les neutrons sont ensuite polarisés par un aimant supraconducteur de 5T avec une probabilité $P > 99\%$, avant d'être acheminés à travers les boîtes switch jusqu'aux chambres de précession. Ces boîtes sont également utilisées pour guider les neutrons des chambres au système de détection lors du vidage, et également directement de la source au système de détection lors de la période de précession pour monitorer le faisceau. La polarisation des UCN est maintenue par des bobines de guidage situées autour des guides neutrons en verre. Ces derniers possèdent un diamètre interne de 130 mm, et sont revêtus d'une couche de NiMo, ayant un potentiel de Fermi de 220 neV. Cela permet de réduire les pertes par collision des UCN. La hauteur entre la

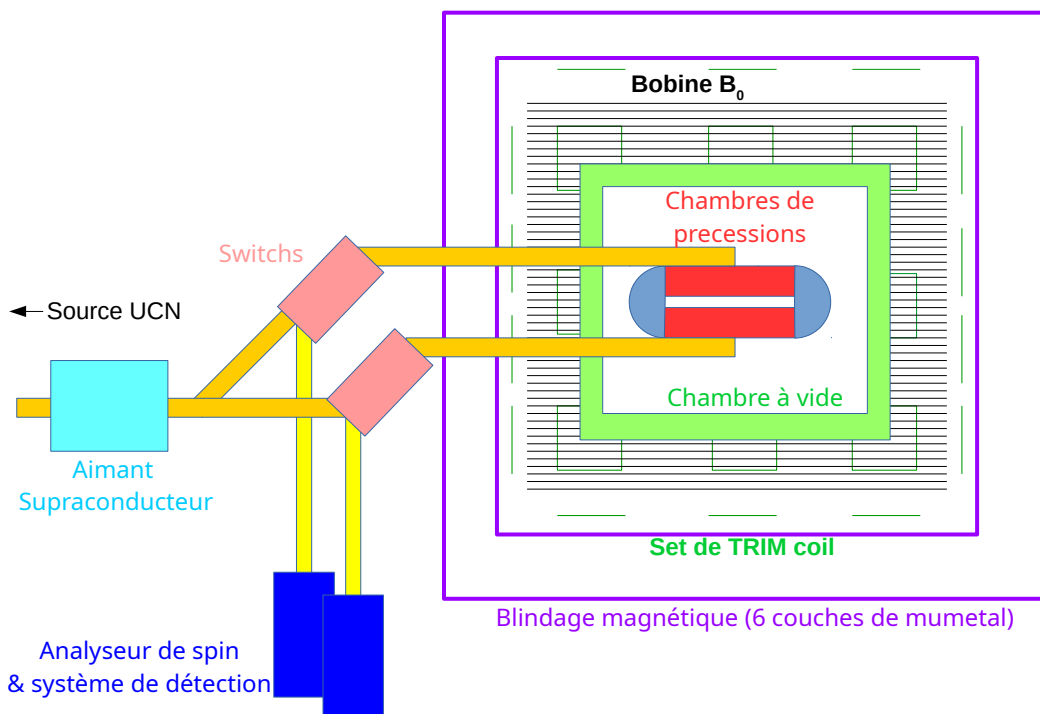


FIGURE 2.4 – Schéma du dispositif expérimental de n2EDM. Les magnétomètres, la haute tension et les SFC ne sont pas montrés ici.

source UCN et la chambre de précession, de 80 cm, a été optimisée pour remplir efficacement les chambres de précession. Une fois dans les chambres de précession, la méthode des champs oscillants séparés de Ramsey est appliquée. Ces chambres ont un diamètre de $D = 80 \text{ cm}$ et une hauteur de $H = 12 \text{ cm}$. Leurs centres sont séparés d'une distance $H' = 17 \text{ cm}$. Les électrodes constituant le haut et le bas des chambres sont fait en aluminium et ont un revêtement de DLC ($V_F = 230 \text{ neV}$). Elles sont à la masse, tandis que l'électrode centrale est opérée avec une haute tension, afin d'avoir un champ électrique de 15 kV/cm. Deux anneaux isolants constituent les parois des chambres. Ils sont constitués de polystyrène (PS) avec un revêtement dPS, leur donnant un potentiel de Fermi $V_F = 160 \text{ neV}$.

Les champs magnétiques de n2EDM sont produits par deux bobines. La première, appelée bobine B_0 , est chargée de créer un champ vertical de 1 μT hautement uniforme. Le design de cette bobine est précisée dans le chapitre 3. La deuxième bobine est appelée bobine RF, et doit produire les pulses RF nécessaires à la méthode des champs séparés de Ramsey. En plus de ces deux bobines, un set de 56 bobines, les TRIM coils sont utilisées pour améliorer l'uniformité du champ B_0 . En outre, plusieurs bobines dites bobines harmoniques devant produire des gradients spécifiques sont requises pour plusieurs buts. Ces deux types de bobine supplémentaires sont détaillés dans le chapitre 4.

En plus de produire le champ magnétique, il faut être capable de le mesurer. Cela se fait à l'aide de deux types de magnétomètres. Le comagnétomètre Mercure (HgM) permet de corriger les variations temporelles du champ magnétique. Son fonctionnement est basé sur des atomes de mercure polarisés envoyés dans la chambre de précession et précessant à leur fréquence de Larmor. Celle-ci est dépendante du champ magnétique. La lecture de la fréquence des atomes de mercure s'effectue en regardant l'absorption des photons d'un laser qui traverse la chambre. Le second type de magnétomètre est une grille de Magnétomètre Césium, situés au dessus et en dessous des chambres de précession. Ils permettent de connaître les variations spatiales du

champ magnétique. En effet, chaque magnétomètre est traversé par un laser dont l'absorption par les atomes de Césium donne l'information sur leur fréquence de précession, qui est relié au champ magnétique à l'emplacement de ce magnétomètre. Regrouper les informations de tout les magnétomètres permet donc d'évaluer les variations spatiales du champ. Enfin, le dispositif expérimental de n2EDM comporte aussi un mapper, qui permet de cartographier le champ magnétique offline. Il sera utilisé pour avoir les cartes magnétiques des bobines du TRIM coils array ainsi que pour mesurer les non-uniformités du champ B_0 .

Afin de se protéger du champ extérieur, le dispositif compte aussi un blindage magnétique composé de 6 couches de mu-métal et de 2 couches d'aluminium pour un facteur de blindage attendu de 70000 à 0.01 Hz et 1000000 à 70 Hz dans les trois directions de l'espace. De plus, un dernier jeu de bobines installé autour du blindage, les SFC, permettent de compenser activement les variations du champ magnétique extérieur.

Finalement, une fois que le temps de précession est achevé, les neutrons sont envoyé dans le système de détection. Celui-ci est constitué de deux éléments : l'analyseur simultané de spin, qui permet de séparer les neutrons de spin up et les neutrons de spin down dans deux bras différents, et les détecteurs gazeux au bout de chaque bras, qui vont détecter les neutrons. Ceux-ci sont rempli d'un mélange de ^3He et de CF_4 , le premier permettant la capture du neutron, via la réaction



et le second permettant la scintillation déclenchée par le proton et le tritium. La lumière émise est ensuite détectée par trois photomultiplicateurs dans les trois directions de l'espace, dont les signaux de sortie sont envoyés au système d'acquisition FASTER.

La bobine B_0

La bobine B_0 a pour but de générer un champ magnétique très homogène de 1 μT dans le volume des chambres de précession. La couche la plus intérieure du blindage, du fait de sa proximité avec la bobine, participe aussi à ce champ magnétique. Les contraintes que le champ doit respectées sont rappelés dans la Table 3.1.

Simulations COMSOL

Avant de s'intéresser au design de la bobine B_0 , nous devons présenter le logiciel COMSOL, utilisé pour les simulations. Ce logiciel est basé sur la méthode des éléments finis (FEM) : il s'agit de décomposer la géométrie à étudier en plusieurs plus petits éléments, appelé mailles. Ces éléments peuvent être des tétraèdres, des parallélépipèdes en 3D, ou encore des triangles, des carrés ou autre en 2D. L'ensemble de ces mailles constitue le maillage de la géométrie. Les sommets de ces mailles sont appelés nœuds. Le principe de la FEM consiste à ne calculer la solution exacte du problème à résoudre qu'aux nœuds du système, et d'ensuite interpoler la solution entre chaque nœuds, à l'aide de fonctions d'interpolations pouvant être linéaires, quadratiques, etc.

Un des points clés de cette méthode est d'ajuster le compromis entre temps de calcul et précision de la solution : en effet, utiliser des mailles de plus petite taille permet d'avoir des nœuds plus proches les uns des autres et donc d'avoir une solution plus précise, mais cela augmente également leur nombre, rendant les temps de calcul plus longs. Il est donc recommandé d'utiliser un maillage fin là où la solution risque de varier le plus, ou là où l'on souhaite une précision plus importante, et d'avoir un maillage plus grossier pour les parties de la géométrie où le résultat attendu ne présente que de faibles variations. Un deuxième levier sur lequel jouer est celui des fonctions d'interpolation : utiliser des fonctions quadratiques permet généralement un résultat plus précis qu'avec des fonctions linéaires, mais requiert également plus de temps. Pour illustrer ces propos, une boucle de courant de rayon $R = 0.25$ m traversée par un courant $I = 0.25/(2\pi)$ A a été simulé avec plusieurs maillages (large, fin et extrêmement fin) et plusieurs fonctions d'interpolations. On cherche à comparer le champ créé par la boucle au centre de celle-ci au résultat analytique $B(\vec{0}) = 100$ nT. On compare également les temps de calculs. Les

Origine de la contrainte	Contrainte sur le champ
Intensité du champ au centre de la bobine	$B_0(\vec{0}) = 1 \mu\text{T}$
Contrainte du champ RF commun au deux chambres	$G_{1,0} < 0.6 \text{ pT/cm}$
Uniformité du champ	$\sigma(B_z) < 170 \text{ pT}$

TABLE 3.1 – Contraintes sur le champ B_0 .

Taille des mailles	Large		Fin		Extrêmement Fin	
Fonctions	Linéaire	Quadratique	Linéaire	Quadratique	Linéaire	Quadratique
Nb d'éléments	3038		81179		1710809	
Taille minimale des éléments (m)	0.26		0.16		0.05	
Taille maximale des éléments (m)	0.47		0.22		0.10	
Temps de calcul (s)	2	3	5	18	70	381
$B(\vec{0})$ (nT)	113.57	105.54	97.55	116.9	100.82	99.87
Erreur (%)	13.6	5.54	2.45	1.69	0.82	0.43

TABLE 3.2 – Comparaison des résultats obtenus avec des fonctions d’interpolation linéaires ou quadratiques et avec différentes tailles de maille à la solution analytique ($B(\vec{0}) = 100 \text{ nT}$).

résultats sont montrés dans la Table 3.2.

On constate qu’utiliser des fonctions quadratiques et un maillage raffiné permet de réduire l’erreur commise, mais augmente les temps de calcul.

Cependant, en utilisant les symétries du système, il est possible de simplifier la simulation et d’ainsi réduire le temps de calcul sans affecter la précision de la solution. Pour l’électromagnétisme dans COMSOL, cela se traduit par des conditions aux bords qui simule les symétrie de courant, et donc du champ magnétique généré. Un plan de symétrie pour les courants correspond à la condition aux bords $\vec{n} \times \vec{H} = 0$, avec \vec{n} le vecteur normal de ce plan, ce qui corresponds donc COMSOL à la condition "Conducteur magnétique parfait". A l’inverse, un plan d’antisymétrie des courants correspond à la condition $\vec{n} \times \vec{A} = 0$ où \vec{A} est le potentiel vecteur du champ magnétique, ce qui est représenté dans COMSOL par la condition "Isolation magnétique". La table Table 3.3 présente les résultats de diverses simulations utilisant les diverses symétries de notre boucle de courant.

Fraction de la géométrie simulée	1	1/2	1/4	1/8	1/16	1/144
Nombre d’éléments	1710809	849274	420690	206754	103297	28734
Temps de calcul (s)	381	201	103	68	26	18
$B(0)$ (nT)	99.57	99.85	100.42	100.18	99.75	99.84
Erreur (%)	0.43	0.15	0.42	0.18	0.25	0.16
Isolation magnétique		✓	✓	✓	✓	✓
Conducteur magnétique parfait					✓	✓

TABLE 3.3 – Comparaison entre plusieurs simulations COMSOL utilisant différentes symétries.

On observe que l’utilisation des symétries réduit considérablement le nombre d’éléments à simuler, et donc le temps de calcul, en conservant une erreur correcte. Il est donc important d’utiliser quand c’est possible les symétries du système étudié.

Design de la bobine B_0

Le but de la bobine est d’obtenir le champ le plus homogène possible. C’est pourquoi nous partons d’une des façons les plus simple pour créer un champ parfaitement uniforme : le solénoïde infini.

Boucle de courant et solénoïde infini

Partons tout d’abord d’une simple boucle de courant de forme carré de côté a situé autour de l’axe z. Le champ créé en un point M situé sur l’axe de la boucle de courant à une hauteur

z par rapport à cette boucle peut être calculé à partir de l'équation de Biot et Savart :

$$\vec{B}(M) = \oint_C \frac{\mu_0}{4\pi} \frac{I d\vec{l} \times \vec{PM}}{\|PM\|^3}. \quad (3.1)$$

où $d\vec{l}$ est un élément de la boucle dont le point P est l'origine, et I est le courant circulant dans la boucle. On obtient après quelques calculs le champ :

$$\vec{B}(M) = \frac{\mu_0 I}{2\pi} \frac{a^2}{(a^2/4 + z^2)\sqrt{a^2/2 + z^2}} \vec{u}_z. \quad (3.2)$$

En supposant maintenant non plus une seule boucle de courant, mais un solénoïde carré infini le long de l'axe z , possédant autour de la position z un nombre Ndz de boucles. Le champ créé au point M par l'ensemble du solénoïde est donc :

$$\begin{aligned} \vec{B}(M) &= \frac{\mu_0 NI}{2\pi} \int_{z=-\infty}^{z=+\infty} \frac{a^2}{(a^2/4 + z^2)\sqrt{a^2/2 + z^2}} dz \vec{u}_z \\ &= \frac{\mu_0 NI}{2\pi} \cdot 2\pi \\ \vec{B}(M) &= \mu_0 NI. \end{aligned} \quad (3.3)$$

En utilisant le théorème d'Ampère avec des contours situés soit entièrement à l'intérieur du solénoïde, soit entièrement à l'extérieur du solénoïde, il est possible de montrer que le champ est parfaitement homogène, et vaut $B_{inside} = \mu_0 NI$ partout dans le solénoïde, et $B_{outside} = 0$ à l'extérieur de celui-ci.

Solénoïde fini dans un blindage magnétique

Bien sûr, il n'est pas possible de construire un solénoïde infini, ni même dans notre cas un solénoïde assez long pour produire un champ suffisamment homogène dans la région d'intérêt. L'astuce est alors d'entourer un solénoïde fini avec un blindage magnétique. Lorsqu'on approche une boucle traversé par un courant I parallèlement à la surface d'un blindage magnétique de perméabilité μ , celui-ci produit une image symétrique de cette boucle avec un courant $I_{image} = \frac{\mu-1}{\mu+1} I$, comme montré à droite de la Fig. 3.1.

Dans le cas où l'on enferme un solénoïde fini dans un blindage magnétique avec une perméabilité μ élevée et de sorte que ses extrémités soit assez proches des parois du blindage, l'image de celui-ci le prolonge artificiellement, et crée ainsi le même champ qu'un solénoïde infini. C'est l'idée qui a inspiré le design de la bobine B_0 . Cependant, à cause du support de la bobine, il n'est pas possible de construire une bobine au contact du blindage. Les deux sont séparés par une distance de 10 cm. L'image magnétique créée par le blindage n'est donc plus exactement le prolongement du solénoïde, et l'ensemble se comporte plutôt comme deux solénoïdes distants de 20 cm. C'est pourquoi la bobine est également pourvues de boucles de courant à ses extrémités appelées courbes de Lamé qui aide à uniformiser le champ aux sorties de la bobine.

Design de la bobine B_0

Le design de la bobine B_0 est un solénoïde cubique vertical avec 181 boucles de courants et 14 courbes de Lamé évoquées précédemment. Ses dimensions sont celle d'un cube de 2.73 m de côté. Le blindage l'entourant est situé à 10 cm de la bobine. Il contribue à la production du champ à la hauteur de 30% et permet de réduire drastiquement ses non-uniformités. Afin d'intégrer les nombreuses ouvertures, comme celle des tubes guidant les UCN par exemple,

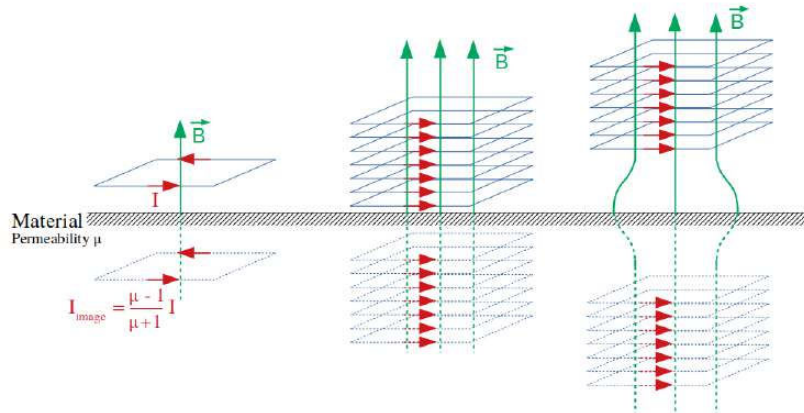


FIGURE 3.1 – A gauche est montrée l'image d'une boucle de courant carrée créée par un matériau de perméabilité μ . Au centre, l'image est celle d'un solénoïde proche de la surface du matériau. On obtient ainsi un champ uniforme. A droite, ce solénoïde est plus éloigné de la surface du matériau. Dans ce cas, le champ perd de son uniformité aux extrémités du solénoïde.

les fils de la bobine contournent celles-ci de manière à altérer le moins possible la densité de courant dans cette région. La figure Fig. 3.2 présente le design actuel de la bobine. Les caractéristiques principales de la bobine sont données dans la Table 3.4. Les courbes de Lamé sont définies par :

$$\begin{cases} x_i &= a_i \cdot \cos^{n_i}(\theta) \\ y_i &= a_i \cdot \sin^{n_i}(\theta) \end{cases}$$

avec $\theta \in [0, \pi/2]$. Cela nous donne un quart de la bobine, dont le reste est construit par symétrie. Les paramètres a_i et n_i de chacune des courbes est indiqué dans la Table 3.5

Nombre de boucles verticales	181
Nombre de boucles aux extrémités	2×7
Ecart entre les fils verticaux	15 mm
Longueur de la bobine	2121.6 m
Courant de la bobine	11.94 mA
Résistance de la bobine	11.34 Ω

$a_0 = 1360$ mm	$n_0 = 0.25$
$a_1 = 1350$ mm	$n_1 = 0.30$
$a_2 = 1340$ mm	$n_2 = 0.30$
$a_3 = 1330$ mm	$n_3 = 0.30$
$a_4 = 1320$ mm	$n_4 = 0.30$
$a_5 = 1310$ mm	$n_5 = 0.30$
$a_6 = 1300$ mm	$n_6 = 0.30$

TABLE 3.4 – Caractéristiques principales de la bobine B_0 .

TABLE 3.5 – Caractéristiques principales des boucles aux extrémités

L'optimisation du design de la bobine a été faite en utilisant le module "Optimisation" implanté dans COMSOL, auquel on demande de minimiser dans un volume de 1 m^3 autour des chambres de précession le champ transverse $B_T = \sqrt{B_x^2 + B_y^2}$. Ce faisant, on optimise les paramètres (tels que a_i et n_i pour les courbes aux extrémités par exemple) qui produisent un champ homogène selon z.

Performances

Afin de jauger les performances de la bobine, plusieurs quantités sont estimées. Tout d'abord, avec un courant de 11.94 mA, le champ au centre de la bobine est de $B(0) = 1.000274 \mu\text{T}$. On peut ensuite s'intéresser à l'uniformité du champ. Celle-ci est définie en re-

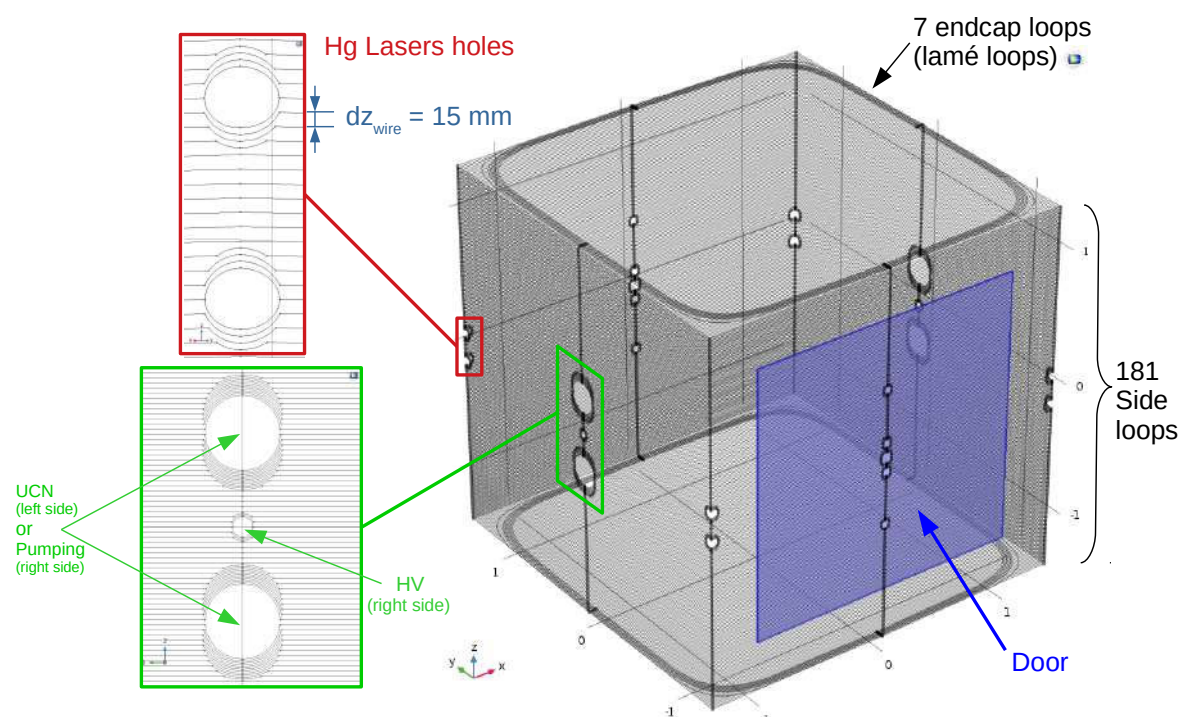


FIGURE 3.2 – Design de la bobine B_0 . L'écart entre les fils verticaux est de 15 mm, sauf autour des ouvertures. La déviation et le resserrement des fils autours des ouvertures des guide UCN et des lasers pour le mercure sont montrés dans les zones zoomées. La zone bleue correspond à l'emplacement de la porte d'entrée, de dimension 2m × 2m.

gardant l'écart-type de la composante principale du champ B_0 , à savoir B_z :

$$\sigma(B_z) = \sqrt{\langle (B_z - \langle B_z \rangle)^2 \rangle} \quad (3.4)$$

Cette uniformité dans le cas de la bobine actuelle est de :

$$\sigma(B_z) = 17.3 \text{ pT}, \quad (3.5)$$

ce qui est en dessous de la contrainte de 170 pT exigée afin notamment d'éviter la dépolarisation des neutrons.

Depuis 2010, la collaboration utilise aussi une base de polynômes harmoniques sur laquelle on peut décomposer le champ en gradients. Celle-ci est présentée en Annexe C. Le champ s'écrit donc :

$$\vec{B}(\vec{r}) = \sum_{l,m} G_{l,m} \begin{pmatrix} \Pi_{x,l,m}(\vec{r}) \\ \Pi_{y,l,m}(\vec{r}) \\ \Pi_{z,l,m}(\vec{r}) \end{pmatrix}. \quad (3.6)$$

Par définition, une harmonique de degré l dépend de la position à l'ordre l . Ainsi, on retrouve en l'ordre $l=0$ les gradients statiques ($G_{0,-1} = B_x$, $G_{0,0} = B_z$, $G_{0,1} = B_y$), ou encore en l'ordre $l=1$ des gradient linéaires ($G_{1,-1} = \frac{\partial B_z}{\partial y}$, $G_{1,0} = \frac{\partial B_z}{\partial z}$, $G_{1,1} = \frac{\partial B_z}{\partial x}$). De part la symétrie des courants due à la géométrie de la bobine et du blindage, seul les gradients $G_{0,0}$, $G_{2,0}$, $G_{2,2}$, $G_{4,0}$, $G_{4,2}$, $G_{4,4}$, etc. sont autorisés (voir l'annexe D pour plus de détails). L'amplitude de ces gradients est donné dans la Table 3.6.

Gradient	Amplitude
$G_{0,0}$	1000275 pT
$G_{2,0}$	$6.71 \times 10^{-2} \text{ pT/cm}^2$
$G_{2,2}$	$1.10 \times 10^{-2} \text{ pT/cm}^2$
$G_{4,0}$	$2.55 \times 10^{-6} \text{ pT/cm}^4$
$G_{4,2}$	$1.04 \times 10^{-6} \text{ pT/cm}^4$
$G_{4,4}$	$1.10 \times 10^{-7} \text{ pT/cm}^4$

TABLE 3.6 – Amplitude des gradients du champ produit par la bobine parfaite B_0 .

La bobine "parfaite", c'est-à-dire sans imperfections mécaniques, respecte donc toutes les exigences.

Influence des défauts mécaniques

La section précédente indique que la bobine produit un champ respectant ses contraintes si elle ne comporte pas d'imperfections mécaniques. Cependant, celles-ci ne pourront pas être évitées lors de la construction et de l'installation de la bobine. Plusieurs d'entre elles ont donc été simulées dans COMSOL afin de voir leurs impacts sur le champ produit.

Ont ainsi été simulés un déplacement global de la bobine en x , y et z , correspondant à un mauvais alignement de celle-ci par rapport au blindage, ainsi que des oscillations aléatoires des fils de la bobine B_0 , ce qui peut se produire étant donné que le diamètre des fils est légèrement inférieur à la largeur des rainures dans lesquelles ils sont contenues. Ont aussi été testés un changement des dimensions de la couche la plus interne du blindage qui ne peuvent être connues avec précision avant son installation, ainsi qu'une variation de la perméabilité entre la haut et le bas du blindage, reflétant le fait que celui-ci est constitué de plusieurs plaques n'ayant pas forcément la même perméabilité.

Parmi toutes ces imperfections, une seule compromet fortement le champ de la bobine : il s'agit du déplacement global de la bobine par rapport au blindage le long de l'axe z .

Dans ce cas, la symétrie de courant par rapport au plan XY est brisée, et la bobine peut produire les gradients suivant : $G_{1,0}$, $G_{3,0}$, $G_{5,0}$, etc. qui peuvent dépasser leurs exigences, ou bien créer un faux EDM $v \times E$ supérieur à $5 \times 10^{-28} e\text{cm}$. Comme le montre la Table 3.7, un déplacement de 0.25 mm constitue déjà un problème, la contrainte sur le gradient $G_{1,0}$ étant dépassé. Un déplacement supérieur à 1 mm quand a lui, entraîne via le $G_{3,0}$ un faux EDM supérieur à $5 \times 10^{-28} e\text{cm}$.

dz (mm)	$B(0)$ (μT)	σB_z (pT)	$G_{1,0}$ (pT/cm)	$G_{3,0}$ (pT/cm^3)	$G_{5,0}$ (pT/cm^5)	$G_{7,0}$ (pT/cm^7)
Contraintes	1	< 170	< 0.6	< 7.17×10^{-5}	< 6.54×10^{-8}	< 7.30×10^{-11}
0	1.000275	17.3	-	-	-	-
0.05	1.000000	17.6	0.33	3.60×10^{-6}	-3.08×10^{-10}	3.28×10^{-15}
0.25	1.000001	19.4	1.62	1.68×10^{-5}	1.50×10^{-9}	7.43×10^{-15}
0.50	1.000000	18.3	3.23	3.42×10^{-5}	3.03×10^{-9}	2.81×10^{-14}
1.00	1.000001	31.0	6.45	6.72×10^{-5}	5.98×10^{-9}	4.88×10^{-14}
3.00	1.000000	72.2	19.4	2.02×10^{-4}	-1.80×10^{-8}	1.56×10^{-13}
5.00	1.000001	115.8	32.3	3.37×10^{-4}	2.99×10^{-8}	2.63×10^{-13}

TABLE 3.7 – Evolution des estimateurs du champ créé par un déplacement vertical de B_0 . Les lignes pointillées indique le déplacement à partir duquel la contrainte correspondante n'est plus respectée.

Pour pallier à ce problème, un ajustement vertical sera effectué lors de l'installation de la bobine dont la précision est estimée à 1 mm, accompagné de campagne de mapping afin de connaître et de sélectionner la position donnant le champ le plus uniforme possible.

En plus des imperfections étudiées ici et simulée par COMSOL, de nombreuses autres sont possibles. N'étant pas possible de toutes des prédire ou même simuler, il est nécessaire d'avoir un système de correction du champ magnétique pour supprimer ses non-uniformités. C'est le rôle du TRIM coils array, décrit dans le chapitre suivant.

Solution technique de la bobine

La bobine B_0 est constituée de plaques de polycarbonate (PC) dans lesquelles des rainures seront creusées. Elles ont une largeur de 2 mm pour une profondeur de 3 mm. Un fil de cuivre de 2 mm de diamètre est ensuite glué dans cette rainure, dont le chemin correspond à la forme de la bobine B_0 . La faisabilité technique de ce processus a été testé au LPC avec certaines des difficultés typiques pouvant être rencontrées, notamment autour des ouvertures pour les guides UCN et pour les lasers, comme le montre la Fig. 3.12.

La porte d'entrée est aussi une partie sensible du système : elle doit être robuste et facile à manipuler. De plus, sa position fermée doit être reproductible ou assurer la reproductibilité du champ. C'est pourquoi un des principaux challenges du design repose sur les connecteurs de la porte. Ils doivent être non-magnétique, correspondre au design de la bobine tout en restant assez flexibles pour accepter de faibles désalignements. Ils doivent être démontables, compacts, et facile et rapide à connecter du fait de leur grand nombre (274 prévus). Plusieurs designs sont actuellement à l'étude. L'un d'eux, pouvant être fabriqué au LPC, consiste en un cylindre fendu que l'on fait glisser pour faire le contact, comme le montre la Fig. 3.4.

Une structure mécanique en profilé d'aluminium sera installé en premier, et fixé aux points de fixation de la MSR. Ensuite, la bobine sera monté sur cette structure. Le poids total de la bobine est estimée autour de 600 kg. L'installation de la bobine est prévue pour 2020.

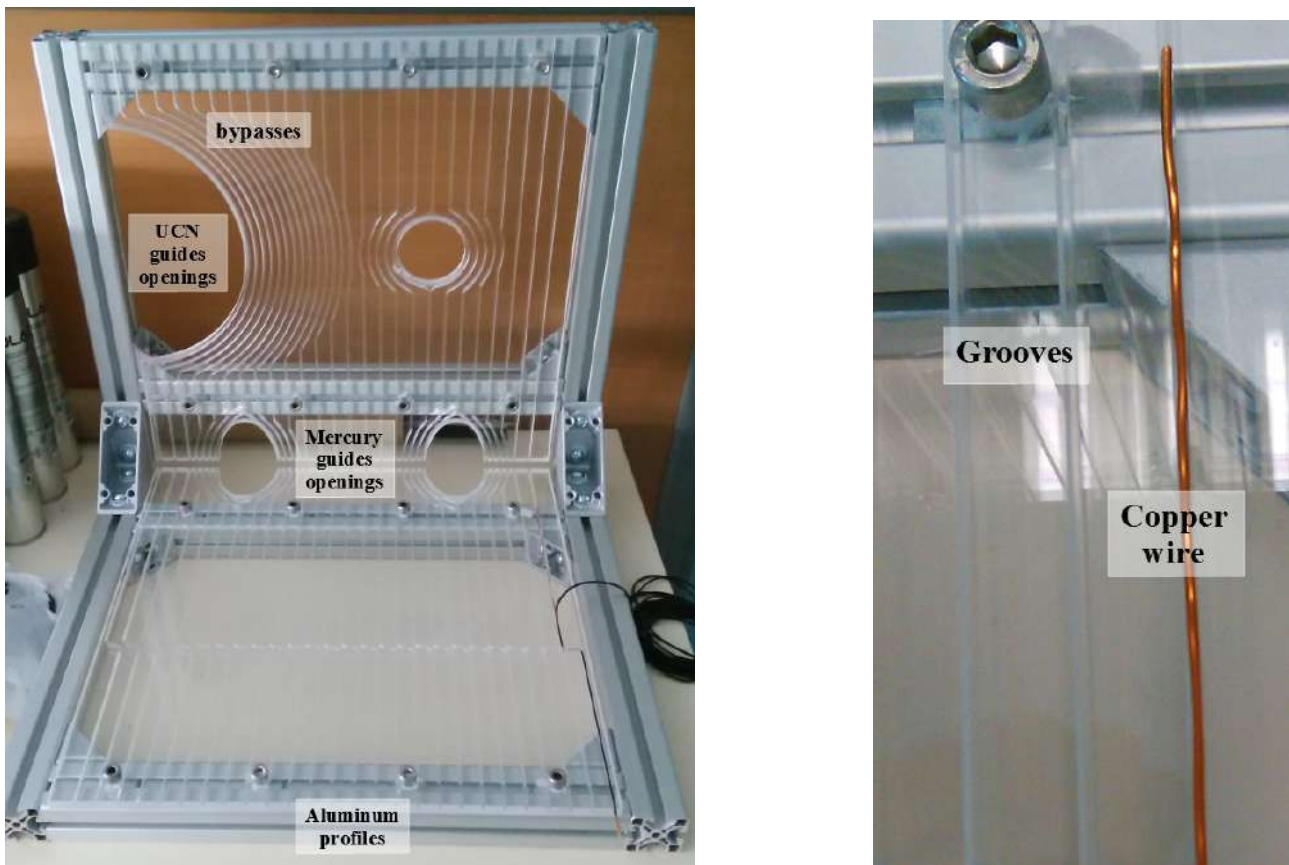


FIGURE 3.3 – La figure de gauche montre le design technique prévu pour la bobine avec une focalisation sur les ouvertures pour les guides UCN (la large ouverture) et les lasers (les petites ouvertures). Les plaques de polycarbonate sont ensuite vissées sur de profilés en aluminium. A droite est montré un fil de cuivre dans une rainure.

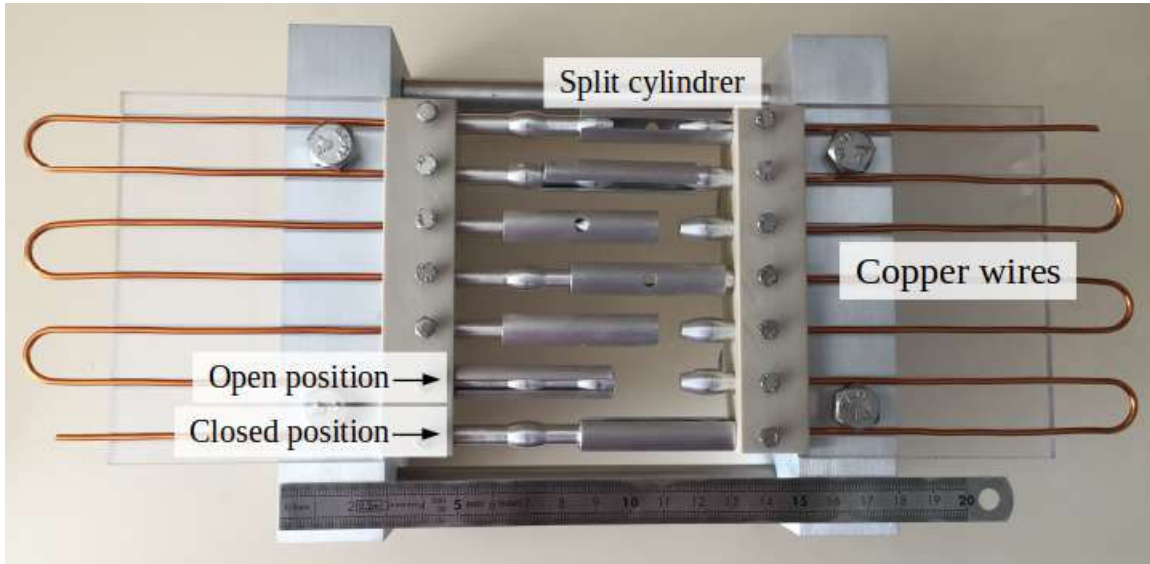


FIGURE 3.4 – Une des solution possible pour les connecteurs est montrée : elle consiste en des cylindres fendus qui peuvent glisser afin de connecter ou déconnecter les fils de cuivres représentant la bobine.

4

Les bobines correctrices

Comme indiqué au chapitre précédent, il n'est pas possible d'anticiper toutes les imperfections mécaniques pouvant se produire. Il est donc nécessaire de se munir d'un système de bobine supplémentaire pour corriger les non-uniformités du champ. C'est le but du TRIM coils array. De plus, l'expérience nécessite pour plusieurs raisons des bobines dédiées à la production de gradient spécifiques, à savoir $G_{1,0}$, $G_{2,0}$, $G_{3,0}$, $G_{1,-1}$ and $G_{1,1}$, ainsi que les composantes transverses du champ $G_{0,-1}$ and $G_{0,1}$. C'est le but des bobines harmoniques.

TRIM coils array

L'objectif du TRIM coil array est de supprimer les non-uniformités du champ B_0 . Il est constitué de 56 bobines carrées, chacune pourvues de sa propre alimentation électrique pouvant fournir une intensité de -200 mA à 200 mA avec une résolution de 1 μ A . A partir des combinaisons de courant de ses 56 bobines il est possible de corriger les gradients du champ jusqu'à l'ordre 6. Leur principe de fonctionnement est le suivant : on commence par mesurer à l'aide d'une campagne de mappage dédiée le champ (et donc les gradients) créé par chacune des bobines avec un courant de $I=1$ mA. Ces gradients sont regroupés dans une matrice G_{TC} composé de 80 lignes (une par gradient jusqu'à l'ordre 8) et de 56 colonnes (une par TRIM coil). La quantité situé à la i-ème ligne et à la j-ème colonne correspond ainsi au i-ème gradient de la j-ème TRIM coil avec un courant de 1 mA. On remplit ensuite une autre matrice G des gradients qui constitue les non-uniformités du champ à corriger. Sa taille est donc de 80×1 . Le but est de trouver les courants à fournir aux TRIM coils pour reproduire ces non-uniformités. On cherche donc comme solution une matrice I_{TC} de taille 56×1 comprenant les courants pour chaque TRIM coils. Ceux-ci sont ensuite obtenus en résolvant via une inversion de matrice $G = G_{TC} \cdot I_{TC}$.

$$\underbrace{\begin{pmatrix} G_{1,-1} \\ G_{1,0} \\ G_{1,-1} \\ \vdots \\ G_{7,8} \end{pmatrix}}_G = \underbrace{\begin{pmatrix} G_{1,-1}^{TC1} & G_{1,-1}^{TC2} & \dots & G_{1,-1}^{TC56} \\ G_{1,0}^{TC1} & G_{1,0}^{TC2} & \dots & G_{1,0}^{TC56} \\ G_{1,1}^{TC1} & G_{1,1}^{TC2} & \dots & G_{1,1}^{TC56} \\ \vdots & \vdots & \ddots & \vdots \\ G_{7,8}^{TC1} & G_{7,8}^{TC2} & \dots & G_{7,8}^{TC56} \end{pmatrix}}_{G_{TC}} \cdot \underbrace{\begin{pmatrix} I_{TC1} \\ I_{TC2} \\ \vdots \\ I_{TC56} \end{pmatrix}}_{I_{TC}} \quad (4.1)$$

Design

Comme évoqué précédemment, le TRIM coil array est constitué de 56 bobines d'un seul tour distribué sur un cube de taille 2.706 m. Les faces haut/bas et devant/derrière sont chacune

composé de 3×3 bobines de 0.3 m de côté. Sur les faces gauche/droite en revanche, la bobine centrale est remplacée par deux autres de 0.4 m de côté, contraint par le passage des guides UCN et des tuyaux de pompages.

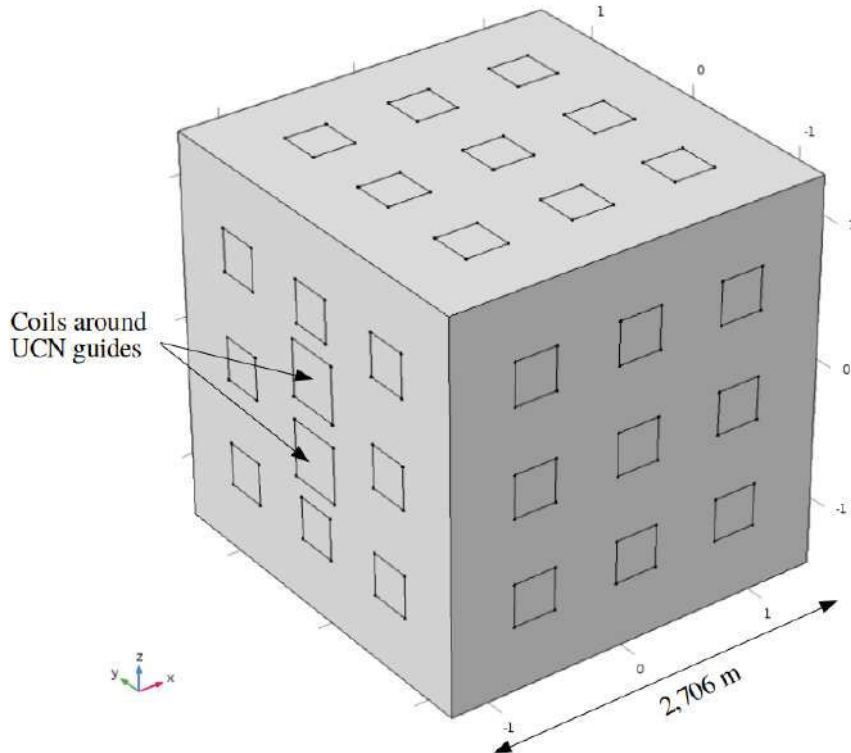


FIGURE 4.1 – Design du TRIM coil array.

Performances

La bobine s'est avérée capable de corriger une carte de champ possédant de larges non-uniformités (dû à un déplacement vertical de la bobine par rapport au blindage de 5 mm). La gamme de courant utilisée pour cette correction est comprise entre [1.4 ; 22.9] mA, ce qui appartient à la gamme de courant délivrée par les alimentations. L'uniformité du champ est ainsi passé de $\sigma(B_z) = 115.8$ pT avant correction à $\sigma(B_z) = 0.009$ pT après correction en conservant un champ au centre de 1 μ T.

Bobines Harmoniques

Objectif des bobines harmoniques

Sept bobines harmoniques sont prévues pour l'expérience n2EDM. Elles doivent chacune produire un gradient spécifique parmi $G_{1,0}$, $G_{2,0}$, $G_{3,0}$, $G_{1,1}$, and $G_{1,-1}$, et également deux composantes statiques $G_{0,1}$, $G_{0,-1}$. Commençons par les trois premières.

Les bobines $G_{1,0}$, $G_{2,0}$ et $G_{3,0}$

Le but principal de ces trois bobines est de contrôler les gradients $G_{1,0}$, $G_{2,0}$ et $G_{3,0}$ afin d'éviter qu'ils ne produisent de faux EDM trop important, et dans le cas du $G_{1,0}$, qui doit également garantir la contrainte du champ RF commun aux deux chambres $G_{1,0} < 0.6$ pT/cm,

de s'assurer que la bobine est capable de produire un champ avec une résolution inférieure à 0.1 pT/cm.

Malheureusement, les symétries des gradients que l'on veux créer sont partagées par d'autres gradients non souhaités, qu'on ne pourra donc pas éviter. C'est le cas des gradients G_{5,0} and G_{7,0} pour les bobines devant produire du G_{1,0} et G_{3,0}, et des gradients G_{4,0} and G_{6,0} pour la bobine G_{2,0}. Au lieu de comparer directement les gradients, qui ne partagent pas la même unité, on s'intéresse plutôt au faux EDM qu'il produisent. Ainsi on définit un critère à maximiser pour les trois bobines :

$$\text{Pour la bobine } G_{1,0} : d_{ratio}(G_{1,0}) = \frac{|d_{n \leftarrow Hg}^{false}(G_{1,0})|}{|d_{n \leftarrow Hg}^{false}(G_{3,0})| + |d_{n \leftarrow Hg}^{false}(G_{5,0})| + |d_{n \leftarrow Hg}^{false}(G_{7,0})|} \quad (4.2)$$

$$\text{Pour la bobine } G_{2,0} : d_{ratio}(G_{2,0}) = \frac{|d_{n \leftarrow Hg}^{false}(G_{2,0})|}{|d_{n \leftarrow Hg}^{false}(G_{4,0})| + |d_{n \leftarrow Hg}^{false}(G_{6,0})|} \quad (4.3)$$

$$\text{Pour la bobine } G_{3,0} : d_{ratio}(G_{3,0}) = \frac{|d_{n \leftarrow Hg}^{false}(G_{3,0})|}{|d_{n \leftarrow Hg}^{false}(G_{1,0})| + |d_{n \leftarrow Hg}^{false}(G_{5,0})| + |d_{n \leftarrow Hg}^{false}(G_{7,0})|} \quad (4.4)$$

Parce que ces bobines partagent les mêmes plans de symétries que la bobine B₀, il a été décidé de les installer sur le même support. Afin d'éviter que les fils soit situés aux mêmes endroits, on doit donc placer les boucles de courant pour ces bobines entre ceux de B₀, ce qui correspond à 180 positions possibles. Pour chaque position, le courant peut aller dans un sens ou dans l'autre. Cependant, un bon usage des symétries nous permet de diviser ce chiffre par deux en regroupant les boucles de courant par paires. Une paire est constitué de deux boucles de courant symétriques par rapport au plan XY en z=0. A cause des symétries du champ qu'elles doivent produire, les paires des bobines G_{1,0} et G_{3,0} sont composées de deux boucles dont le courant est opposé, tandis qu'il est du même sens pour les boucles de courant des paires de la bobine G_{2,0}. On simule ensuite toutes les combinaisons de n paires possibles, avec n ≤ 4 pour des raisons de temps de calcul. On compare ensuite le critère défini plus haut, et on sélectionne le design maximisant ce critère.

Les designs des bobines G_{1,0} et G_{3,0} présentés dans la Fig. 4.2 maximisent leur critères respectifs à $d_{ratio}(G_{1,0}) > 5000$ et $d_{ratio}(G_{3,0}) > 60$. Elles sont toutes deux composées de deux paires de boucles de courant. Malheureusement, il n'a pas été possible de trouver un design de la bobine G_{3,0} satisfaisant dont les fils ne traversent pas la porte d'entrée. L'alimentation de la bobine de G_{1,0} à une résolution de courant de 500 nA, ce qui conduit à une résolution sur le gradient de $G_{1,0} = 0.012 \text{ pT/cm}$, inférieur au 0.1 pT/cm requis.

Le design de la bobine G_{2,0} montrée dans la Fig. 4.3 est composé de trois paires de boucles de courants. Elle permet d'atteindre un critère de $d_{ratio}(G_{2,0}) > 200$.

Les bobines G_{1,-1} et G_{1,1}

Les magnétomètres Césium disposés au dessus et en dessous des chambres de précession ont pour but de mesurer la distribution spatiale du module du champ magnétique. Il faut donc que leurs positions soit précisément connues. C'est pourquoi, en plus de les positionner précisément mécaniquement, les bobines G_{1,-1} et G_{1,1} (et G_{1,0}) sont requises pour déterminer leur position. En effet, la composante verticale du champ de ces gradients est respectivement proportionnelle à y, x et z. En mesurant ce champ par les magnétomètres, on peut donc remonter à leur position. Néanmoins, le fait que les Magnétomètres Cs ne sont capables que de mesurer la norme du champ (et non la composante verticale) et que les bobines vont aussi produire d'autres gradients également autorisés par les symétries du champ sont deux obstacles à cette mesure. Pour contrer le second, on considère le champ créé par gradients non-souhaités comme

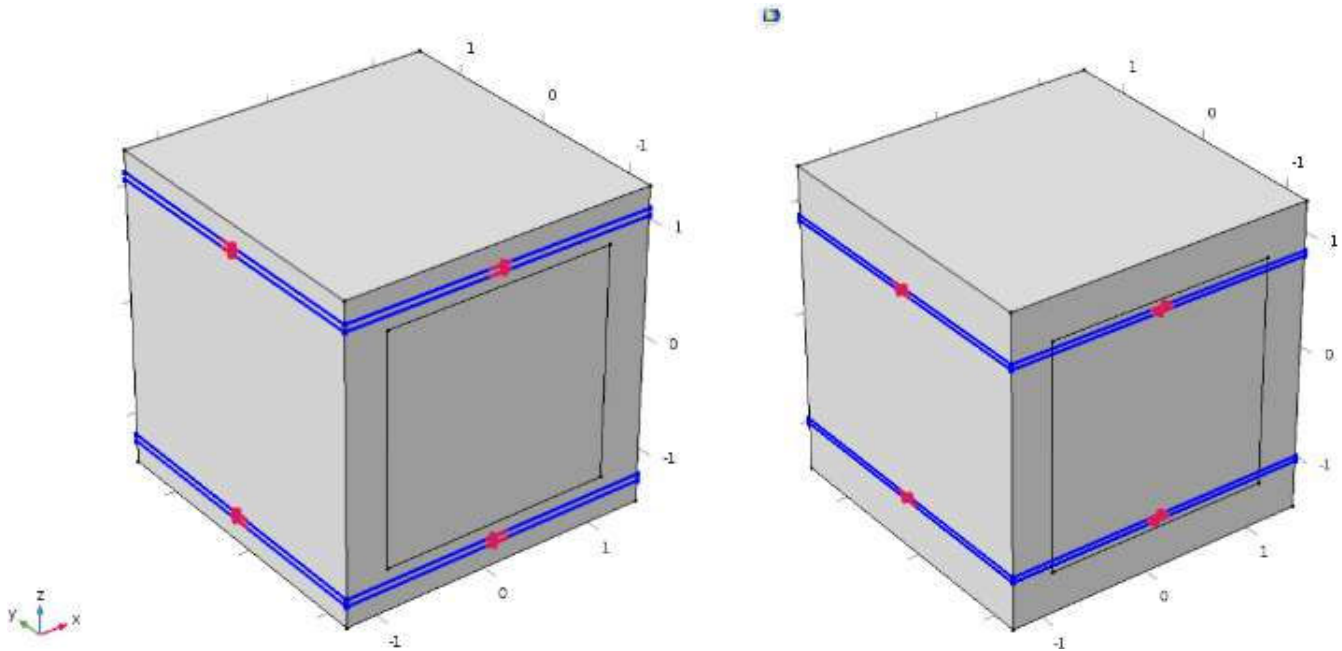


FIGURE 4.2 – Design de la bobine $G_{1,0}$ à gauche et de la bobine $G_{3,0}$ à droite. Le carré central représente la porte d'entrée.

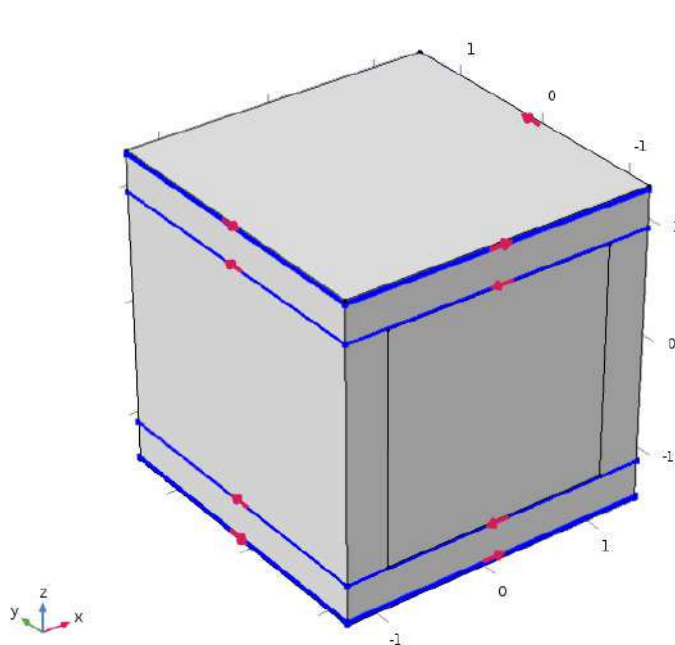


FIGURE 4.3 – Design de la bobine $G_{2,0}$.

la conséquence d'un champ issu d'une bobine parfaite (ne créant pas de tels gradients) mais à une position $x+dx$:

$$B_z(x) = B_z^{G_{1,1}}(x) + B_z^{G_{other}}(x) = G_{1,1} \cdot (x + dx) \quad (4.5)$$

En mesurant B_z entre $x=-40$ cm et 40 cm, on obtient plusieurs valeurs de dx . On établit donc un critère sur la déviation standard sur dx :

$$\sigma(dx) < 1 \text{ mm}. \quad (4.6)$$

Le premier problème est lui résolu en regardant cette quantité pour plusieurs valeurs de z. Le design optimisé de la bobine $G_{1,1}$, présenté sur la Fig. 4.4, permet d'avoir une valeur de $\sigma(dx)$ en dessous de 1 mm si leur hauteur est en dessous de 37 cm. Le design de la bobine $G_{1,-1}$ est le même que celui de $G_{1,1}$ tourné de 90 degrés.

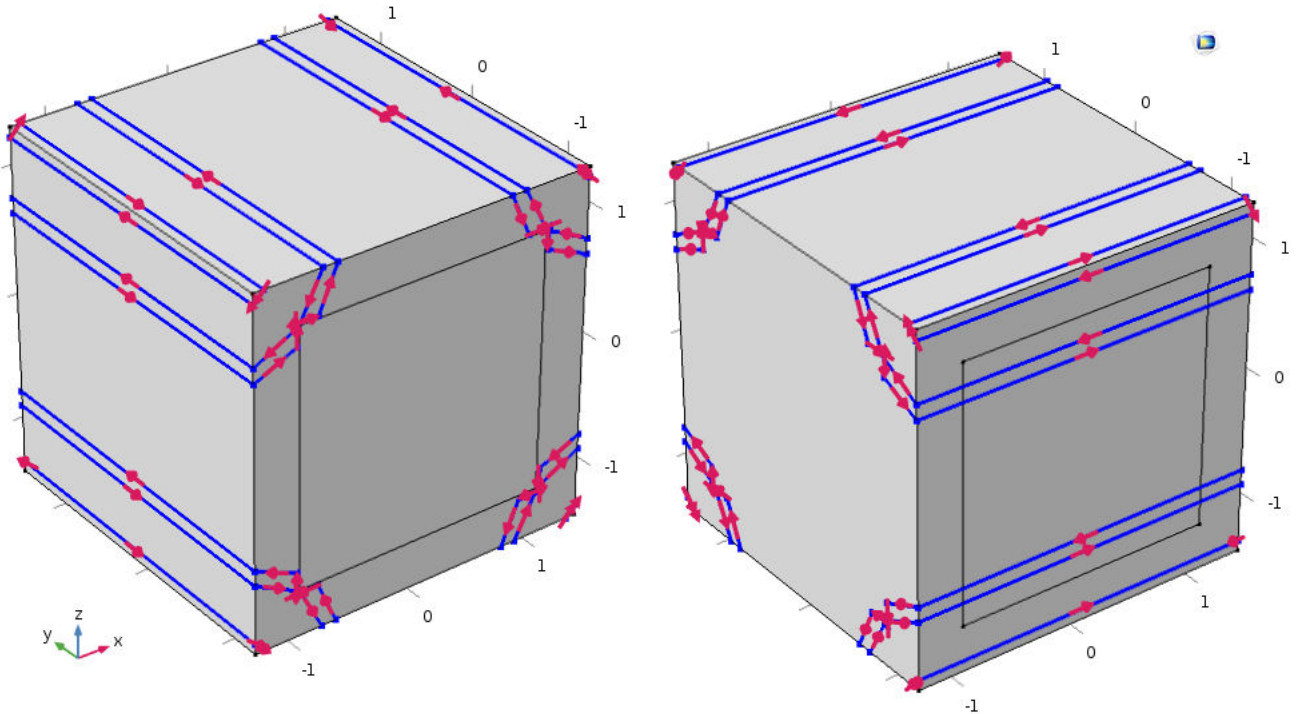


FIGURE 4.4 – Design de la bobine $G_{1,1}$ à gauche et $G_{1,-1}$ à droite.

Les bobines $G_{0,-1}$ et $G_{0,1}$

Les bobines $G_{0,-1}$ et $G_{0,1}$ doivent produire chacune un champ transverse statique, respectivement B_y et B_x d'une intensité maximale de 300 pT avec une uniformité inférieure à 1% afin de produire des champs assez puissants pour sonder l'effet du déplacement lumineux [82]. Ces bobines sont basés sur le concept des bobines de Helmoltz. L'optimisation de leur design s'est effectué en cherchant à minimiser les quantités $\sqrt{B_y^2 + B_z^2}$ pour $G_{0,1}$ et $\sqrt{B_x^2 + B_z^2}$ pour $G_{0,-1}$ en faisant varier le nombre de boucles de courant utilisés, l'orientation de leurs courants et leur nombre. Le design optimisé des bobines est montré sur la Fig. 4.5. Ces bobines créent un champ $B_x = 1.7$ nT/mA (ou $B_y = 1.7$ nT/mA) avec une uniformité $\sigma(B_x) = 0.09$ pT (ou $\sigma(B_y) = 0.09$ pT)

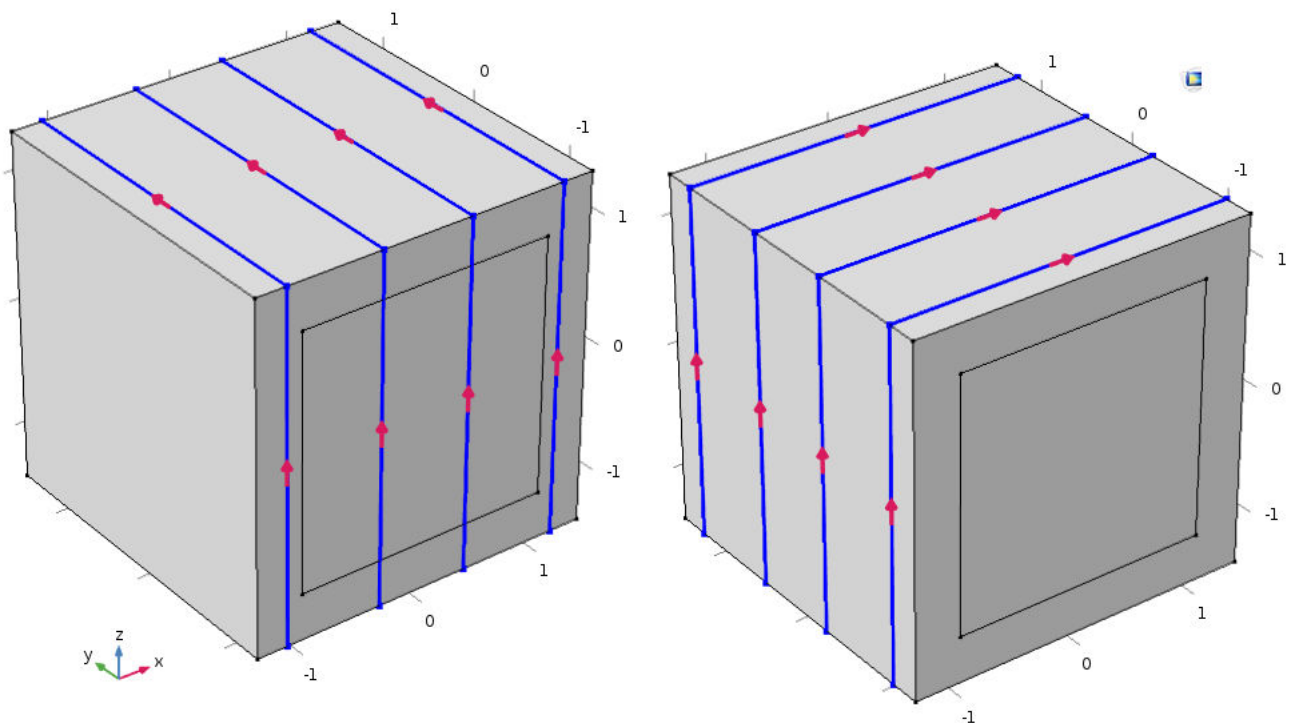


FIGURE 4.5 – Design des bobines $G_{0,1}$ à gauche et $G_{0,-1}$ à droite.

Influence d'un dipôle magnétique et ses contraintes

Faux EDM produit par un dipôle magnétique

Un dipôle situé aux coordonnées (x,y,z) avec un moment magnétique \vec{m} crée un champ $\vec{B}(\vec{r})$ à une distance r :

$$\vec{B}(\vec{r}) = \frac{\mu_0}{4\pi} \left[\frac{3\vec{r}(\vec{m} \cdot \vec{r})}{r^5} - \frac{\vec{m}}{r^3} \right] \quad (5.1)$$

Ce champ local est à l'origine de non-uniformités qui induisent un faux EDM, calculé par :

$$d_{false}^{dip} = -\frac{\hbar|\gamma_n\gamma_{Hg}|}{2c^2} \langle xB_x^{dip} + yB_y^{dip} \rangle. \quad (5.2)$$

Ce faux EDM est partiellement corrigé par la technique du point de croisement (pour nEDM) ou le gradient G_{TB} (pour n2EDM) (voir la partie sur le faux EDM v×E du chapitre 2). Le faux EDM résiduel s'évalue par :

$$d_{res} = -\frac{\hbar|\gamma_n\gamma_{Hg}|}{2c^2} \left(\langle xB_x^{dip} + yB_y^{dip} \rangle + \frac{R^2}{4} \langle \frac{\partial B_z^{dip}}{\partial z} \rangle \right). \quad (5.3)$$

Si le moment magnétique est orienté selon x,y ou z, il est possible de le mettre en facteur de l'équation. Le faux EDM est alors linéairement proportionnel à ce moment. Cela est exploité pour imposer une limite sur le moment magnétique correspondant une exigence sur l'EDM, appelé d_{target} .

Le cas de l'expérience nEDM

Le faux EDM produit par le dipôle magnétique, ainsi que le faux EDM résiduel sont calculés pour nEDM dans une chambre de précession de rayon R=23.5 cm et de hauteur H=12 cm centrée à l'origine du système. La figure Fig. 5.1 montre un exemple de ces deux EDM pour un dipôle avec un moment $m_z = 10 \text{ nA.m}^2$. La chambre est montrée au centre (en blanc). La figure de droite montre le faux EDM créé par le dipôle dans le plan XZ ($y=0$), et celle de droite montre l'EDM résiduel dans ce même plan. On constate globalement que l'intensité de l'EDM résiduel est inférieure d'un facteur 10 à celle de l'EDM créée par le dipôle. Ce faux EDM résiduel est de l'ordre de grandeur de $10^{-28} e \text{ cm}$ autour de la chambre de précession, ce qui n'est pas loin de l'ordre de grandeur de notre mesure.

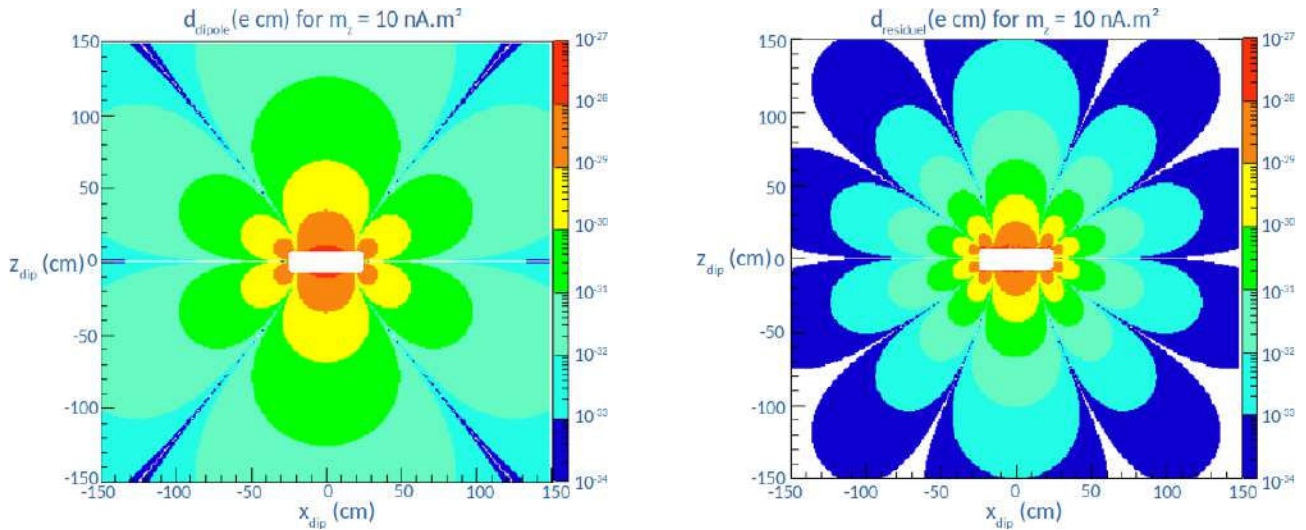


FIGURE 5.1 – Le faux EDM d_{false}^{dip} (à gauche) et l'EDM résiduel d_{res} (à droite) induit par un dipôle $m_z = 10 \text{ nA.m}^2$ dans le plan XZ. Le rectangle blanc correspond à la chambre de précession.

Le cas de l'expérience n2EDM

Pour n2EDM, le faux EDM est estimé comme étant la moyenne des faux EDM créé par un dipôle dans la chambre du haut et dans la chambre du bas. On a donc :

$$\begin{aligned} d_{dip} &= \frac{d_{dip}^T + d_{dip}^B}{2} \\ &= -\frac{\hbar |\gamma_n \gamma_{Hg}|}{2c^2} \frac{\langle xB_x^{dip} + yB_y^{dip} \rangle^T + \langle xB_x^{dip} + yB_y^{dip} \rangle^B}{2}. \end{aligned} \quad (5.4)$$

La correction de l'EDM est également différente, puisqu'elle utilise le gradient G_{TB} . On a donc au final l'EDM résiduel :

$$d_{res} = -\frac{\hbar |\gamma_n \gamma_{Hg}|}{2c^2} \left[\frac{\langle xB_x^{dip} + yB_y^{dip} \rangle^T + \langle xB_x^{dip} + yB_y^{dip} \rangle^B}{2} + \frac{R^2}{4} \frac{\langle B_z \rangle^T - \langle B_z \rangle^B}{H'} \right] \quad (5.5)$$

La figure de gauche de Fig. 5.2 montre le faux EDM crée par un dipôle avec un moment magnétique aligné selon l'axe z avec un moment $m_z = 10 \text{ nA.m}^2$ dans le plan XZ ($y=0 \text{ m}$). La figure de droite elle montre l'EDM résiduel dans ce même plan.

De la même façon que pour nEDM, on peut regarder quelle position du dipôle sur la chambre à vide ou sur la bobine B_0 va créer le plus large EDM. Par proportionnalité, on obtient ainsi des limites sur le moment magnétique de tels dipôles. Ainsi pour n2EDM, un dipôle situé sur la bobine B_0 doit avoir un moment inférieur à 56306 nA.m^2 pour produire un EDM inférieur à $1 \times 10^{-28} \text{ e cm}$, et inférieur à 1431 nA.m^2 s'il est situé sur la chambre à vide.

Assumons maintenant que l'on ait non plus un dipôle, mais N dipôles. Si l'on assume une orientation aléatoire du dipôle, une approche conservative serait de considérer tout ces dipôles localisés à la position créant le plus grand EDM. En ce cas, le faux EDM produit par ces N dipôles est donné par $\sqrt{N} \cdot d_{max}$. Ainsi, pour 100 dipôles localisés sur la chambre à vide, la contrainte magnétique sur ceux-ci devient $1431/\sqrt{100} = 143.1 \text{ nA.m}^2$.

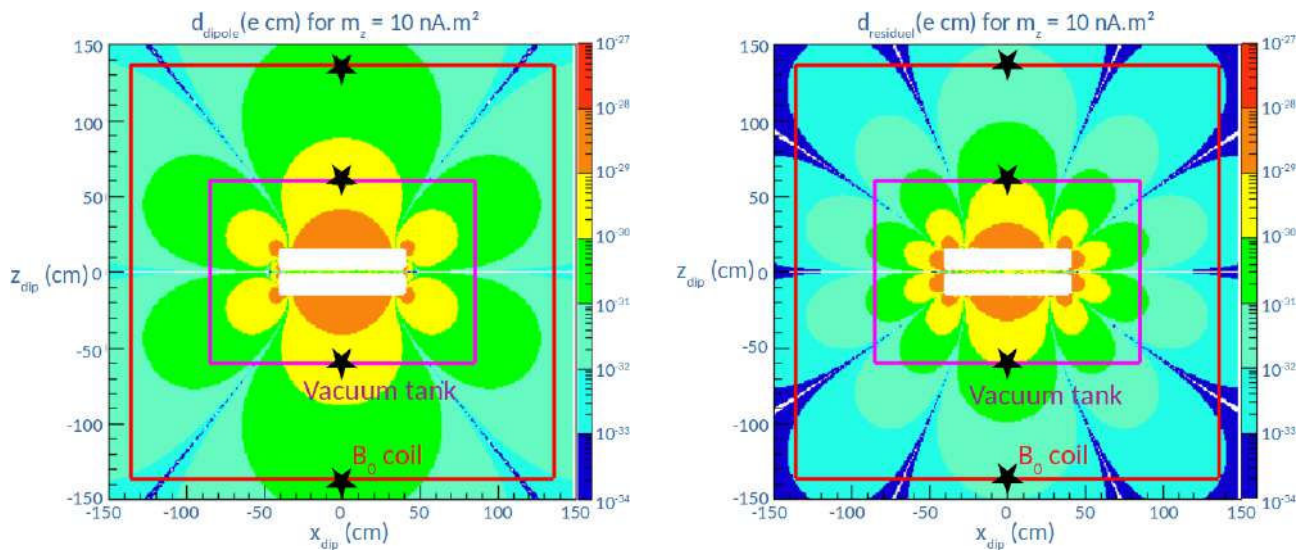


FIGURE 5.2 – Le faux EDM d_{dip} induit par un dipôle de moment $m_z = 10 \text{ nA} \cdot \text{m}^2$ dans le plan XZ ($y=0 \text{ m}$) est montré dans la figure de gauche. Dans celle de droite est montré l'EDM résiduel dans le même plan que précédemment. Le carré rouge montre les contours de la bobine B_0 , le rectangle violet celui de la chambre à vide, et enfin les petits rectangles blancs correspondent aux chambres de précessions. Les étoiles noires correspondent à la position du dipôle produisant le plus grand EDM (selon que le dipôle soit sur la chambre à vide ou sur la bobine B_0).

Conclusion

Le but de cette thèse est d'étudier le design du système de bobines pour l'expérience n2EDM. Cette expérience a pour but d'abaisser la limite supérieure du nEDM dans la gamme 10^{-27} - 10^{-28} e cm. Cela nécessite d'améliorer l'uniformité du champ magnétique et de réduire les erreurs systématiques.

Le design de la bobine B_0 qui doit produire le champ magnétique principal de l'expérience a été présenté. La bobine B_0 produit un champ de 1 μT en son centre avec une uniformité $\sigma(B_z) < 170$ pT en utilisant un courant de 11.94 mA. Cependant, les imperfections mécaniques, et notamment un déplacement vertical de la bobine par rapport au blindage, créent des non-uniformités. Un tel déplacement de 0.25 mm induit déjà un champ qui dépasse les exigences. C'est pourquoi l'installation de la bobine sera accompagné d'une campagne de mapping du champ magnétique afin d'ajuster au mieux la position verticale de la bobine. De plus, des bobines correctrices vont corriger les non-uniformités restantes.

Ces bobines sont introduites dans le chapitre quatre. Tout d'abord les TRIM coils array ont été étudiées. Elles consistent en 56 bobines ayant chacune son alimentation. Il a été montré qu'elles permettent de corriger de grandes non-uniformité du champ dans la gamme de courant prévue. L'expérience a également besoin de plusieurs bobines devant produire chacune un gradient spécifique : ce sont les bobines harmoniques. Les bobines $G_{1,0}$, $G_{2,0}$ et $G_{3,0}$ doivent notamment permettre de supprimer le gradient correspondant afin de satisfaire les exigences sur le champ magnétique. Les bobines $G_{1,1}$ et $G_{1,-1}$ doivent être capable de mesurer la position des magnétomètres Césium avec une déviation standard < 1 mm. Enfin, les bobines $G_{0,1}$ et $G_{0,-1}$ doivent produire un champ transverse statique de 300 pT avec une uniformité de 1%. Le design optimisé de chacune de ces bobine est montré. Elles satisfont leurs exigences respectives.

Enfin, l'étude de l'influence d'un dipôle magnétique dans le cas des expériences nEDM et n2EDM a été étudié. Il permet de contraindre le moment magnétique de ces dipôles selon leur localisation. Pour le cas n2EDM notamment, un dipôle localisé sur la chambre à vide doit avoir un moment magnétique inférieur à environ 1400 nA.m^2 , et inférieur à environ 56300 nA.m^2 s'il est localisé sur la bobine B_0 .

En addition du système de bobine étudié dans cette thèse, l'expérience n2EDM bénéficie de plusieurs améliorations notables : l'usage de deux chambres de précession (contre une pour nEDM) qui augmente considérablement le nombre de neutrons et donc la sensibilité statistique, l'usage d'un champ électrique plus intense, un contrôle du champ magnétique plus poussé, avec un blindage de 6 couches de mu-metal, et un monitorage de celui ci via deux types de magnétomètres, les comagnétomètres mercures et les magnétomètres césium. Toutes ses améliorations devraient permettre à l'expérience n2EDM de sonder la gamme de 10^{-27} e cm, et ouvre la perspective d'une version amélioré de n2EDM, utilisant deux chambres plus large avec un diamètre

de 100 cm, et une valeur "magique" du champ magnétique de 10 μT pour lequel l'effet systématique principal est fortement supprimé. De telles améliorations pourront permettre d'explorer la gamme du $10^{-28} e \text{cm}$, et ainsi de contraindre la physique au delà du modèle standard.

Appendices

A

The Wigner-Eckart theorem

Given a observable $T^{(k)}$ with $2k+1$ component $T_q^{(k)}$ (with $-k \leq q \leq k$) and an angular momentum state $|lm\rangle$, the Wigner-Eckart theorem allows the state $\langle l'm'|T_q^{(k)}|lm\rangle$ to split into:

$$\langle l'm'|T_q^{(k)}|lm\rangle = \langle l'|\|T^{(k)}||l\rangle\langle l'm'kq|lm\rangle. \quad (\text{A.1})$$

Applying this theorem to a vector operator \vec{v} , like \vec{d} or $\vec{\mu}$ for instance, and to a $1/2$ spin particle, we get :

$$\left\langle \frac{1}{2}m' \left| \vec{v}_q \right| \frac{1}{2}m \right\rangle = \left\langle \frac{1}{2} \left| |\vec{v}| \right| \frac{1}{2} \right\rangle \left\langle \frac{1}{2}m'kq \left| \frac{1}{2}m \right. \right\rangle. \quad (\text{A.2})$$

$$\left\langle \frac{1}{2}m' \left| \vec{S}_q \right| \frac{1}{2}m \right\rangle = \left\langle \frac{1}{2} \left| |\vec{S}| \right| \frac{1}{2} \right\rangle \left\langle \frac{1}{2}m'kq \left| \frac{1}{2}m \right. \right\rangle. \quad (\text{A.3})$$

Dividing Eq. A.2 by Eq. A.3, we get :

$$\left\langle \frac{1}{2}m' \left| \vec{v}_q \right| \frac{1}{2}m \right\rangle = \frac{\left\langle \frac{1}{2} \left| |\vec{v}| \right| \frac{1}{2} \right\rangle}{\left\langle \frac{1}{2} \left| |\vec{S}| \right| \frac{1}{2} \right\rangle} \cdot \left\langle \frac{1}{2}m' \left| \vec{S}_q \right| \frac{1}{2}m \right\rangle \quad (\text{A.4})$$

Finally, multiplying by the vector \vec{e}_q and summing on all q , we get :

$$\vec{v} = \frac{\left\langle \frac{1}{2} \left| |\vec{v}| \right| \frac{1}{2} \right\rangle}{\left\langle \frac{1}{2} \left| |\vec{S}| \right| \frac{1}{2} \right\rangle} \cdot \vec{S} \quad (\text{A.5})$$

It means that a vector operator \vec{v} of a $1/2$ spin particle (like \vec{d} or $\vec{\mu}$ for the neutron for instance) must be aligned along the spin, and implies that the transformations under symmetries of this vector will be the same as the spin's transformations.

B

General description of COMSOL

The simulations used to design the coils system are performed with the COMSOL multiphysics simulation software (version 5.2a). This software use the Finite Element Method (FEM), which will be discussed in section B. As for many simulation softwares, the balance is in between the computation loads and the level of detail wanted for the on the simulation. This is why the influence of the meshing as well as the use of symmetries will be presented in this chapter.

General Steps to use COMSOL

This section briefly explains how to operate the COMSOL software. An extensive documentation can be found on the COMSOL website¹.

Once started, COMSOL proposes to start either with a blank model, or with a model wizard. In the second case, it is possible to choose between several kind of geometries (3D, 2D, 1D, 0D,...), to select the physics that you want to simulate (AC/DC, Heat Transfer,...) and the kind of study that you want to perform (stationary, time-dependent,...). This choice is not definitive and everything can be changed once with the main interface.

The interface is shown in Fig. B.1. The model builder, in violet, shows every part of the simulations. The main parts are :

- **The geometry section** is used to built the geometry. It allows to create several geometrical shapes, as rectangles, spheres, etc. and integrates several tools such as unions, differences, rotations, and so on. It is also possible to import a pre-built geometry from COMSOL, and from other software as CATIA for instance.
- **The material section** is required in most of the physics studies. It allows to select the materials used in the geometry and attributes to them their physical properties. Many are already defined in the COMSOL library. However it is also possible to totally define a material, or to change its defined physical properties (the permeability of a material for exemple).
- **The Physics section** is were you define the physical system to study. It can be done by setting boundary conditions (which can also be used to reproduce the system symmetries, see 3.1.2), apply a current on an edge, a temparature on a surface, etc.
- **The Mesh section** is one of the most important section. It defines the meshing of the geometry, a primordial step for FEM resolution. Several kind of meshes are available (using tetrahedric or quadrilaterals elements or different size elements for instance). However the user can entirely customize the way the meshing is performed.

1. <https://www.comsol.fr/documentation>

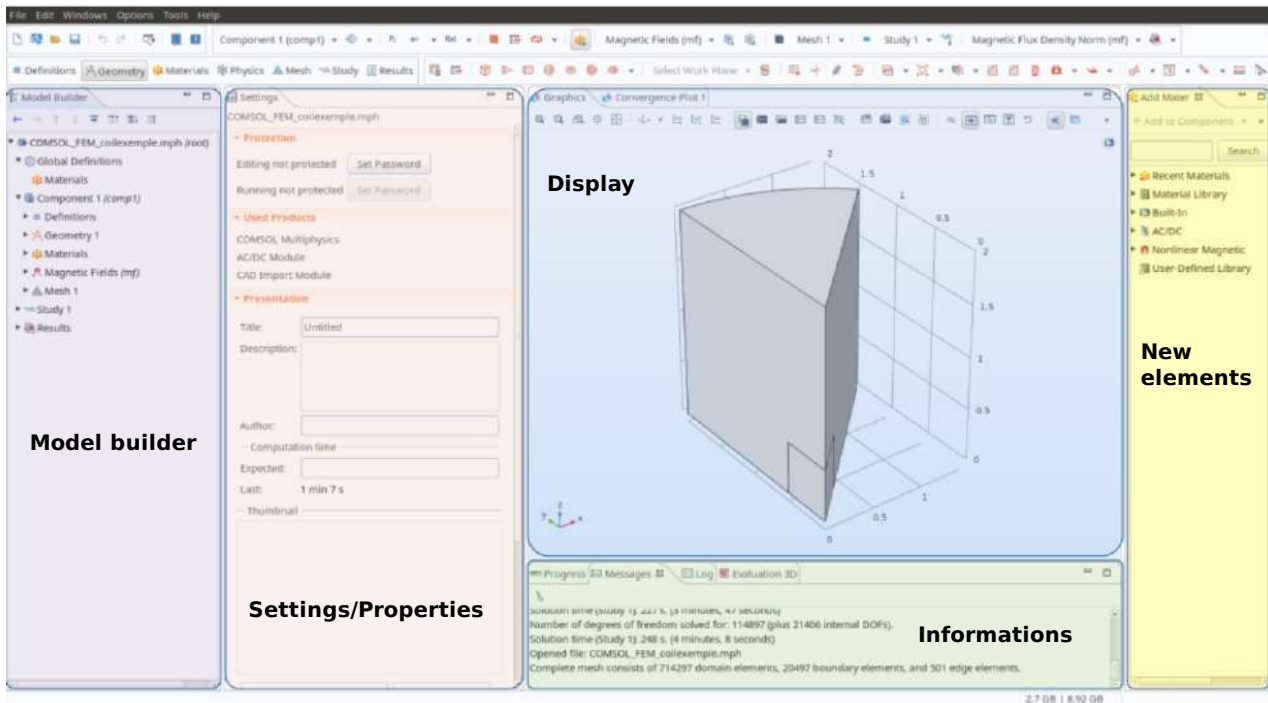


Figure B.1 – The COMSOL interface. The violet region corresponds to the model builder, the orange region to the settings/properties window, the blue region is the display, the yellow region is used to implement new parts (Physics, study, materials..) and the green region displays all the informations like the computing progress, the table and text results, and more general informations. It also have a log.

- **The Study section** defines how a physical problem can be solved. For a time-dependent study for exemple, there is timestep to be declared. It is also possible ot ask for several studies by modifying a parameter, with a parametric sweep, or an optimisation.
- **The Result section** displays the final results. Many tools are available to see the solution in a particular region, to get an averaged quantity in a volume, to look at the meshing, to produce graphs, tables and so on. It also contains the export part from which data files, geometries or figures can be extracted.

Finite Element Method (FEM)

The Finite Element Method relies on the discretisation of the geometry with a meshing, which separates the geometry into elements. The exact solution of the input calculations is computed at those element nodes, and then is extrapolate between ever pairs of nodes. Different kind of elements, size or extrapolating functions can be used. Let's study an exemple to better understand the procedure (from [84]).

One Dimension exemple

The goal is to solve the equation :

$$\frac{d^2u(x)}{dx^2} - f(x) = 0 \text{ with } x \in \Omega = [0, 1] \text{ and } f(x) = x ; \quad (\text{B.1})$$

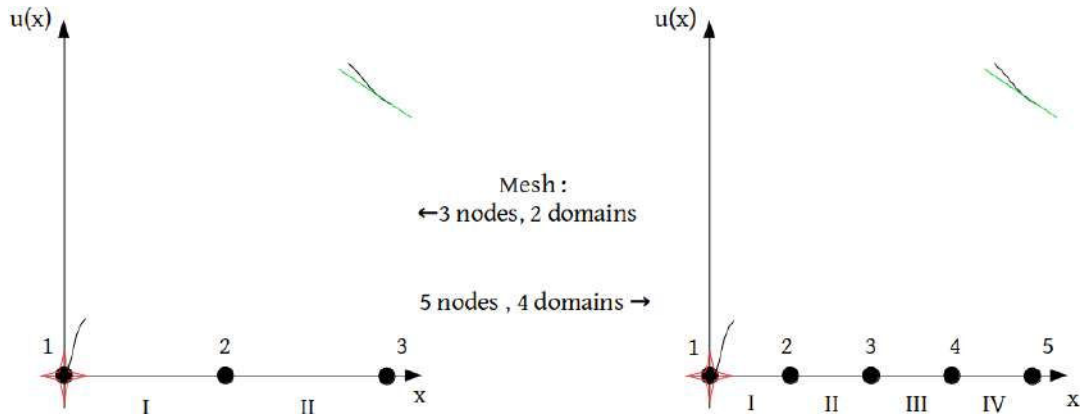


Figure B.2 – Finite Element Method meshing in a 1D case. The red star and the green line corresponds to the boundary conditions.

knowing the boundary conditions :

$$\begin{cases} u(0) = 0 & \text{(the red star),} \\ \frac{du(x)}{dx} = G & \text{(the green line).} \end{cases} \quad (\text{B.2})$$

The FEM need at first a mesh. For this we define a certain amount N of mesh nodes i for whom $x=X_i$, and $u(X_i)=U_i$. Each successives two nodes i and $i+1$ is defining an element domain $\Omega_e =]X_i, X_{i+1}[$, such that $\Omega = \cup_e \Omega_e$. We then have $N_e = N - 1$ element domain.

The goal is to find the solutions U_i on the nodes, and to interpolate between each of them to build the solution.

To simplify the situation, we consider an evenly space between each node.

For our exemple, we will solve our problem on two different meshes : the first one is composed of 3 nodes and 2 domains, whereas the second one is made of 5 nodes and 4 domains. The two meshes as well as the boundary conditions presented in Eq. B.2 are shown in Fig. B.2.

Now to get the values U_i , we will need to work on each element one by one. We starts by doing an isomorphism between each point x of the element Ω_e and the points ξ of the element $\hat{\Omega} =]-1, 1[$. This element is called parent element. The coordinates x and ξ are linked by the equations :

$$x(\xi) = \xi \frac{(X_{e+1} - X_e)}{2} + \frac{(X_{e+1} + X_e)}{2}, \quad (\text{B.3})$$

$$\xi(x) = \frac{2x - (X_{e+1} + X_e)}{(X_{e+1} - X_e)}. \quad (\text{B.4})$$

Now we can define on the parent element $\hat{\Omega}$ a number p of nodes k , in which $\xi = \Xi_k$. On each of those nodes is associated a polynomial function Φ of degree $p-1$, defined so that it equals 1 at this node and 0 on the other nodes . In our exemple, we chose $p=2$ points, on the coordinates $\xi = -1$ and $\xi = 1$. Thus, we will end with 2 linear functions:

$$\Phi_1^e(\xi) = (1 - \xi)/2 \text{ associated to the node } p=1, \quad (\text{B.5})$$

$$\Phi_2^e(\xi) = (1 + \xi)/2 \text{ associated to the node } p=2. \quad (\text{B.6})$$

We can also get their derivatives :

$$\Phi_{1,\xi}^e(\xi) = -1/2 \quad (\text{B.7})$$

$$\Phi_{2,\xi}^e(\xi) = 1/2. \quad (\text{B.8})$$

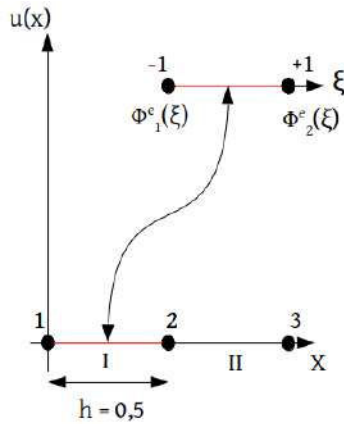


Figure B.3 – The Domain X is divided in 2 domains (I and II) divided by 3 nodes (1,2 and 3). Each domain can be transformed on the element domain $\hat{\Omega} = [-1, 1]$ on which ξ is the variable. On this interval are defined two nodes and their associated functions $\Phi_1^e(\xi)$ and $\Phi_2^e(\xi)$.

From this we can write the relation between x and ξ :

$$x^e(\xi) = X_e \Phi_1^e(\xi) + X_{e+1} \Phi_2^e(\xi), \quad (\text{B.9})$$

The Fig. B.3 shows in the 3 nodes mesh the isomorphism between the domain 1 and the parent element.

The initial problem Eq. B.1 can be rewritten as:

$$A \cdot U = B + G, \quad (\text{B.10})$$

The matrices A and B are built from the elements matrices A^e and B^e assiociated to the elements e .

The elements of those matrices are computed from the local functions, their derivatives, and the function f . We have:

$$\begin{aligned} A_{kl}^e &= \int_e [\Phi_{k,x}^e(x)] [\Phi_{l,x}^e(x)] dx \\ &= \int_{-1}^1 \left[\Phi_{k,\xi}^e(\xi) \frac{d\xi}{dx} \right] \left[\Phi_{l,\xi}^e(\xi) \frac{d\xi}{dx} \right] \frac{dx}{d\xi} d\xi \\ &= \int_{-1}^1 \Phi_{k,\xi}^e(\xi) \Phi_{l,\xi}^e(\xi) \frac{d\xi}{dx} dx \\ A_{kl}^e &= \frac{2}{X_{e+1} - X_e} \int_{-1}^1 \Phi_{k,\xi}^e(\xi) \Phi_{l,\xi}^e(\xi) d\xi \end{aligned} \quad (\text{B.11})$$

and

$$\begin{aligned} B_k^e &= \int_e [f(x)] [\Phi_k^e(x)] dx \\ &= \int_{-1}^1 [f(x(\xi))] [\Phi_k^e(\xi)] \frac{dx}{d\xi} d\xi \\ B_k^e &= \frac{X_{e+1} - X_e}{2} \int_{-1}^1 f(x(\xi)) \Phi_k^e(\xi) \frac{dx}{d\xi} d\xi \end{aligned} \quad (\text{B.12})$$

in which k,l are two nodes of the element $\hat{\Omega}$.

Now we can compute for each domain e the matrices A^e and B^e . It gives for the domain I :

$$A^I = \frac{1}{h} \begin{bmatrix} 1 & -1 \\ -1 & 1 \end{bmatrix}; B^I = \frac{h}{6} \begin{bmatrix} 1/2 \\ 1 \end{bmatrix}, \quad (\text{B.13})$$

and for the domain II:

$$A^{II} = \frac{1}{h} \begin{bmatrix} 1 & -1 \\ -1 & 1 \end{bmatrix}; B^{II} = \frac{h}{6} \begin{bmatrix} 2 \\ 5/2 \end{bmatrix}. \quad (\text{B.14})$$

Finally we can concatenate the A and B matrices of the two elements to get the global matrix A and B following :

$$A_{i,i-1} = A_{21}^{e=i-1}; \quad (\text{B.15})$$

$$A_{i,i} = A_{22}^{e=i-1} + A_{11}^{e=i}; \quad (\text{B.16})$$

$$A_{i,i+1} = A_{12}^{e=i}; \quad (\text{B.17})$$

$$B_i = B_2^{e=i-1} + B_1^{e=i}. \quad (\text{B.18})$$

The other elements, such as A_{13} for instance, are equal to 0. Also, the elements which are not defined, such as the $e=0$ or $e=3$ elements in this exemple, equal 0 too.

It gives:

$$A = \frac{1}{h} \begin{bmatrix} 1 & -1 & 0 \\ -1 & 2 & -1 \\ 0 & -1 & 1 \end{bmatrix} \quad (\text{B.19})$$

and

$$B = \frac{h}{6} \begin{bmatrix} 1/2 \\ 6/2 \\ 5/2 \end{bmatrix}. \quad (\text{B.20})$$

Now,we can solve Eq. B.10. To simplify the problem, we will consider that $G = \frac{du(1)}{dx} = 0$.

$$\frac{1}{h} \begin{bmatrix} 1 & -1 & 0 \\ -1 & 2 & -1 \\ 0 & -1 & 1 \end{bmatrix} \cdot \begin{bmatrix} U_1 \\ U_2 \\ U_3 \end{bmatrix} = \frac{h}{6} \begin{bmatrix} 1/2 \\ 6/2 \\ 5/2 \end{bmatrix} \quad (\text{B.21})$$

The boudary conditions given by Eq. B.2 needed $U_1 = u(0) = 0$. We then only have to solve :

$$\frac{1}{h} \begin{bmatrix} 2 & -1 \\ -1 & 1 \end{bmatrix} \cdot \begin{bmatrix} U_2 \\ U_3 \end{bmatrix} = \frac{h}{6} \begin{bmatrix} 6/2 \\ 5/2 \end{bmatrix}, \quad (\text{B.22})$$

which gives the solutions:

$$\begin{bmatrix} U_1 = 0 \\ U_2 = 11/48 \\ U_3 = 1/3 \end{bmatrix} \quad (\text{B.23})$$

To complete the solution, we need to interpolate linearly the solution between those nodes. We end with the solution presented in Fig. B.5 (left panel).

Lets now solve this problem with a finer mesh, made of 5 nodes separating 4 domains, as shown in Fig. B.4. Note that the lenght of each domain is now $h = 0.25$, compare to the previous $h = 0.5$.

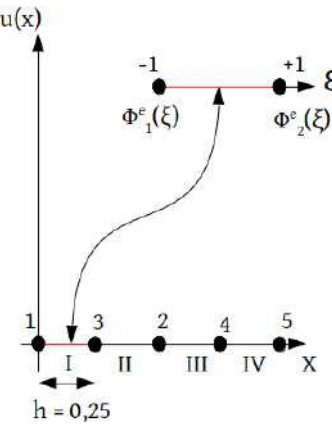


Figure B.4 – The Domain X is now divided in 4 domains (I to IV) divided by 5 nodes (1 to 5). The lenght of each domain is $h = 0.25$.

We can again compute for each domain the matrix A^e and B^e :

$$A^I = \frac{1}{h} \begin{bmatrix} 1 & -1 \\ -1 & 1 \end{bmatrix} ; \quad B^I = \frac{h}{6} \begin{bmatrix} 1/4 \\ 1/2 \end{bmatrix}, \quad (\text{B.24})$$

$$A^{II} = \frac{1}{h} \begin{bmatrix} 1 & -1 \\ -1 & 1 \end{bmatrix} ; \quad B^{II} = \frac{h}{6} \begin{bmatrix} 1 \\ 5/4 \end{bmatrix}, \quad (\text{B.25})$$

$$A^{III} = \frac{1}{h} \begin{bmatrix} 1 & -1 \\ -1 & 1 \end{bmatrix} ; \quad B^{III} = \frac{h}{6} \begin{bmatrix} 7/4 \\ 2 \end{bmatrix}, \quad (\text{B.26})$$

$$A^{IV} = \frac{1}{h} \begin{bmatrix} 1 & -1 \\ -1 & 1 \end{bmatrix} ; \quad B^{IV} = \frac{h}{6} \begin{bmatrix} 5/2 \\ 11/4 \end{bmatrix}. \quad (\text{B.27})$$

The new system to solve is then:

$$\frac{1}{h} \begin{bmatrix} 1 & -1 & 0 & 0 & 0 \\ -1 & 2 & -1 & 0 & 0 \\ 0 & -1 & 2 & -1 & 0 \\ 0 & 0 & -1 & 2 & -1 \\ 0 & 0 & 0 & -1 & 1 \end{bmatrix} \cdot \begin{bmatrix} U_1 \\ U_2 \\ U_3 \\ U_4 \\ U_5 \end{bmatrix} = \frac{h}{6} \begin{bmatrix} 1/4 \\ 6/4 \\ 12/4 \\ 18/4 \\ 11/4 \end{bmatrix}. \quad (\text{B.28})$$

Again, the boundary conditions gives us the solution $U_1 = 0$, so we only have to solve:

$$\frac{1}{h} \begin{bmatrix} 2 & -1 & 0 & 0 \\ -1 & 2 & -1 & 0 \\ 0 & -1 & 2 & -1 \\ 0 & 0 & -1 & 1 \end{bmatrix} \cdot \begin{bmatrix} U_2 \\ U_3 \\ U_4 \\ U_5 \end{bmatrix} = \frac{h}{6} \begin{bmatrix} 6/4 \\ 12/4 \\ 18/4 \\ 11/4 \end{bmatrix}, \quad (\text{B.29})$$

which gives us the solution :

$$\begin{cases} U_1 = 0 \\ U_2 = 47/384 \\ U_3 = 11/48 \\ U_4 = 39/128 \\ U_5 = 1/3 \end{cases} \quad (\text{B.30})$$

Notice that the solutions for U_1 , U_3 and U_5 corresponds to the previous solutions with 3 nodes. Then, the resolutions for each point between those nodes are obtain using a linear approximation. In that simple case, the analytical solution can be computed, and is $u(x) = \frac{x(3-x^2)}{6}$.

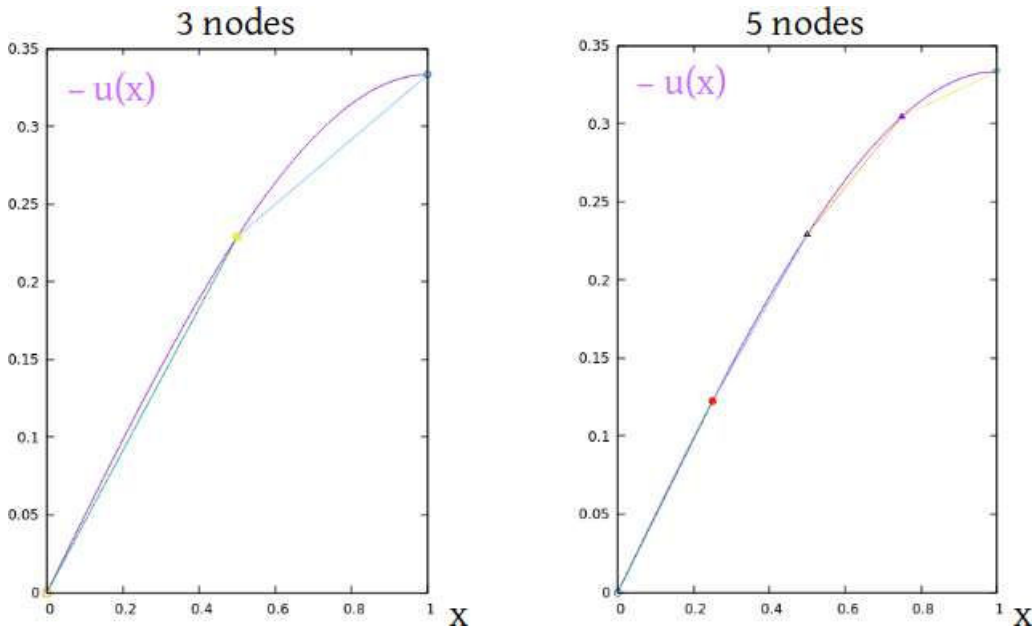


Figure B.5 – On both graphs, the analytical solution is plotted in purple. The approximated solution using a mesh of 3 nodes and 2 domains is shown on the left, and the one with a mesh of 5 nodes and 4 domains is on the right.

Domain	Ω	$\Omega_e =]X_i, X_{i+1}[$	$\bar{\Omega} =]-1, 1[$
Variable	x	x	ξ
Number of nodes	N	2	p
Name of nodes	i	i	k
Variable at nodes	X_i	X_i	Ξ_k
Solution at nodes	U_i	U_i	-
local function	-	-	$\Phi_k^e(\xi) = \delta_{kl}$
matrix A	A	A	A^e
matrix B	B	B	B^e

Table B.1 – Quantities introduced for the FEM.

The Fig. B.5 compares this exact solution with the approximate ones given by the two studied meshes. One can see that for a 1D case, the analytical and FEM nodes solutions are identical. It is not always the same at higher dimensions. The other point shown here is that a finer mesh leads to a better solution.

The Table B.1 summarises the quantities introduced previously, and in which domain they belongs.

Two Dimension exemple

We know consider a 2 Dimensionnal problem, we want to solve :

$$\nabla^2 u(x, y) - 1 = 0 ; 0 < x < 2 , 0 < y < 2 \quad (\text{B.31})$$

with the bondary conditions :

$$u(x, 0) = u(x, 2) = 0 , \quad 0 < x < 2; \quad (\text{B.32})$$

$$u(0, y) = u(2, y) = 0 , \quad 0 < y < 2. \quad (\text{B.33})$$

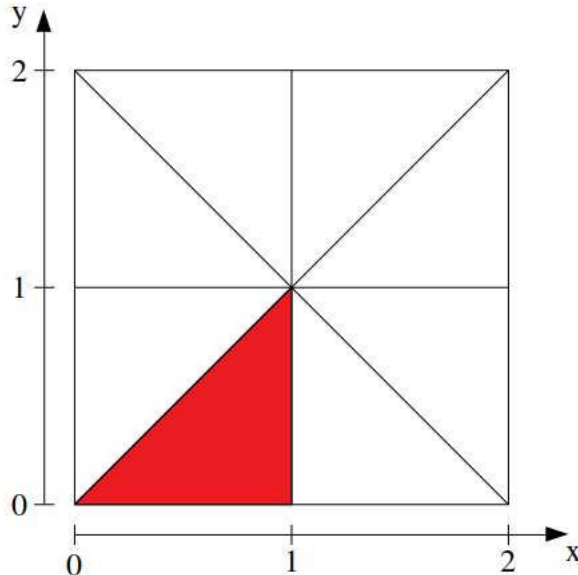


Figure B.6 – The symmetries of the geometry allows to solve the equation only on the red area.

The system is shown in Fig. B.6. However, due to its symmetries, we can solve the equation only for the red part. With a 2D dimension, we will have to translate our variable (x,y) to a 2D dimension parent domain $\hat{\Omega}$, in which those variables isomorphism are ξ and η . The local functions will in that case dependent of those two variables.

As we saw earlier, one way to get more accurate solutions is to refine the mesh, as shown in Fig. B.7.



Figure B.7 – Here is shown one mesh refinement, for a mesh made of 1 domain to a mesh made of 64 domain. Usually, the finer the mesh is, the better the solution will be.

One other way is to change the local functions, by we could also used quadratic functions by doubling the number of nodes p on which the quadratic local function are defined.

The Fig. B.8 shows the two cases : on the left panel, 3 nodes are defined on the parent domain, which leads to the linear functions:

$$\Phi_1^e(\xi, \eta) = 1 - \xi - \eta \quad (B.34)$$

$$\Phi_2^e(\xi, \eta) = \xi \quad (B.35)$$

$$\Phi_3^e(\xi, \eta) = \eta, \quad (B.36)$$

The right panel of Fig. B.8 shows that same element domain on which 6 nodes are defined.

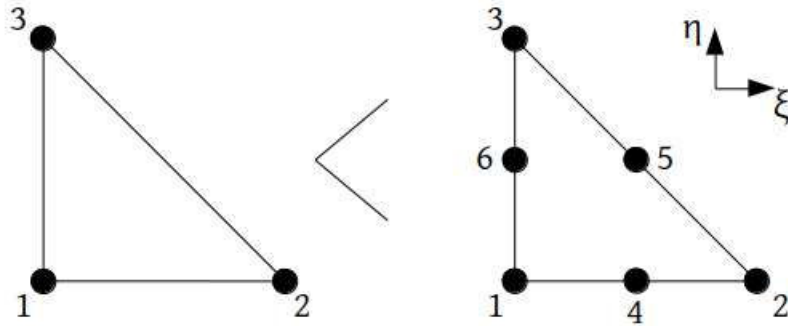


Figure B.8 – Comparision of the nodes for linear functions (on the left) and quadratic functions (on the right) on the element domain.

We can then assiocate to each point a quadratic function: B.8:

$$\Phi_1^e(\xi, \eta) = 1 - 3(\xi + \eta) + 2(\xi + \eta)^2 \quad (\text{B.37})$$

$$\Phi_2^e(\xi, \eta) = \xi(2\xi - 1) \quad (\text{B.38})$$

$$\Phi_3^e(\xi, \eta) = \eta(2\eta - 1) \quad (\text{B.39})$$

$$\Phi_4^e(\xi, \eta) = 4\xi(1 - \xi - \eta) \quad (\text{B.40})$$

$$\Phi_5^e(\xi, \eta) = 4\xi\eta \quad (\text{B.41})$$

$$\Phi_6^e(\xi, \eta) = 4\eta(1 - \xi - \eta). \quad (\text{B.42})$$

The analytical solution of this problem is:

$$u(x, y) = - \sum_{m, n} \frac{64}{\pi^4(m^2 + n^2)mn} \sin\left(\frac{m\pi x}{2}\right) \sin\left(\frac{n\pi y}{2}\right). \quad (\text{B.43})$$

We compare the solutions given by the linear and quadratic functions for different number of elements compared to the analytical value at the central point $u(1, 1) = -0.2946$ in Table B.2.

Domains		Linear Functions			Quadratic Functions		
$N_{domains}$	h	N_{nodes}	$u(1,1)$	error	N_{nodes}	$u(1,1)$	error
1	1	3	-0.3333	13.1%	6	-0.3000	1.83%
4	1/2	6	-0.3125	6.1%	15	-0.2950	0.14%
16	1/4	15	-0.3013	2.3%	45	-0.2947	0.03%
64	1/8	45	-0.2969	0.8%			

Table B.2 – Comparison of the results from the linear and quadratic functions with several number of elements to the analytical value $u(1,1) = -0.2946$.

The case presenting in Fig. B.8 corresponds to the 1 raw, with 1 domain. We can see that using quadratic functions instead of linear ones helps to obtain a more accurate value. Moreover, as it was previously on the 1D problem, refining the mesh (i.e. increasing the number of $N_{domains}$) aslo leads to a more accurate solution.

However, we can instinctively understood that this refinement of the solution is at the price of higher computation loads. This will be shown in the following exemple.

C

The Harmonic polynomial Basis

n°	l	m	Π_x	Π_y	Π_z
1	0	-1	0	1	0
2	0	0	0	0	1
3	0	1	1	0	0
4	1	-2	y	x	0
5	1	-1	0	z	y
6	1	0	-x/2	-y/2	z
7	1	1	z	0	x
8	1	2	x	-y	0
9	2	-3	2xy	(x - y)(x + y)	0
10	2	-2	2yz	2xy	2xy
11	2	-1	-xy/2	-(x ² + 3y ² - 4z ²)/4	2yz
12	2	0	-xz	-yz	-(x ² + y ² - 2z ²)/2
13	2	1	-(3x ² + y ² - 4z ²)/4	-xy/2	2xz
14	2	2	2xz	-2yz	(x - y)(x + y)
15	2	3	(x - y)(x + y)	-2xy	0
16	3	-4	y(3x ² - y ²)	x(x ² - 3y ²)	0
17	3	-3	6xyz	3z(x - y)(x + y)	y(3x ² - y ²)
18	3	-2	-y(3x ² + y ² - 6z ²)/2	-x(x ² + 3y ² - 6z ²)/2	6xyz
19	3	-1	-3xyz/2	-z(3x ² + 9y ² - 4z ²)/4	-3y(x ² + y ² - 4z ²)/4
20	3	0	3x(x ² + y ² - 4z ²)/8	3y(x ² + y ² - 4z ²)/8	-z(3x ² + 3y ² - 2z ²)/2
21	3	1	-z(9x ² + 3y ² - 4z ²)/4	-3xyz/2	-3x(x ² + y ² - 4z ²)/4
22	3	2	-x(x ² - 3z ²)	y(y - 3z ²)	3z(x - y)(x + y)
23	3	3	3z(x - y)(x + y)	-6xyz	x(x ² - 3y ²)
24	3	4	x(x ² - 3y ²)	-y(3x ² - y ²)	0
25	4	-5	4xy(x - y)(x + y)	(x ² - 2xy - y ²)(x ² + 2xy - y ²)	0
26	4	-4	4yz(3x ² - y ²)	4xz(x ² - 3y ²)	4xy(x - y)(x + y)
27	4	-3	-xy(3x ² + y ² - 12z ²)	-(3x ⁴ + 6x ² y ² - 24x ² z ² + 5y ⁴ + 24y ² z ²)/4	4yz(3x ² - y ²)
28	4	-2	-2yz(3x ² + y ² - 2z ²)	-2xz(x ² + 3y ² - 2z ²)	-2xy(x ² + y ² - 6z ²)
29	4	-1	xy(x ² + y ² - 6z ²)/2	(x ⁴ + 6x ² y ² - 12x ² z ² + 5y ⁴ - 36y ² z ² + 8z ⁴)/8	-yz(3x ² + 3y ² - 4z ²)
30	4	0	xz(3x ² + 3y ² - 4z ²)/2	yz(3x ² + 3y ² - 4z ²)/2	(3x ⁴ + 6x ² y ² - 24x ² z ² + 3y ⁴ - 24y ² z ² + 8z ⁴)/8
31	4	1	(5x ⁴ + 6x ² y ² - 36x ² z ² + y ⁴ - 12y ² z ² + 8z ⁴)/4	xy(x ² + y ² - 6z ²)/2	-xz(3x ² + 3y ² - 4z ²)
32	4	2	-4xz(x - y)(x + y)	4yz(y - z)(y + z)	-(x - y)(x + y)(x ² + y ² - 6z ²)
33	4	3	-(5x ⁴ - 6x ² y ² - 24x ² z ² - 3y ⁴ + 24y ² z ²)/4	xy(x ² + 3y ² - 12z ²)	4xz(x ² - 3y ²)
34	4	4	4xz(x ² - 3y ²)	-4yz(3x ² - y ²)	(x ² - 2xy - y ²)(x ² + 2xy - y ²)
35	4	5	(x ² - 2xy - y ²)(x ² + 2xy - y ²)	-4xy(x - y)(x + y)	0

Table C.1 – Harmonic Polynomial basis up to the 4th order.



Allowed Gradients due to broken symmetries

The current symmetries implies to have a field symmetries. Because the field can be decomposed into gradient, those gradient have also to respect the symmetries, otherwise they can exist. For a perfect B_0 and a perfect shield, the current are antisymmetric with respect to the XZ and YZ plane, and symmetric with respect to the XY plane. This implies for the field gradient that the harmonic component have to respect :

$$\text{YZ antisym. plane} \quad \text{XZ antisym. plane} \quad \text{XY sym. plane}$$

$$\Pi_x(-x) = -\Pi_x(x); \quad \Pi_x(-y) = \Pi_x(y); \quad \Pi_x(-z) = -\Pi_x(z) \quad (\text{D.1})$$

$$\Pi_y(-x) = \Pi_y(x); \quad \Pi_y(-y) = -\Pi_y(y); \quad \Pi_y(-z) = -\Pi_y(z) \quad (\text{D.2})$$

$$\Pi_z(-x) = \Pi_z(x); \quad \Pi_z(-y) = \Pi_z(y); \quad \Pi_z(-z) = \Pi_z(z) \quad (\text{D.3})$$

Taking for example two gradients $G_{1,0}$ and $G_{2,0}$, with their corresponding harmonic functions :

$$\Pi(G_{1,0}) = \begin{cases} \Pi_x = -x/2 \\ \Pi_y = -y/2 \\ \Pi_z = z \end{cases} \quad \text{and} \quad \Pi(G_{2,0}) = \begin{cases} \Pi_x = -xz \\ \Pi_y = -yz \\ \Pi_z = -(x^2 + y^2 - 2z^2)/2 \end{cases} \quad (\text{D.4})$$

As we can see, the harmonic function $\Pi_{2,0}$ respects all the conditions imposed by the symmetries; it is the an "allowed" gradient. However, the $\Pi_{1,0}$ doesn't respect the condition Eq. D.3, because $\Pi_z(-z) = -z \neq \Pi_z(z) = z$. Thus, it cannot be part of the magnetic field and is considered as a "forbidden" gradient.

If we consider now a global displacement of the coil with respect to the shield along the z axis, the XY symmetric current plane vanished (i.e. the z symmetry is broken), and the Eq. D.3 has no reason to be respected. Therefore, the gradient $G_{1,0}$ is no longer forbidden.

The Table D.1 shows if the gradients up to the 5th order are allowed or forbidden considering all possible case of symmetry breaking.

Gradients		Broken symmetries							
1	m	None	X	Y	Z	X & Y	X & Z	Y & Z	X & Y & Z
0	-1								
0	0								
0	1								
1	-2								
1	-1								
1	0								
1	1								
1	2								
2	-3								
2	-2								
2	-1								
2	0								
2	1								
2	2								
2	3								
3	-4								
3	-3								
3	-2								
3	-1								
3	0								
3	1								
3	2								
3	3								
3	4								
4	-5								
4	-4								
4	-3								
4	-2								
4	-1								
4	0								
4	1								
4	2								
4	3								
4	4								
4	5								
5	-6								
5	-5								
5	-4								
5	-3								
5	-2								
5	-1								
5	0								
5	1								
5	2								
5	3								
5	4								
5	5								
5	6								

Table D.1 – Formidden (red cell) and allowed (green cell) gradient depending of the broken symmetries un to the 5th order.

E

Description of the others Harmonic Coils

In this appendix are described the Harmonic coils that are not shown in the Section 4.2.

$G_{1,0}$, $G_{2,0}$ and $G_{3,0}$ coils characteristics

This section gives a more complete description of the $G_{1,0}$, $G_{2,0}$ and $G_{3,0}$ coils characteristics in the respective tables Table E.1, Table E.2 and Table E.3.

G _{1,0} coil	
wire height (compared to MSR center)	current direction
$z = -1177.5$ mm	clockwise
$z = +1177.5$ mm	anticlockwise
$z = -1117.5$ mm	clockwise
$z = +1117.5$ mm	anticlockwise
Estimator name	Estimator value (with $I=1$ mA)
$G_{1,0}$	24.87 pT/cm
$G_{3,0}$	$-3.51 \times 10^{-7} \text{ pT/cm}^3$
$G_{5,0}$	$-1.58 \times 10^{-8} \text{ pT/cm}^5$
$G_{7,0}$	$2.57 \times 10^{-13} \text{ pT/cm}^7$
$d_{ratio}(G_{1,0})$	5377

Table E.1 – Characteristics of $G_{1,0}$ coil.

G _{2,0} coil	
wire height (compared to MSR center)	current direction
$z = -1342.5$ mm	anticlockwise
$z = +1342.5$ mm	anticlockwise
$z = -1327.5$ mm	anticlockwise
$z = +1327.5$ mm	anticlockwise
$z = -1012.5$ mm	clockwise
$z = +1012.5$ mm	clockwise
Estimator name	Estimator value (with $I=1$ mA)
$G_{2,0}$	$5.77 \times 10^{-2} \text{ pT/cm}$
$G_{4,0}$	$-1.20 \times 10^{-7} \text{ pT/cm}^3$
$G_{6,0}$	$-7.15 \times 10^{-11} \text{ pT/cm}^5$
$d_{ratio}(G_{2,0})$	206

Table E.2 – Characteristics of $G_{2,0}$ coil.

G _{3,0} coil	
wire height (compared to MSR center)	current direction
$z = -938.5 \text{ mm}$	clockwise
$z = +938.5 \text{ mm}$	anticlockwise
$z = -893.5 \text{ mm}$	anticlockwise
$z = +893.5 \text{ mm}$	clockwise
Estimator name	Estimator value (with $I=1 \text{ mA}$)
$G_{1,0}$	$-7.09 \times 10^{-5} \text{ pT/cm}$
$G_{3,0}$	$3.64 \times 10^{-5} \text{ pT/cm}^3$
$G_{5,0}$	$-1.32 \times 10^{-9} \text{ pT/cm}^5$
$G_{7,0}$	$-4.49 \times 10^{-14} \text{ pT/cm}^7$
$d_{ratio}(G_{3,0})$	62

Table E.3 – Characteristics of G_{3,0} coil.

G_{1,1} and G_{1,-1} design

This section develops the design of the G_{1,1} and G_{1,-1} Harmonic coils.

One of the idea for the Harmonic coils was to built what we called "Crawford Coils", which are obtained by solving the Laplace equations given boundary conditions linked to the coil we want to design[85]. Such a coil for G_{1,1} is shown in Fig. E.1. However, because of its complexity, it has been decided to not build such coil, but it still constitute our starting point to design a simplified version of those coil.

We can notice that an important part of the geometry of the G_{1,1} Crawford coil is that the wires are diagonals on the corner of the cube of side l (representing the frame holding the coil), and almost vertical with a 90 degree turn if the wire is at the center of the coil. We decided to reproduce such an aspect by first parametrize the distance along the x axis between the center of the cube and our coil i , namely parameter $a_i \in]0, l[$, and to give a tilt to the wire with respect to the vertical axis z , namely α_i , such as :

$$\alpha_i = \frac{a_i \cdot (\pi/4)}{l}. \quad (\text{E.1})$$

In that way, a wire at the center of the cube ($a = 0 \text{ m}$) have a null angle, and is vertical, whereas a wire at the extremity of the cube ($a = l$) have an angle of $\pi/4 \text{ rad}$, so is a diagonal.

The second important modification to the geometry is linked to the door. In order to preserve the coil stability, we want as much as possible to avoid the door. This is why we posses two type of design for the loops geometry.

The first design, presented in Fig. E.2, is built for the loops who should cross the door. The quantities shown in the scheme are computed following:

$$l_i = 1.01 + i \cdot 0.01(m), \quad (\text{E.2})$$

$$b_i = (l - l_i) \cdot \tan(\alpha_i). \quad (\text{E.3})$$

The second design is chosen when we don't have to avoid the door. It is shown in Fig. E.3. The quantities shown in that figure are given by :

$$c_i = l - a_i, \quad (\text{E.4})$$

$$d_i = c_i \cdot \tan(\alpha_i), \quad (\text{E.5})$$

$$e_i = \frac{c_i^2}{c_i + d_i}, \quad (\text{E.6})$$

$$f_i = c_i - e_i. \quad (\text{E.7})$$

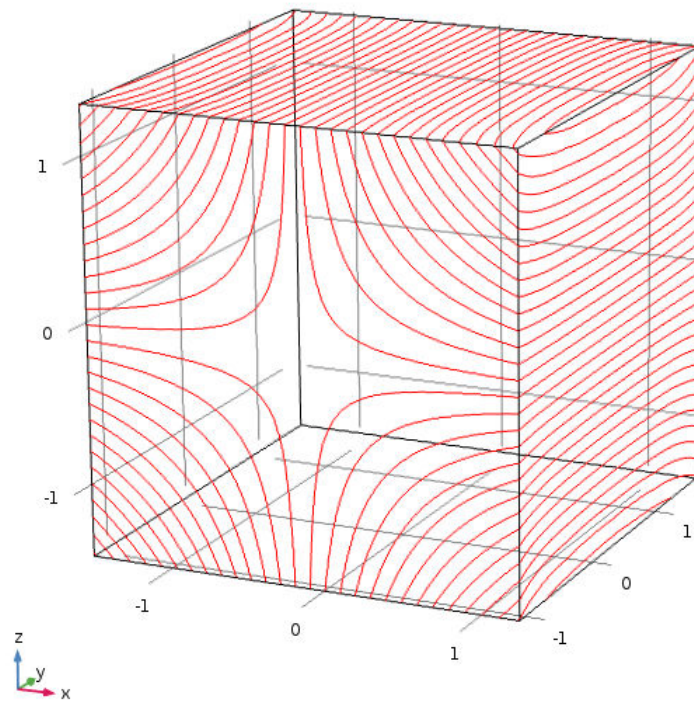


Figure E.1 – G_{1,1} Crawford Coil design.

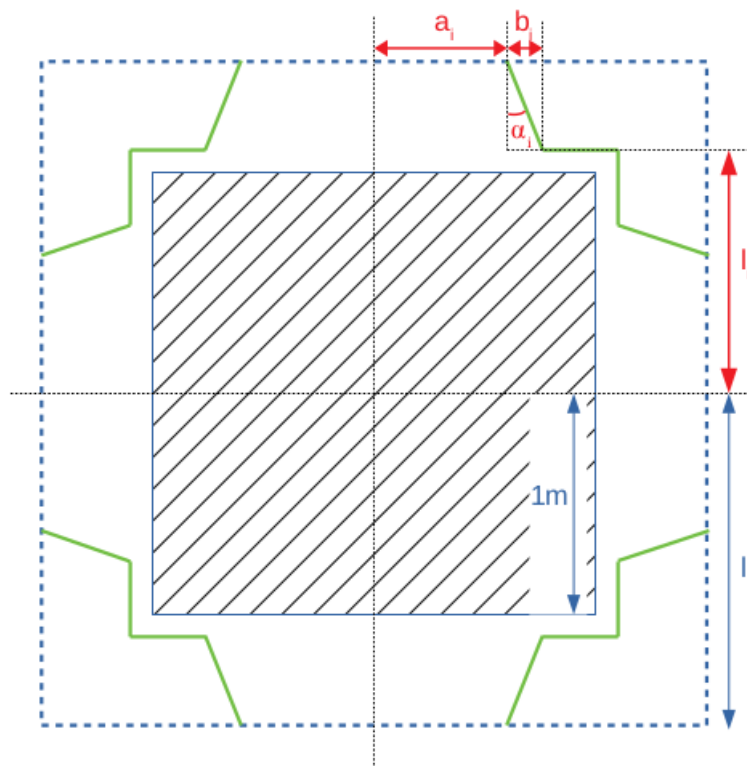
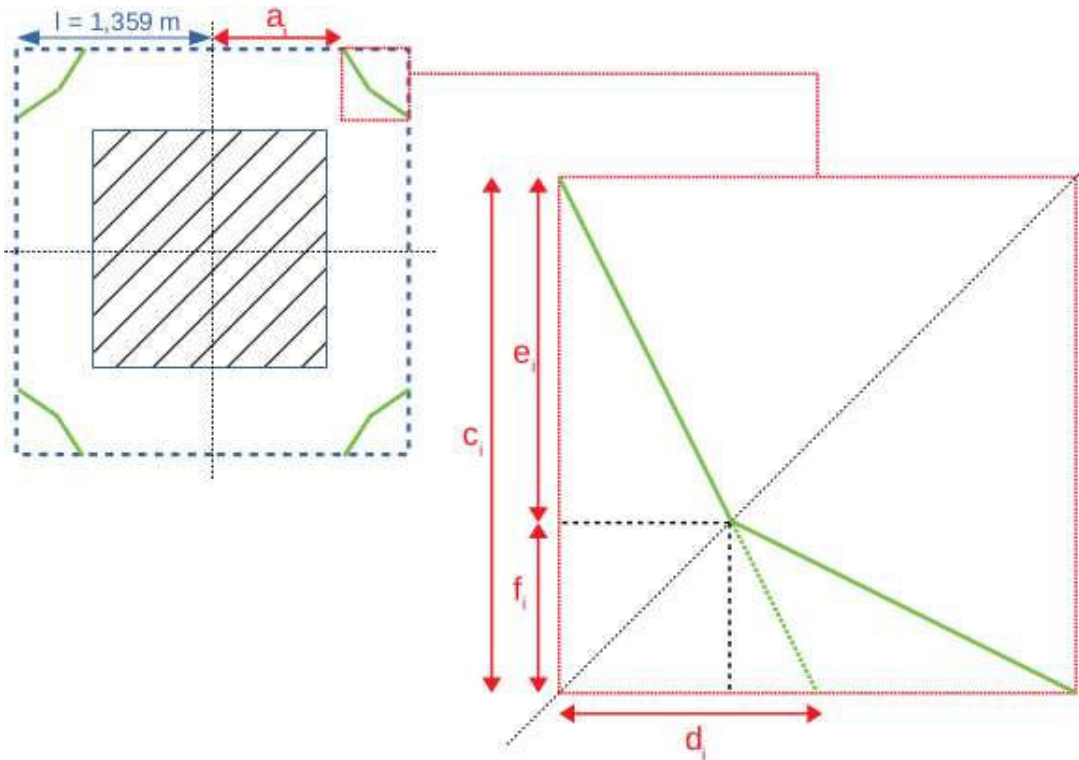


Figure E.2 – The first G_{1,1} loop design, which bypasses the door.

Figure E.3 – The second $G_{1,1}$ loop design.

wire i	l_i	a_i	α_i	b_i	c_i	d_i	e_i	f_i	limit	design
1	1.02 m	0.635 m	0.367 rd (21.0°)	0.130 m	-	-	-	-	0.84092	1
2	1.03 m	0.800 m	0.462 rd (26.5°)	0.164 m	-	-	-	-	0.85321	1
3	1.04 m	1.200 m	0.694 rd (39.7°)	-	0.159 m	0.132 m	0.087 m	0.072 m	0.86562	2

Table E.4 – Numerical values of the quantities defining the $G_{1,1}$ loops

The design choice is dependant of a_i . The moment we go choose the second design instead of the first one is given by :

$$\begin{aligned} c_i &= l - l_i \\ \Leftrightarrow \frac{l_i - a_i}{l - l_i} &= \tan\left(\frac{a_i \cdot (\pi/4)}{l}\right). \end{aligned} \quad (\text{E.8})$$

Solving this equation gives us limits for a_i : Below that limit we have to apply the first design, above we can use the second model.

The table Table E.4 summarises for each wires the numerical value of the quantities defined earlier, as well as the limit between the two design and which design is used.

Bibliography

- [1] E. M. Purcell and N. F. Ramsey. On the Possibility of Electric Dipole Moments for Elementary Particles and Nuclei. *Physical Review*, 78:807, April 1950.
4 citations pages 15, 22, 25, and 106
- [2] A. D. Sakharov. Violation of CP invariance, C asymmetry, and baryon asymmetry of the universe. *JETP Letters*, 5:24–27, 1967.
3 citations pages 15, 19, and 105
- [3] J. M. Pendlebury and al. Revised experimental upper limit on the electric dipole moment of the neutron. *Physics Review D*, 92(9), November 2015.
5 citations pages 15, 22, 25, 29, and 108
- [4] S. Abel and Lebedev. O. Neutron–Electron EDM Correlations in Supersymmetry and Prospects for EDM Searches. *High Energy Physics*, 95(1), January 2006. *Cited page 15*
- [5] ATLAS collaboration. Observation of a new particle in the search for the Standard model Higgs boson with the ATLAS detector at the LHC. *Physics Letters B*, 716:1–29, 2012.
3 citations pages 18, 19, and 105
- [6] CMS collaboration. Observation of a new boson at a mass of 125 GeV with the CMS experiment at the LHC. *Physics Letters B*, 716:30–61, 2012. *3 citations pages 18, 19, and 105*
- [7] A. Bosma. *The distribution and kinematics of neutral hydrogen in spiral galaxies of various morphological types*. PhD thesis, University of Groningen, 1978. *Cited page 18*
- [8] P. J. E. Peebles and B. Ratra. The cosmological constant and dark energy. *Reviews of Modern Physics*, 75:559–599, April 2003. *Cited page 18*
- [9] Super-Kamiokande Collaboration. Evidence for Oscillation of Atmospheric Neutrinos. *Physical Review Letters*, 81(8):1562–1567, August 1998. *Cited page 18*
- [10] S. Riemer-Sørensen and E. Jenssen. Nucleosynthesis Predictions and High-Precision Deuterium Measurements. *Universe*, 3(2):44, May 2017. *2 citations pages 18 and 105*
- [11] Planck collaboration. Planck 2015 results : Cosmological parameters. *Astronomy & Astrophysics*, 594(A13), 2016. *2 citations pages 18 and 105*
- [12] J. Weenink. Baryogenesis. *Seminar Cosmology 2008-2009*, February 2009. *Cited page 18*
- [13] A. G. Cohen, D. B. Kaplan, and A. E. Nelson. Baryogenesis at the weal phase transition. *Nuclear Physics B*, 349:727–742, February 1991. *2 citations pages 19 and 21*
- [14] F. R. Klinkhamer and N. S. Manton. A saddle-point solution in the Weinberg-Salam theory. *Physical Review D*, 30(10):2212–2220, November 1984. *Cited page 19*
- [15] F. Csikor, Z. Fodor, and J. Heitger. End Point of the Hot Electroweak Phase Transition. *Physical Review Letters*, 82(1):21–24, January 1999. *Cited page 19*

- [16] K. Fuyuto and E. Senaha. Sphaleron and critical bubble in the scale invariant two Higgs doublet model. *Physics Letters B*, 747:152–157, May 2015. *Cited page 19*
- [17] T. D. Lee. *Particle Physics and Introduction to Field Theory*. Harwood Academic Publishers, 1981. *2 citations pages 20 and 106*
- [18] V. Kostelecký and N. Russell. Data tables for Lorentz and CPT violation. *Review of Modern Physics*, 83:11–31, March 2011. *2 citations pages 20 and 106*
- [19] J. H. Smith, E. M. Purcell, and N. F. Ramsey. Experimental Limit to the Electric Dipole Moment of the Neutron. *Physical Review Journal*, 108(120), October 1957. *4 citations pages 22, 25, 29, and 106*
- [20] T. D. Lee and C. N. Yang. Question of Parity Conservation in Weak Interactions. *Physical Review*, 104(1):254–258, October 1956. *Cited page 22*
- [21] C. S. Wu and al. Experimental Test of Parity Conservation in Beta Decay. *Physical Review*, 105:1413–1415, January 1957. *Cited page 22*
- [22] C. A. Baker, D. D. Doyle, P. Geltenbort, and al. Electric-dipole-moment searches: Reexamination of frequency shifts for particles in traps. *Physical Review Letters*, 95(131801), September 2006. *4 citations pages 22, 29, 48, and 108*
- [23] R. D Peccei and H. R. Quinn. CP Conservation in the Presence of Pseudoparticles. *Physical Review Letters*, 38(25):1440–1443, June 1977. *Cited page 22*
- [24] C. Abel and al. Search for Axionlike Dark Matter through Nuclear Spin Precession in Electric and Magnetic Fields. *Physics Review X*, 7(041034), November 2017. *Cited page 23*
- [25] H. Banerjee, D. Chatterjee, and P. Mitra. Is there still a strong CP problem? *Physics Letters B*, 573:109–114, August 2003. *Cited page 23*
- [26] J. H. Christenson, J. W. Cronin, V. L. Fitch, and R. Turlay. Evidence for the 2π Decay of the K_2^0 Meson. *Physical Review Letters*, 13(4):138–140, July 1964. *Cited page 23*
- [27] KTeV Collaboration. Observation of Direct CP Violation in $K_{S,L} \rightarrow \pi\pi$ Decays. *Physical Review Letters*, 83(1):22–27, July 1999. *Cited page 23*
- [28] NA48 Collaboration. A new measurement of direct CP violation in two pion decays of the neutral kaon. *Physics Letters B*, 465:335–348, October 1999. *Cited page 23*
- [29] BABAR Collaboration. Measurement of CP-Violating Asymmetries in B^0 Decays to CP Eigenstates. *Physical Review Letters*, 86(12):2515–2522, March 2001. *Cited page 23*
- [30] Belle Collaboration. Observation of Large CP Violation in the Neutral B Meson System. *Physical Review Letters*, 87(9), August 2001. *Cited page 23*
- [31] LHCb Collaboration. First Observation of CP Violation in the Decays of B_s^0 Mesons. *Physical Review Letters*, 110(221601), May 2013. *Cited page 23*
- [32] LHCb Collaboration. Observation of CP Violation in Charm Decays. *Physical Review Letters*, 122(211803), May 2019. *Cited page 23*
- [33] A. Czarnecki and B. Krause. On the Dipole Moments of Fermions at Two Loops. November 1997. *Cited page 23*
- [34] A. Czarnecki and B. Krause. Neutron Electric Dipole Moment in the Standard Model: Complete Three-Loop Calculation of the Valence Quark Contributions. *Physical Review Letters*, 78(23):4339–4342, June 1997. *Cited page 23*
- [35] M. Pospelov and A. Ritz. Electric dipole moments as probes of new physics. *Annals of Physics*, 318:119–169, May 2005. *Cited page 23*
- [36] I. B. Khriplovich and A. R. Zhitnitsky. What is the value of the neutron electric dipole moment in the Kobayashi-Maskawa model? *Physics Letters*, 109B(6):490–492, March 1982. *Cited page 24*

- [37] E. E. Salpeter. Some Atomic Effects of an Electronic Electric Dipole Moment. *Physical Review*, 112(5):1642–1648, December 1959. *Cited page 25*
- [38] T. Liu, Z. Zhao, Z. L. Li, and H. Gao. Experimental constraint on quark electric dipole moments. *Physical Review D*, 97(7):965–968, April 2018. *Cited page 25*
- [39] ACME collaboration. Improved limit on the electric dipole moment of the electron. *Nature*, 562(7727):355–360, October 2018. *Cited page 25*
- [40] G. W. Bennett and al. (muon (g-2) collaboration). Improved limit on the muon electric dipole moment. *Physical Review D*, 80(5), September 2009. *Cited page 25*
- [41] Belle Collaboration. Search for the Electric Dipole Moment of the τ Lepton. *Physics Letters B*, 551(1-2):16–26, 2003. *Cited page 25*
- [42] B. Graner, Y. Chen, and B. R. Lindahl, E. G. and Heckel. Reduced Limit on the Permanent Electric Dipole Moment of ^{199}Hg . *Physical Review Letters*, 116(16), April 2016. *Cited page 25*
- [43] N. Yamanaka. Electric dipole moment of the deuteron in the standard model with NN - ΛN - ΣN coupling. *Nuclear Physics A*, 963:33–51, July 2017. *Cited page 25*
- [44] M. A. Rosenberry and T. E. Chupp. Atomic Electric Dipole Moment Measurement Using Spin Exchange Pumped Masers of ^{129}Xe and ^3He . *Physical Review Letters*, 86(1):22–25, January 2001. *Cited page 25*
- [45] M. Bishof and al. Improved limit on the ^{225}Ra electric dipole moment. *Physical Review C*, 94(2), August 2016. *Cited page 25*
- [46] B. C. Regan, E. D. Commins, and D. Schmidt, C. J. and DeMille. New Limit on the Electron Electric Dipole Moment. *Physical Review Letters*, 88(7), February 2002. *Cited page 25*
- [47] S. A. Murthy, D. Krause Jr., Z. L. Li, and L. R. Hunter. New Limits on the Electron Electric Dipole Moment from Cesium. *Physical Review Letters*, 63(9):965–968, August 1989. *Cited page 25*
- [48] E. S. Ennsberg. Experimental Upper Limit for the Permanent Electric Dipole Moment of Rb^{85} by Optical-Pumping Techniques. *Physical Review*, 153(1):36–43, January 1967. *Cited page 25*
- [49] J. Chadwick. The existence of a neutron. *Proceedings of the Royal Society A*, 136(830):682–708, June 1932. *Cited page 25*
- [50] V. Bondar and al. Losses and depolarization of ultracold neutrons on neutron guide and storage materials. *Physical Review C*, 96(035205), September 2017. *2 citations pages 26 and 45*
- [51] R. Golub, D. Richardson, and S. K. Lamoreaux. *Ultra-Cold Neutrons*. CRC Press, 1991. *Cited page 26*
- [52] I. B. Khriplovich and S. K. Lamoreaux. *CP Violation Without Strangeness: Electric Dipole Moments of Particles, Atoms, and Molecules*. Springer Science and Business Media, 2012. *Cited page 27*
- [53] Victor Hélaine. *Mesure du moment dipolaire électrique du neutron: analyse simultanée de spin et analyse de données*. PhD thesis, Université de Caen/Basse-Normandie, 2014. *3 citations pages 28, 36, and 41*
- [54] Becker and al. Neutron production and thermal moderation at the PSI UCN source. *Physic Research A*, 777:20–27, March 2015. *2 citations pages 28 and 53*
- [55] F. M. Piegsa and al. New source for ultracold neutrons at the Institut Laue-Langevin. *Physical Review C*, 90, July 2014. *Cited page 28*

- [56] I. S. Altarev and al. A search for the electric dipole moment of the neutron using ultracold neutrons. *Nuclear Physics A*, 341:269–283, June 1980. *Cited page 29*
- [57] W. B. Dress, P. D. Miller, J. M. Pendlebury, P. Perrin, and N. F. Ramsey. Search for an electric dipole moment of the neutron. *Physical Review D*, 15(1):9–21, January 1977. *Cited page 29*
- [58] P.J. Mohr, D.B. Newell, and B.D. Taylor. CODATA Recommended Values of the Fundamental Physical Constants: 2014. *Reviews of Modern Physics*, 88(3):16–26, September 2016. *2 citations pages 30 and 108*
- [59] S. Afach and al. A device for simultaneous spin analysis of ultracold neutrons. *The European Physical Journal A*, 51(11):143, November 2015. *Cited page 36*
- [60] N. F. Ramsey. A Molecular Beam Resonance Method with Separated Oscillating Fields. *Physical Review*, 78(6):695–699, June 1950. *Cited page 41*
- [61] C. A. Baker and al. Improved Experimental Limit on the Electric Dipole Moment of the Neutron. *Physical Review Letters*, 97, September 2006. *2 citations pages 41 and 51*
- [62] C. A. Baker and al. Apparatus for measurement of the electric dipole moment of the neutron using a cohabiting atomic-mercury magnetometer. *Nuclear Instruments and Methods in Physics Research A*, 736:184–203, February 2014. *Cited page 42*
- [63] The nEDM collaboration. Technical design report 2018. To be published, 2018. *3 citations pages 44, 46, and 56*
- [64] P. G. Harris, J. M. Pendlebury, and N. E. Devenish. Gravitationally enhanced depolarization of ultracold neutrons in magnetic-field gradients. *Physical Review D*, 89, January 2014. *2 citations pages 45 and 47*
- [65] S. Afach and al. Gravitational Depolarization of Ultracold Neutrons: Comparison with Data. *Physics Review D*, 92(052008), September 2015. *Cited page 46*
- [66] A. G. Redfield. The Theory of Relaxation Processes. *Advances in Magnetic Resonance*, 1:1–32, 1965. *Cited page 46*
- [67] G. Pignol, M. Guigue, A. Petukhov, and R. Golub. Frequency shifts and relaxation rates for spin-1/2 particles moving in electromagnetic fields. *Physical Review A*, 92(053407), November 2015. *3 citations pages 46, 47, and 48*
- [68] J. M. Pendlebury and al. Geometric-pahse-induced false electric dipole moment signals for particles in traps. *Physical Review A*, 70, September 2004. *Cited page 47*
- [69] S. Afach and al. Measurement of a false electric dipole moment signal from ^{199}Hg atoms exposed to an inhomogeneous magnetic field. *European Physical Journal D*, 69(225), October 2015. *Cited page 47*
- [70] C. Abel and al. The n2EDM experiment at the Paul Scherrer Institute. *arXiv:1811.02340*, February 2019. *Cited page 52*
- [71] Dieter Ries. *The Source for Ultracold Neutrons at the Paul Scherrer Institute - Characterisation, Optimisation, and International Comparison*. PhD thesis, ETH Zürich, 2016. *Cited page 53*
- [72] G. Bison, Daum. M., K. Kirch, B. Lauss, D. Riel, P. Schmidt-Wellenburg, and G. Zsigmond. Comparison of ultracold neutron sources for fundamental physics measurements. *Physical Review C*, 95, April 2017. *Cited page 53*
- [73] G. Zsigmond. The MCUCN simulation code for ultracold neutron physics. *Nuclear Instruments and Methods A*, 881:16–26, February 2018. *Cited page 53*
- [74] K. Green and al. Performance of an atomic mercury magnetometer in the neutron EDM experiment. *Nuclear Instruments and Methods in Physics Research A*, 404:381–393, February 1998. *Cited page 55*

- [75] P. Schmidt-Wellenburg. The quest to find an electric dipole moment of the neutron. *ArXiv:1607.06609v2*, October 2017. *Cited page 56*
- [76] P. Curie. Sur la symétrie dans les phénomènes physiques, symétrie d'un champ électrique et d'un champ magnétique. *Journal de Physique Théorique et Appliquée*, 3(1):393–415, 1894. *Cited page 61*
- [77] P. Hammond. Electric and magnetic images. *Proceeding of the IEE part C*, 107:306–313, September 1960. *Cited page 68*
- [78] G. Quémener. Notes on a new set of harmonic polynomial series expansions to parametrize a magnetic field. Internal note, May 2011. *Cited page 71*
- [79] G. Pignol. Standardized adequate basis of harmonic polynomials to parametrize the magnetic field in the nEDM experiment. Internal note, July 2016. *Cited page 71*
- [80] C. Abel and al. Magnetic-field uniformity in neutron electric-dipole-moment experiments. *Physical Review A*, 99(042112), April 2019. *2 citations pages 72 and 93*
- [81] G. Bison and D. Pais. Private communication. *2 citations pages 84 and 87*
- [82] Yoann Kermaïdic. *Mesure du moment dipolaire électrique du neutron : Analyse de données et développement autour du ^{199}Hg* . PhD thesis, Université de Grenoble, 2016. *3 citations pages 84, 88, and 133*
- [83] G. Pignol and S. Roccia. Improved Experimental Limit to the Electric Dipole Moment of the Neutron. *Physical Review*, 85(042105), April 2012. *Cited page 91*
- [84] V. Legat. INTRODUCTION AUX ELEMENTS FINIS ...et au génie logiciel numérique en langage C. notes de cours MECA1120, Ecole polytechnique de Louvain, 2018. *Cited page 146*
- [85] M. Maldonado-Veláquez, L. Barrón-Palos, C. Crawford, and W. M. Snow. Magnetic field devices for neutron spin transport and manipulation inprecise neutron spin rotation measurements. *Nuclear Instruments and Methods in Physics Research A*, 854:127–133, May 2017. *Cited page 160*

**Mesure du moment dipolaire électrique du neutron à l’Institut Paul Scherrer :
Production de champs magnétiques pour l’expérience n2EDM**

Résumé

Le travail réalisé au cours de cette thèse concerne le développement du système de bobines de l’expérience n2EDM à l’Institut Paul Sherrer (PSI). Le but de cette expérience est de mettre en évidence de nouvelles sources de violation CP à travers la mesure du moment dipolaire électrique du neutron. L’actuelle limite supérieure sur la mesure de nEDM, 2.9×10^{-26} e.cm (90% C.L.) a été obtenue par la collaboration RAL-Sussex-ILL en 2006.

L’expérience n2EDM vise à améliorer d’un ordre de grandeur la sensibilité statistique en gardant sous contrôle les effets systématiques. Cela requiert la production d’un champ magnétique très uniforme. Les non-uniformités de ce dernier sont en effet responsable de la dépolarisation des neutrons et impliqués dans plusieurs effets systématiques.

Dans le premier chapitre, les motivations physiques sont discutées. Le second chapitre décrit le principe de mesure de l’expérience n2EDM, ainsi que l’importance de l’uniformité du champ magnétique. Le chapitre s’achève par une présentation globale du dispositif expérimental. Le troisième chapitre présente le logiciel COMSOL et discute du design et des performances de la bobine B_0 , en charge de la production du champ magnétique principal. Dans le quatrième chapitre, le système de bobines correctrices chargées de corriger les non-uniformités du champ magnétique et celles devant produire des gradients spécifiques sont présentées. Finalement, le cinquième et dernier chapitre présente l’étude des dipôles magnétiques localisés et de leur influence sur l’expérience.

Mots-clés : UCN, champ magnétique, COMSOL, EDM



Measurement of the neutron electric dipole moment at the Paul Scherrer Institute : Production of magnetic fields for the n2EDM experiment

Abstract

This work presents the design of the coils system developed for the n2EDM experiment at the Paul Sherrer Institute (PSI). The goal of this experiment is to reveal new sources of CP violation through the measurement of the neutron electric dipole moment. The current upper limit of the nEDM measurement, 2.9×10^{-26} e.cm (90% C.L.) was achieved by the RAL-Sussex-ILL collaboration in 2006.

The n2EDM experiment aims at improving by one order of magnitude the statistical sensitivity while keeping under control the systematics effects. It requires to produce a very uniform field, its non-uniformities being responsible of the neutron’s depolarization and of severals systematic effects.

In the first chapter, the theoretical motivation are discussed. The second chapter describes the measurement principle of the n2EDM experiment, as well as the importance of the magnetic field uniformity. This chapter ends by an overview of the apparatus. The third chapter introduces the COMSOL software and discuss the design and the performances of the B_0 coil, in charge of the production of the main magnetic field. In the fourth chapter, the correcting coils used to suppress the non-uniformities of the magnetic field and the ones which produce specific gradients are presented. Finally, the fifth and last chapter talks about the study of localised magnetic dipoles and their influence on the experiment.

Keywords : UCN, magnetic fields, COMSOL, EDM